# Investigating flotation at the bench scale - the effect of design modifications on flotation performance and the link to particle size

**Isobel Mackay**

Department of Earth Science and Engineering
Imperial College London

Supervisor: Dr. Pablo Brito-Parada & Prof. Jan Cilliers

submitted in partial fulfilment of the requirements for the degree of
Doctor of Philosophy in Engineering and
the Diploma of Imperial College

September 25, 2019

# Abstract

There is a huge potential to optimise the froth flotation industry as even small improvements in the extraction of metals from the mineral ores can translate to a substantially higher revenue. Typically, laboratory studies into froth flotation involve batch tests where the system does not operate at steady-state, making it difficult to directly apply results to industrial systems. In this work, a continuously overflowing flotation cell, which does operate at steady state, has been used to investigate the effects of different operating conditions on flotation performance. This work used two experimental systems which are more comparable to industrial systems than previous studies using the same bench scale flotation cell.

The first system investigated in this thesis used a copper tailings ore. The effects of varying the particle size distribution on the flotation performance and froth stability were investigated. For the first time, a direct comparison between two measures of stability was made, and both measures showed an optimum in froth stability with an intermediate particle size distribution. This optimal particle size distribution also resulted in an improved copper recovery which has important implications for the reprocessing of tailings material via froth flotation.

The second system investigated used a synthetic magnetite-silica ore. This ore allows more control over the system, whilst still providing a good proxy for industrial flotation. This system was used to investigate the effects that inserting two retrofit design modifications (horizontal meshes) into the cell had on flotation performance. These meshes were designed to provide a more quiescent environment at the pulp-froth interface (PFI) and reduce particle detachment. The “basic mesh” shifted the grade-recovery curve to an improved grade, while the “blocked mesh” resulted in a significant improvement in recovery and a reduction in entrained magnetite.

Positron emission particle tracking (PEPT), a technique that tracks the movement of radioactive tracer particles, was used to investigate the mechanisms that resulted in the improved flotation performance when using the meshes. PEPT experiments were performed with different tracer types and tracer sizes. It was shown that the presence of the mesh reduced the presence of swirl at the pulp-froth interface, and formed a secondary, more quiescent, pulp zone with a shallower froth. In some cases, a mixing loop formed in this secondary pulp zone which promoted the reattachment of detached valuable mineral. It was also shown that both meshes improved the flotation of the coarsest tracer size indicating that the meshes can be used to improve the recovery of coarse particles.

For the first time, a continuous bench scale flotation cell has been used to investigate the relationship between design modifications, particle size and the flotation performance. This was done using two different ores, both more complex than what has previously been

investigated in similar equipment. These experiments also utilised PEPT to further the understanding of the effect that design modifications have on the flotation performance of different types of particle.

The results of this work have two primary applications to improving the flotation of both fine and coarse particles for improving the sustainability of the minerals processing industry. The first application relates to fine particle flotation by finding an optimal feed particle size distribution. This will enhance the ability to reprocess tailings material by froth flotation and therefore improve the sustainability of the industry. The second application relates to coarse particle flotation by using a simple retrofit design modification to increase the floatability of these particles. This will improve sustainability within minerals processing by reducing the comminution requirements and therefore energy consumption. There is, however, more work needed to investigate these modifications further to ensure they are applicable at an industrial scale.

## Plagiarism declaration

I hereby declare that all of the work presented in this thesis – except that which is appropriately acknowledged and referenced as such – is my own, and that it has not been submitted in fulfilment of the requirements of any other degree at Imperial College London or elsewhere.

*Isobel Mackay*

*September 25, 2019*

The copyright of this thesis rests with the author and is made available under a Creative Commons Attribution Non-Commercial No Derivatives licence. Researchers are free to copy, distribute or transmit the thesis on the condition that they attribute it, that they do not use it for commercial purposes and that they do not alter, transform or build upon it. For any reuse or redistribution, researchers must make clear to others the licence terms of this work.



# Acknowledgements

The financial support of EPSRC and SCI for this thesis are gratefully acknowledged.

I would first like to thank Dr. Pablo Brito-Parada for his outstanding supervision and unwavering support. Thank you for giving me such fantastic opportunities not only in my academic career, but also giving me the freedom to pursue other activities that I am passionate about. And thank you for putting up with my inability to use commas correctly! Thank you also to Prof. Jan Cilliers for supervising me over the past four years and of course for his engaging Minerals Processing lectures that inspired me to do this PhD in the first place. In addition, I would like to thank Prof. Alvaro Videla for his supervision and care whilst I was working in Chile, and his continued supervision via Skype. I am also grateful for the support and friendship from the varied members of the Advanced Minerals Processing Research Group over the years, especially Kathryn and Stephen for their expertise, and Alex, Angus, Pancho and Diego not only for their technical help, but also their great friendship. A big thank you goes to Michael van Heerden at the iThemba labs for all of his help in conducting the PEPT experiments.

Thank you to both Lizzie and Ian, for not only supporting me through my undergraduate degree, but also continuing their fantastic support and mentorship throughout my PhD. Thank you also for a thoroughly enjoyable time herding cats, spotting goats and eating ice cream in Cyprus.

I would not have been able to do this PhD without the fantastic support of all of my friends. A special shout out goes to the many different tenants of Ralph Court especially Aki, Florian, Reuben and Merlin. A day in the office would not have been complete without coffee/lunch/crossword with Pancho, Cata, Becky, Diego, Dobbin, Pablo, Dennis, Jorge and of course Chandra. Thank you to my friends in choir, quiz and scouting for helping me to maintain my sanity and giving me a good excuse to leave the lab.

Finally, I am extremely thankful for my family. I would not be where I am today without their love and understanding, emotional support and their eternal belief in me. To my Mum: It'll be your turn soon, but I know you can do it. I am so proud of you! And of course to Peter, who has been my rock through this entire process. Thank you for always making me smile, even through floods of tears, for being eternally patient and for not taking my grumpiness personally. I love you.

*To Mum, Dad and Hugh,*

*and to Peter.*

# Contents

**List of Tables** **10**

**List of figures** **11**

**List of Abbreviations and Symbols** **16**

**1 Introduction** **17**
1.1 Motivation . . . 17
1.2 Objectives . . . 18
1.3 Thesis structure . . . 19

**2 Background** **21**
2.1 Introduction . . . 21
2.2 Principles of Flotation . . . 22
2.3 Flotation Chemistry . . . 24
2.3.1 Collectors . . . 25
2.3.2 Frothers . . . 26
2.3.3 Regulators . . . 26
2.4 Flotation Performance . . . 27
2.4.1 Metallurgical performance . . . 27
2.4.2 Froth stability . . . 29
2.4.3 Particle size effects . . . 31
2.4.4 Particle size and froth stability . . . 35
2.5 Flotation Cell Design . . . 37
2.5.1 Mechanical vs. column flotation . . . 37
2.5.2 Design modifications . . . 38
2.5.3 Laboratory scale research . . . 41
2.6 Positron Emission Particle Tracking . . . 42
2.6.1 PEPT in flotation . . . 43
2.7 Conclusions . . . 45

**3 Experimental Techniques** **47**
3.1 Introduction . . . 47
3.2 Flotation Equipment . . . 47
3.2.1 Laboratory scale, non-overflowing flotation column . . . 47
3.2.2 Continuous bench scale cell . . . 48
3.3 Flotation Environments . . . 49
3.3.1 Copper tailings ore . . . 50
3.3.2 Two-species system . . . 51
3.4 Data Collection . . . 54
3.4.1 Dynamic froth stability experiments . . . 54
3.4.2 Air recovery experiments . . . 55
3.4.3 Data processing . . . 57

3.5 Sample Collection . . . 58
3.5.1 Non-overflowing column . . . 58
3.5.2 Continuously overflowing cell . . . 58
3.6 Sample Analysis . . . 58
3.6.1 Solids flowrate as a proxy for recovery . . . 58
3.6.2 Grade and mineralogical analysis of the copper tailings ore . . . 59
3.6.3 Concentrate grade of the magnetite silica ore . . . 60
3.6.4 Particle size . . . 60
3.7 Positron Emission Particle Tracking . . . 61
3.7.1 Tracer production . . . 62
3.7.2 Tracer usage and disposal . . . 63
3.7.3 Data collection and analysis . . . 63

**4 The effects of particle size on the flotation performance of a copper tailings ore 68**
4.1 Introduction . . . 68
4.1.1 Ore characterisation . . . 69
4.2 Froth Stability . . . 71
4.2.1 Dynamic froth stability . . . 71
4.2.2 Air Recovery . . . 73
4.2.3 Comparison between stability measures . . . 75
4.3 Flotation Performance . . . 76
4.3.1 Dynamic froth stability . . . 76
4.3.2 Air recovery . . . 77
4.4 Discussion . . . 79
4.4.1 Implications for reprocessing mine tailings via froth flotation . . . 80
4.5 Conclusions . . . 81

**5 Assessing the effect of retrofit modifications on flotation performance 83**
5.1 Introduction . . . 83
5.2 Steady State Operation . . . 85
5.3 Froth Stability . . . 85
5.4 Flotation Performance . . . 88
5.4.1 Entrainment . . . 89
5.5 Particle Size Effects . . . 92
5.6 Conclusions . . . 94

**6 Investigating the impact of flotation cell retrofit design modifications on particle behaviour 96**
6.1 Introduction . . . 96
6.2 Bulk Tracer Flow . . . 99
6.3 Velocities . . . 106
6.4 Occupancy . . . 117
6.5 Discussion . . . 124
6.6 Conclusions . . . 128

**7 Analysing the effect of different flotation cell retrofit design modifications on different particle sizes 130**
7.1 Introduction . . . 130
7.2 Bulk Tracer Flow . . . 131
7.3 Velocities . . . 140
7.4 Occupancy . . . 151
7.5 Discussion . . . 158
7.6 Conclusions . . . 159

**8 Conclusions** **161**
8.1 Key findings . . . . . 161
8.2 Further work . . . . . 164

**References** **167**

**Appendices** **174**

**A Publications** **175**
A.1 Dynamic froth stability of copper flotation tailings
(Minerals Engineering - *published May 2018*) . . . . . 175
A.2 The link between particle size and froth stability - implications for reprocessing of flotation tailings
(Journal of cleaner production - *published September 2019*) . . . . . 175

**B Analysis of variance results from the experiments with the two-species system in chapter 5.** **193**
B.1 Flotation Performance . . . . . 193
B.1.1 Entrainment . . . . . 194
B.2 Particle Size . . . . . 195

**C PEPT tracer locations** **196**

**D Figure Replication Permissions** **200**

# List of Tables


3.1 Particle size distributions for the hydrocyclone overflow and underflow and the seven feeds used for dynamic froth stability tests (subscript $\Sigma$) and the three feeds used for air recovery tests (subscript $\alpha$) in chapter 4. . . . . 52

4.1 Particle size distributions of feeds used in dynamic froth stability experiments. 69
4.2 Particle size distributions and copper content for the three different feeds used in air recovery experiments. . . . . 69
4.3 Average equilibrium heights, $H_{eq}$, and dynamic froth stability factors, $\Sigma$, for all particle size distributions and superficial gas velocities, $J_g$, investigated. 72
4.4 ANOVA table of air recovery with particle size distribution. Variables that are significant are highlighted. . . . . 74
4.5 ANOVA table of concentrate grade with particle size distribution and superficial gas velocity. Variables that are significant are highlighted. . . . . 78
4.6 ANOVA table of copper recovery with particle size distribution and superficial gas velocity. Variables that are significant are highlighted. . . . . 78

5.1 ANOVA table of air recovery for changes in superficial gas velocity and the different design modifications. Significant values are highlighted. . . . . 87

B.1 Silica Recovery . . . . . 193
B.2 Silica Grade . . . . . 193
B.3 Water Flowrate . . . . . 194
B.4 Magnetite Flowrate . . . . . 194
B.5 Entrainment Factor . . . . . 194
B.6 Flowrate of $< 10\,\mu\mathrm{m}$ particles . . . . . 195
B.7 Flowrate of $> 80\,\mu\mathrm{m}$ particles . . . . . 195

# List of Figures


2.1 A mechanical flotation cell showing the froth and pulp zones. . . . . 23
2.2 Foam structure illustrating the Plateau borders between bubbles (Neethling et al., 2003). . . . . 24
2.3 Schematic of a collector adsorbed onto the surface of a mineral particle and then attached to a bubble. . . . . 25
2.4 Idealised grade-recovery curve, with the different coloured curves representing different hypothetical operating conditions. . . . . 28
2.5 Industrial data showing the relationship between (a) solids content of the concentrate and relative grade and (b) solids flowrate to the concentrate and relative recovery (Norori-McCormac et al., 2017). . . . . 28
2.6 Recovery by particle size from industrial flotation of a variety of different sulfide ores (Kohmuench et al., 2018). . . . . 31
2.7 Comparison between mechanical flotation cells and column flotation cells. . 38
2.8 A Denver flotation cell showing PEPT tracer motions (Waters et al., 2008). . 44

3.1 Illustration of the non-overflowing laboratory scale flotation column. . . . . 48
3.2 Details of the design of the continuously overflowing flotation cell. The concentrate is pumped from the launder back into the pulp zone of the cell. Measurements given in the schematic in (a) are in millimetres. . . . . 49
3.3 Particle size distributions of the hydrocyclone overflow and underflow streams from the copper tailings reprocessing plant. . . . . 51
3.4 Particle size distribution of the synthetic magnetite and silica ore. . . . . 53
3.5 The two different mesh designs used in this chapter: (a) "Basic Mesh" and (b) "Blocked Mesh". Both meshes have a thickness of $20\,\mathrm{mm}$, other illustrated dimensions are in millimetres. . . . . 54
3.6 Froth height growth for experiments with d90 of $279\,\mu\mathrm{m}$ over 30 minutes of operation at two different superficial gas velocities. Intervals represent one standard deviation . . . . . 55
3.7 Screen shots of measuring (a) froth height with labVIEW and (b) froth velocity with Froth Tracker . . . . . 56
3.8 The 3D printed scoop inserted into the launder of the cell. . . . . 59
3.9 The Accupyc II 1340 Gas Pycnometer (a) and the $1\,\mathrm{cm}^3$ sample cup (b). . . 61
3.10 The continuously overflowing flotation cell inside the PET camera. . . . . 62
3.11 Different $N$ and $f$ combinations for a hydrophobic tracer in the unmodified cell . . . . . 65
3.12 (a) Illustration of how the cell is divided into voxels for processing, wedges averaged to create vertical slices are indicated by the shaded regions. The two different mesh designs used in this chapter: (b) basic mesh and (c) blocked mesh, with holes labelled $A - D$. Red arrows indicate the six wedges averaged to create the vertical slices. . . . . 66

3.13 Graph of tracer height over time for the $500\,\mu\mathrm{m}$ tracer in the unmodified cell. The pink dashed line shows the height of the lip of the cell, the yellow line shows the height of the baffles and the black dashed line shows the height of the plane of the impeller. . . . . 67

4.1 Mineral composition of the different feeds, from the QEMSCAN analysis, split into (a) minerals that comprise more than 5% of the feed and (b) minerals that are less than 2.5% of the feed. . . . . 70
4.2 Chalcopyrite liberation by size from QEMSCAN analysis of the three different feeds. . . . . 71
4.3 Dynamic froth stability for different particle size distributions at a range of superficial gas velocities. Error bars represent one standard deviation. . . . 72
4.4 The variation in air recovery over time at a constant condition, with 10 minute measurement windows highlighted by light grey vertical bands and a confidence band for the average value of air recovery represented by the dark grey horizontal band. Error bars represent a 95% confidence interval. . 73
4.5 Heat map of air recovery for different feed $d_{90}$s and superficial gas velocities. 74
4.6 The variation in air recoveries with varying feed size at different superficial gas velocity. Error bars are one standard deviation. . . . . 74
4.7 Comparison of dynamic froth stability (pink and left hand axis) and air recovery (blue and right hand axis) for the same batch of copper tailings ore. Error bars are one standard deviation. . . . . 75
4.8 Concentrate grade from batch flotation tests and dynamic froth stability at a superficial gas velocity of $1.44\,\mathrm{cm\,s^{-1}}$ . Error bars represent one standard deviation. . . . . 76
4.9 Copper recovery from batch flotation tests and dynamic froth stability at a superficial gas velocity of $1.44\,\mathrm{cm\,s^{-1}}$ . Error bars represent one standard deviation. . . . . 76
4.10 Concentrate grade for samples taken at $0.92\,\mathrm{cm\,s^{-1}}$ and $1.18\,\mathrm{cm\,s^{-1}}$. Error bars are 1 standard deviation. . . . . 78
4.11 Copper recovery to the concentrate for samples taken at $0.92\,\mathrm{cm\,s^{-1}}$ and $1.18\,\mathrm{cm\,s^{-1}}$. Error bars are 1 standard deviation. . . . . 79

5.1 The two different mesh designs used in this chapter: (a) "Basic Mesh" and (b) "Blocked Mesh". Dimensions are in millimetres. . . . . 84
5.2 (a) The variation in air recovery over time at a constant condition, with 10 minute measurement windows highlighted by light grey vertical bands. The average values for each of these 10 minute windows is shown in sub-figure (b) with error bars representing the 95% confidence interval. . . . . 86
5.3 Adjusted air recovery data for all three design types investigated. Error bars are 95% confidence intervals. . . . . 87
5.4 Adjusted flotation performance data Grade-Recovery Curve. Arrows point in direction of increasing superficial gas velocity. Error bars are 95% confidence intervals. . . . . 89
5.5 (a) Water flowrate to the concentrate, (b) Magnetite flowrate and (c) entrainment factor of magnetite in the concentrate for changing design modifications and superficial gas velocities. Error bars 95% confidence intervals. 91
5.6 Indicative recovery of fine particles (a) and coarse (b) particles. Error bars are 95% confidence intervals. . . . . 93

6.1 (a) Illustration of how the flotation cell volume is divided into voxels for processing, wedges averaged to create vertical slices are indicated by the shaded regions. The two different mesh designs used in this chapter: (b) basic mesh and (c) blocked mesh, with holes labelled $A - D$. Red arrows indicate the location of the six wedges averaged to create the vertical slices. 98
6.2 Streamlines within the cell, with each of the design types, for (a) the hydrophobic and (b) hydrophilic tracers. Both tracer types are $500\,\mu\mathrm{m}$ in diameter. Red arrows are added to highlight some flow patterns and are indicative only. The impeller and the level of the overflowing lip are shown in dashed blue lines and the position of the mesh shown in solid blue lines. . 102
6.3 Bulk flow of the hydrophobic tracer, in the unmodified cell, at different heights through the cell. . . . . 103
6.4 Bulk flow of the hydrophilic tracer, in the unmodified cell, at different heights through the cell. . . . . 104
6.5 Horizontal slices of streamlines of the (a) hydrophobic and (b) hydrophilic tracer in the different cell designs at a height of $120\,\mathrm{mm}$. The location of the mesh is outlined in black. . . . . 105
6.6 Horizontal slices of streamlines of the (a) hydrophobic and (b) hydrophilic tracer in the different cell designs at a height of $140\,\mathrm{mm}$. The location of the mesh is outlined in black. . . . . 105
6.7 Tracer vertical velocity within the cell for (a) the hydrophobic and (b) hydrophilic tracers. Blue shades are negative velocities, red are positive and the darker the colour represents high magnitudes. White corresponds to 0 vertical velocity. . . . . 110
6.8 Vertical velocity of the hydrophobic tracer, in the unmodified cell, at different heights through the cell. . . . . 111
6.9 Vertical velocity of the hydrophilic tracer, in the unmodified cell, at different heights through the cell. . . . . 112
6.10 Plot of vertical velocity with radial location for different heights within the froth of the cell. Error bars are the standard error after averaging the value across 6 slices. The mesh is located between h=100 and h=120. . . . . 113
6.11 Plot of vertical velocity with height at different radii from the centre of the cell. Error bars are the standard error after averaging the value across 6 slices. The mesh is located between h=100 and h=$120\,\mathrm{mm}$. . . . . 114
6.12 Horizontal slices of vertical velocity of different tracers though the meshes for the (a) hydrophobic tracer and (b) hydrophilic tracer. The location of the mesh is outlined in black. . . . . 115
6.13 Azimuthal velocity component of the tracer in the froth for the (a) hydrophobic and (b) hydrophilic. Positive is defined as the same direction as the impeller rotation. . . . . 116
6.14 Tracer occupancy within the cell for (a) the hydrophobic and (b) hydrophilic tracers. Both tracer types are $500\,\mu\mathrm{m}$ in diameter.occupancy calculated by totalling the time the tracer spent each voxel then normalising by total length of time the tracer spent in that slice and normalised by the volume of the voxel. Darker blue shades represent higher occupancys i.e. voxels where the tracer spent a higher proportion of time. . . . . 120
6.15 Plot of occupancy with radial location for different heights within the froth of the cell. Error bars are the standard error after averaging the value across 6 slices. The mesh is located between h=100 and h=$120\,\mathrm{mm}$. . . . . 121
6.16 Plot of occupancy with height at different radii from the centre of the cell. Error bars are the standard error after averaging the value across 6 slices. The mesh is located between h=100 and h=120. . . . . 122

6.17 Horizontal slices of occupancy of different tracers though the meshes; (a) hydrophobic tracer, (b) hydrophilic tracer. The location of the mesh is outlined in black. . . . . 123
6.18 Schematics of the different zones in the unmodified cell and when a mesh is inserted. . . . . 126

7.1 Streamlines of the tracer in the froth, with each of the cell designs, for hydrophobic tracers of different sizes (a) $400\,\mu\mathrm{m}$ and (b) $500\,\mu\mathrm{m}$ and (c) $600\,\mu\mathrm{m}$. Red arrows are added to highlight some flow patterns and are indicative only. The impeller and the level of the overflowing lip are shown in dashed blue lines and the position of the mesh shown in solid blue lines. . 134
7.2 Bulk flow of the $400\,\mu\mathrm{m}$ tracer at different heights through the unmodified cell. . . . . 135
7.3 Bulk flow of the $500\,\mu\mathrm{m}$ tracer at different heights through the unmodified cell. . . . . 136
7.4 Bulk flow of the $600\,\mu\mathrm{m}$ tracer at different heights through the unmodified cell. . . . . 137
7.5 Horizontal slices of streamlines through the meshes at a height of $120\,\mathrm{mm}$ for the (a) $400\,\mu\mathrm{m}$, (b) $500\,\mu\mathrm{m}$ and (c) $600\,\mu\mathrm{m}$ tracers. The location of the mesh is outlined in black. . . . . 138
7.6 Horizontal slices of streamlines above the meshes at a height of $140\,\mathrm{mm}$ for the (a) $400\,\mu\mathrm{m}$, (b) $500\,\mu\mathrm{m}$ and (c) $600\,\mu\mathrm{m}$ tracers. The location of the mesh is outlined in black. . . . . 139
7.7 Vertical velocity component of the tracer in the froth for hydrophobic tracers of different sizes (a) $400\,\mu\mathrm{m}$ and (b) $500\,\mu\mathrm{m}$ and (c) $600\,\mu\mathrm{m}$. . . . . 143
7.8 Vertical velocity of the $400\,\mu\mathrm{m}$ tracer at different heights through the unmodified cell. . . . . 144
7.9 Vertical velocity of the $500\,\mu\mathrm{m}$ tracer at different heights through the unmodified cell. . . . . 145
7.10 Vertical velocity of the $600\,\mu\mathrm{m}$ tracer at different heights through the unmodified cell. . . . . 146
7.11 Plot of Vertical Velocity with radial location for different heights within the froth of the cell. Error bars are the standard error after averaging the value across 6 slices. The mesh is located between h=100 and h=120. . . . . 147
7.12 Plot of Vertical Velocity with height at different radii from the centre of the cell. Error bars are the standard error after averaging the value across 6 slices. The mesh is located between h=100 and h=$120\,\mathrm{mm}$. . . . . 148
7.13 Horizontal slices of Vertical Velocity of the different tracers through the mesh; (a) $400\,\mu\mathrm{m}$ tracer, (b) $500\,\mu\mathrm{m}$ tracer, (c) $600\,\mu\mathrm{m}$ tracer. The location of the mesh is outlined in black. . . . . 149
7.14 Azimuthal velocity component of the tracer in the froth for hydrophobic tracers of different sizes (a) $400\,\mu\mathrm{m}$ and (b) $500\,\mu\mathrm{m}$ and (c) $600\,\mu\mathrm{m}$. Positive is defined as the same direction as the impeller rotation. . . . . 150
7.15 occupancy of the tracer in the froth for hydrophobic tracers of different sizes (a) $400\,\mu\mathrm{m}$ and (b) $500\,\mu\mathrm{m}$ and (c) $600\,\mu\mathrm{m}$. . . . . 154
7.16 Plot of occupancy with radial location for different heights within the froth of the cell. Error bars are the standard error after averaging the value across 6 slices. The mesh is located between h=100 and h=$120\,\mathrm{mm}$ . . . . . 155
7.17 Plot of occupancy with height at different radii from the centre of the cell. Error bars are the standard error after averaging the value across 6 slices. The mesh is located between h=100 and h=$120\,\mathrm{mm}$. . . . . 156
7.18 Horizontal slices of occupancy of the different tracers through the mesh; (a) $400\,\mu\mathrm{m}$ tracer, (b) $500\,\mu\mathrm{m}$ tracer, (c) $600\,\mu\mathrm{m}$ tracer. The location of the mesh is outlined in black. . . . . 157

C.1 Tracer height over time for tracers in the unmodified cell. . . . . 197
C.2 Tracer height over time for tracers with the basic mesh inserted into the cell. 198
C.3 Tracer height over time for tracers with the blocked mesh inserted into the cell. . . . . 199

# List of Sybmols and Abbreviations

## Symbols

| | |
|---|---|
| $\alpha$ | Air recovery |
| $\rho_M$ | Magnetite density |
| $\rho_S$ | Silica density |
| $\rho_T$ | Total density |
| $\Sigma$ | Dynamic froth stability |
| $d_{10}$ | 10% passing particle size |
| $d_{50}$ | 50% passing particle size |
| $d_{90}$ | 90% passing particle size |
| $Ent$ | Entrainment Factor |
| $f$ | Fraction of PEPT events to keep |
| $G_M$ | Magnetite grade |
| $G_S$ | Silica grade |
| $h$ | Overflowing froth height |
| $H_{eq}$ | Equilibrium froth height |
| $H_{max}$ | Maximum froth height |
| $J_g$ | Superficial gas velocity |
| $M_C$ | Mass in the concentrate |
| $M_{dry}$ | Mass of dry material |
| $M_F$ | Mass in the feed |
| $N$ | Number of PEPT events to use |
| $P_a$ | Probability of attachment |
| $P_c$ | Probability of collision |
| $P_d$ | Probability of detachment |
| $Q_{a,in}$ | Flowrate of air into the cell |
| $Q_{a,out}$ | Flowrate of air out of the cell |
| $Q_C$ | Flowrate of the concentrate |
| $Q_F$ | Flowrate of the feed |
| $t$ | Time |
| $V_f$ | Froth volume |
| $v_f$ | Overflowing froth velocity |
| $w$ | Lip length |

## Abbreviations

| | |
|---|---|
| **ANOVA** | Analysis of Variance |
| **LOR** | Line of response |
| **PAR** | Peak Air Recovery |
| **PEPT** | Positron Emission Particle Tracking |
| **PFI** | Pulp froth interface |
| **PGM** | Platinum group metal |
| **QEMSCAN** | Quantitative Evaluation of Materials by Scanning Electron Microscopy |
| **R.O.I** | Region of interest |

# Chapter 1

# Introduction

## 1.1 Motivation

Froth flotation is one of the most important and widely used processes for separating minerals from waste rock. It has been used for over a century and the principle largely remains the same. A great deal of research has been done to improve and optimise flotation for the application to improving mineral concentration, however there is still plenty of scope for more research, especially with regards to flotation of different particle sizes, where there are still huge inefficiencies, both for fine and coarse particles. Due to its wide usage and the fact that it is the minerals separation process with the largest tonnage throughput, even small improvements in metallurgical recovery will quickly translate into a significant economic benefit. This is especially important to the industry as decreasing deposit head grades (Calvo et al., 2016) result in the separation process becoming more challenging and costly.

As head grades of new ore deposits decline, the industry is looking to other metal and mineral sources to meet the demands of an exponentially growing global population. One such potential source is historic tailings dams which can contain grades of the order of 0.75% (Gordon, 2002). Reprocessing such tailings material has many benefits to the industry. Firstly there is no comminution requirement and secondly, reprocessing the material can help reduce the significant environmentally damaging impact from the tailings dams. However, there are challenges associated with floating tailings material. The primary challenge is the fine nature of this material, as the relationship between particle size, froth stability and flotation performance is not fully understood. Improving our un-

derstanding of this relationship is vital if the efficiency of tailings reprocessing, via froth flotation, is to be improved.

Froth flotation only recovers particles up to a size of approximately $100\,\mu\mathrm{m}$ efficiently (Kohmuench et al., 2018). Huge energy expenditure in comminution is required to grind ore to below this upper bound of the particle size range in order to achieve efficient flotation. This expenditure can therefore be reduced by investigating ways to increase this upper bound. This will not only translate into money saved by the industry through reduced processing costs, but will additionally improve the sustainability of the industry as a whole, by reducing the energy required to process each tonne of ore. Several studies have presented new flotation cell designs for coarse particle recovery, however, installation of these new cells requires a huge capital expenditure. Investigation of design modifications that can be retrofitted to existing flotation cells is therefore the preferred approach.

Testing such modifications at the industrial scale is unfeasible due to the extreme cost involved; however, the majority of laboratory tests do not adequately replicate the behaviour of industrial flotation cells. Using a laboratory cell comparable to industrial cells is therefore an important first step in developing suitable design modifications to be deployed at full scale. Whilst it is relatively easy to quantify the effect of design modifications on froth flotation performance, it is much more challenging to determine their effect on the sub-processes which bring about overall changes in this performance. Improving our understanding of how these sub-processes are altered is therefore vital to develop retrofit design modifications further.

## 1.2 Objectives

With the above needs in mind, this thesis aims to:

- Improve our understanding of the effects of particle size on flotation and how this can be applied to reduce the energy used by the minerals processing industry with a focus on tailings reprocessing.
- Expand and improve on the retrofit design modifications for coarse particle flotation, first proposed by Norori-McCormac (2015), using a mineral system more representative of industrial systems.
- Further the understanding of how these retrofit design modification affect the flota-

tion performance by using PEPT to investigate the designs in conjunction with a variety of different tracer types and sizes.

## 1.3 Thesis structure

This thesis starts by presenting the theory of froth flotation and an in-depth analysis of the current literature on the topic, in chapter 2. A description of the fundamentals of froth flotation and the effects that different operating conditions have on flotation performance and froth stability, with a particular focus on particle size, is presented. The chapter then goes on to describe different aspects of flotation cell design including a discussion of the different design modifications used to improve coarse particle flotation. The use of Positron Emission Particle Tracking (PEPT) for understanding the mechanisms involved in opaque systems, particularly in relation to froth flotation, is discussed.

Chapter 3 presents the three main experimental techniques used in this thesis. Firstly, the use of a laboratory scale, non-overflowing flotation column to investigate the froth stability of a complex copper tailings ore. Secondly, the use of a continuously overflowing, bench scale flotation cell, with two flotation environments; a complex copper tailings ore, and a synthetic magnetite and silica two species ore. Thirdly, the experimental process used for PEPT and how the data were analysed.

Chapter 4 presents the results of investigating the effects of particle size distribution of a copper tailings ore on the flotation performance, both in terms of stability and metallurgical performance. Two different measures of froth stability were used; dynamic froth stability and air recovery. These two measures were compared to further the understanding of the relationship between particle size and froth stability and how this translate to metallurgical performance. The implications of these results on the ability to reprocess tailings material via froth flotation are discussed.

Chapter 5 presents the results of retrofit design modifications on the flotation of a synthetic two species ore. Two different design modifications were investigated and compared to the unmodified cell in terms of froth stability, metallurgical performance and recovery of different particle sizes.

Chapters 6 and 7 present the results from PEPT experimentation using the synthetic two species ore. Both chapters present the differences in bulk flow, particle velocities and

occupancy in the cell, for different design modifications and types of tracers. In chapter 6, two different tracers of the same size, one hydrophobic and one hydrophilic, are used to investigate the effect that the different design modifications have on particle behaviour. In chapter 7, three different tracers, all hydrophobic, but with different particle diameters are used to investigate specifically how the design modifications affect the flotation of different sizes of valuable material. The results in both chapters are used to explain the results presented in chapter 5.

Finally, chapter 8 presents the overall conclusions of this thesis and potential avenues for further work.

# Chapter 2

# Background

## 2.1 Introduction

This chapter introduces the process of froth flotation, one of the primary methods used to separate valuable material from waste material in the minerals processing industry. Froth flotation has been utilised by the industry for over a century, yet there is still plenty of scope for improving the process especially as the decreasing grades of ore deposits mean that mineral separation is becoming more challenging and costly.

The fundamentals of the froth flotation process will be discussed, with particular focus on the different zones within a flotation cell: the pulp and the froth, the functions of different chemical reagents and how flotation performance is quantified in different ways. The effects that different operating parameters have on different measures of froth stability and flotation performance will be presented with an emphasis on particle size. The differences in flotation cell design, both at industrial and laboratory scales, especially for improving flotation performance will also be discussed.

A technique for imaging the processes that occur within the flotation cell, positron emission particle tracking (PEPT), will be discussed. This technique tracks the motion of a particle, that has been labelled with a radionuclide, as it moves through a system, in this case a flotation cell. The data can then be used to determine how different operating conditions and design changes affect the flotation of different particles.

## 2.2 Principles of Flotation

Flotation is one of the most widely used techniques in the minerals processing industry for particle separation due to its relative versatility, particularly with complex and low grade ores (Wills and Finch, 2015). Whilst the concept of froth flotation is simple, i.e. differences in surface properties are utilised to separate valuable minerals from gangue material, the theory behind the mechanisms occurring within the flotation process are more complex due to the three phase nature of the system (Wills and Finch, 2015).

In order to achieve separation of the valuable and gangue minerals the surface properties of the particles are altered chemically. Chemical reagents are selected for the specific system to render the valuable material hydrophobic relative to the gangue. The chemically altered feed is then pumped into a flotation cell. Air is injected into the cell and an impeller is used to agitate the slurry and suspend the particles, whilst also breaking up the air bubbles. The hydrophobic particles will attach to the air bubbles and rise to the top of the cell, forming a froth layer. The froth will then overflow the cell, separating the valuable mineral from the gangue, forming an enriched concentrate stream and a depleted tailings stream. The flotation cells are arranged in banks where the tailings from the first cell become the feed to the second, and so on, to increase the grade and recovery of the valuable mineral further (Wills and Finch, 2015).

Within a flotation cell there are two main zones which serve different purposes. The first is the pulp zone, at the base of the cell, where bubble-particle attachment occurs. The second is the froth zone, at the top of the cell, where particles are recovered to the concentrate (figure 2.1).

The pulp zone is the aerated zone at the base of the cell where solid particles are suspended in water, forming a slurry (King, 2012). Air is injected into the cell and bubbles are formed within the pulp. An impeller allows the particles to be suspended and shears the bubbles to increase the surface area available for attachment (Ata, 2012). The purpose of the pulp zone is to provide an adequate environment for the particle to attach to the bubble so that it can be transferred to the froth. In order for this to occur, several conditions must be met (King, 2012). Firstly, the particle must be suspended in the pulp and be sufficiently hydrophobic. Secondly, there must be a collision with a rising bubble and the particle must attach to the bubble and not be subsequently detached. And thirdly the environment in the pulp must be sufficiently turbulent for particles to be suspended

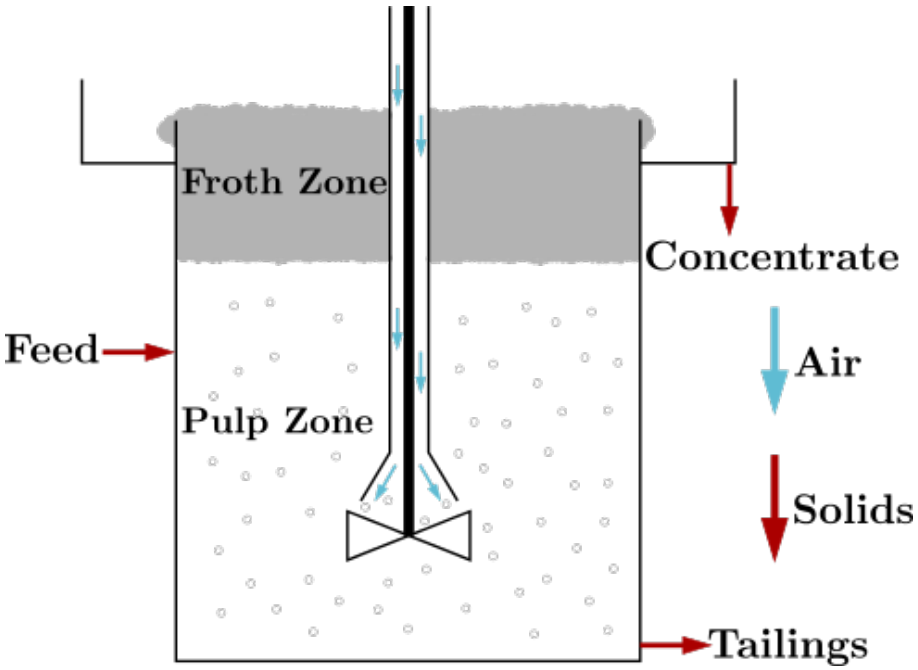



**Figure 2.1:** A mechanical flotation cell showing the froth and pulp zones.

whilst not being so turbulent that particles are easily detached from bubbles.

In order for a particle to be captured by a bubble the two need to be sufficiently close to each other. If this happens then the film of liquid separating them will rupture and drain. The contact line between the three phases; solid, liquid and gas, will move to establish a new stable wetting perimeter (Nguyen et al., 1997). This will result in a stable contact between the bubble and the particle (Ralston et al., 1999). Much research has been conducted into understanding the interactions between bubbles and particles in this zone. Nguyen et al. (1997) discussed that there are many forces acting between the bubble and particle that need to be overcome for successful attachment, such as electrodynamic, electrostatic and structural forces.

There are three primary mechanisms by which particles can be transferred from the pulp to the froth. The first, and by far the most important mechanism is true flotation by which the hydrophobic particles are attached to the air bubbles. The second mechanism is when particles are entrained in the water between the bubbles, this is a non-selective process and so the gangue minerals are also able to pass into the froth zone, reducing the grade of the concentrate. The third mechanism is particle aggregation, by which free particles can be trapped between attached particles. Again this is non-selective and will therefore reduce the overall grade of the concentrate (Wills and Finch, 2015).

At the top of the flotation cell, there is a layer of froth where particle laden bubbles

concentrate, forming the froth zone. The primary purpose of this zone is the recovery of the valuable minerals, from the pulp, into the concentrate. Due to the injection of air in the pulp zone and the continual rising of bubbles to the pulp-froth interface, the froth overflows the cell into a launder where it is collected as concentrate. The bubbles in the froth are separated by thin films of liquid and these films are connected and form a network of Plateau borders (Neethling et al., 2003) (figure 2.2). Solids present in the froth can be divided into two categories; firstly hydrophobic particles attached to bubbles, and secondly particles moving freely in the Plateau borders (Neethling et al., 2003). The latter particles can either be hydrophilic particles that are entrained, or hydrophobic particles that have become detached from bubbles, either through bubble coalescence or bubble bursting at the froth surface (Neethling et al., 2003). These free particles can settle through the Plateau borders and be lost from the froth back to the pulp and therefore not recovered to the concentrate.

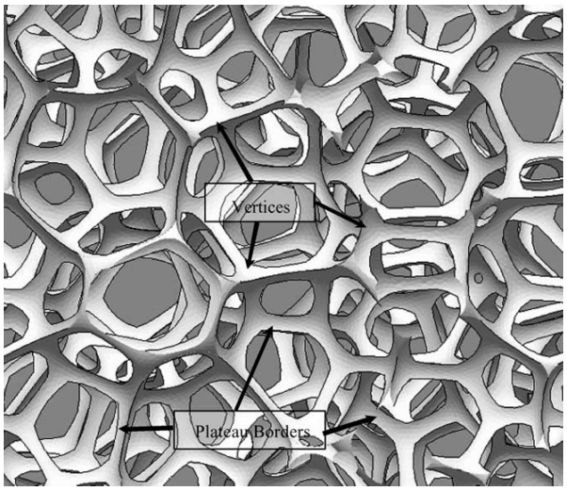



**Figure 2.2:** Foam structure illustrating the Plateau borders between bubbles (Neethling et al., 2003).

## 2.3 Flotation Chemistry

In the process of froth flotation the most important elements for successful flotation are the chemical reagents. Improving the use of reagents has made up a significant amount of the major advances in the field (Bulatovic, 2007). Flotation reagents can be broadly divided into three groups depending on their function. Collectors are used to aid with the collection of the mineral particles, frothers are used to maintain and control bubble size in the pulp and stability within the froth, and regulators are used to modify the effect of the

collector on the specific minerals in the system (Gupta and Yan, 2006). There has been extensive research into how using different reagents can improve flotation performance, however these studies are generally specific to a particular ore.

### 2.3.1 Collectors

Collectors are added to the pulp phase with the primary purpose of acting as a surfactant and aiding with the collection of particles (Wills and Finch, 2015). Collectors need to adsorb onto the surface of the particle in order to form a hydrophobic layer (Bulatovic, 2007). They are added to the pulp during agitation and conditioning time is required in order to allow an adequate coating to form on the mineral surface (Wills and Finch, 2015). A collector is comprised of a non-polar group and a polar group. The polar group allows the collector to be water soluble and the non-polar group is a hydrocarbon chain (Gupta and Yan, 2006). If a mineral surface is present the polar groups will be adsorbed onto the surface rendering it hydrophobic (Gupta and Yan, 2006), with the non-polar group remaining in the water phase (Bulatovic, 2007). When an air bubble is present, the hydrocarbon chain will move into the air phase and if the bond is sufficiently strong this will allow the mineral particle to be lifted (Gupta and Yan, 2006) (figure 2.3).

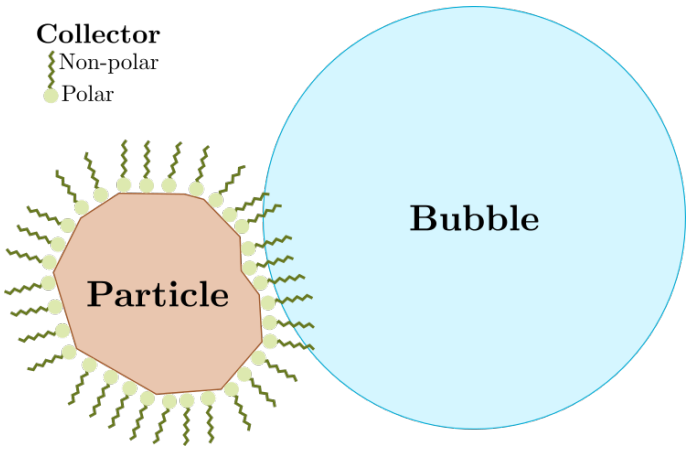



**Figure 2.3:** Schematic of a collector adsorbed onto the surface of a mineral particle and then attached to a bubble.

There are many different types of collector that can be used. The type and amount chosen will depend on the mineral being floated (Wills and Finch, 2015). Adding too much collector to a system can lead to adverse effects on the froth such as immobilisation and dryness. The effectiveness of a collector can be described by the contact angle that forms between the mineral surface and the air bubble (Gulsoy, 2005). The contact angle

will increase with increased collector concentration up, improving the flotation rate up to a point where the maximum contact angle is achieved. This maximum is a characteristic of the specific collector being used and, to some extent, of the mineral (Gupta and Yan, 2006).

### 2.3.2 Frothers

Frothers are surfactants that are used in order to ensure that the bubble formation in the pulp phase is stable enough to hold floated minerals (Wills and Finch, 2015). They are absorbed at the air/water interface to lower the surface tension in the water (Gupta and Yan, 2006). This produces small bubbles with an increased strength (Bulatovic, 2007). Many frothers also act as collectors, they can therefore help to reduce the consumption of the collector, allowing the rate of flotation to improve. This is particularly the case when considering cationic flotation with amine collectors (Bulatovic, 2007). However, having a frother that also has collecting properties can result in complications when trying to separate out the collecting and frothing functions of the reagent. The addition of a frother will cause the surface tension to drop rapidly until it levels out at a constant minimum value. The greatest froth stability is not achieved at the minimum, but at the point where the surface tension changes rapidly, as this helps prevent film rupture (Gupta and Yan, 2006).

By ensuring stable bubble formation, frothers help create a froth that is stable enough to be sustained, whilst still allowing the entrained gangue particles to drain (Wills and Finch, 2015). Too little or too much frother will cause the froth to be unstable and collapse. The addition of even a little too much frother will also have a negative impact by producing a froth that is too tight which will inhibit the settling of entrained gangue particles (Gupta and Yan, 2006). Ata (2011) showed that the addition of a frother can help reduce the number of particles detached from the bubble due to it reducing the amount of bubble deformation that occurs.

### 2.3.3 Regulators

In many systems, particularly those with mixed ores, the flotation rate constants of different minerals may all be of the same order of magnitude. This renders them more challenging to separate (Gupta and Yan, 2006). Regulators are commonly regarded as the

most important reagents as they modify the action of the collector for individual minerals in the system to improve the separation efficiency (Bulatovic, 2007). They can have two main functions either activating or depressing a mineral and which action a specific regulator performs is dependent on the system and the specific minerals (Bulatovic, 2007). An activating regulator will act to make the mineral surface more hydrophobic. A depressing regulator will do the opposite by rendering the minerals hydrophilic, hence preventing flotation, this type of regulator will commonly be used in reverse flotation, where the gangue mineral is the one being floated (Wills and Finch, 2015). Both activators and depressors are often used in the same system to increase the relative difference in floatability of the minerals allowing easier and more effective separation. Another type of regulator that can be used is a pH regulator that will adjust the pH of the system to allow other reagents to perform optimally (Gupta and Yan, 2006).

## 2.4 Flotation Performance

### 2.4.1 Metallurgical performance

The most widely used measures of flotation performance are grade and recovery. The grade is the fraction of valuable mineral in the concentrate stream and it is therefore desirable to maximise it in order to achieve a purer product. The mineral recovery is the fraction of mineral in the feed that is recovered to the concentrate. In a mineral processing context this is often just as, if not more, important as maximising the recovery. In order to have 100% recovery of a valuable mineral, the grade of the concentrate would be equal to the grade of the feed. Similarly, in order to achieve a 100% grade the recovery would be very low as even particles containing only a small amount of gangue would be rejected. There is therefore a trade off between the two, as can be seen from figure 2.4, showing an idealised grade-recovery curve. The grade and recovery of a system will depend on a wide variety of different factors within the system itself such as superficial gas velocity, the reagent suite, the physical design of the cell and the characteristics of the ore. Altering any of these parameters will cause a shift along the grade-recovery curve or a shift to a different curve.

In some systems it is non-trivial to measure the grade and recovery of a particular mineral. This was the case for the single species experiments performed by Norori-McCormac

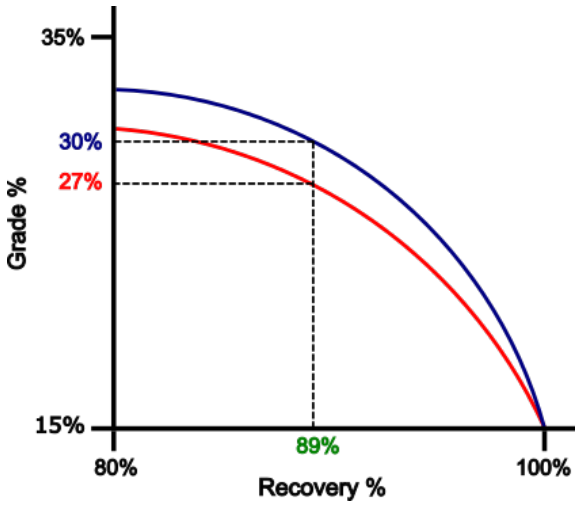
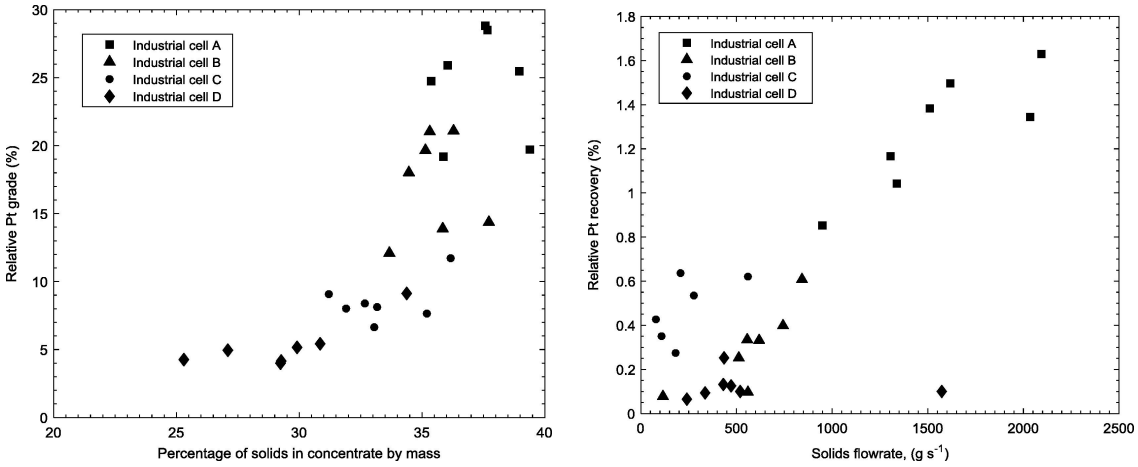



**Figure 2.4:** Idealised grade-recovery curve, with the different coloured curves representing different hypothetical operating conditions.

et al. (2017) and Morrison et al. (2017). Both of these studies used the solids content of the concentrate as a proxy for grade and solids flowrate, or mass pull as a proxy for recovery. Norori-McCormac et al. (2017) presented data from industrial flotation cells showing that these proxies were appropriate for comparing different operating conditions due to the positive correlations shown in figure 2.5.




(a) Relationship between solids content and grade

(b) Relationship between solids flowrate and recovery

**Figure 2.5:** Industrial data showing the relationship between (a) solids content of the concentrate and relative grade and (b) solids flowrate to the concentrate and relative recovery (Norori-McCormac et al., 2017).

Particle entrainment is also an important factor to consider when investigating flotation performance as high levels of entrainment reduce the grade of the concentrate. The recovery of entrained gangue material is linearly proportional to the water recovery (Neethling and Cilliers, 2009). The constant of proportionality, the entrainment factor, can be calculated using equation 2.1 (Neethling and Cilliers, 2009), where $M$ denotes the

mass flow of the entrained material, and $Q$ is the volumetric water flowrate; a subscript of $C$ refers to the concentrate and of $F$ refers to the feed. An entrainment factor of 1 represents the fact that the amount of gangue material in the concentrate relative to the water is the same as the ratio of gangue to water in the pulp phase. Entrainment factors $> 1$ indicate that more gangue material is recovered than expected from just the water flowrate, while values $< 1$ indicate that there is less gangue recovered than expected.

$$Ent = \frac{M_C Q_F}{M_F Q_C} \tag{2.1}$$

### 2.4.2 Froth stability

Froth stability is an important factor to consider in froth flotation, as it has a significant impact on flotation performance. In a stable froth, the bubbles do not easily burst, this results in improved recovery due to a minimisation of particle detachment. On the other hand, highly stable froths are generally made up of smaller bubbles, and so the froths contain more water and therefore more entrained material, reducing the grade. There are many factors that affect the stability of the froth such as particle size and hydrophobicity, and the air flowrate (Aktas et al., 2008).

The effect of particles on the froth stability has been the subject of many studies. Johansson and Pugh (1992) showed that whether or not a particle will stabilise or destabilise the froth depends on the particle size, shape and hydrophobicity. Dippenaar (1982) demonstrated that froth stability is impeded by the presence of a small number of hydrophobic particles, however this can be counteracted by having a larger number of small particles in the system. Aktas et al. (2008) found that fine particles in the system will increase the height of the froth in a column and hence increase the stability.

Dippenaar (1982) showed that there is a maximum contact angle where a stable film could form. Above this contact angle, the thin films in the froth would be destroyed which impacts the froth stability. For smooth particles the maximum contact angle is $90°$, however for rougher particles rupture occurs at lower contact angles and an optimum contact angle of $65°$ was found. Results from Ata et al. (2002) correlated with this as they found maximum flotation recoveries occurred when the contact angles were between $63°$ and $66°$. Aktas et al. (2008) showed that froth stability decreased with an increase in conditioning time, which correlated to the degree of hydrophobicity.

There has been a significant amount of work devoted to investigating the best way to quantify froth stability. Two ways are discussed in this thesis: the dynamic froth stability, and the air recovery.

**Dynamic froth stability**

The Bikerman test was developed to investigate the foam stability of dynamic systems using a flotation column (Bikerman, 1948). In this test gas is bubbled through a porous membrane into liquid in the column, allowing a foam layer to form at the top. This foam will rise until it reaches a steady state where the volume of gas entering the system, as bubbles, is equal to the volume of gas escaping when the bubbles burst (Bikerman, 1948). Many studies have shown that the height of the column of foam is proportional to the rate of flow of gas in the system and Bikerman (1948) defines the rate of proportionality as the dynamic foam stability ($\Sigma$), equation 2.2, where $V_f$ is the volume of the foam, $Q_a$ is the volumetric flow rate of the gas, $H$ is the foam height of the system at steady state, and $J_g$ is the superficial gas velocity. This rate of proportionality does not only apply to foams but also to froths and can also be described as the average lifetime of a bubble in the froth (Bikerman, 1973).

$$\Sigma = \frac{V_f}{Q_a} = \frac{H}{J_g}, \tag{2.2}$$

**Air recovery**

The air recovery is the fraction of air overflowing the cell as unburst bubbles, equation 2.3, where $\alpha$ is the air recovery, $v_f$ is the overflowing froth velocity, $h$ is the height of the overflowing froth over the cell lip, $w$ is the overflowing lip length and $Q_a$ is the air flowrate, either into or out of the cell.

$$\alpha = \frac{Q_{a,out}}{Q_{a,in}} = \frac{v_f h w}{Q_{a,in}} \tag{2.3}$$

Barbian et al. (2006) clearly showed that this was a valid measure with a linear relation between the fraction of air overflowing the cell, air recovery, and the froth stability factor. Hadler and Cilliers (2009) established that, by varying the air flowrate a peak in air recovery can be seen. A high air recovery means that there will be less air lost through the

bursting of bubbles at the top of the cell, which results in a more stable froth. At low air rates, the froth will be stable, however it will have a lower mobility and so is more likely to burst before overflow happens, resulting in a low air recovery (Hadler and Cilliers, 2009). At high air rates the froth will also be unstable due to excessive coalescence and bursting. This results in the presence of a peak in air recovery (PAR). At the PAR there is a high flowrate of solids due to the presence of a mobile froth and the bubbles being stabilised by the presence of attached particles. Hadler et al. (2010) showed, that in an industrial setting changing the air flowrate to the PAR caused an increased mineral recovery with only a small drop in the grade of the concentrate.

### 2.4.3 Particle size effects

Most modelling of flotation performance with increasing particle size suggests that an increase in size causes an increase in efficiency, however this is not reflected by experimental results (Fuerstenau et al., 2007). As can be seen in figure 2.6, there is clearly a peak in recovery with a change in particle size and recovery of the finest and coarsest particles is challenging.

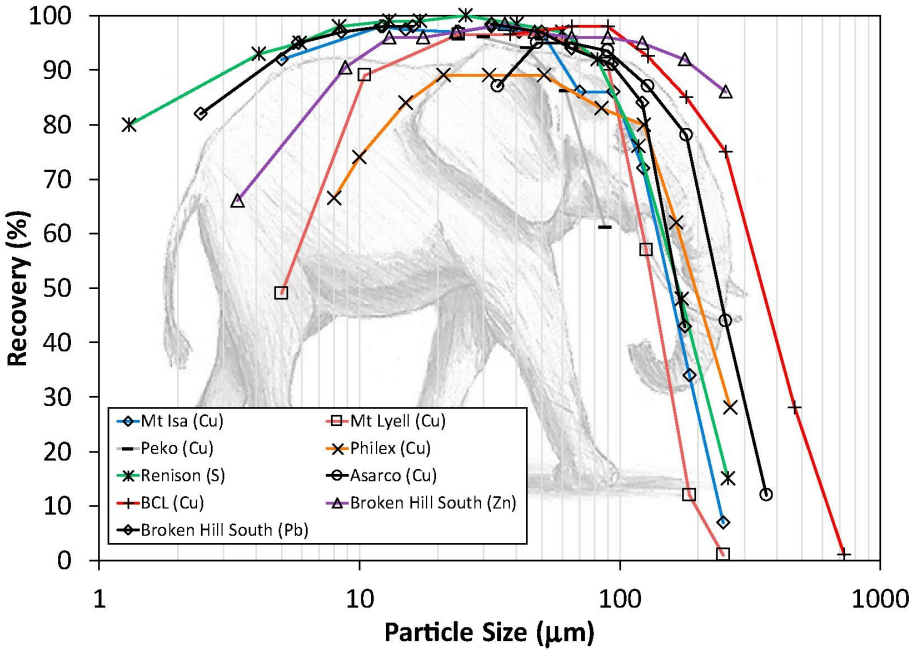



**Figure 2.6:** Recovery by particle size from industrial flotation of a variety of different sulfide ores (Kohmuench et al., 2018).

The probability of a particle being successfully collected and recovered by a bubble is given by equation 2.4. Where $P_c$ is the probability of bubble-particle collision, $P_a$ is the

probability of attachment and $P_d$ is the probability of detachment.

$$P = P_c P_a (1 - P_d), \tag{2.4}$$

It is therefore important to provide an environment that can maximise the probability of collision and attachment, whilst minimising the probability of detachment. In order to do this, there needs to be a balance between the impeller speed and the bubble size. If the impeller speed is too low, and there is not enough turbulence, then particles will not be adequately suspended and they will settle to the base of the tank, thus reducing the probability of collision and attachment. However, if the impeller speed is too high the environment will be too turbulent and the probability of detachment will be high. On the other hand, bubbles need to be big enough to lift the particles, but not so big that the recovery is low due to a decreased surface area (Ahmed and Jameson, 1989). The optimum levels of bubble size and impeller speed are very different for coarse and fine particles and so finding conditions to float a wide range of particle sizes together can be challenging. Ahmed and Jameson (1985) suggested that a possible solution would be to separate the different size fractions of the feed and treat them under different operating conditions.

**Fine particles**

As can be seen in figure 2.6, the recovery of fine particles, less than $10\,\mu\mathrm{m}$ in diameter, is challenging. Improving the recovery of such particles is imperative for the minerals processing industry, not only because it will improve the overall recovery of valuable material but also because it is a particular concern for situations where feeds are already fine. One example of such a feed is when reprocessing tailings material - an area that is becoming increasingly interesting to the minerals processing industry.

The main problem with fine particle flotation is the reduced bubble-particle collision probability due to their low inertia (Schulze et al., 1989). Fine particles will also tend to travel along streamlines as they do not have sufficient kinetic energy (due to their low mass) to displace the thin film of liquid between the bubble and the particle (Hewitt et al., 1993) and expand the three phase line of contact (Scheludko et al., 1976). Chipfunhu et al. (2011) showed that whilst this is the case, if a particle is sufficiently hydrophobic (beyond the critical contact angle) then it will float.

The two key ways to increase the bubble particle collision efficiency are to reduce bubble size or to increase the apparent size of the particles (Miettinen et al., 2010). Whilst decreasing bubble size is well understood to improve the collision efficiency, the low rise velocity of small bubbles results in a much higher residence time (Miettinen et al., 2010). Added to this, smaller bubbles results in a higher water recovery (Schwarz and Grano, 2005), which will increase entrainment and reduce concentrate grade.

The apparent particle size can be increased by forming flocs or aggregates of fine particles (Miettinen et al., 2010). However, it can be difficult to do this selectively and entrapment of gangue between valuable minerals is a major problem (Rubio et al., 2003). Liu and Wannas (2004) suggested that this problem could be mitigated by using a depressant to also flocculate the gangue minerals, which would reduce the possibility of entrapment.

Another issue with fine particle flotation is that due to the small size of the particles they have a lower settling velocity and are therefore more easily entrained (Neethling and Cilliers, 2009). In addition, due to their higher specific surface area than other particles, fine particles require larger quantities of reagents to be floated (Feng and Aldrich, 1999).

**Coarse particles**

Figure 2.6 shows an upper particle size limit of the order of $100\,\mu\mathrm{m}$ for flotation. The size of this upper limit is dependant on the mineral being floated. This is a key area of interest for minerals processing research. By increasing this upper size limit, less energy would be needed to grind each tonne of rock prior to flotation (Fuerstenau et al., 2007). There are many reasons for the lower recovery of coarse particles, the first is that, due to their increased size, and therefore increased mass, a highly turbulent environment is required to provide the particles with enough energy to remain in suspension and to attach to bubbles (Schulze, 1977). The second is that due to this turbulent environment coarse particles will easily detach from bubbles (Wills and Finch, 2015). The third is that when they are entrained they are more likely to drop back from the froth into the pulp phase (Schulze, 1977). There are three key problems when considering coarse particle flotation; the requirement for sufficient buoyancy to lift the particles, the forces that are acting within the froth zone and the detachment forces (Fuerstenau et al., 2007). It is widely considered that turbulence is the most important limiting factor to the upper particle size

for flotation (Schulze, 1977) as this is the main cause of detachment of coarse particles.

The first problem with coarse particle flotation is the requirement for sufficient buoyancy in order to lift and float the particle. There are two elements to this, firstly there will be a minimum degree of hydrophobicity required to float a particle and this increases with particle size (Trahar, 1981). In order for coarse particles to achieve the same recovery as fine particles, they need a greater surface coverage of collector (Crawford and Ralston, 1988). The presence of fines in the system can therefore be detrimental to the recovery of coarse particles, due to their increased surface area as they will have a higher consumption of the collector meaning the surface coverage on coarse particles may be insufficient (Trahar, 1981). Secondly, the bubbles need to be large enough to provide the buoyancy to lift the particles. Schulze et al. (1989) used the definition of buoyancy to show that a minimum bubble size can be calculated. Given a big enough bubble, it should always be possible to lift a particle, however there is an upper limit on the bubble size due to the turbulence created by the impeller causing large bubbles to become unstable and break up. It is important to note that the maximum particle size that can be raised will be larger than the maximum size that can be floated due to the other forces present within flotation (Gontijo et al., 2008). Ata and Jameson (2005) have observed that bubbles can form clusters in a flotation cell when there are solids in the system as solids can form bridges between multiple bubbles. These clusters can be potentially beneficial for coarse particle flotation as they increase the buoyancy.

A second problem occurs in the froth zone. As the size of the particles increases, the froth stability will decrease (Rahman et al., 2012); this is due to the fact that large particles will cause the thin films between bubbles to rupture more easily. This results in more solids settling, particularly particles with more mass which will drop back through the froth into the pulp phase. It is also seen that when a bubble-particle aggregate transitions across the pulp-froth interface it loses kinetic energy. This is often sufficient to detach large particles from the bubbles, resulting in the coarse particles being harder to transfer into the froth zone (Fuerstenau et al., 2007). This problem can be reduced by introducing the coarse particles directly into the froth as has been done by Ata and Jameson (2013).

The third problem is the detachment of the particles, this is seen as the largest problem to overcome when considering improvements to coarse particle flotation. When a particle is attached to a bubble there is a capillary force acting at the three phase contact line. If the centrifugal force in the system, caused by the turbulence and shear from the impeller is

greater than this capillary force then the particle will detach from the bubble (Fuerstenau et al., 2007).

### 2.4.4 Particle size and froth stability

Rahman et al. (2012) and Bournival et al. (2014) showed that the presence of fine particles can actually help improve coarse particle flotation by stabilising the froth, preventing film rupture and bubble coalescence. There is therefore some controversy over whether the presence of fine particles hinders or aids coarse particle flotation.

Whilst it is well known that the recoveries of fine particles are reduced in flotation, there have also been several papers investigating the effects that the amount of fine particles in the feed has on the recovery of other particle sizes. Vieira and Peres (2007) investigated how varying the proportion of fine silica particles, 38-$74\mu\mathrm{m}$, in the feed affected the recovery of different particle sizes. The optimal fraction of fines required for increased recovery of all particle sizes from the feed was shown to be 11%. The authors suggested that this was due to the fine particles stabilising the froth.

Leistner et al. (2017) investigated the recovery of fine and ultrafine valuable material, in this case magnetite, in the presence of fine and ultrafine gangue material, in this case quartz ,using a Denver cell. The results showed that the presence of fine gangue particles increased the recovery of both sizes of valuable particles, whilst the presence of ultra fine gangue particles reduced the recovery of both sizes of the valuable particles. This indicates that the size of the gangue particles has a strong effect on the recovery of the valuable ones.

It is also important to understand the effect that different particle sizes have on froth stability. There have been several different bodies of work on this topic, yet the results are inconclusive. Most work measures the dynamic froth stability (essentially the average life time of a bubble in the froth) in non-overflowing laboratory scale columns.

Johansson and Pugh (1992) showed that whether or not fine particles will destabilise the froth depends on hydrophobicity. They varied the contact angles of the particles in the feed and measured the resulting dynamic froth stability. The results showed that at low contact angles, ($< 40°$) fine particles had little effect on the stability, intermediate contact angles ($\sim 65°$) gave the best stability whilst higher contact angles ($> 80°$) destabilised the froth. Ip et al. (1999) measured the dynamic froth stability in a column with different

particle sizes of a synthetic silica only feed and showed that, in general, smaller mean particle sizes led to an increase in froth stability, however this was not a smooth relationship. Conversely, Tao et al. (2000) showed that a small increase in the amount of $10\,\mu\mathrm{m}$ coal increased the water recovery in a laboratory scale column which suggests a decrease in stability.

Barbian et al. (2003) used a modified Denver cell with a Platinum Group Metal (PGM) ore and observed that the dynamic froth stability factor decreased with an increase in superficial gas velocities. However, the superficial gas velocities in their work ranged between $0.13\,\mathrm{cm\,s^{-1}}$ and $0.66\,\mathrm{cm\,s^{-1}}$ and were therefore low compared to industrial flotation cells. Aktas et al. (2008) used a similar cell, again with a PGM ore, and observed the same relationship between dynamic froth stability and superficial gas velocity, again investigating the effects at low superficial gas velocities, between $0.26\,\mathrm{cm\,s^{-1}}$ and $0.53\,\mathrm{cm\,s^{-1}}$. In addition to varying the gas velocity Aktas et al. (2008) also varied the particle size and found that as the particle size increased the dynamic froth stability decreased, however, only four different sizes were used and these were coarse (d90 of $118\,\mu\mathrm{m}$ to $306\,\mu\mathrm{m}$) and so the study doesn't give information about a broad range of both fine and coarse particles.

More recently, Liang et al. (2015) investigated the effects of coal particles of different sizes on the froth stability again using a modified stability column. Four different size fractions were used here, namely $-74\mu\mathrm{m}$, $-125+74\,\mu\mathrm{m}$, $-250+125\,\mu\mathrm{m}$ and $-500+250\,\mu\mathrm{m}$. Whilst these sizes consider a wider overall distribution than other studies, each of the size ranges tested was quite broad. These experiments were also run at low gas velocities of $0.2\,\mathrm{cm\,s^{-1}}$. McFadzean et al. (2016a) studied the effects of particle size on dynamic froth stability for three different ores: a synthetic silica and pyrite ore, a PGM ore, and an Itabirite ore. The results for all three ores showed a smooth decreasing power law relationship when increasing the average feed particle size. Whilst the particle size of the synthetic ore ranges from around $16\,\mu\mathrm{m}$ to $210\,\mu\mathrm{m}$ the other two ores had smaller size ranges, between $29\,\mu\mathrm{m}$ and $71\,\mu\mathrm{m}$. These experiments were run at a superficial gas velocity of $0.98\,\mathrm{cm\,s^{-1}}$.

Barbian et al. (2005) developed a froth stability column to be used at industrial scale, allowing froth stability to be correlated to flotation performance. The results, from a copper sulphide ore, showed that the highest dynamic froth stability resulted in the highest copper grade but lowest recovery. McFadzean et al. (2016b) also showed a link between dynamic froth stability and flotation performance in their work. Their study investigated

the effects of different frother blends on the froth stability of a PGM ore with an agitated laboratory scale column. The results showed that a higher froth stability resulted in higher recovery, but that there was little correlation with grade. The results from these two studies are contradictory suggesting that the relationship between froth stability and flotation performance is more complicated.

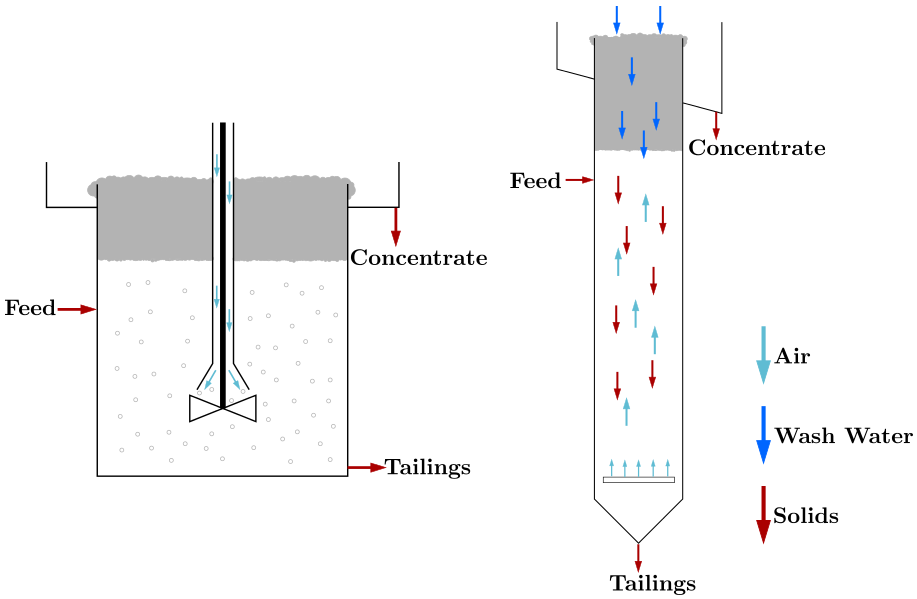
Unlike most of these studies Norori-McCormac et al. (2017) investigated the effects of particle size in a laboratory scale, continuously overflowing, mechanical flotation cell and used air recovery (equation 2.3) as the measure of froth stability. These results showed that the relationship between particle size and froth stability is not a simple one, it also depends on the superficial gas velocity in the system. At high superficial gas velocities the relationship is the same as those seen in Aktas et al. (2008) and McFadzean et al. (2016a) in that the smaller feed sizes result in the higher stability. On the other hand, at lower superficial gas velocities it is an intermediate feed size gave the optimal stability. This highlights that there could be more work done to further the understanding of the relationship between particle size and froth stability and how this then translates into changes in metallurgical performance. As the work performed by Norori-McCormac et al. (2017) used a different measure of stability to other studies, it would also be interesting to directly compare the two measures of stability to see how results differ between the two for the same ore.

## 2.5 Flotation Cell Design

### 2.5.1 Mechanical vs. column flotation

Flotation cells can be divided into two main types; mechanical cells and columns. The mechanical cell, which is the focus of this work, is a stirred aerated tank. The impeller provides a mixing zone in the tank to promote contact and therefore attachment between particles and bubbles. There needs to be a balance of the impeller providing enough lift for the particles to come into contact with the bubbles whilst not causing the particles to detach. Flotation columns are taller and narrower than their mechanical counterparts, thus requiring a smaller footprint. These cells are not stirred, instead air is injected at the bottom and the feed is introduced close to the top of the pulp zone. As the solid particles move down in the cell they come into contact with the rising bubbles and attachment

can occur. The froth in a column cell is much deeper than in a mechanical cell and wash water is applied at the top to aid with the drainage of entrained particles. Figure 2.7 shows a comparison between mechanical flotation cells and flotation columns in the same processing plant.




(a) Schematic of the differences between a mechanical cell (left) and a column cell (right).



(b) Own photograph showing mechanical flotation cells (blue) and flotation columns (red) at a processing plant in Chile.

**Figure 2.7:** Comparison between mechanical flotation cells and column flotation cells.

### 2.5.2 Design modifications

Since the original patent of the mechanical flotation cell in 1908, there have been several modifications to the design to improve flotation performance as grades of deposits

decrease. With regards to altering the physical design of the cell these modifications can be split into two broad categories: completely new cell designs or retrofit modifications.

The majority of cell manufacturers are designing new flotation cells that are larger in order to increase throughput to the plant, while minimising capital expenditure. The size of cells has increased enormously over the past century (Mesa and Brito-Parada, 2019). One of the biggest problems when increasing the size of the cells is that the properties of the froth do not scale and large stagnant sections can form in the centre of the froth due to the increased distance that the froth needs to travel to the lip of the cell (Zheng et al., 2004). There are two primary design modifications that can be used to overcome this issue. Firstly, introducing crowders into the centre of the cell will reduce the area of the froth at the top of the cell and improve froth mobility (Cole et al., 2012). Secondly, implementing more complicated launders to increase the effective lip length of the cells, which increases froth recovery. Internal launders also have the added benefit of reducing the distance that the froth has to travel, eliminating stagnant zones (Zheng et al., 2004). There are various different launder designs, and two of the most common are the radial and the doughnut launders (Mesa and Brito-Parada, 2019).

While launders and crowders are retrofit design modifications that affect the froth phase, it is also important to look at design modifications that affect the pulp phase, such as designs that can either promote mixing or modify the turbulent zone within the pulp. The mixing environment can easily be modified by changing the type of impeller or the shape of the cell. The impeller introduces mixing loops, where gangue particles can be transferred to the froth zone. Vertical baffles are used to breakdown these loops (Yianatos et al., 2005). As previously discussed, turbulence in the pulp is desired as this suspends the particles and promotes bubble particle attachment, however if there are high levels of turbulence in the pulp, close to the interface with the froth, then this can cause detachment of particles from the bubbles.

Horizontal baffles have been used and researched extensively in flotation columns. Recently these have also been used in two different sized laboratory scale mechanical flotation cells, with simplified single species systems. The first was a 4L cell developed by Norori-McCormac (2015), the horizontal baffles were designed as a mesh with a honeycomb like structure. Several different meshes were tested with different pore sizes and different thicknesses. The effectiveness of these meshes in improving flotation performance was determined by measuring the air recovery, solids content and solids flowrate

of the concentrate as well as using positron emission particle tracking to image the motion of a particle within the cell (see section 2.6). These meshes proved effective at improving the solids flowrate to the concentrate (indicative of the recovery) in particular the one with a 30mm pore size showed the best performance when compared to an unmodified cell. The meshes also improved air recovery whilst there was no clear improvement in indicative grade compared to the base case. Similar horizontal meshes were also studied by Morrison et al. (2017), however these meshes had a square pore rather than hexagonal. In the same way, a variety of pore sizes and thicknesses were analysed and showed that optimal performance, improved indicative grade and recovery, was achieved with a pore size of approximately 125mm. However, there was no clear indication that the mesh improved air recovery.

There are several design modification to the flotation cell primarily focused on the improvement of flotation of different particle sizes. One of these is the Jameson cell (Clayton et al., 1991), in this cell the slurry is introduced as a liquid jet through a downcomer at the top of the cell. Air is entrained in this jet, which generates a large number of very small bubbles. There is good particle collection due to the mixing zone in the downcomer. Flotation time is also rapid due to the high bubble surface area flux, meaning this cell is useful for cleaning and fine particle flotation.

Another novel flotation cell design is a cell with a liquid fluidised bed and a minimal froth zone (Jameson, 2010). The feed is fluidised with an upflow of water and bubbles are introduced into the cell. This produces a favourable environment for flotation of coarse particles due to the absence of turbulence. There is also a much higher bubble particle collision rate due to the higher volume fraction of solids than in a conventional flotation cell. Results from Jameson (2010) showed that the use of such a cell resulted in between 95% and 100% recovery of galena particles up to a size of $850\,\mu\mathrm{m}$. Commercial examples of a fluidised bed flotation cell included the NovaCell (Jameson and Emer, 2019) and the HydroFloat (Awatey et al., 2013). Both of these cells have been shown to significantly improve coarse particle recovery. Jameson and Emer (2019) showed that the NovaCell resulted in 100% recovery of chalcopyrite particles up to a size of $300\,\mu\mathrm{m}$. Awatey et al. (2013) showed that the recovery of $1180\,\mu\mathrm{m}$ galena particles improved from 41% in a Denver cell to 86% in the HydroFloat cell.

Flash flotation cells are used as a way of treating coarse particles (Newcombe et al., 2012). When processing minerals with high specific gravity, such as sulphides, it can be

common for them to report to the hydrocyclone underflow stream where they will then be reground until fine enough to report to the overflow stream. This can incur losses due to the challenges in floating fine particles as discussed in section 2.4.3. Flash flotation cells can reduce this problem by being used to remove these valuable materials from the grinding circuit to prevent over grinding. The cell is designed so that very coarse material will bypass the flotation area of the cell and go straight to the discharge and only this material will be reground. This cell has the benefit of acting as both a flotation machine and a classifier.

Xia et al. (2010) presented a new retrofit rotor stator design from Outotec where the stator blades are separate and are mounted on a pedestal which aims to increase mixing for the same aeration rate as a traditional setup, this has many benefits but one is to increase the suspension of coarse particles therefore improving the recovery of coarse particles. Coleman and Rinne (2011) showed that this design slightly improves the copper recovery of all size fractions when compared to a standard design, however there are few published results using this design.

Whilst the different design modifications listed for improvement of coarse particle flotation have been shown to be successful, the majority have one major drawback,: the high capital cost involved in implementing new infrastructure. It would therefore be beneficial to industry to implement a retrofit design modification to a conventional mechanical flotation cell that would improve the flotation of coarse particles.

### 2.5.3 Laboratory scale research

Industrial flotation cells are challenging to use when conducting experiments due to their size and the complex nature of industrial ores resulting in high variability in conditions between tests. It is for this reason that the majority of flotation research is initially performed at the laboratory scale, before moving to pilot plant testing, before finally being implemented in a flotation plant (Wills and Finch, 2015). Often, reagent environment tests are performed using commercially available batch cells such as the Denver cell. Most processing plants will have these cells on site in order to perform “hot” flotation tests using feed straight from different streams on the plant. These tests are ideal to obtain a snapshot of flotation performance. The other benefit of using such cells is their relative simplicity and ubiquity meaning that their hydrodynamics are well understood. The ubiq-

uity of batch tests also means that data collected in these tests can easily be compared across the literature.

Whilst batch cells can be incredibly useful for certain types of studies, especially reagent studies, there are pitfalls in using these cells to understand froth flotation. The biggest downfall of such batch tests is that they are limited in the short length of time that floatable material is present in the cell, which results in steady state being difficult to achieve (Wills and Finch, 2015). One way to overcome this issue is to perform tests on a pilot plant, however, this is not an ideal solution for investigating different design modifications as pilot scale cells can be difficult to modify. In order to test different design modifications the simple batch cells need to be heavily modified, as in work by Barbian et al. (2003), or a bespoke system needs to be developed.

The easiest way to overcome the problem of batch cells not reaching steady state is to use a laboratory scale, continuous, or semi-continuous, cell. There have been several studies in recent years that have used such systems. These cells will generally pump both the concentrate and the tailings material into a mixing tank that then becomes the feed for the cell, allowing a closed loop system to form. McFadzean et al. (2016b), Wang et al. (2017) and Hemmati Chegeni et al. (2016) used semi-continuous columns for their studies while Li et al. (2016), Norori-McCormac et al. (2017) and Morrison et al. (2017) used semi-continuous mechanical cells. All of these systems were shown to operate at steady state and were used with ores of varying degrees of complexity. The mechanical cell used by Norori-McCormac et al. (2017) is unique, in that there is no separate mixing tank recombining the tailings and the concentrate. Instead the concentrate is pumped directly from the launder back into the base of the cell and there is no tailings stream. The designs of the cells used by Norori-McCormac et al. (2017) and Morrison et al. (2017) are based on the standard mixing tank but at different scales: $4\,\mathrm{L}$ and $87\,\mathrm{L}$ respectively. The fact that these cells are based on the same design but are different scales allows for scale up work to further understand how effects of different design modifications at the laboratory scale may translate to the effects that may be seen at the industrial scale.

## 2.6 Positron Emission Particle Tracking

Positron emission particle tracking (PEPT) is a useful technique that can be used to map the position of particles within a flotation tank over time. The principle of PEPT has been

developed from positron emission tomography (PET), a technique widely used in medicine where a patient is injected with a radioactive tracer and a PET scanner detects gamma rays (Parker et al., 1993). When used for tracking particles, a tracer is made by labelling a particle with a radionuclide such as $F^{18}$. This decays by $\beta^+$ emission, i.e. a positron is emitted. This positron is annihilated when it comes into contact with an electron and will then emit two, back to back, gamma rays. A positron emission tomography (PET) camera detects the pair of gamma rays and their trajectories are then triangulated to determine the location of the tracer (Waters et al., 2008). A 3D image is then constructed from a large collection of locations and this can be used to track how a tracer moves through a system (Parker et al., 2002). For medical applications the tracer is a fluid, however Bemrose et al. (1988) found that the position of a single solid particle can be detected using the same method, even when it is moving.

Since its first use, PEPT has been successfully applied to a wide range of minerals processing research such as; froth flotation (Cole et al., 2012; Waters et al., 2008, 2009), 2D foams (Cole et al., 2010), comminution (Govender et al., 2010; Morrison et al., 2016) and hydrocyclones (Radman et al., 2014). It is important to validate the use of a new technique with against older methods. Pianko-Oprych et al. (2009) performed a direct comparison between PEPT and Particle Image Velocimetry (PIV) in a stirred tank and showed that there was good correlation between the two. Chiti et al. (2011) used a similar stirred tank and showed a good comparison between the particle velocities from PEPT and from those in the literature utilising other techniques.

### 2.6.1 PEPT in flotation

Due to the presence of solids in a froth flotation system, the pulp and froth phases are optically opaque, so techniques such as particle image velocimetry are unsuitable. This has greatly hindered the understanding of the processes that occur in froth flotation, making PEPT vital to froth flotation research as it can be used to visualise motion in opaque systems (Cole et al., 2010). PEPT helps to fill this gap by allowing research to be done to further the understanding of the dynamic physical processes that are going on inside a flotation cell.

Waters et al. (2008) carried out initial work, in a batch cell, showing that there was considerable potential for PEPT to be used within froth flotation using it successfully to

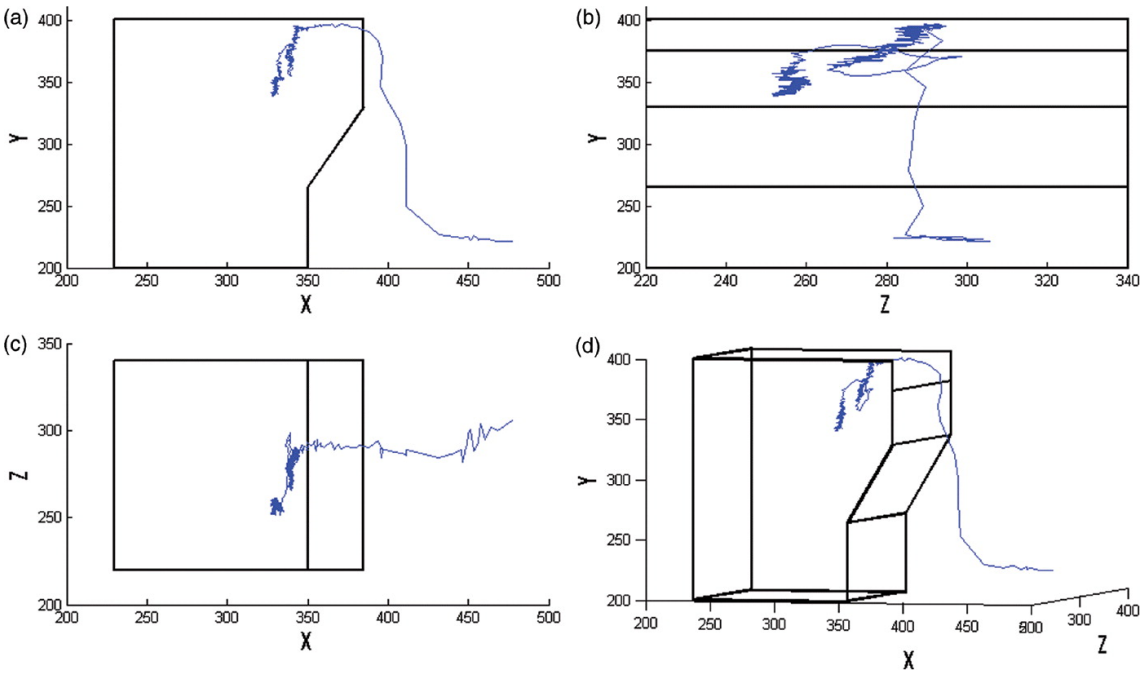



**Figure 2.8:** A Denver flotation cell showing PEPT tracer motions (Waters et al., 2008).

map both a hydrophilic and hydrophobic tracer within a flotation cell (figure 2.8). The work also clearly showed fundamental particle behaviours in the froth such as particle attachment and detachment. Cole et al. (2010) further developed the PEPT method for accurate use within froth flotation research. They combined PEPT with high speed digital imaging in a foam column and showed a 95% confidence in the location of the tracer within $\pm$ 2.7 mm. Since then, Cole et al. (2014) varied the size of tracers showing that they can be modified and selected to match the specific properties of the feed such as particle size, density and hydrophobicity. This allows a tracer either to act as a gangue particle or a valuable particle allowing a better understanding of the motion of either species in the system.

Norori-McCormac (2015) used PEPT to investigate the effects of different retrofit designs on the bulk flow within the continuous flotation cell used in this work, as well as turbulence on different particles in the system at the pulp-froth interface. This work showed that the use of a retrofit mesh with a hole size of 30 mm helps to transport hydrophobic particles from the pulp to the froth with very little downward flow. This hole size also optimises pathways for the tracer to be recovered from the pulp to the froth. This mesh also exhibited high liquid flow rates, resulting in increased entrainment. This is something that needs to be investigated further to determine if this can be improved. The presence of meshes in the system was shown to break down the swirl at the top of the pulp phase reducing turbulence. There were a few problems with this system however;

firstly there were high liquid flow rates with the mesh; secondly, this feed was made up of a single species ore and so whilst a hydrophillic tracer was used this could not accurately represent the flow of gangue material as there was none in the system; and thirdly, the froths were not sufficiently particle stabilised, meaning that they were not representative of true flotation systems.

## 2.7 Conclusions

Whilst froth flotation has been used as a separation technique in the minerals processing industry for over a century, there is still plenty of scope for improvement, especially when considering that even small changes in metallurgical recoveries will translate to huge economic benefits. There has been a significant amount of work devoted to understanding the mechanisms at different points within the flotation cell. However, it is challenging to fully understand the sub-processes occurring in an opaque system. It is well known from the literature that both coarse and fine particle flotation can be challenging and that there are great benefits, both economically and environmentally, to improving the flotation efficiency of these particles.

Laboratory scale testing is a vital step towards understanding how changes to the froth flotation process will impact performance. However, the majority of such tests do not operate at steady state. A continuously overflowing flotation cell was previously developed as an alternative to bench scale flotation investigations that runs at steady state. This was successful, however it has only been shown to work with a single species in a flotation system that does not exhibit true separation. This thesis develops this cell further with the use of more complex ores.

There is still a lack of solid understanding of the effects of fine particles on flotation, this is especially important when considering that tailings reprocessing is likely to become a more significant part of the minerals processing industry with a move towards improving sustainability. This thesis builds on previous work by Mackay et al. (2018) to help improve the understanding by varying the particle size of a copper tailings ore and investigating the effects on flotation performance and stability using the continuously overflowing flotation cell.

In addition to research into fine particle flotation, there is a focus on coarse particle

flotation which will lead to a reduction in energy consumption and improve the efficiency of flotation. There have been several flotation cell design modifications presented as solutions to coarse particle flotation, however the vast majority of these require completely new equipment and there has been little investigation into retrofit design modifications. The latter would be more beneficial to industry due to the low capital expenditure for installation. This thesis further develops previously proposed retrofit design modifications at the bench scale.

The effect of different design modifications in this cell were previously investigated, whilst these proved to be successful to some extent, again they were only used in the study of a simplified system. They also increased the liquid content of the froth relative to the unmodified case which leads to a reduction in grade. The optimal retrofit design was used in this thesis with a more complex ore, and was also further developed with the aim of reducing the liquid content.

In previous work positron emission particle tracking (PEPT) has proved to be a useful technique for a better understanding of the sub-processes involved in froth flotation. In this thesis, PEPT will be used to study the effects of design modification in a true separation system with the continuously overflowing flotation cell. For the first time a variety of different tracer sizes will also be used to investigate retrofit design modifications with the aim of furthering the understanding of the effects of particle size on flotation.

This thesis will aim to address the gaps in the literature as described above. The next chapter will discuss the tools and methodology used in the thesis to achieve this aim.

# Chapter 3

# Experimental Techniques

## 3.1 Introduction

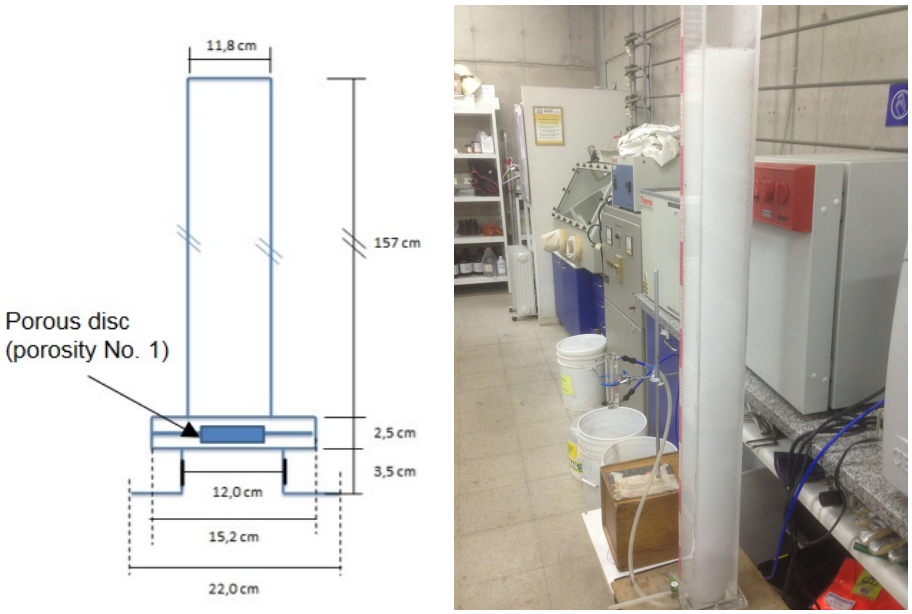
There are three main experimental methodologies used in this thesis. The first methodology involved a laboratory scale, non-overflowing flotation column which was used to conduct the dynamic froth stability experiments in chapter 4. The second methodology was the use of a continuously overflowing, bench scale mechanical flotation cell, initially developed by Norori-McCormac et al. (2017) which was used to conduct the experiments in chapters 4, 5, 6 and 7. The third methodology was positron emission particle tracking (PEPT), which was used in the experiments in chapters 6 and 7.

## 3.2 Flotation Equipment

### 3.2.1 Laboratory scale, non-overflowing flotation column

One of the most commonly used laboratory measures of froth stability is the dynamic froth stability ($\Sigma$) which is measured using a modified Bikerman test (with froth rather than foam), as described in section 2.4.2. In chapter 4, a laboratory scale, unstirred, non-overflowing column was used to conduct such tests (figure 3.1). This set up is similar to the systems used in a variety of other studies (Cilek and Karaca, 2015; Ip et al., 1999; Li et al., 2017). The column was $157\,\mathrm{cm}$ tall with graduations on the front wall and a square cross sectional area of $139.2\,\mathrm{cm}^2$. Air was injected into a chamber at the base of the column where it then passed through a porous disk (porosity No. 1) of sintered glass,

8 cm in diameter in order to produce bubbles. Between each experiment the column and frit were cleaned thoroughly by rinsing each wall with water and then ethanol twice and then finishing with a final rinse with water to ensure no ethanol remained on the walls.




(a) Schematic of the column. Adapted from Molina et al. (2016).

(b) Photograph of the column.

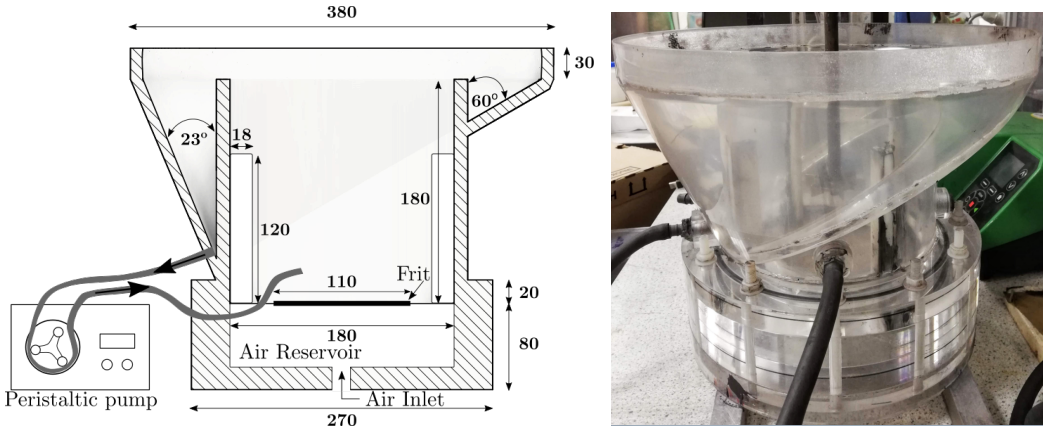
**Figure 3.1:** Illustration of the non-overflowing laboratory scale flotation column.

### 3.2.2 Continuous bench scale cell

As discussed in chapter 2, bench scale flotation tests are important to further our understanding of the mechanics of flotation and are incredibly useful for designing improvements to flotation cells. However, conventional batch flotation cells have their downfalls in that they do not operate at steady state. Norori-McCormac et al. (2017) developed a bench scale cell that overflows continuously, where the concentrate is pumped out of the launder and back into the base of the cell rejoining the pulp. This allows steady state to be achieved and the cell can operate over long periods of time. Due to the continuous nature of the cell, air recovery is used to measure froth stability as described in section 2.4.2.

A key feature of the cell is that it needs to be easily modifiable and also to have well understood hydrodynamics. The design and dimensions of the cell used in this work were adapted from that described in Costes and Couderc (1988). Figure 3.2 shows a schematic of the continuously overflowing cell along with a photograph of the cell in the laboratory.

The proportions of the cell are the same as presented for a standard mixing tank in Costes and Couderc (1988). The internal diameter and height of the cell are 180 mm and




(a) Schematic of the flotation cell (b) Photograph of the flotation cell

**Figure 3.2:** Details of the design of the continuously overflowing flotation cell. The concentrate is pumped from the launder back into the pulp zone of the cell. Measurements given in the schematic in (a) are in millimetres.

there are four baffles, equally spaced around the cell, with a height of $120\,\mathrm{mm}$ from the base of the cell and protruding $18\,\mathrm{mm}$ from the wall. A six bladed Rushton impeller is used to stir the tank and is connected via a Huco T Gearbox (supplied by RS Components Ltd.) to a Marelli $0.37\,\mathrm{kW}$ AC Motor (supplied by Inverter Drive Supermarket). The plane of the impeller is $60\,\mathrm{mm}$ above the base of the cell. At the base of the cell there is an air reservoir, that is separated from the cell by a $110\,\mathrm{mm}$ diameter and $1.3\,\mathrm{mm}$ thick frit (supplied by Carbis Filtration Ltd). The frit is comprised of multiple sintered layers producing a mesh hole-size of $20\,\mu\mathrm{m}$. A flowmeter is attached to the reservoir at the base of the cell to allow control of the air flowrate into the cell. The launder is angled in such a way as to allow the concentrate to drain down to the front where there are two recycle points. These recycle points are connected to two peristaltic pumps (Watson Marlow 530SN/R), the concentrate is pumped into the base of the cell on either side. The two pumps were operated at the same flowrate to prevent there being an imbalance in the flow from one side of the cell to the other.

## 3.3 Flotation Environments

In this thesis, two different flotation environments were investigated. The first environment used a copper porphyry tailings ore obtained from a Chilean processing plant that reprocesses material from a tailings dam (chapter 4). The second environment used a simple, synthetic two-species ore of magnetite and silica (chapters 5,6 & 7). For experiments in the laboratory scale flotation column, the solids content of the slurry was kept at

9%$_{wt}$, comprised of $600\,\mathrm{g}$ solids combined with $6\,\mathrm{L}$ of deionised water. For experiments in the continuous bench scale cell, regardless of the ore used, the solids content of the pulp was kept constant at 24%$_{wt}$, comprised of $900\,\mathrm{g}$ solids combined with $2.9\,\mathrm{L}$ of deionised water. At the beginning of all experiments the slurry was pumped into the cell and agitated with the impeller at $950\,\mathrm{rpm}$ for a duration of 10 minutes to ensure the particles were sufficiently suspended and flow well developed.

### 3.3.1 Copper tailings ore

Samples of a Chilean copper tailings ore were obtained from a minerals processing plant that reprocesses tailings material. This processing plant takes material from a local tailings dam as the feed to the plant, this material is then sent through a primary hydrocyclone to separate the fine and coarse material. Technical reports from the plant state that the ore is primarily comprised of chalcopyrite and pyrite (Henderson, 2016). For the purposes of this thesis, the mineralogy of the specific batch of material used was analysed in more detail using QEMSCAN (quantitative evaluation of minerals by scanning electron microscopy). The details of this analysis are discussed in section 3.6.2.

For this work, samples were obtained from the overflow and underflow streams of the hydrocyclone. These samples were then dried and recombined in varying proportions in order to vary the particle size distribution of the feed. The particle size distributions of the overflow and underflow of the feed were measured using laser diffraction as described in section 3.6.4 and can be seen in figure 3.3 and in table 3.1. The reagent environment used was initially developed by Molina et al. (2016). The collector used was Sodium Isopropyl Xanthate at $50\,\mathrm{g\,t^{-1}}$ (supplied by Grinding Solutions Ltd.) and the frother was DowFroth 400 (supplied by Nasaco Ltd.) at $20\,\mathrm{g\,t^{-1}}$. Lime, *CaO* (supplied by Arcos Organics), was added to the slurry to ensure a constant pH of 9 across all experiments. The reagents were all added to the system at the same time and the environment was kept the same for both experiments measuring dynamic froth stability and those measuring air recovery. For the dynamic froth stability experiments, the solids, water and reagents were added to the column at the same time with the air on to ensure the slurry was well mixed. After two minutes the air was turned off and as soon as the froth had completely collapsed was turned back on again for the start of the experiment. For the air recovery experiments, the slurry was agitated in the cell for 15 minutes at $950\,\mathrm{rpm}$ for conditioning, prior to turning

on the air.

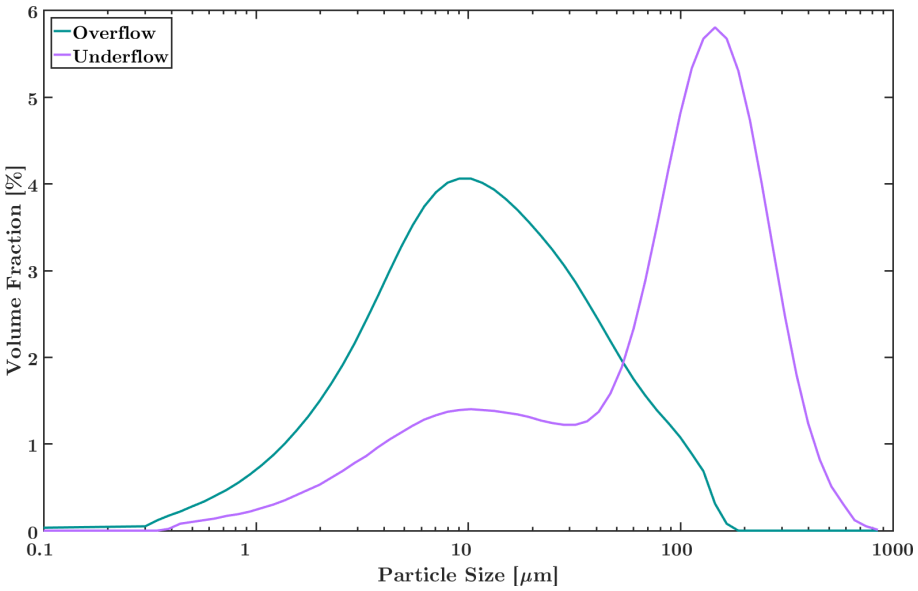



**Figure 3.3:** Particle size distributions of the hydrocyclone overflow and underflow streams from the copper tailings reprocessing plant.

This copper tailings flotation environment was used to investigate the effects of changing the feed particle size distribution on flotation performance. For the dynamic froth stability experiments in the non-overflowing flotation column, seven different particle size distributions were used ($A_\Sigma - G_\Sigma$ in table 3.1) each at three different superficial gas velocities that ranged between $0.96\,\mathrm{cm\,s^{-1}}$ and $1.92\,\mathrm{cm\,s^{-1}}$. It is important to note that since a wide range of conditions were evaluated, not all cases could be run at the same three values of superficial gas velocity. For fine particles at high air rates the froth was very stable and would quickly reach the full height of the column and overflow. At the other extreme, coarse particles at low air rates did not produce a stable froth at all. For the air recovery experiments in the continuously overflowing flotation cell, three different feeds were used ($A_\alpha - C_\alpha$ in table 3.1) at four different gas velocities each: $0.92\,\mathrm{cm\,s^{-1}}$, $1.05\,\mathrm{cm\,s^{-1}}$, $1.18\,\mathrm{cm\,s^{-1}}$ and $1.31\,\mathrm{cm\,s^{-1}}$.

### 3.3.2 Two-species system

For the experiments with the synthetic magnetite and silica ore, reverse cationic flotation was used, where the gangue, in this case silica, was the mineral that was floated and the valuable, magnetite, remained in the pulp. The system followed that from Filippov et al. (2010). The collector used was Dodecylaime at 98% purity at a concentration of $300\,\mathrm{g\,t^{-1}}$ of silica. The activator used was 1-Tridecanol at a concentration of $100\,\mathrm{g\,t^{-1}}$ of silica. The

**Table 3.1:** Particle size distributions for the hydrocyclone overflow and underflow and the seven feeds used for dynamic froth stability tests (subscript $\Sigma$) and the three feeds used for air recovery tests (subscript $\alpha$) in chapter 4.

| Feed | d10, [$\mu$m] | d50, [$\mu$m] | d90, [$\mu$m] |
|---|---|---|---|
| Overflow | 2.6 | 13.1 | 63.6 |
| Underflow | 5.8 | 104.8 | 278.7 |
| $A_\Sigma$ | 2.6 | 13.1 | 63.6 |
| $B_\Sigma$ | 3.4 | 36.1 | 117.4 |
| $C_\Sigma$ | 4.2 | 89.0 | 171.2 |
| $D_\Sigma$ | 4.6 | 70.5 | 198.2 |
| $E_\Sigma$ | 5.0 | 81.9 | 224.9 |
| $F_\Sigma$ | 5.3 | 88.8 | 241.1 |
| $G_\Sigma$ | 5.8 | 104.8 | 278.7 |
| $A_\alpha$ | 2.6 | 23.0 | 179.3 |
| $B_\alpha$ | 2.9 | 30.2 | 219.1 |
| $C_\alpha$ | 3.3 | 47.1 | 253.4 |

depressant was modified corn starch at a concentration of $1875\,\mathrm{g\,t^{-1}}$ of magnetite. All three of these chemicals were supplied by Sigma-Aldrich. The native pH of the slurry was 10 and so was not modified. The frother used in this work was Methyl isobutyl carbinol, MIBC, (supplied by Sigma-Aldrich) at an initial dose of 12ml of a dilute $0.32\,\mathrm{v/v\%}$ solution (made with deionised water). This corresponded to a concentration of 13ppm MIBC in the slurry. As MIBC is volatile the dilute solution was re-dosed at a rate of $6\,\mathrm{ml\,h^{-1}}$ (equivalent to $0.019\,\mathrm{ml\,h^{-1}}$ pure MIBC).

As previously mentioned, $900\,\mathrm{g}$ of solids was used in each experiment, this was comprised of 85 % Magnetite (supplied by LKAB minerals) and 15 % silica (supplied by Hodge Clemco LTD). The magnetite was sieved before use to remove the $<38\,\mu\mathrm{m}$ material to prevent sliming. The size distribution of the feed was measured by laser diffraction using a Mastersizer 2000 (see section 3.6.4) and can be seen in figure 3.4 . After 10 minutes agitating just the solids and deionised water, the activator and depressant were added to the cell and left to condition for five minutes. The collector was then added and left to condition for a further 10 minutes to allow sufficient adsorption onto the surface of the silica. The MIBC was subsequently added and left to condition for two minutes before the air was turned on at the desired initial air rate. The MIBC dosing was started immediately after the air was turned on.

The two-species flotation environment was used to investigate the effects of superficial gas velocity and different retrofit mesh designs on flotation performance and particle size in chapter 5. Three superficial gas velocities were used: $0.65\,\mathrm{cm\,s^{-1}}$, $0.82\,\mathrm{cm\,s^{-1}}$ and

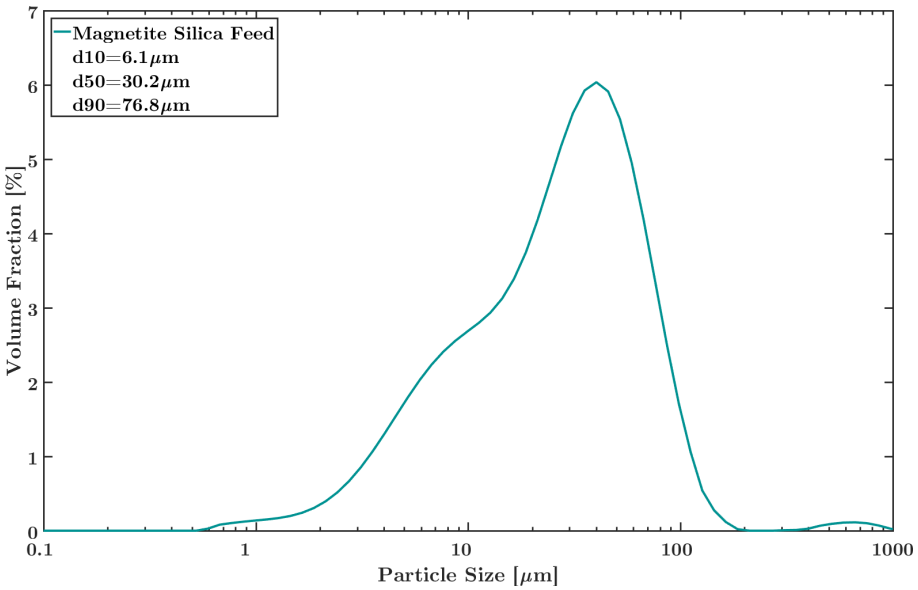
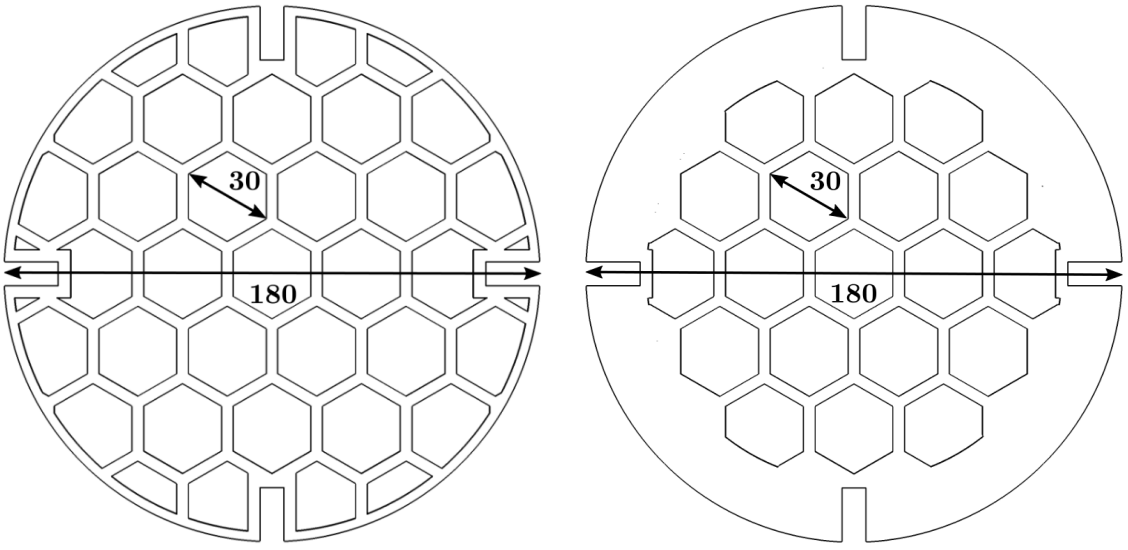



**Figure 3.4:** Particle size distribution of the synthetic magnetite and silica ore.

$0.98\,\mathrm{cm\,s^{-1}}$. Three different design cases were used, firstly the unmodified cell as the base case and then two different retrofit meshes shown in figure 3.5. The purpose of the retrofit meshes was to introduce a quiescent zone at the pulp froth interface in order to reduce the detachment of coarser particles. As such, the meshes were inserted in the cell, flush with the top of the baffles in order for the meshes to sit just below the pulp froth interface.

The meshes used in this study were based on the honeycomb meshes initially investigated by Norori-McCormac (2015). The first mesh used in this work, the "basic mesh", had a thickness of $20\,\mathrm{mm}$ and a pore size of $30\,\mathrm{mm}$. This was chosen as when used in a single-species system by Norori-McCormac (2015) it was shown to result in the best improvement in the indicative recovery, as well as the air recovery, in comparison to the unmodified cell. Norori-McCormac (2015) also investigated this mesh using PEPT, where it was shown to reduce the swirl at the pulp froth interface. The basic mesh design (figure 3.5(a)) was chosen for this study as it has been previously studied in a similar system and will therefore provide a good baseline for comparison of the two-species system to the single-species system. The results from the PEPT experimentation conducted by Norori-McCormac (2015) indicated that there was an increased flowrate of water at the walls of the cell, this was thought to explain why there was no improvement in grade with the mesh. For the present study, the mesh design was adapted to try and counteract the increased water flowrate, and therefore entrainment, by blocking in the outside holes of the mesh. This "blocked mesh" (figure 3.5(b)) otherwise had the same dimensions as the

"basic mesh" and was used in the same way. Both of the meshes were designed using Sketch Up CAD software and exported as an "stl" file before being 3D printed. All three cases were run at three superficial gas velocities and experiments were duplicated.




(a) Basic Mesh (b) Blocked Mesh

**Figure 3.5:** The two different mesh designs used in this chapter: (a) "Basic Mesh" and (b) "Blocked Mesh". Both meshes have a thickness of $20\,\mathrm{mm}$, other illustrated dimensions are in millimetres.

## 3.4 Data Collection

### 3.4.1 Dynamic froth stability experiments

In order to measure the dynamic froth stability (equation 2.2) in the non-overflowing flotation column, the maximum height of the froth for each condition needed to be measured. Measurements of the froth height, to the nearest $0.5\,\mathrm{cm}$, were recorded regularly over a 30 minute period and each experiment was duplicated to obtain an average height. Figure 3.6 shows froth height for the experiments at two different air rates for the coarsest particle size distribution, with a d90 of $279\,\mu\mathrm{m}$. Each curve represents average data across duplicated experiments, with intervals representing one standard deviation. This illustrates that the froth height initially increased and after a period of 5 minutes slightly decreased again, reaching steady state. Previous work has referred to the maximum froth height, $H_{max}$, when calculating $\Sigma$, however as can be seen from these experiments the maximum height the froth achieved was not the froth height at steady state. In this work, when calculating the dynamic froth stability the equilibrium height, $H_{eq}$, which was the

steady state froth height reached after approximately 30 minutes of operation was used instead of the maximum height.

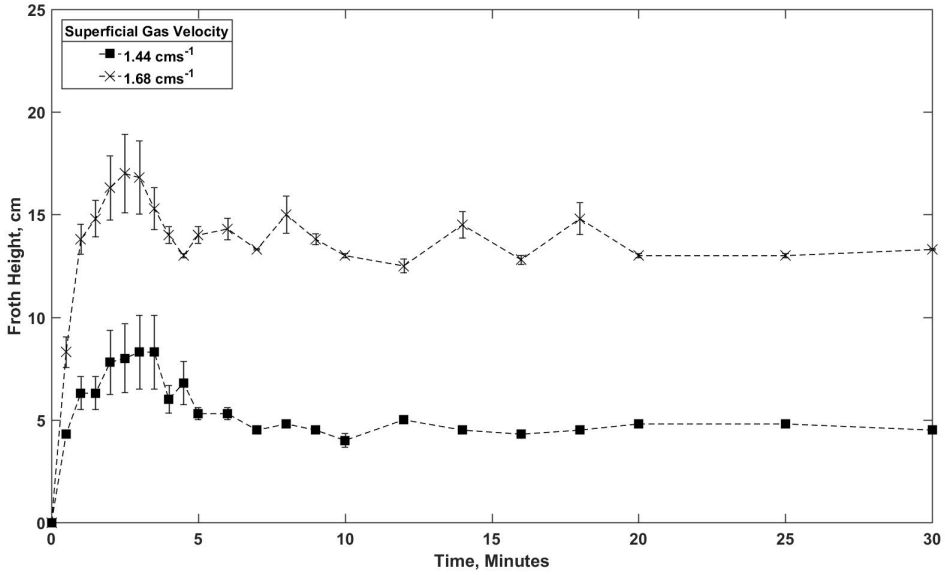


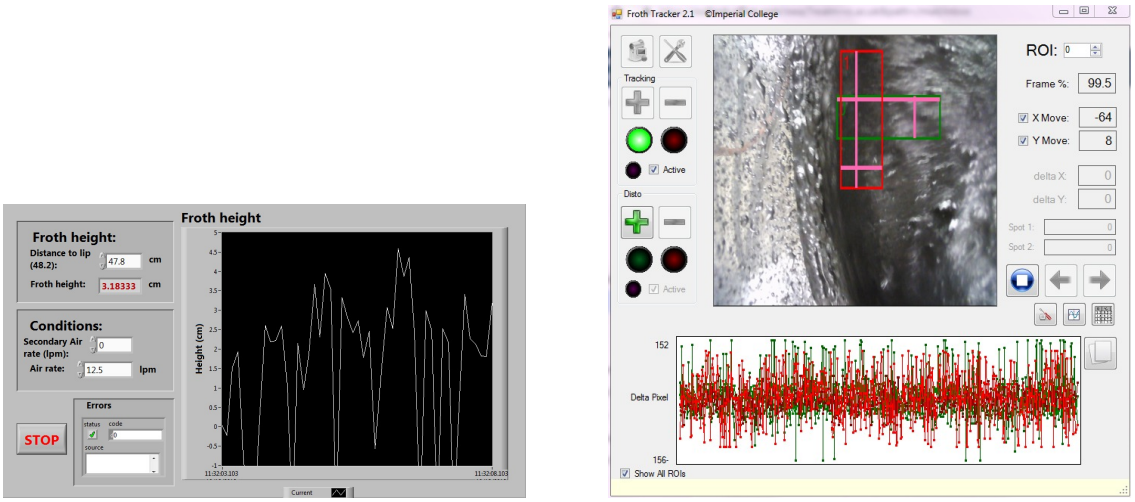

**Figure 3.6:** Froth height growth for experiments with d90 of $279\,\mu\mathrm{m}$ over 30 minutes of operation at two different superficial gas velocities. Intervals represent one standard deviation

### 3.4.2 Air recovery experiments

In order to measure air recovery (equation 2.3) in the continuously overflowing flotation cell, overflowing froth velocity and overflowing froth height were measured continuously. An optical level sensor (ifm electronics, 01D300) was used to measure the froth height via LabVIEW (figure 3.7 (a)). A web camera (AUSDOM AW615) was used to measure the froth velocity via Froth Tracker, an in house image analysis program using block matching. This works by the user highlighting a region of interest (R.O.I), the program then finds a point within the R.O.I of the current frame, then matches this to the next frame. From this, the velocity in change in pixels per frame was determined. This was then converted to centimetres per second according to the calibration of the camera. A section of the froth can be seen in figure 3.7(b) showing two R.O.Is used by Froth Tracker, for the work in this thesis only the red R.O.I was used to calculate the velocity. There can be several sources of error associated with the block matching algorithm such as the lighting contrast and the quality of the camera. To minimise these effects the region of interest was well lit by a floodlight to ensure that there was good enough contrast in the camera to pick up changes frame by frame. In addition to this, a web camera without auto focus was chosen

to ensure that the calibration from pixels to centimetres stayed true. Another important factor to consider is that the conversion from pixels to centimetres using the calibration relies on knowing the distance between the camera and the froth, however the height of the froth changes. To counteract this the froth height data, combined with the known distance between the camera and the lip of the cell, were used to more accurately convert from pixels into centimetres.

The height data from LabVIEW and velocity data from Froth Tracker were then loaded into MATLAB to calculate the air recovery, using equation 2.3, every second. Due to the nature of the experiments, and the fact that bubbles will often burst, the air recovery data is very noisy. In order to smooth this data and to aid interpretation, a 30 second moving average was calculated




(a) LabVIEW (b) Froth Tracker

**Figure 3.7:** Screen shots of measuring (a) froth height with labVIEW and (b) froth velocity with Froth Tracker

Over the course of an experiment several different operating conditions can be run. This is one of the benefits of having a system that runs continuously for an extended period of time. Each condition was run for a total of 15 minutes, however only the data from the last 10 minutes was used to calculate the average air recovery at that condition in order to allow 5 minutes for the cell to reach steady state at each new condition. The condition that was run at the beginning of the experiment was also repeated as the final condition, allowing for any changes over the course of the experiment to be taken into account. From these data, the change in air recovery due to varying different conditions; air rate, feed size and cell design, can be established.

### 3.4.3 Data processing

#### Analysis of variance

For the experiments performed using the continuous bench scale flotation cell in chapters 4 & 5 an analysis of variance test (ANOVA) was performed to determine if the means of the different conditions were statistically different. This test assumes that the observations are independent, the distributions of the residuals are normal and that the variance of the data in the groups are the same. For each variable investigated (e.g. air recovery, grade, etc.), an ANOVA test was conducted using the measured values of the variable as the input data and the superficial gas velocity and the design (feed particle size in chapter 4 and physical design modification in chapter 5) as the two factors. The significance of the interaction between these two factors was also determined.

#### Linear regression

For the experiments presented in chapter 5 there was a dependence in the results on the date of the experiment and the time when the sample was taken throughout the experiment, this is linked to variations in conditions such as ambient temperature and humidity. This was established by repeating conditions within one experimental run and also repeating all experimental runs. The effects of date and time were determined by using them as predictors to apply a step-wise linear regression model to the data. A quadratic model was chosen for this which uses the interaction terms between predictors and their self interactions. Each of the predictors were normalised between -1 and 1 in order to negate the effects of the different orders of magnitude of each predictor. The resulting model takes the form of equation 3.1, where $y$ is the response, $a$ is the coefficient and $P$ is the predictor. This model was then used to adjust the data to negate the differences caused by date and time. Both of these steps were done using MATLAB. By doing this the effects of changing the superficial gas velocity for each of the design cases is highlighted and the effects of change in environment, due to date and time, are minimised.

$$y = a_0 + a_1.P_1 + a_2.P_2 + ... + a_{1,2}.P_1.P_2 + ... + a_{1,1}.P_1^2 + ... \tag{3.1}$$

## 3.5 Sample Collection

### 3.5.1 Non-overflowing column

Due to the fact the dynamic froth stability tests necessitated a non-overflowing column, it was not possible to obtain direct samples of the froth. Instead preliminary flotation performance tests for selected particle size distributions were conducted in a 3L Denver cell with a cross-sectional area of $169\,\mathrm{cm}^2$ at a superficial gas velocity of $1.44\,\mathrm{cm\,s}^{-1}$. This air rate was chosen to match the air rate for which dynamic froth stability experiments were run for all seven of the particle size distributions. These tests were performed with the same reagent environment and solids concentration as in the column flotation tests. The Denver cell was operated with an agitation speed of 1200 rpm, a conditioning time of 5 minutes and a flotation time of 10 minutes. The performance of three particle size distributions were investigated in this set of experiments, those with d90s of $117\,\mu\mathrm{m}$, $225\,\mu\mathrm{m}$ and $279\,\mu\mathrm{m}$. The concentrate samples from the flotation performance experiments were analysed chemically using atomic adsorption spectrometry to determine copper content.

### 3.5.2 Continuously overflowing cell

In order to measure the flotation performance of the experiments in the continuously overflowing cell, samples of the concentrate were obtained. A 3D printed scoop (figure 3.8) was designed for this purpose that fits exactly in the launder at the front of the cell allowing for the concentrate to overflow the lip of the cell and into the scoop. A five second sample of the concentrate was collected for most conditions, however, for conditions that had a significantly slower overflow, a 10 second sample was taken. The mass of the concentrate sample was then measured before the sample was dried and the dry weight of solids was measured.

## 3.6 Sample Analysis

### 3.6.1 Solids flowrate as a proxy for recovery

In the continuously overflowing flotation cell, due to the fact that the concentrate is recycled back into the pulp of the cell and there is no tailings stream, calculating mineral recovery is non-trivial. Instead, solids flowrate to the concentrate can be calculated and



**Figure 3.8:** The 3D printed scoop inserted into the launder of the cell.

from that a recovery per unit time. The length of the lip of the scoop is a quarter of the length of the lip of the cell so this is factored in to ensure calculating solids flowrate for the whole cell and not just the section sampled. This was calculated using equation 3.2, where $t$ is the length of time over which the sample was collected and $M_{dry}$ is the mass of the dried sample.

$$Flowrate = 4 * \frac{M_{dry}}{t} \tag{3.2}$$

Once the grade had been determined using the appropriate method for the ore being used, this flowrate was converted into the flowrate of valuable material to the concentrate by multiplying equation 3.2 by the grade.

### 3.6.2 Grade and mineralogical analysis of the copper tailings ore

The copper grade of the tailings ore was measured by Wheal Jane Laboratories (*Cornwall, UK*). The samples were first prepared by hydrochloric acid attack and then the copper content analysed using a Thermo Fisher Scientific iCE 3300 Atomic Absorption Spectrometer.

The detailed mineralogy of each of the different feeds used for the air recovery experiments was determined using QEMSCAN (quantitative evaluation of minerals by scanning electron microscopy). A QEMSCAN E430 in bulk mineralogical analysis measurement mode was used with a measurement time of 2.5 hrs and an acceleration voltage of 20kV. The software used were iMeasure v.4.3 for data acquisition and iDiscover v.4.3 for data processing. The QEMSCAN was calibrated using Quartz, Copper and Gold standards, with preset values of 44, 130 and 232 respectively.

### 3.6.3 Concentrate grade of the magnetite silica ore

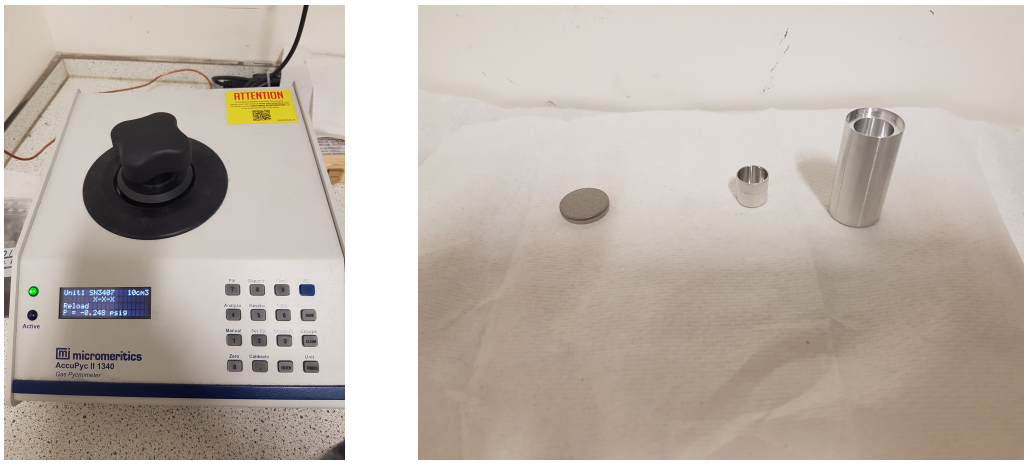
For the magnetite silica ore, the grade of the samples was calculated in house using the Accupyc II 1340 Gas Pycnometer (figure 3.9). This technique calculates the density of the sample using gas displacement (with helium) to measure the volume of the void space in the chamber and hence the volume of solids. The dry sample was inserted into the appropriately sized sample cup to ensure using the maximum amount of sample for analysis as possible. If all of the sample was not used up in the first round then a second sample was analysed to ensure that the data were representative of the whole sample. As the masses of the samples were small, rolling and quartering was not an appropriate method to obtain a representative section of the sample, instead only small amounts of the sample were added to the cup at a time and from different sections of the sample until the cup was full. The density of each sample was measured 10 times in one analysis and the average used as the final density for the sample. The densities of pure magnetite and silica were measured first in order to calculate the grade. These were $5.10\,\mathrm{g\,cm^{-3}}$ and $2.47\,\mathrm{g\,cm^{-3}}$ respectively. The grade of magnetite, $G_M$, was calculated using equation 3.3, and similarly the grade of silica, $G_S$, using equation 3.4 where $\rho_T$, $\rho_M$ and $\rho_S$ are the densities of the total sample, magnetite and silica, respectively. As this system is reverse flotation, a lower magnetite grade and a higher silica grade indicate a better performance.

$$G_M = \frac{\frac{1}{\rho_T} - \frac{1}{\rho_S}}{\frac{1}{\rho_M} - \frac{1}{\rho_S}}, \tag{3.3}$$

$$G_S = \frac{\frac{1}{\rho_M} - \frac{1}{\rho_T}}{\frac{1}{\rho_M} - \frac{1}{\rho_S}}, \tag{3.4}$$

### 3.6.4 Particle size

The particle size of the feed and concentrate samples for all experiments was analysed using a Malvern Mastersizer 2000 particle analyser. A small section of each sample (approx. 1g) was diluted to $20\,\mathrm{mL}$ using DI water in a graduated test tube. The test tube was then agitated by hand to ensure the solids were in suspension before a small amount was removed using a pipette an added to the Mastersizer. The obscurity was kept to approximately 12 % for all samples. Each sample was analysed twice to ensure accuracy. For the feed samples of the copper tailings ore, a second sample was taken from the bulk sample




(a) Gas Pycnometer (b) Sample Cup

**Figure 3.9:** The Accupyc II 1340 Gas Pycnometer (a) and the $1\,\mathrm{cm}^3$ sample cup (b).

and analysed twice using the Mastersizer as there was a higher variability in the particle size. The $d_{10}$, $d_{50}$ and $d_{90}$ sizes were then calculated as well as the volume fraction in each size class in order to determine particle size distributions.

## 3.7 Positron Emission Particle Tracking

Positron emission particle tracking (PEPT) experiments were carried out for the work in chapters 6 and 7. The PEPT experiments were conducted at the PEPT Cape Town facility, part of the iThemba LABS (*South Africa*). The Positron Emission Tomography (PET) camera used at this facility is the ECAT HR++ (Model: CTI/Siemens 966). This camera has high resolution and sensitivity (Buffler et al., 2018). The experiments in chapters 6 & 7 were carried out using the magnetite silica system with the same reagent environment used in the similar experiments performed in London (section 3.3.2). The same three design cases were used for the PEPT work, however only one superficial gas velocity was used ($0.82\,\mathrm{cm\,s}^{-1}$). In order to ensure a good resolution of the tracer throughout the whole cell the experiments were run at one condition for an extended period of time (approximately 2hrs for each tracer depending on the initial activity of the tracer). The only modification to the system was a decrease in the height of the rig and the length of the impeller by $20\,\mathrm{cm}$ in order to fit it into the camera, however the height of the plane of the impeller remained constant relative to the cell (figure 3.10).

Before each experiment started it was important to know exactly where the cell was within the camera and so a location marker was used. This was a small perspex cylinder

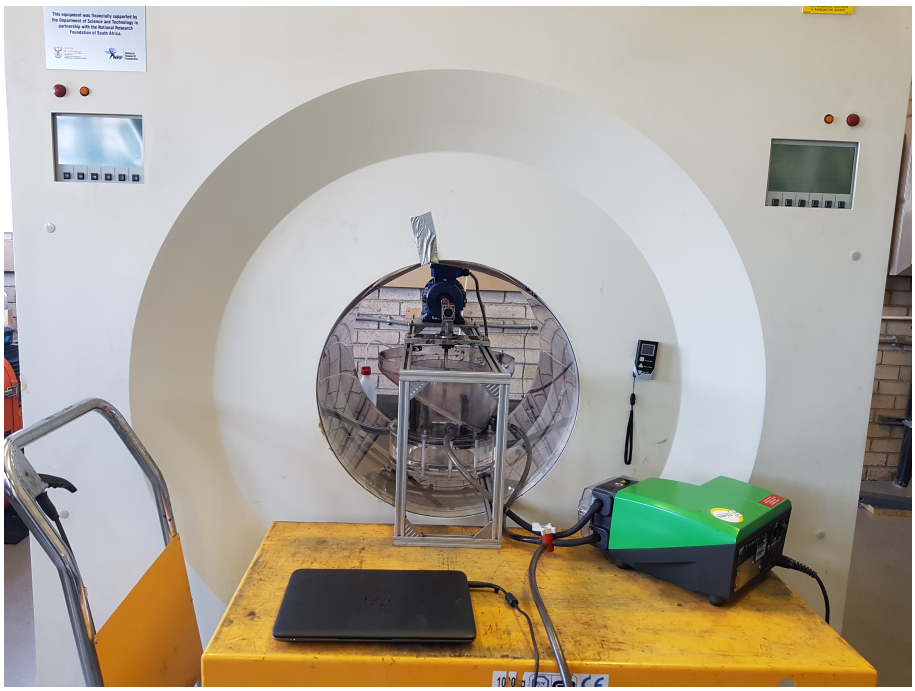


**Figure 3.10:** The continuously overflowing flotation cell inside the PET camera.

containing a $^{22}$Na radionuclide that was stuck onto the outside of the base of the cell. Once the location of the marker had been recorded it was then moved to four further locations around the cell at the same height. This produced a ring of known locations that can then be used for the processing of the data.

### 3.7.1 Tracer production

The tracers for each experiment were produced by staff from PEPT Cape Town using an ion exchange resin bead core, that was labelled with $^{68}$Ga and then coated with particles depending on the desired tracer type. This tracer was chosen due to its half life of $68\,\mathrm{min}$ as this is sufficient to provide a strong enough signal for the length of each experiment, but it will also have decayed enough that once the experiment has been concluded it can be disposed of as radioactive waste. The initial activity of the tracers ranged between $950\,\mu\mathrm{Ci}$ and $1850\,\mu\mathrm{Ci}$. A detailed explanation of the production of the tracers can be found in Cole et al. (2014). For this work four different types of tracers were used: three hydrophobic (coated in silica) and one hydrophilic (coated in magnetite). The three hydrophobic tracer particles measured approximately $400\,\mu\mathrm{m}$, $500\,\mu\mathrm{m}$ and $600\,\mu\mathrm{m}$ in diameter and the hydrophilic tracer particles measured $500\,\mu\mathrm{m}$ in diameter. It is important to note that these tracers are much larger than the size of the particles in the system due to the limitations in the tracer manufacture process, but allow for a systematic investigation of particle size ef-

fects, while maintaining a representative particle size distribution of the feed. The density of the tracers was not modified or measured, due to limitations in the tracer manufacture process. The density of the resin used to make the core is known to be approximately $1\,\mathrm{g\,cm^{-3}}$ (Cole et al., 2014), and so the total density of the finished coated tracers would have been less than that of either the silica or especially the magnetite. This lower density may mean that the silica tracer floated more easily than the silica particles in the feed, and that the magnetite tracer was more likely to be recovered by entrainment than the magnetite particles in the feed. However, when analysing the data it was determined, from experiments in the unmodified cell, that the tracers were behaving as expected for hydrophobic and hydrophilic tracers. In addition, the tracer manufacture procedure was constant for all experiments, allowing a comparison of the effect that the different design modifications had on the different types of particle within the system.

### 3.7.2 Tracer usage and disposal

Once the tracer had been produced it was inserted into the pulp of the experiment during conditioning, before the air was turned on and the froth started overflowing. An experiment was then performed until the tracer activity reduced to a point where the data was not usable. Due to the radioactive nature of these experiments the tracer had to be extracted from the system post experiment. This was done by pumping small amounts of slurry out of the cell at a time and checking for the tracer with a Geiger counter. Once the tracer was located it was placed behind lead shielding. The remaining slurry was then pumped out of the cell and left overnight for any activity that had leached into the slurry to decay before it was disposed of.

### 3.7.3 Data collection and analysis

The data from the camera was collected in 20 minute blocks at a rate of 1000 counts per second that were then processed to determine the raw position of the tracer within the system.

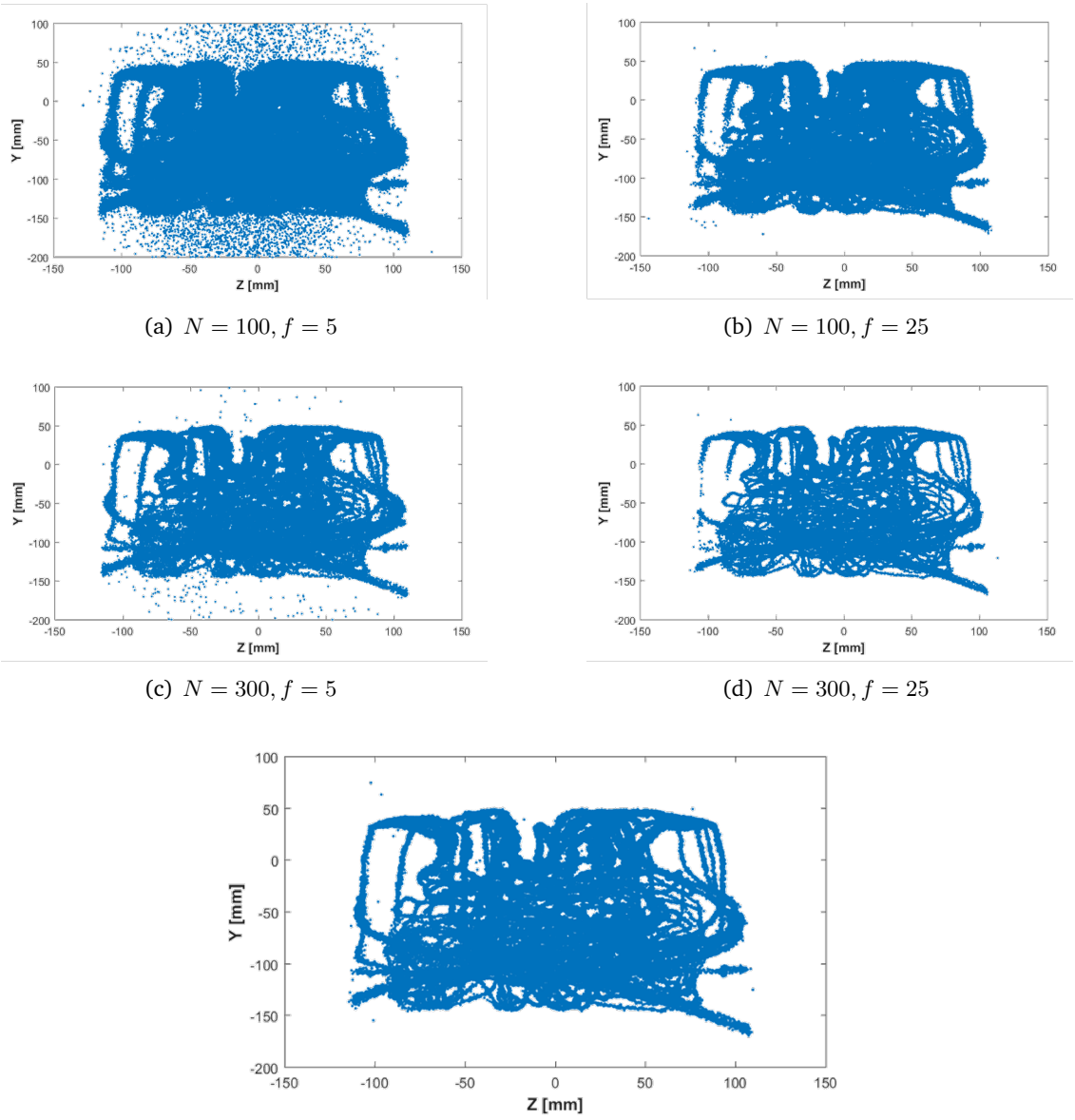
The first step of processing the data was to use a triangulation algorithm (Parker et al., 1993) in order to locate the position of the tracer for each of the annihilation events. This uses the fact that the PET camera will detect the gamma rays and their lines of response (LORs) can be determined. In theory, where these LORs intersect will be the location of

the tracer and therefore only two are required. In reality, many of the LORs detected will occur due to Compton scattering or from detecting gamma rays from separate annihilation events (Buffler et al., 2018) resulting in a much larger number of LORs being required to determine the location of the tracer. Added to this, the LORs will not intersect exactly at a single point and so the point used will be the one that minimises the distances to all the LORs. The data from the LORs were then transformed into Cartesian coordinates for the position and a time for use in the processing. The number, $N$, of events to be grouped and the proportion, $f$, of these events to be kept in the analysis were then defined. The necessity to choose an $f$ value is due to the fact that Compton scattering will cause anomalous events and so some data needs to be discarded.

In order to determine the optimal $N$ and $f$ values for processing the PEPT data in this study an optimisation test was run. For this, a subset of data sets were processed using all combinations of $N$ and $f$ values with $N$ values increasing from 50 to 300 in increments of 50, and $f$ values increasing from 5 to 25 in increments of 5. The different data sets chosen included samples from different design modifications, different types of tracer, different initial activities of tracer, and different points throughout the experiment. After the data had been processed the resulting coordinates of the tracer through time were plotted and used to decide an optimal pairing of $N$ and $f$. Figure 3.11 shows examples of different $N$ and $f$ combinations for an experiment using a hydrophobic tracer in the unmodified cell. This indicates that a low $f$ value leads to spurious data points outside the physical space of the cell, and a high $N$ value leads to loss of some data. After analysing the subset of data in this way it was determined that values of $N = 250$ and $f = 15$ gave optimal results for all experiments.

After the optimal $N$ and $f$ values were determined all of the data sets obtained from the PEPT experiments were processed with these values. Subsequently, the processed data was then filtered to remove points known to be outside of the cell (i.e. in the launder or recycling tubes) and then smoothed and processed in MATLAB to determine the tracer speed, stream lines and occupancy throughout the cell.

The flotation cell was divided into 36 segments to provide voxels that had a cross section of $10\,\mathrm{mm}$ by $10\,\mathrm{mm}$ and were $10^{\circ}$ wide as illustrated in the schematic in figure 3.12(a). The tracer location data were then binned into these voxels to represent how the tracer behaved in different sections of the cell. The size of the voxels was chosen to give enough information about varying zones in the cell whilst taking into account the




(a) $N = 100, f = 5$

(b) $N = 100, f = 25$

(c) $N = 300, f = 5$

(d) $N = 300, f = 25$

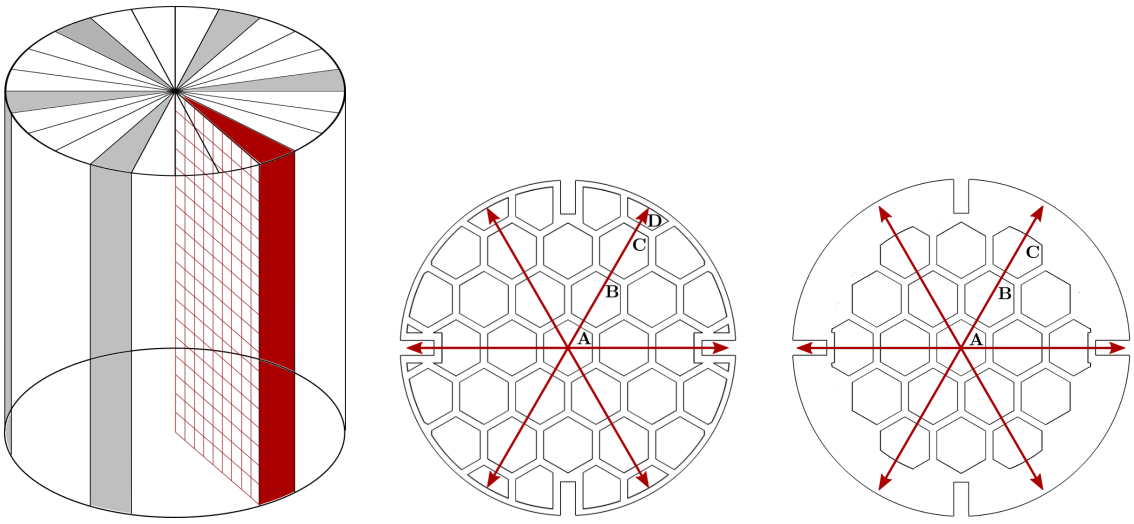
(e) $N = 250, f = 15$

**Figure 3.11:** Different $N$ and $f$ combinations for a hydrophobic tracer in the unmodified cell

accuracy of the tracer location. Once binned, the location of the tracer was processed in different ways to determine a range of variables about the tracer. The first variable that was calculated was the velocity of the tracer in each direction and therefore also the speed. This was done by comparing the current tracer location to the next and calculating the change in distance and time. As the tracer locations were noisy this was done over 15 data points in order to smooth the data to some extent. The average value for each velocity component in each voxel was calculated, which gave an indication of the general movement of the tracer in that region of the cell. The second variable was the occupancy of the tracer within the cell. This was calculated as the length of time the tracer spent in

a voxel as a proportion of the total experiment time. This value was also normalised by volume to account for the different volumes of voxels in a cylindrical system.

In order to determine how the different variables vary throughout the dimensions of the cell, 6 wedges from the centre of the cell were taken, as illustrated by the shaded areas in figure 3.12(a). The voxels were then averaged between the slices to produce an average slice through the cell and to obtain a standard error of how the values change in different locations through the cell. The slices were chosen so that the mesh profile was the same through all of them, as illustrated in figure 3.12(b) & (c). This was to ensure that the effects of the presence of the mesh could be fully understood. In addition to calculating the velocity components and the occupancy of the tracer in each voxel in the cell, the average streamlines of the tracer in the vertical slices were calculated. This was done using the values of the vertical and radial velocity components in each voxel in the averaged slice with the *"streamslice"* function in MATLAB. The streamline density for this function was chosen as 0.5 so as to represent the flow of the tracer throughout the slice at a similar resolution to the voxel size.




(a) Division of the cell for PEPT data processing (b) Basic Mesh (c) Blocked Mesh

**Figure 3.12:** (a) Illustration of how the cell is divided into voxels for processing, wedges averaged to create vertical slices are indicated by the shaded regions. The two different mesh designs used in this chapter: (b) basic mesh and (c) blocked mesh, with holes labelled $A - D$. Red arrows indicate the six wedges averaged to create the vertical slices.

Occasionally, the tracer appears as though it was stuck in a particular location. In fact this was not stuck, the tracer was just moving incredibly slowly. This suggests potential areas of froth that are stagnant. These locations were always just below the lip of the cell and at the wall, however were not always at the same place around the cell. These

zones were not seen in all experiments but were seen in all design modifications, however they occurred more frequently in the cases where there was a mesh. For the bulk of the interpretation of the PEPT data these points were filtered out of the data set as they obscured the bulk flow of the tracer. Before analysis of the PEPT data, the location of the tracer, over time, for each experiment was plotted to ensure that the tracer was floating appropriately. In some experiments the tracer would be recovered to the concentrate frequently, however, after a period of time it would then stop floating at all. This indicates that the hydrophobic coating broke preventing the tracer from being recovered. In these cases the data after this point was not used in the analysis. Figure 3.13 shows that this was the case for the $500\,\mu\mathrm{m}$ tracer in the unmodified cell as the frequency with which the tracer was in the froth dropped after approximately 30 minutes. In this example only the first 20 minutes of data was used in the analysis. Plots of time versus height for all other tracers can be found in appendix C.

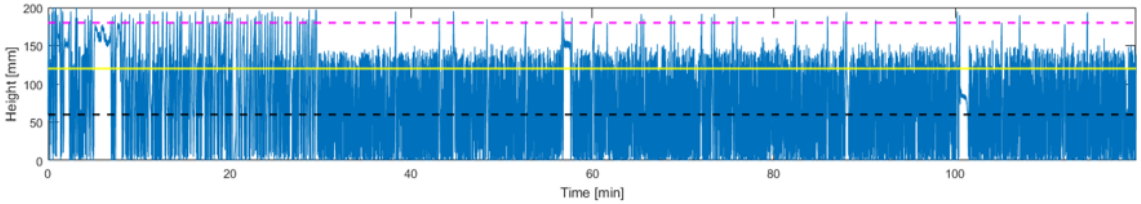



**Figure 3.13:** Graph of tracer height over time for the $500\,\mu\mathrm{m}$ tracer in the unmodified cell. The pink dashed line shows the height of the lip of the cell, the yellow line shows the height of the baffles and the black dashed line shows the height of the plane of the impeller.

# Chapter 4

# The effects of particle size on the flotation performance of a copper tailings ore

## 4.1 Introduction

This chapter[1] aims to improve the understanding of the relationships between particle size of the feed and the superficial gas velocity, and froth stability for a copper tailings ore. Two different measures of froth stability are used, dynamic froth stability ($\Sigma$) and air recovery ($\alpha$), allowing a direct comparison between the two. The dynamic froth stability was measured in a non-overflowing laboratory scale flotation column (section 3.2.1) and the air recovery was measured in the bench scale, continuously overflowing mechanical flotation cell first used by Norori-McCormac et al. (2017) (section 3.2.2).

In the work presented in this chapter, the non-overflowing flotation column was used to investigate the dynamic froth stability of seven particle size distributions. Due to limited quantities of material, it was necessary to investigate fewer particle size distributions with the continuously overflowing mechanical flotation cell. Three distributions were chosen to investigate further the trends seen from the dynamic froth stability results. An experiment with a fourth, coarser, particle size distribution was attempted, however during experimentation there was an air leak in the cell impacting the reliability of the results and so

[1]The results from this chapter have been published in two papers, the dynamic froth stability results in Mackay et al. (2018) (appendix A.1) and the air recovery results in Mackay et al. (2019) (appendix A.2)

these are not included. Due to limited quantities of copper ore this experiment was not able to be repeated.

The two measures of froth stability are directly compared in this chapter and the implications of the results are discussed in relation to improving the reprocessing of copper tailings via froth flotation.

### 4.1.1 Ore characterisation

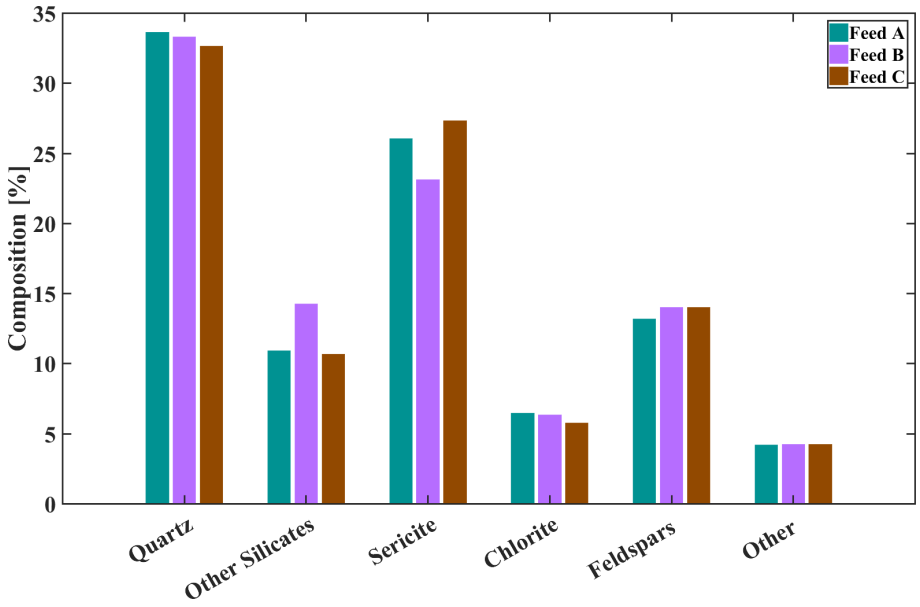
The samples used in this chapter were obtained from a Chilean processing plant that reprocesses both historic and fresh copper tailings with copper grades of 0.27 % and 0.12 %, respectively. Due to the nature of tailings, approximately 50 % of the material entering the plant is less than $10\,\mu\mathrm{m}$. The plant uses a primary hydrocyclone to split the material for processing. The hydrocyclone overflow stream has a $d_{90}$ of $63.7\,\mu\mathrm{m}$ and the underflow stream has a $d_{90}$ of $279\,\mu\mathrm{m}$. The underflow stream is then processed via flotation. Samples were obtained from the underflow and overflow streams of the primary hydrocyclone, as slurry, and then dried, resulting in two samples with different particle size distributions. This allowed the two samples to be combined in different ratios to produce the different particle size distributions investigated in this chapter. The particle size distributions used in the dynamic froth stability experiments are shown in table 4.1, and those used in the air recovery measurements are shown in table 4.2. These particle size distributions were determined using a Malvern Mastersizer 2000 particle analyser.

**Table 4.1:** Particle size distributions of feeds used in dynamic froth stability experiments.

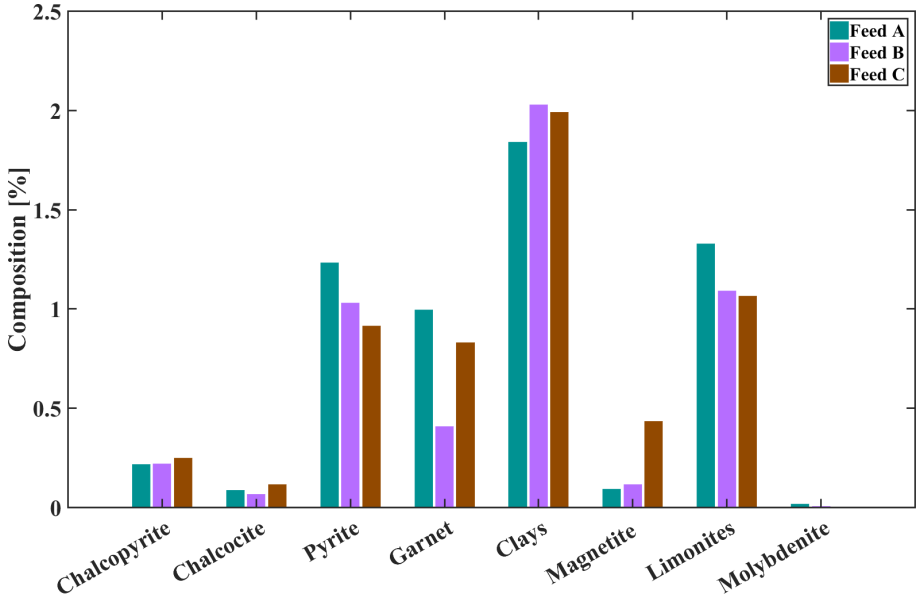
| Feed | d10, [$\mu$m] | d50, [$\mu$m] | d90, [$\mu$m] |
|---|---|---|---|
| $A_\Sigma$ | 2.6 | 13.1 | 63.6 |
| $B_\Sigma$ | 3.4 | 36.1 | 117.4 |
| $C_\Sigma$ | 4.2 | 89.0 | 171.2 |
| $D_\Sigma$ | 4.6 | 70.5 | 198.2 |
| $E_\Sigma$ | 5.0 | 81.9 | 224.9 |
| $F_\Sigma$ | 5.3 | 88.8 | 241.1 |
| $G_\Sigma$ | 5.8 | 104.8 | 278.7 |

**Table 4.2:** Particle size distributions and copper content for the three different feeds used in air recovery experiments.

| Feed | d10, [$\mu$m] | d50, [$\mu$m] | d90, [$\mu$m] |
|---|---|---|---|
| $A_\alpha$ | 2.6 | 23.0 | 179.3 |
| $B_\alpha$ | 2.9 | 30.2 | 219.1 |
| $C_\alpha$ | 3.3 | 47.1 | 253.4 |




(a) Mineralogy for high value minerals




(b) Mineralogy for low value minerals

**Figure 4.1:** Mineral composition of the different feeds, from the QEMSCAN analysis, split into (a) minerals that comprise more than 5% of the feed and (b) minerals that are less than 2.5% of the feed.

The detailed mineralogy of each of the three feeds used for the air recovery experiments ($A_\alpha - C_\alpha$) in this chapter was determined using QEMSCAN (as described in section 3.6.2) and can be seen in figure 4.1. The mineralogy shows that, in general, there was no large difference in the mineralogy of the different feeds used. The liberation by size of the chalcopyrite, for particles greater than $75\,\mu\mathrm{m}$ and less than $75\,\mu\mathrm{m}$, is shown figure 4.2. For all three feeds, the majority of the chalcopyrite had a liberation of lower than 50% and this poorly liberated chalcopyrite was mostly over $75\,\mu\mathrm{m}$. Feeds $A$ and $B$ contained no chalcopyrite that was more than 50% liberated and over $75\,\mu\mathrm{m}$, whereas feed $C$ contained

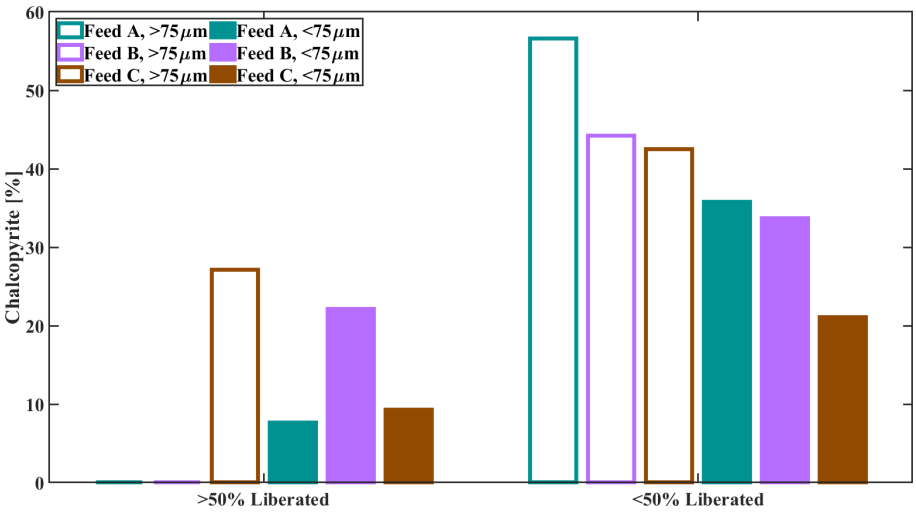



**Figure 4.2:** Chalcopyrite liberation by size from QEMSCAN analysis of the three different feeds.

a large proportion of chalcopyrite that fits into this category. The chalcopyrite in feeds $B$ and $C$ was better liberated than feed $A$, with a higher proportion of the chalcopyrite being over 50% liberated.

## 4.2 Froth Stability

### 4.2.1 Dynamic froth stability

The dynamic froth stability factor, Equation 2.2, was calculated for each experiment using the equilibrium heights, which can be found in Table 4.3. Figure 4.3 shows the dynamic froth stability factor, for different particle size distributions at constant air rates. For all particle size distributions, decreasing the superficial gas velocity lead to a decrease in dynamic froth stability factor. This is contrary to what was found by Aktas et al. (2008). It is important to note that the superficial gas velocities used in this work were higher than those use in previous work and are more similar to industrial values.

From the results in figure 4.3, there is an overall decrease in dynamic froth stability with increasing particle size. However, the decrease is not smooth and two stability regimes can be seen. The first is at finer particle size distributions, below $171\,\mu\mathrm{m}$, where the dynamic froth stability factor decreases as d90 increases. At the coarser particle size distributions, above $171\,\mu\mathrm{m}$, there is a local maximum in froth stability at a given superficial gas velocity. This maximum is much more pronounced at higher superficial gas velocities.

**Table 4.3:** Average equilibrium heights, $H_{eq}$, and dynamic froth stability factors, $\Sigma$, for all particle size distributions and superficial gas velocities, $J_g$, investigated.

| Feed, [$\mu$m] | $J_g$, [cm s$^{-1}$] | $H_{eq}$, [cm] | $\Sigma$, [s] |
|---|---|---|---|
| $A_\Sigma$ | 0.96 | 11.7 | 12.2 |
| $A_\Sigma$ | 1.20 | 19.6 | 16.3 |
| $A_\Sigma$ | 1.44 | 30.2 | 20.9 |
| $B_\Sigma$ | 0.96 | 3.8 | 3.9 |
| $B_\Sigma$ | 1.20 | 7.8 | 6.5 |
| $B_\Sigma$ | 1.44 | 23.4 | 16.3 |
| $C_\Sigma$ | 1.20 | 4.1 | 3.44 |
| $C_\Sigma$ | 1.44 | 15.7 | 10.9 |
| $C_\Sigma$ | 1.68 | 30.2 | 18.0 |
| $D_\Sigma$ | 1.20 | 7.0 | 5.8 |
| $D_\Sigma$ | 1.44 | 14.8 | 10.3 |
| $D_\Sigma$ | 1.68 | 42.0 | 25.0 |
| $E_\Sigma$ | 1.20 | 3.9 | 3.2 |
| $E_\Sigma$ | 1.44 | 17.6 | 12.2 |
| $E_\Sigma$ | 1.68 | 47.9 | 28.5 |
| $F_\Sigma$ | 1.20 | 2.9 | 2.4 |
| $F_\Sigma$ | 1.44 | 7.5 | 5.2 |
| $F_\Sigma$ | 1.68 | 21.6 | 12.8 |
| $G_\Sigma$ | 1.44 | 4.7 | 3.2 |
| $G_\Sigma$ | 1.68 | 13.2 | 7.9 |
| $G_\Sigma$ | 1.92 | 25.8 | 13.4 |

It is clear that, when operating towards the right hand side of the graph, there is an optimal particle size distribution that will improve the dynamic froth stability. This suggests that if the tailings reprocessing plant were to slightly lower the cut size of the primary hydrocyclone they could improve the froth stability in the flotation cells.

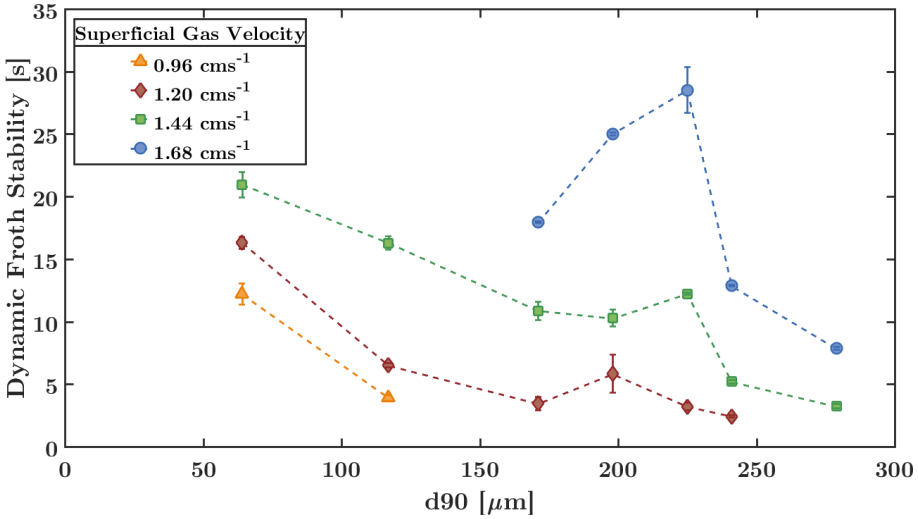



**Figure 4.3:** Dynamic froth stability for different particle size distributions at a range of superficial gas velocities. Error bars represent one standard deviation.

### 4.2.2 Air Recovery

In order to further investigate the local maximum in froth stability seen in figure 4.3, experiments were conducted in the continuously overflowing flotation cell measuring air recovery. These experiments were performed using three particle size distributions with $d_{90}$ between $170\,\mu\mathrm{m}$ and $260\,\mu\mathrm{m}$ to encompass this local maximum. When conducting air recovery tests, it is important to verify that the changes in air recovery are caused by changes in operating conditions and not by changes in the system with time. To do this a test was run for an hour and a half to ensure the operation remained at steady state. Figure 4.4 shows the moving average of the air recovery over 90 minutes for an experiment at a $J_g$ $=0.92\,\mathrm{cm\,s^{-1}}$. The data was divided into six, 15 minute windows and the data in the last 10 minutes of each window were averaged (the data in the light grey vertical bands) to analyse the change in air recovery over time. The average value for each of these 10 minute windows is presented in figure 4.4, with red dots and error bars representing a 95% confidence interval. The overall 95% confidence interval is presented in figure 4.4 with a horizontal dark grey band.

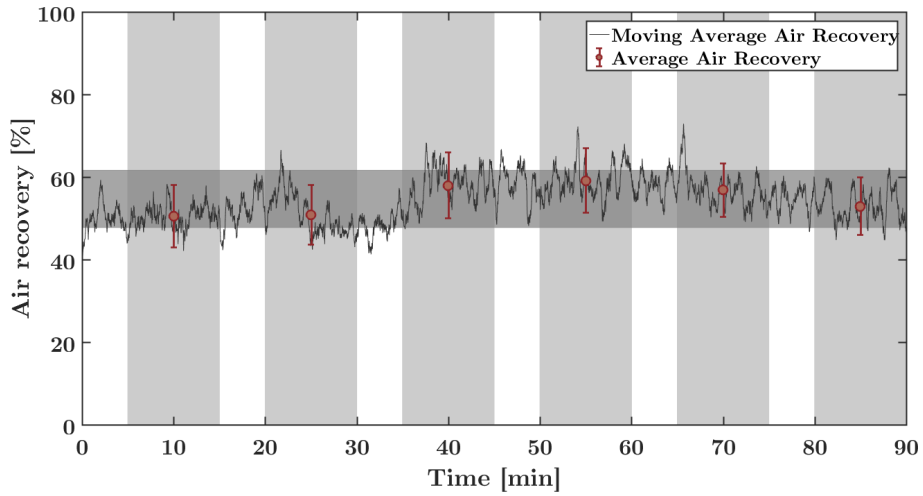



**Figure 4.4:** The variation in air recovery over time at a constant condition, with 10 minute measurement windows highlighted by light grey vertical bands and a confidence band for the average value of air recovery represented by the dark grey horizontal band. Error bars represent a 95% confidence interval.

A heat map of the air recovery data for varying feed size distributions and superficial gas velocities can be seen in figure 4.5. When investigating the effects of varying superficial gas velocity for a constant feed size (the rows of the heat map) only feed $A$ displays a peak in air recovery which is at a superficial gas velocity of $1.18\,\mathrm{cm\,s^{-1}}$. At coarser feeds, there is no peak in air recovery. Figure 4.5 shows that varying the particle size distribution of the feed for a given superficial gas velocity (the columns of the heat map) has a stronger

effect on the air recovery; feeds $B$ and $C$ result in higher air recoveries for all superficial gas velocities investigated.

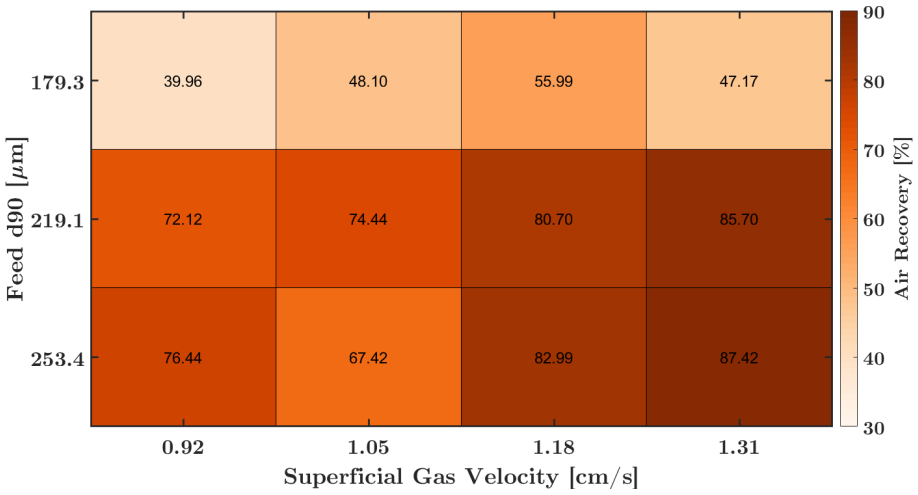



**Figure 4.5:** Heat map of air recovery for different feed $d_{90}$s and superficial gas velocities.

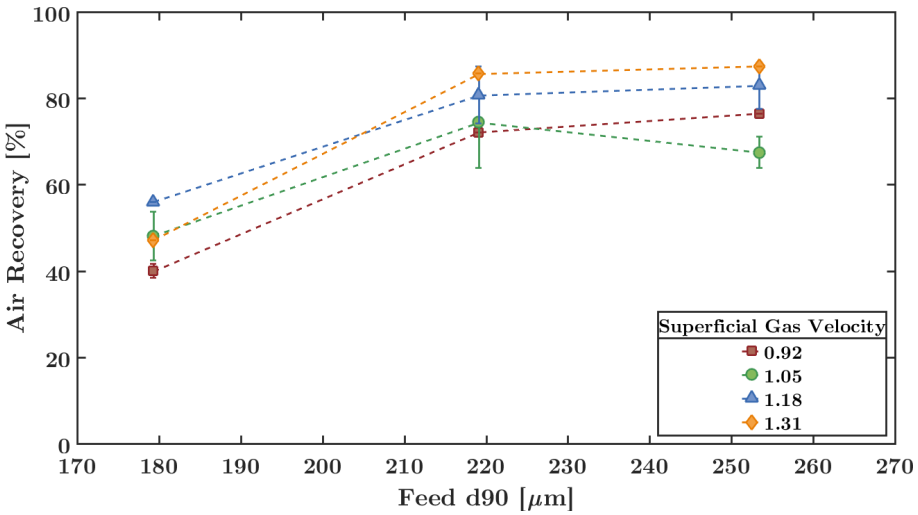



**Figure 4.6:** The variation in air recoveries with varying feed size at different superficial gas velocity. Error bars are one standard deviation.

**Table 4.4:** ANOVA table of air recovery with particle size distribution. Variables that are significant are highlighted.

| Source | Sum of Squares | Degrees of Freedom | Mean of Squares | $F$-Stat | $p$-Value |
|---|---|---|---|---|---|
| **Feed Size** | 3330 | 2 | 160 | 10.8 | 0.010 |
| Superficial Gas Velocity | 436 | 3 | 145 | 0.94 | 0.477 |
| Interaction | 223 | 6 | 37.1 | 0.24 | 0.947 |
| Error | 926 | 6 | 154 | | |
| Total | 5490 | 17 | | | |

For a better understanding of the relationship between feed size and air recovery, the data are presented in more detail in figure 4.6. The air recovery with varying feed size is plotted for each superficial gas velocity with error bars as one standard deviation. An

ANOVA test was performed on these data (table 4.4), which shows that only changing the feed size had a statistically significant effect on the air recovery. This indicates that, regardless of the superficial gas velocity used, there is a clear improvement in froth stability at intermediate feed sizes, with $d_{90}$ between $220\,\mu\mathrm{m}$ and $260\,\mu\mathrm{m}$. These data also correlate well with the relationships shown in the experiments performed by Norori-McCormac et al. (2017) at the lower two superficial gas velocities they investigated, and the relationship shown by Mackay et al. (2018).

### 4.2.3 Comparison between stability measures

Both the dynamic froth stability and the air recovery experiments were conducted using the same batch of copper tailings ore, allowing a direct comparison between the two measures of froth stability to be made. Figure 4.7 shows the two data sets plotted together, with dynamic froth stability on the left hand axis and air recovery on the right hand axis. Both data sets showed high froth stabilities at approximately the same feed size, $d_{90}$ of $\sim 220\,\mu\mathrm{m}$. The air recovery data, however, does not have a clear maximum value. It is likely that a maximum occurs at a feed particle size distribution between $B$ and $C$ corresponding directly with the peak in dynamic froth stability.

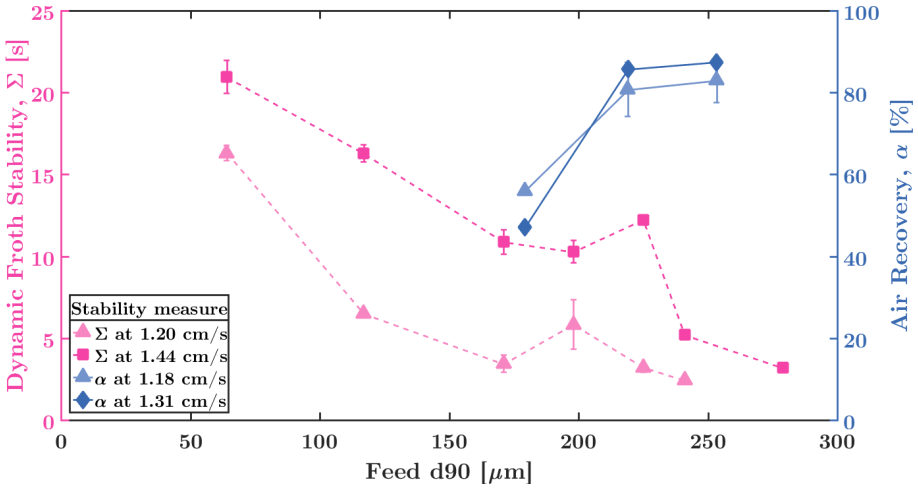



**Figure 4.7:** Comparison of dynamic froth stability (pink and left hand axis) and air recovery (blue and right hand axis) for the same batch of copper tailings ore. Error bars are one standard deviation.

## 4.3 Flotation Performance

### 4.3.1 Dynamic froth stability

In order to understand the effect of particle size distribution, not only on dynamic froth stability but also on flotation performance, preliminary experiments were conducted using batch flotation tests. These were performed on three particle size distributions with a superficial gas velocity of $1.44\,\mathrm{cm\,s^{-1}}$ (condition numbers 6, 14 and 19 from Table 4.3). The three particle size distributions chosen were *i*) the closest to the feed to the primary hydrocyclone, *ii*) the local maximum in dynamic froth stability, and *iii*) the size currently being sent to the flotation circuit. Figures 4.8 and 4.9 respectively show the results of copper grade of the concentrate and copper recovery as a function of particle size (d90).

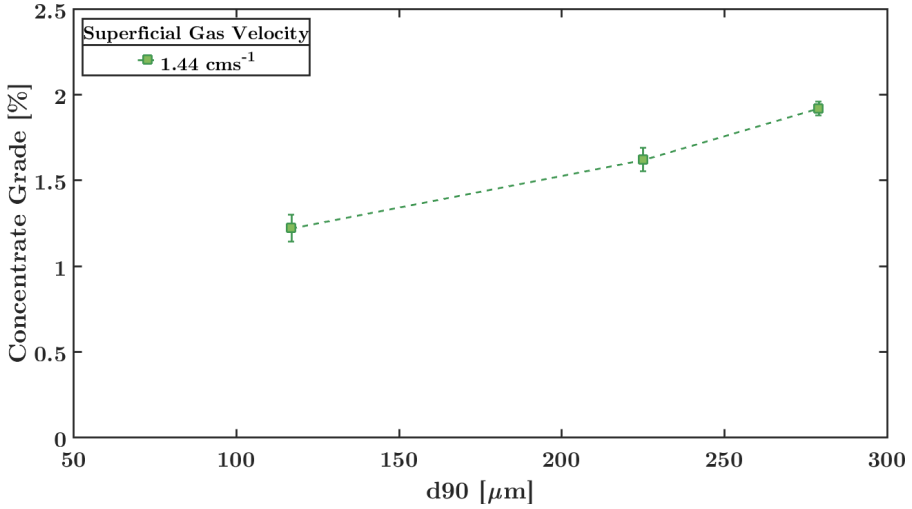



**Figure 4.8:** Concentrate grade from batch flotation tests and dynamic froth stability at a superficial gas velocity of $1.44\,\mathrm{cm\,s^{-1}}$ . Error bars represent one standard deviation.

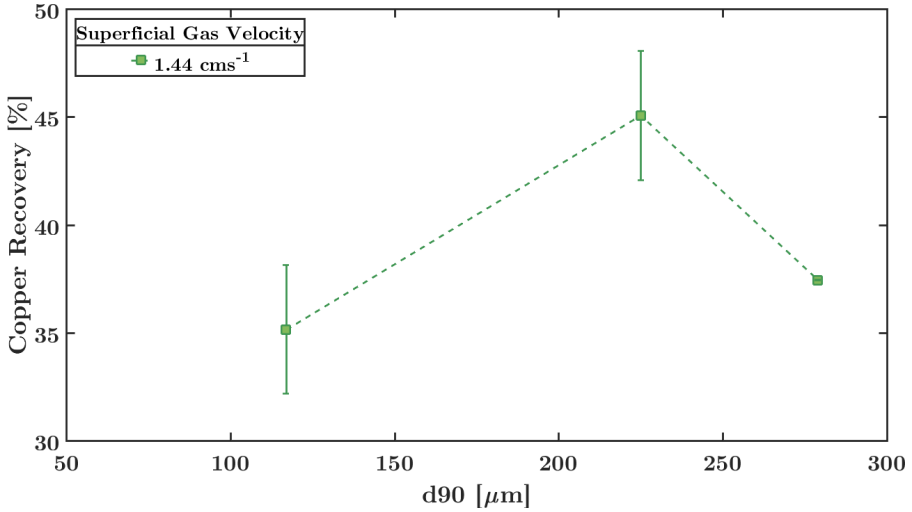



**Figure 4.9:** Copper recovery from batch flotation tests and dynamic froth stability at a superficial gas velocity of $1.44\,\mathrm{cm\,s^{-1}}$ . Error bars represent one standard deviation.

The highest copper grade (figure 4.8) was achieved at the largest particle size, with a d90 of $279\,\mu\mathrm{m}$, which corresponds to the lowest dynamic froth stability. This is the opposite effect to that which was reported in Barbian et al. (2005). It is observed that at the particle size distribution where there is the local peak in dynamic froth stability, d90 of $225\,\mu\mathrm{m}$, there is also a peak in copper recovery (figure 4.9). It is also interesting to note that out of the three particle sizes the one with highest dynamic froth stability, d90 of $117\,\mu\mathrm{m}$, actually corresponds to the lowest copper recovery. This indicates that there is not always a direct correlation between dynamic froth stability and copper recovery, contrary to the results from McFadzean et al. (2016b). The results here show that dynamic froth stability alone cannot be used to determine an optimal particle size for performance, but it is also important to consider which of the two stability regimes is being investigated.

### 4.3.2 Air recovery

Whilst the feeds $B$ and $C$ were shown to result in the highest froth stability, it is important to understand how this trend is reflected in the flotation performance. One of the benefits of running experiments in the continuously overflowing cell, is that the air recovery can be measured while, at the same time, samples of the overflowing froth can be taken to determine flotation performance. The copper content of the feed and concentrate samples was analysed to determine grade and recovery. This was done for experiments with superficial gas velocities of $0.92\,\mathrm{cm\,s^{-1}}$ and $1.18\,\mathrm{cm\,s^{-1}}$.

Figure 4.10 shows the copper grade of the concentrate from experiments with a superficial gas velocity of $0.92\,\mathrm{cm\,s^{-1}}$ and $1.18\,\mathrm{cm\,s^{-1}}$. It is observed that the grade decreases as superficial gas velocity increases. The analysis of variance results in table 4.5 show that this change was significant. This behaviour is expected, as higher superficial gas velocities will result in higher entrainment factors and therefore a reduced grade (Neethling and Cilliers, 2009). The analysis also shows that there is no statistically significant difference in the concentrate grade with different feed sizes.

Figure 4.11 shows that the copper recovery is higher for the higher superficial gas velocity which is often associated with and increase in mass pull. Feed $B$, which showed an improvement in air recovery, also has the best copper recovery at both superficial gas velocities. The analysis of variance in table 4.6 shows that both the feed size and the superficial gas velocity had a significant effect on the copper recovery. This is in line with

**Table 4.5:** ANOVA table of concentrate grade with particle size distribution and superficial gas velocity. Variables that are significant are highlighted.

| Source | Sum of Squares | Degrees of Freedom | Mean of Squares | $F$-Stat | $p$-Value |
|---|---|---|---|---|---|
| Feed Size | 0.019 | 2 | 0.010 | 2.29 | 0.144 |
| **Superficial Gas Velocity** | 0.276 | 1 | 0.276 | 66.1 | 0 |
| Interaction | 0.005 | 2 | 0.002 | 0.55 | 0.593 |
| Error | 0.050 | 12 | 0.004 | | |
| Total | 0.396 | 17 | | | |

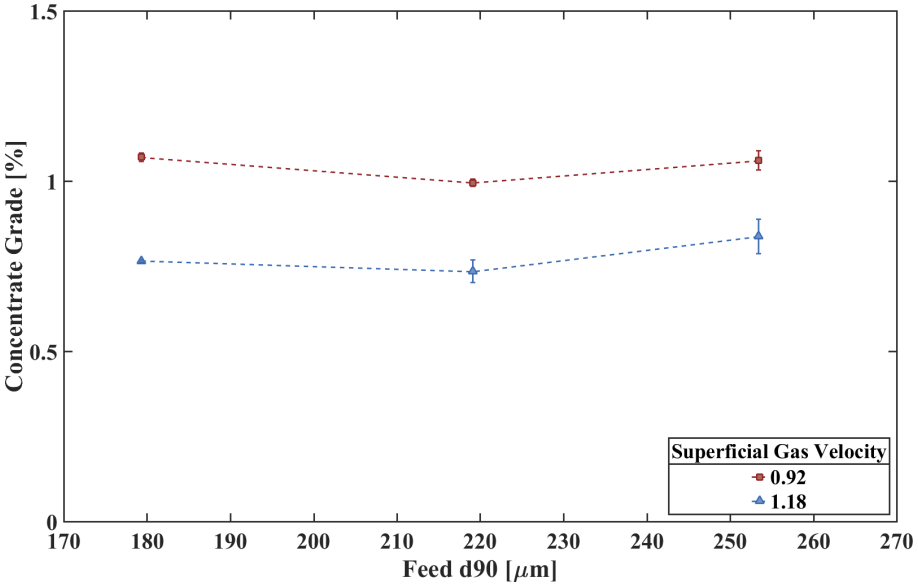



**Figure 4.10:** Concentrate grade for samples taken at $0.92\,\mathrm{cm\,s^{-1}}$ and $1.18\,\mathrm{cm\,s^{-1}}$. Error bars are 1 standard deviation.

the experimental results presented in Mackay et al. (2018), which showed that the feed with a similar particle size distribution to $B$, and which yielded a local peak in dynamic froth stability, corresponded to an improvement in copper recovery. Feed $C$, with a similar air recovery value to feed $B$, shows a decrease in flotation performance, despite the fact that they also have similar mineralogical composition. This indicates that the particle size distribution of feed $B$ is optimal for an improvement in flotation performance.

**Table 4.6:** ANOVA table of copper recovery with particle size distribution and superficial gas velocity. Variables that are significant are highlighted.

| Source | Sum of Squares | Degrees of Freedom | Mean of Squares | $F$-Stat | $p$-Value |
|---|---|---|---|---|---|
| **Feed Size** | 301 | 2 | 151 | 5.43 | 0.021 |
| **Superficial Gas Velocity** | 198 | 1 | 198 | 7.12 | 0.021 |
| Interaction | 29.5 | 2 | 14.7 | 0.53 | 0.601 |
| Error | 333 | 12 | 27.7 | | |
| Total | 882 | 17 | | | |

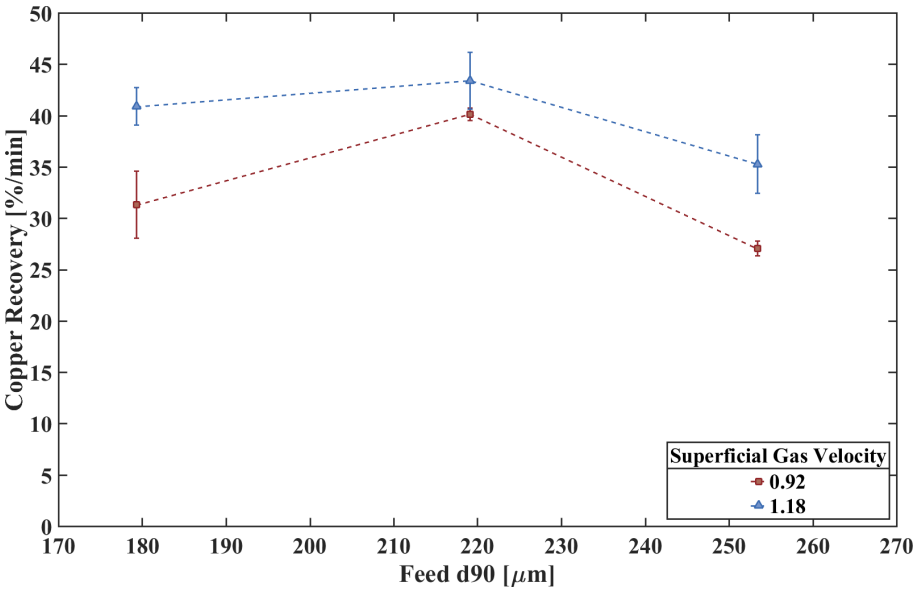



**Figure 4.11:** Copper recovery to the concentrate for samples taken at $0.92\,\mathrm{cm\,s^{-1}}$ and $1.18\,\mathrm{cm\,s^{-1}}$. Error bars are 1 standard deviation.

## 4.4 Discussion

Previous work by Aktas et al. (2008), Liang et al. (2015) and McFadzean et al. (2016a) only reported a decrease in dynamic froth stability with an increase in particle size. However, the work done in this thesis has shown that there were two stability regimes. The first is at lower feed d90s, where there was a decrease in froth stability for an increase in particle size. The second is at higher feed d90s, where dynamic froth stability goes through a maximum as the d90 of the feed increases. There are differences in experimental method between this work and that of previous studies (as discussed in detail in section 2.4.4), such as the range of particle sizes considered and the superficial gas velocities used, meaning that a similar maximum may exist in those systems but was not encompassed by the data. At the lower of two air rates investigated in the dynamic froth stability experiments, the data was smoother and the local maximum was less pronounced. These air rates were similar to the one used in experiments by McFadzean et al. (2016a), suggesting that it is not just the particle size that plays an important role in froth stability but there is also a superficial gas velocity effect. These results also show that the relationship is more complex than previously thought. This is similar to the findings from Norori-McCormac et al. (2017) when investigated the effects particle size and superficial gas velocity have on the air recovery. Whilst Ip et al. (1999) discuss that their results illustrate the same decrease in froth stability with an increase in size as presented by other authors, the relationship was not smooth. In fact, the data shows a plateau at a similar particle size to where there

local maximum is seen in the data in this chapter.

In order to investigate this local peak in dynamic froth stability further, experiments were conducted using the same ore, but in the continuously overflowing flotation cell measuring air recovery. Three particle size distributions were used for the air recovery experiments, chosen to be in the second regime at the higher d90s. The air recovery results also showed that there was a maximum in froth stability at approximately the same values of d90 as was seen with the dynamic froth stability results. This confirms that the relationship between particle size and stability is more complicated than has previously been discussed.

It was also important to establish how this peak in froth stability correlates to flotation performance. For both sets of experiments grade and recovery were measured. In the dynamic froth stability experiments this had to be done separately in Denver cells as the column was not an overflowing one (to necessitate the calculation of the dynamic froth stability). However, in the experiments with air recovery the grade and recovery could directly be measured at the same time as froth stability - one of the benefits of using the continuously overflowing flotation cell. Both sets of analysis showed that the local peak in stability corresponded to a clear improvement in copper recovery, with little impact on the grade.

### 4.4.1 Implications for reprocessing mine tailings via froth flotation

The samples of copper tailings used in this chapter were obtained from a plant currently reprocessing historic and fresh tailings material from a mine in Chile. The plant uses a primary hydrocyclone to split the material before processing. The underflow from the hydrocyclone, with a $d_{90}$ of $279\,\mu\mathrm{m}$, is then processed via froth flotation.

The findings from section 4.3 indicate that the size distribution of the material currently being sent to flotation in this plant is not optimal. Instead, altering the cutsize of the hydrocyclone to produce a feed particle size distribution with a $d_{90}$ of approximately $220\,\mu\mathrm{m}$ would result in improved copper recovery from the tailings material. Altering the particle size distribution of the feed to the flotation circuit would also reduce the amount of material sent to final tailings, therefore reducing the environmental impacts from mine waste.

Previous work by other authors (Ip et al., 1999; Norori-McCormac et al., 2017) has

shown that the relationship between particle size and froth stability is not a simple one. The work in this paper compounds that fact, clearly showing that there can be an optimal particle size distribution for froth stability that correlates to an improvement in flotation performance. Evidence suggests that this behaviour is exhibited by a variety of particle systems. It would therefore be wise for a tailings reprocessing plant to conduct simple froth stability tests to determine the optimal particle size distribution to improve recovery.

## 4.5 Conclusions

The experiments in this chapter investigated the effects of feed particle size distribution, at a range of superficial gas velocities, on the froth stability and flotation performance of a copper tailings ore. These experiments were performed using two different methodologies for two different measures of stability. The first method used a laboratory scale, non-overflowing column to measure the dynamic froth stability. The second method used a continuously overflowing bench scale flotation cell which is more representative of industrial systems than cells used for traditional batch tests. This flotation cell had previously only been used to investigate a single-species, idealised system. In this chapter, the cell was used to investigate a complex copper tailings ore, and was shown to be able to operate at steady state for an extended period of time.

The experiments in this chapter have enabled the relationship between feed particle size distribution, superficial gas velocity and froth stability to be investigated further. For the first time, there has been a direct comparison between two different measures of froth stability: dynamic froth stability and air recovery. The results have shown that, for the same tailings ore, the feed particle size distribution that resulted in a local maximum in dynamic froth stability also yielded a maximum in air recovery. This strongly indicates that an intermediate distribution can result in the best froth stability. This effect was observed at multiple superficial gas velocities.

The flotation performance was also investigated and the results showed that the particle size distribution which had the optimal froth stability, both in terms of air recovery and dynamic froth stability, resulted in the highest copper recovery. In the case of the processing plant from where the samples in this chapter were obtained, altering the particle size distribution of the material sent to flotation, to the optimal shown in this chapter, would translate to improved flotation performance and therefore also reduce the amount

of material sent to final tailings. The findings in this chapter have important implications for the reprocessing of mineral resources from tailings, suggesting that froth stability tests to find the optimal particle size distribution should be carried out before reprocessing tailings by froth flotation. This will allow for enhanced mineral recoveries to be achieved, thus contributing to a more efficient use of resources and the reduction of environmental impacts associated with mineral tailings.

Whilst the results in this chapter have shown that the continuously overflowing cell can be used successfully with a complex real ore, there are two key limitations that need to be considered for future test work using the continuous flotation cell. Firstly, it is challenging to control the mineralogy, and specifically the content of valuable mineral, in the feed. Secondly, in order for the system to operate at steady state it was necessary for the concentrate samples to be small, so that not too much material is removed from the cell. This means that the concentrate samples are too small to analyse for mineralogy and liberation and gain a better understanding of which particles are floating. Due to these limitations the following chapters will use a simpler system, with a synthetic two-species ore. This will allow more control over the mineralogical content of the feed and a better understanding of the composition of the concentrate samples, whilst still being more representative of industrial flotation tests than a single-species ore.

# Chapter 5

# Assessing the effect of retrofit modifications on flotation performance

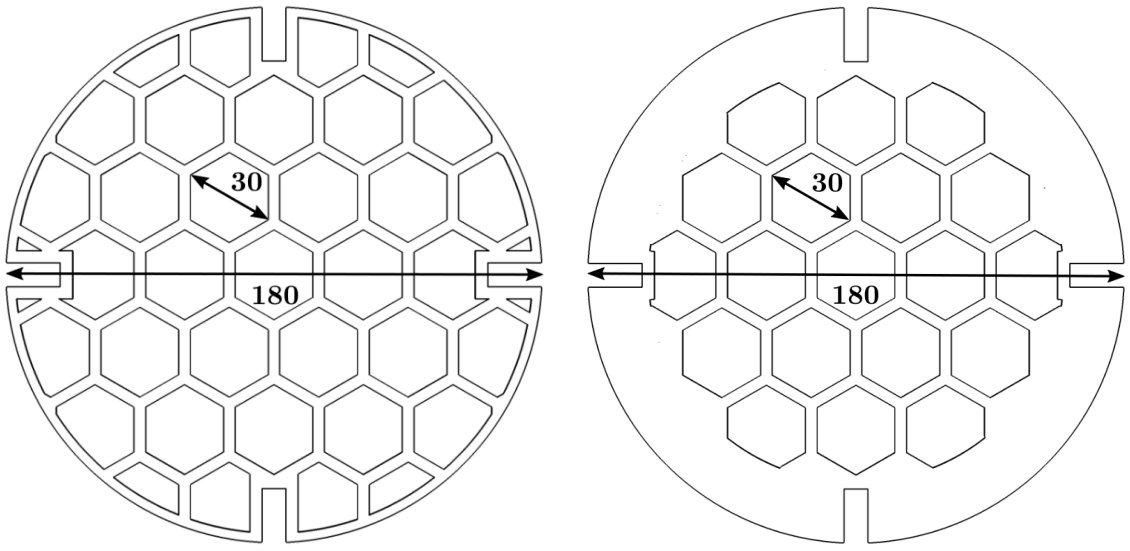
## 5.1 Introduction

In chapter 4, the continuously overflowing flotation cell (described in section 3.2.2) was used to investigate the effects of feed particle size distribution on the froth stability and flotation performance of a copper tailings ore. This ore was more complex than has previously been studied in this cell. The results from chapter 4 had important implications for the reprocessing of tailings material via froth flotation, however, there were limitations as it was difficult to control the mineralogical composition of the ore and, due to the maximum size of concentrate samples that can be taken using this cell, it was challenging to get a full overview of the mineralogical composition of the concentrate samples.

In this chapter, the continuous flotation cell was used with a synthetic ore. This ore allowed for more control on the composition of the feed than a real ore, as well as the ability to obtain a full analysis of the concentrate samples, whilst still being more representative of industrial flotation cells than a single-species ore. The flotation environment used was reverse flotation of magnetite and silica as described in section 3.3.2. This chapter illustrates that the reverse flotation system runs at steady state for over an hour, allowing the superficial gas velocity to be varied multiple times within a single experiment.

Both Norori-McCormac (2015) and Morrison et al. (2017) showed that using retrofit

design modifications of horizontal meshes inserted at, or near to, the pulp-froth interface could improve the flotation performance relative to the unmodified cell. The purpose of the design modifications is to provide a more quiescent environment at the pulp-froth interface, in order to reduce particle detachment and therefore improve performance. Both of these studies, however, used simplified single-species ores, and so it is important to assess if the horizontal meshes will still result in an improvement in flotation performance with a more representative two-species ore. Two different horizontal meshes (figure 5.1) were assessed in this chapter. Both meshes were $20\,\mathrm{mm}$ thick and had a diameter of $180\,\mathrm{mm}$ and the holes measured $30\,\mathrm{mm}$ across the diagonal. The meshes sat below the pulp-froth interface, at the top of the vertical baffles in the cell, $120\,\mathrm{mm}$ from the base of the cell. The first mesh investigated was the mesh that was shown to be optimal by Norori-McCormac (2015). The second mesh has a similar design but the outermost holes were blocked in with the aim of reducing the water content at the cell wall and hence reduce solids entrainment. The different design modifications were assessed for the effect that they had on froth stability, metallurgical performance and particle size of the concentrate in comparison to the unmodified cell.




(a) Basic Mesh (b) Blocked Mesh

**Figure 5.1:** The two different mesh designs used in this chapter: (a) "Basic Mesh" and (b) "Blocked Mesh". Dimensions are in millimetres.

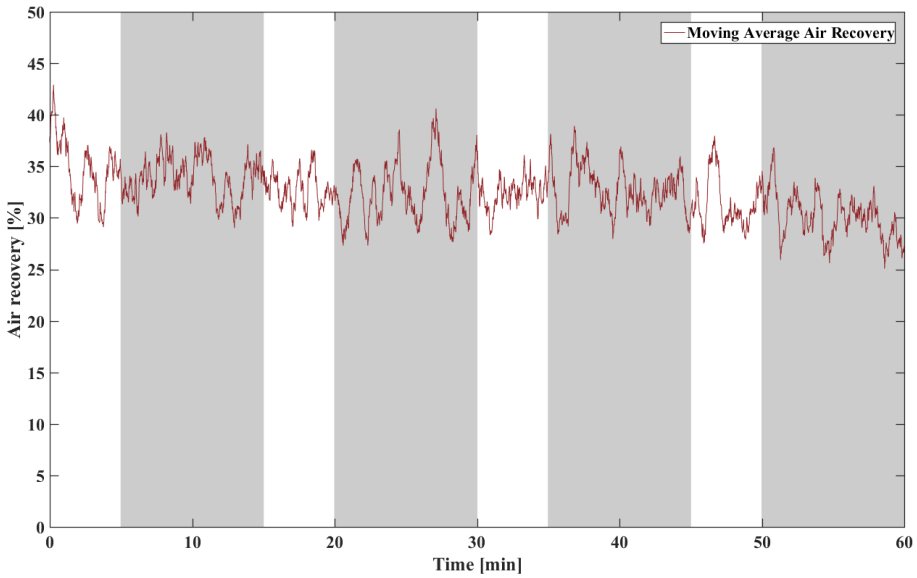
## 5.2 Steady State Operation

The purpose of using the continuously overflowing bench scale flotation cell is to use a steady state system to measure air recovery and flotation performance at a variety of different operating conditions which can be changed multiple times within as single experiment. It is therefore important to determine that the system does actually run at steady state for the desired period of time. In order to verify this, an experiment was conducted where the operating conditions were not changed. Figure 5.2(a) shows the moving average of the air recovery over time for an experiment with no physical design modifications and a superficial gas velocity of $0.82\,\mathrm{cm\,s^{-1}}$. The moving average is quite noisy due to the high sampling frequency of the froth height and velocity. In experiments where the conditions were changed, each condition was run for a total of 15 minutes. The first five minutes of operation at each condition were taken as conditioning time, and the data for the remaining 10 minutes was averaged to obtain the air recovery value for that condition (represented by the light grey vertical bands).

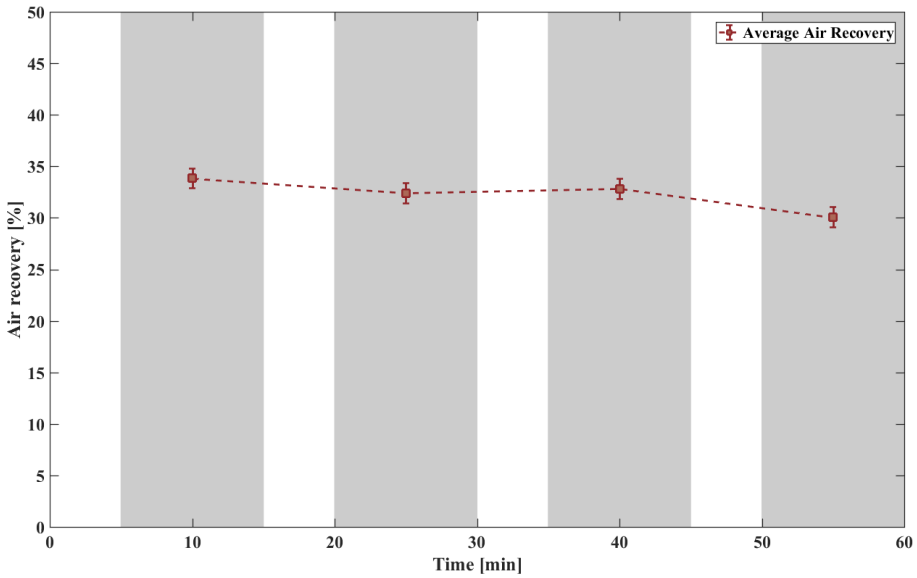
The moving average of air recovery does not change significantly over time showing that the system can operate at steady state for approximately an hour with results being reproducible over time. There is however a slight drop off in the last measurement window (50-60 minutes). Figure 5.2(b) shows the average air recovery for each of the 10 minute measurement windows. This shows that the mean of the air recovery in the final window is statistically significantly different from the other means. This difference suggests that there was a small depreciation in the system over time. This was corrected for by repeating the initial operating condition as the last condition and the data then being processed using a linear regression model as described in section 3.4.3. All data in the remainder of this chapter have been adjusted in this way.

## 5.3 Froth Stability

As discussed in section 2.4.2, previous work suggests that there would be a peak in air recovery (PAR) when the superficial gas velocity ($J_g$) is increased. This phenomenon has been observed both in the lab and industrially (Hadler and Cilliers, 2009). The PAR has also been observed in work by Norori-McCormac (2015) when using meshes, however results from Morrison et al. (2017) in a similar, but larger, cell also implementing meshes




(a) 30 Second Moving Average of Air Recovery




(b) Average Air Recovery for each window

**Figure 5.2:** (a) The variation in air recovery over time at a constant condition, with 10 minute measurement windows highlighted by light grey vertical bands. The average values for each of these 10 minute windows is shown in sub-figure (b) with error bars representing the 95% confidence interval.

showed the air recovery decreased monotonically with increasing superficial gas velocity.

Figure 5.3 shows the relationship between the adjusted air recovery and superficial gas velocity. It is clear that none of the design conditions show a peak in air recovery. An analysis of variance (ANOVA) test was performed on these data (table 5.1) which showed that the effect of changing the superficial gas velocity on the air recovery was significant, whilst the effect of changing the mesh was not significant. It also showed that the effect that changing the superficial gas velocity has on the air recovery was dependent on the mesh used, with statistical significance.

**Table 5.1:** ANOVA table of air recovery for changes in superficial gas velocity and the different design modifications. Significant values are highlighted.

| Source | Sum of Squares | Degrees of Freedom | Mean of Squares | F-Stat | P-Value |
|---|---|---|---|---|---|
| **Superficial Gas Velocity** | 55.5 | 2 | 27.7 | 8.17 | 0.004 |
| Design Modification | 8.35 | 2 | 4.17 | 1.23 | 0.320 |
| **Interaction** | 144 | 4 | 36.1 | 10.6 | $2.74 \times 10^{-4}$ |
| Error | 50.9 | 15 | 3.39 | | |
| Total | 266 | 23 | | | |

The different relationships between superficial gas velocity and air recovery are evident from figure 5.3. The unmodified cell shows that there was a minimum in air recovery at $J_g = 0.82\,\mathrm{cm\,s^{-1}}$ and that the highest air recovery was achieved at the highest superficial gas velocity. For the basic mesh, the relationship between superficial gas velocity and air recovery is flat and for the blocked mesh, the air recovery decreased as the superficial gas velocity increases. Whilst, for a given superficial gas velocity, there was no statistical difference in the air recovery for all three designs, there was a statistical difference between the unmodified cell and the blocked mesh. The maximum air recovery for the unmodified cell was achieved at a $J_g = 0.98\,\mathrm{cm\,s^{-1}}$, whilst for the blocked mesh this maximum was achieved at a $J_g = 0.65\,\mathrm{cm\,s^{-1}}$. This indicates that using the blocked mesh will provide a better froth stability at lower superficial gas velocities than the unmodified cell.

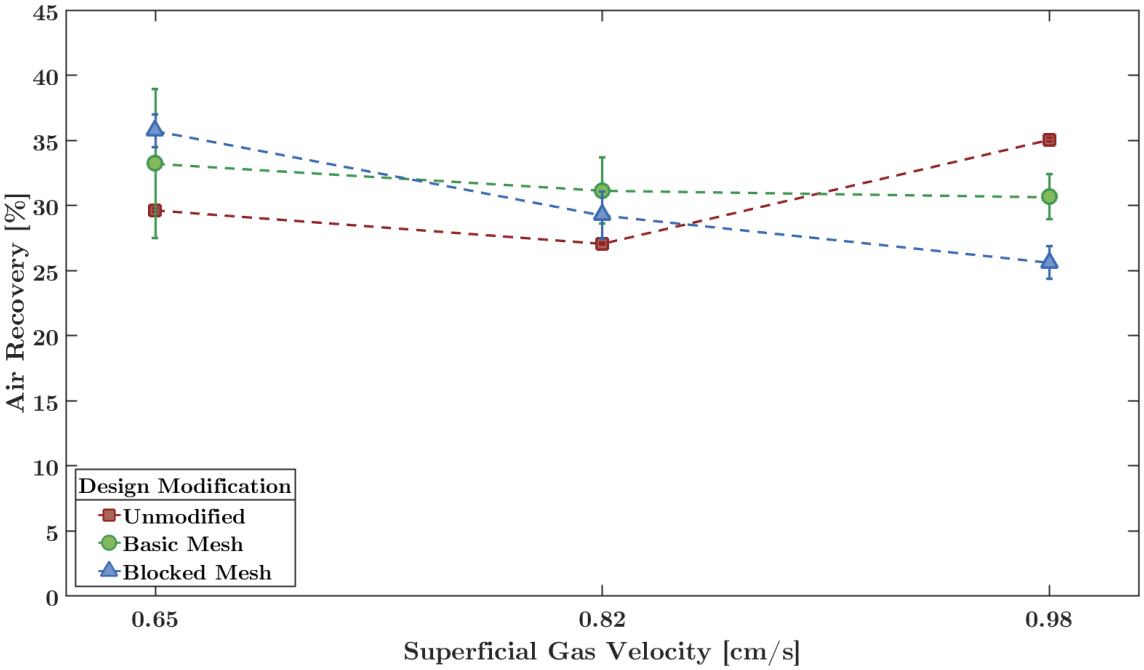



**Figure 5.3:** Adjusted air recovery data for all three design types investigated. Error bars are 95% confidence intervals.

Whilst none of the designs showed a peak in air recovery (PAR), as was expected from previous studies, only three superficial gas velocities were investigated and so it may be the case that the PAR is not within the range investigated, or that it is at an intermediate value of $J_g$. The data in figure 5.3 indicate that the PAR may be at a higher $J_g$, for the unmodified cell, yet for the blocked mesh that PAR may be at a lower $J_g$.

## 5.4 Flotation Performance

The grade-recovery curves for all three design modifications (figure 5.4) show that as superficial gas velocity increases the grade of the concentrate decreases. This is due to the fact that at higher superficial gas velocities there is a higher water recovery and so increased entrainment (Neethling and Cilliers, 2009). It is also the case that, broadly, as superficial gas velocity increases the silica recovery increases. This is due to the higher mass pull at higher superficial gas velocities. Analysis of variance tables (appendix B.1) show that the effects of both the superficial gas velocity and design modification on both the grade and the recovery are statistically significant.

Both the unmodified cell and the basic mesh show that increasing the superficial gas velocity had a large impact on the silica grade of the concentrate with $\Delta Grade \approx 9\%$ for the unmodified cell and $\Delta Grade \approx 6\%$ for the basic mesh. Whilst increasing the superficial gas velocity did increase the recovery, the change was much smaller, with $\Delta Recovery \approx 0.3\,\mathrm{g\,s^{-1}}$ for the unmodified cell and $\Delta Recovery \approx 0.5\,\mathrm{g\,s^{-1}}$ for the basic mesh. On the other hand, for the blocked mesh, increasing the superficial gas velocity only slightly decreased the grade of the concentrate with $\Delta Grade \approx 3\%$, however there was a substantial increase in the silica recovery with $\Delta Recovery \approx 1\,\mathrm{g\,s^{-1}}$. This was most likely due to an increased mass pull; however, it is interesting that this does not also reduce the grade of the concentrate.

For the unmodified cell and the basic mesh, the grade-recovery curves have very typical shapes, with a clear trade off between grade and recovery. The optimal condition in terms of flotation performance, for both design modifications was at a $J_g = 0.82\,\mathrm{cm\,s^{-1}}$, as this resulted in an improvement in recovery without too much of a reduction in grade. Using the basic mesh had the effect of shifting the grade-recovery curve to the left, indicating that there was a reduction in silica recovery relative to the unmodified cell, however this was also accompanied by an improvement in grade. This is the opposite effect to what

was seen in previous work by Norori-McCormac (2015), suggesting that the effect of the retrofit design modifications can be system specific.

The grade-recovery curve for the blocked mesh does not show the same trend as for the unmodified cell or the basic mesh. At the lowest two superficial gas velocities, the blocked mesh showed similar recoveries to the unmodified cell; however, at the highest superficial gas velocity, the recovery with the blocked mesh was substantially higher. The grades at all three superficial gas velocities with the blocked mesh were very similar to the grade for the unmodified mesh at a $J_g = 0.82\,\mathrm{cm\,s^{-1}}$. This indicates that there was a substantial improvement in recovery with the blocked mesh, with very little impact on the grade of the concentrate. These data have shown that the optimal operating condition in terms of flotation performance, for this system, would be to use the blocked mesh with a superficial gas velocity of $0.98\,\mathrm{cm\,s^{-1}}$.

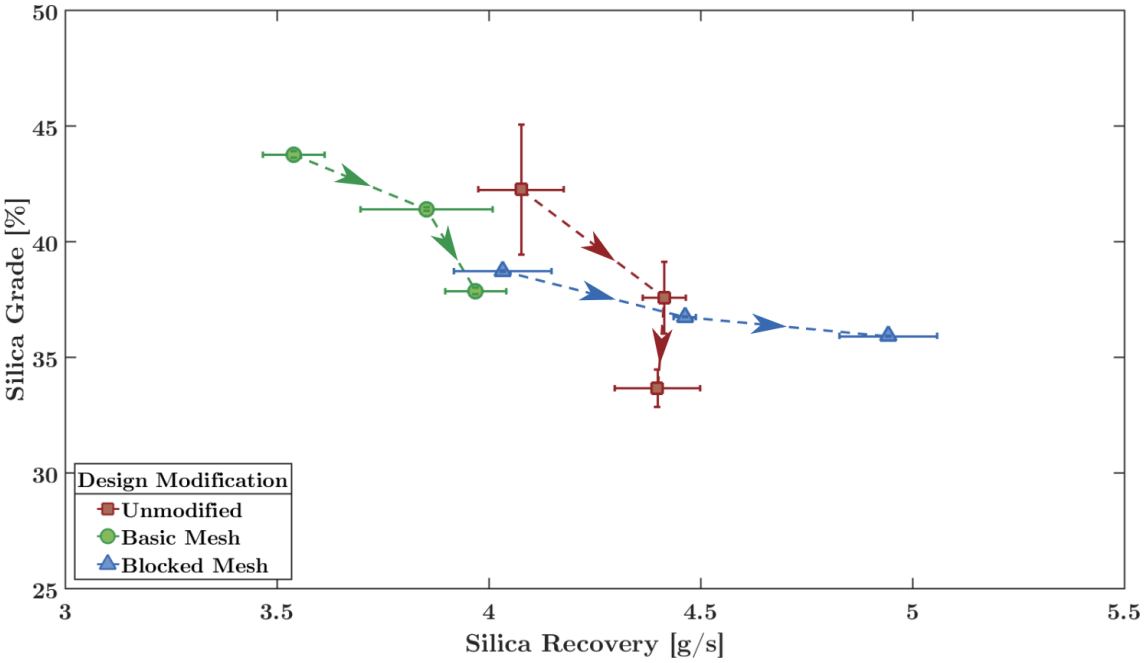



**Figure 5.4:** Adjusted flotation performance data Grade-Recovery Curve. Arrows point in direction of increasing superficial gas velocity. Error bars are 95% confidence intervals.

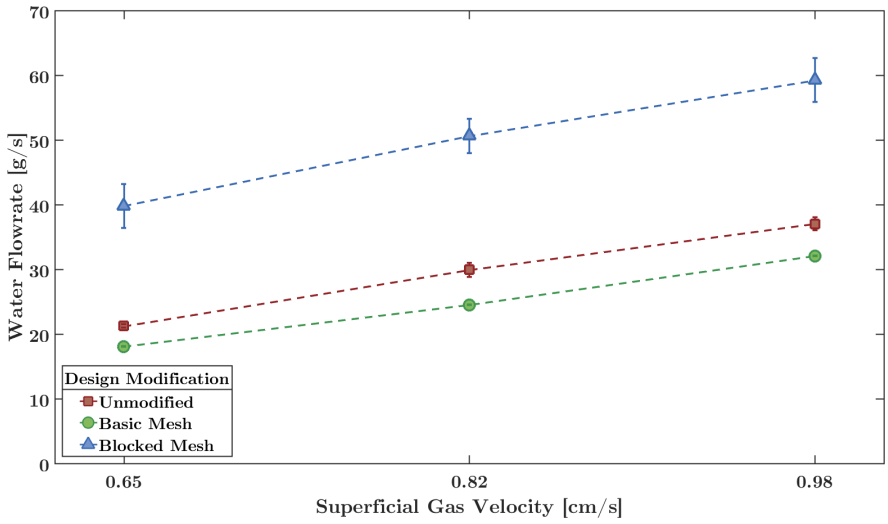
### 5.4.1 Entrainment

Figure 5.5(a) shows that, for all designs, the water flowrate increased linearly with an increase in superficial gas velocity, this is as expected from the literature. Both the superficial gas velocity and the design modification were statistically significant in terms of how they effect the water flowrate to the concentrate. All three design cases show approximately the same gradient, as the interaction between the mesh and the superficial gas velocity

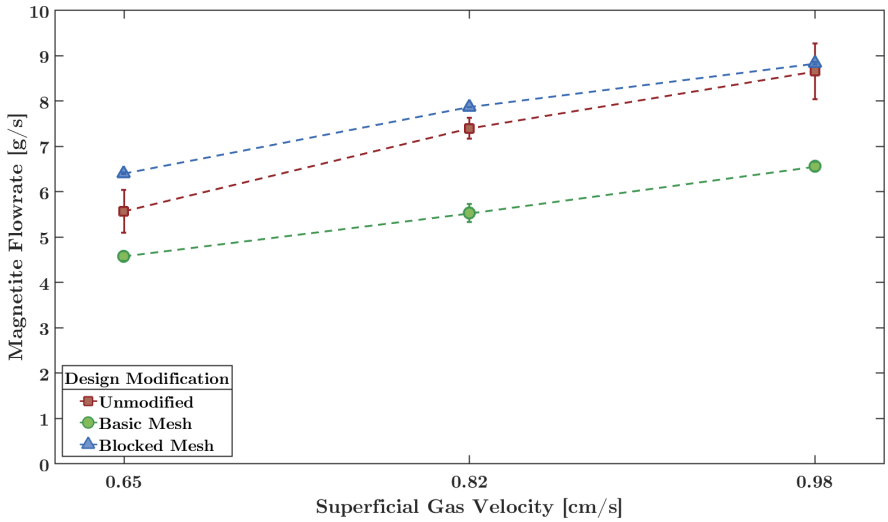
was not statistically significant (appendix B.1.1).

Including the basic mesh in the cell has the effect of slightly reducing the water flowrate in the concentrate in comparison to the unmodified cell. On the other hand, the presence of the blocked mesh substantially increases the water flowrate. This is the opposite of the effect that this mesh was intended to have. It would be expected that an increase in water flowrate to the concentrate would result in a decreased silica grade due to the increase in entrained solids being recovered, i.e. an increased magnetite flowrate (Neethling and Cilliers, 2009). Whilst this was the case (figure 5.5(b)), the magnetite flowrate using the blocked mesh was not substantially higher than in the other cases as would be expected from the high water flowrate. This suggests that there was less entrainment occurring with the blocked mesh, despite the higher water recovery.

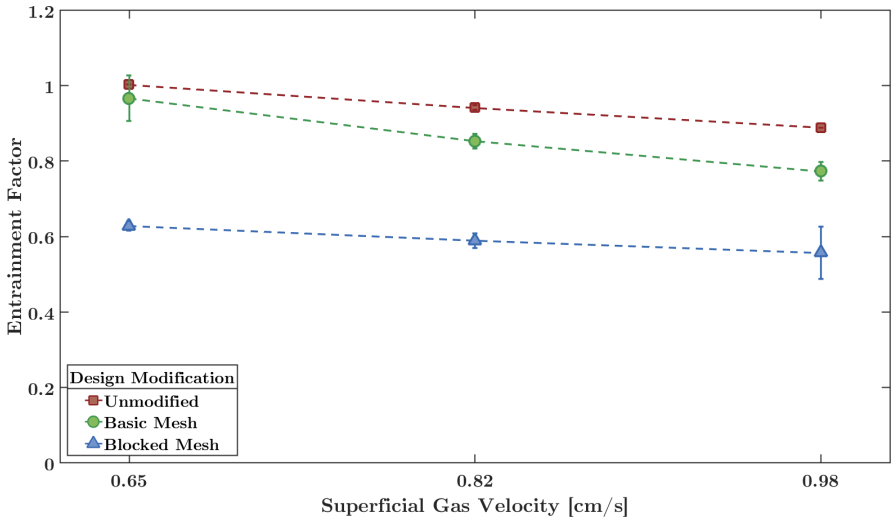
The entrainment factor is the amount of magnetite overflowing the cell as a ratio to what would be expected to overflow due to the water recovery (equation 2.1). It can be seen in figure 5.5(c) that for the unmodified case the entrainment factor was close to 1 for all superficial gas velocities. The entrainment factor for the basic mesh decreased slightly more as superficial gas velocity increased suggesting that the higher superficial gas velocity was preventing magnetite from being entrained. The presence of the blocked mesh drastically lowered the entrainment factor, suggesting that this mesh prevented the hydrophilic particles from being entrained in the froth phase and hence not reporting to the concentrate.




(a) Water flowrate




(b) Magnetite flowrate




(c) Magnetite Entrainment Factor

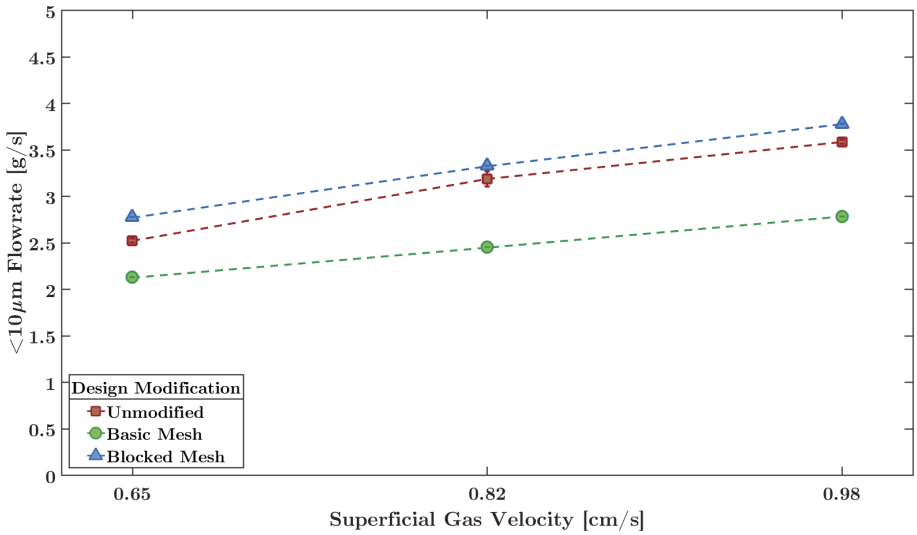
**Figure 5.5:** (a) Water flowrate to the concentrate, (b) Magnetite flowrate and (c) entrainment factor of magnetite in the concentrate for changing design modifications and superficial gas velocities. Error bars 95% confidence intervals.

## 5.5 Particle Size Effects

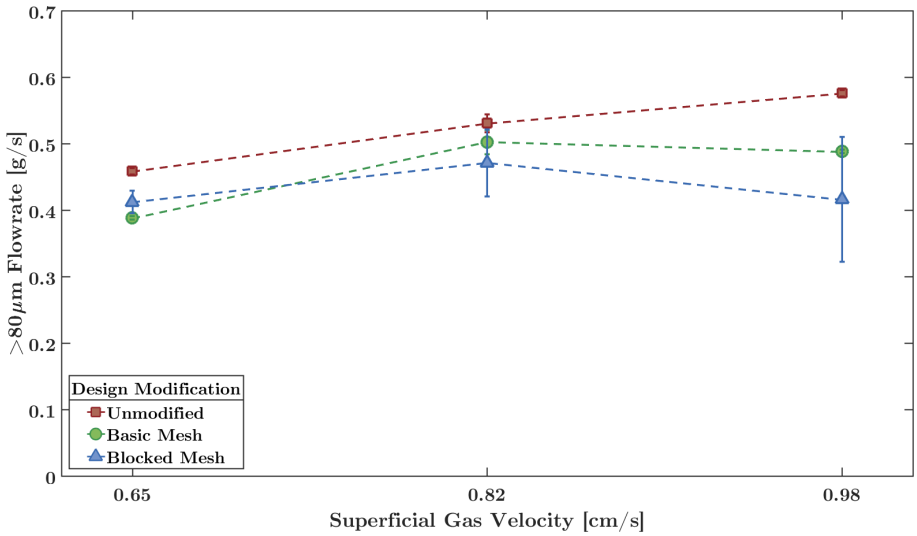
The overall purpose of the retrofit design modifications is to introduce a quiescent pulp-froth interface and improve the recovery of coarse particles. Whilst the size distribution of the magnetite-silica ore was not especially coarse, it is still interesting to look at the recovery of different particle sizes to the concentrate to gain an understanding of how the retrofit design modifications affect the flotation of different particle sizes. The flowrate to the concentrate of particles less than $10\,\mu\mathrm{m}$, and greater than $80\,\mu\mathrm{m}$ is shown in figures 5.6(a) and (b) respectively. The flowrate is indicative of the recovery of each of these sizes. Analysis of variance tables (appendix B.2) show that the effects of both the superficial gas velocity and design modification for both flowrates were statistically significant.

For all design cases, increasing the superficial gas velocity increased the recovery of fine particles to the concentrate (figure 5.6(a)). This is as expected, due to the increased water flowrate and therefore more entrained particles, which are more likely to be fine. The relationship between superficial gas velocity, design and fine particle recovery was very similar to that for the magnetite recovery (figure 5.5(b)); this further indicates that these fine particles are entrained gangue. The basic mesh had a lower recovery of fine particles, at all superficial gas velocities, this is likely due to the lower water recovery that this mesh exhibited. The blocked mesh had a similar, but slightly higher, fine particle recovery to that of the unmodified cell. As with the magnetite flowrate, the fine particle flowrate would be expected to be higher than for the unmodified cell, given the substantial increase in water recovery; this again indicates that the blocked mesh is reducing the entrainment of the magnetite.

The data for the unmodified cell showed that increasing the superficial gas velocity improved the recovery of particles $> 80\,\mu\mathrm{m}$ to the concentrate (figure 5.6(b)). The unmodified cell also had a better recovery of coarser particles in comparison to both the meshes. It is also noted that there was no statistical difference between the coarse particle recoveries for the two mesh designs; these both show that increasing the superficial gas velocity from $J_g = 0.65\,\mathrm{cm\,s^{-1}}$ to $J_g = 0.82\,\mathrm{cm\,s^{-1}}$ improved the flowrate of coarse particles, but increasing it further to $J_g = 0.98\,\mathrm{cm\,s^{-1}}$ had little effect. Both meshes therefore showed an optimal recovery of particles over $80\,\mu\mathrm{m}$ particles at $J_g = 0.82\,\mathrm{cm\,s^{-1}}$.




(a) Fine particle ($< 10\,\mu$m) flowrate




(b) Coarse particle ($> 80\,\mu$m) flowrate

**Figure 5.6:** Indicative recovery of fine particles (a) and coarse (b) particles. Error bars are 95% confidence intervals.

## 5.6 Conclusions

In this chapter, the previously developed continuously overflowing flotation cell has been used to assess the effects of different operating conditions on the flotation performance of a two-species feed. Two different modifications were investigated and the experimental results compared to the unmodified cell. The design modifications used were horizontal meshes inserted below the pulp-froth interface in order to introduce a more quiescent interface. The first mesh investigated was the "basic mesh" which was previously used in the same cell with a single-species, silica ore in Norori-McCormac (2015). In previous work, this mesh was shown to improve the air recovery and the indicative recovery, however there was little improvement in the concentrate grade. The second mesh investigated in this chapter was the "blocked mesh" which had the same thickness and hole size as the first mesh, but with the outer holes blocked in in order to reduce the liquid flow at the walls of the cell and therefore reduce entrainment.

In the experiments with the unmodified flotation cell, the grade-recovery curve showed that an optimal flotation performance was achieved at a superficial gas velocity of $0.82\,\mathrm{cm\,s^{-1}}$. The particle size distribution of the concentrate became finer as the superficial gas velocity was increased, suggesting that there was more entrainment, which is reflected in the decreasing grade.

The insertion of the basic mesh resulted in an improvement in the concentrate grade, however the recovery was substantially lower in comparison to the unmodified cell. This is contrary to what was seen previously in the same cell and with the same mesh by Norori-McCormac (2015), however that study used a single-species system compared to the two-species system used in the experiments in this thesis. This design modification resulted in an optimal recovery of coarse particles at a $J_g = 0.82\,\mathrm{cm\,s^{-1}}$, corresponding to the optimal condition for flotation performance with this mesh.

The blocked mesh resulted in a similar maximum in froth stability as the unmodified cell, however for a lower superficial gas velocity. The grade of the concentrate was not improved by blocking in the outer walls, as was originally hypothesised, although the silica recovery was improved. There was also a substantial increase in water recovery. It would be expected that the increase in water recovery would lead to a substantial decrease in grade due to increased entrainment, however this was not the case. This indicates that, whilst the presence of the blocked mesh did not reduce the liquid content, it did

reduce the entrainment factor for hydrophilic particles. This is a phenomenon that will be especially interesting to investigate further with the use of positron emission particle tracking (PEPT). Similarly to the basic mesh, the blocked mesh also resulted in an optimal recovery of coarse particles at a $J_g = 0.82\,\mathrm{cm\,s^{-1}}$.

Inserting meshes below the pulp-froth interface strongly affects the flotation performance of the magnetite silica system. Using the basic mesh, that was previously studied, improved the concentrate grade, whilst the blocked mesh improved the recovery and reduced the entrainment factor. Both meshes had a similar effect on recovery of particles $>80\,\mu\mathrm{m}$, with a peak at a $J_g = 0.82\,\mathrm{cm\,s^{-1}}$, however this was still slightly lower than the unmodified cell.

The use of PEPT to investigate both of these design modifications and a variety of tracer types and sizes will help further the understanding of how using horizontal meshes effects the flow within the cell and how this relates to flotation performance and froth stability. This is explored in chapters 6 and 7.

# Chapter 6

# Investigating the impact of flotation cell retrofit design modifications on particle behaviour

## 6.1 Introduction

In chapter 5, a continuously overflowing flotation cell was used to investigate two retrofit design modifications with a two-species ore. The purpose of the design modifications was to provide a more quiescent environment, at the pulp-froth interface, in order to promote the flotation of coarse particles. These design modifications consisted of horizontal meshes that were inserted into the flotation cell at a height of 100-120 mm, from the base of the cell, so that the top of the mesh lay flush with the top of the baffles.

The first mesh investigated was the "basic mesh" (as previously used, with a single-species ore, by Norori-McCormac (2015)). In chapter 5, this mesh was shown to improve the concentrate grade, however, the recovery of valuable mineral to the concentrate was reduced. The second mesh investigated was the "blocked mesh", which had a very similar design to the basic mesh, but with the outer ring of holes blocked in. The rationale behind the design of this mesh was that the blocked holes would reduce the liquid flow at the cell wall, thereby reducing the entrainment. In fact, the water content of the froth was much higher than either the unmodified cell or the basic mesh. An increased water recovery would suggest the potential for more entrainment and so a lower concentrate grade (Neethling and Cilliers, 2009). However, this was not the case with the blocked

mesh, as the grade was not substantially reduced given the amount of water recovered.

In order to fully understand the reasons behind the changes in performance caused by the retrofit design modifications, it is necessary to investigate the effects that these modifications have on the flow of particles in both the pulp and the froth, in relation to the froth stability and flotation performance data from chapter 5. This can be achieved with the use of positron emission particle tracking (PEPT). PEPT is a technique which allows radioactive labelled tracer particles, both hydrophobic and hydrophilic, to be tracked throughout the cell to provide information on the behaviour of valuable and gangue particles.

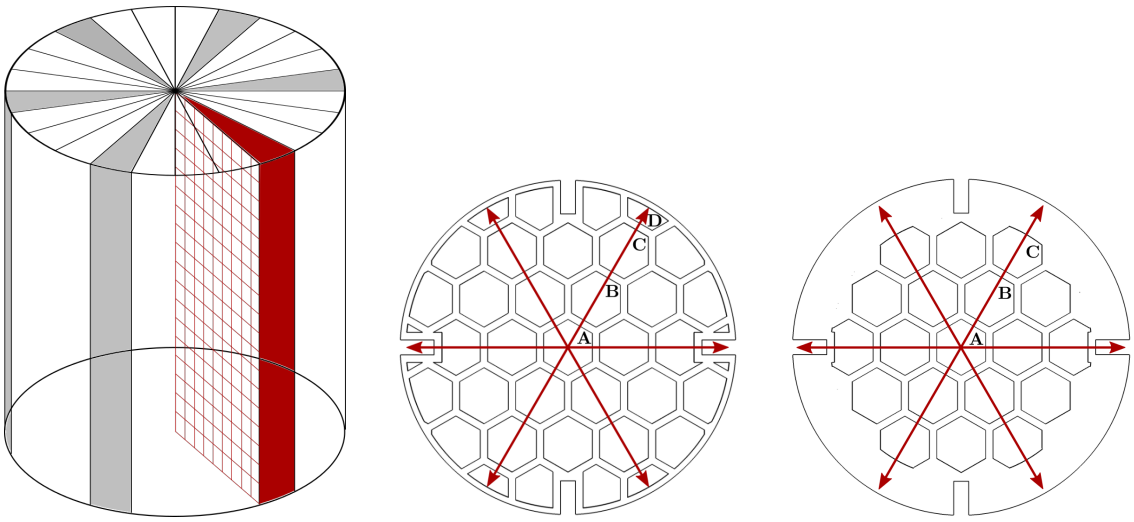
The same experimental system was used as in chapter 5, with only minor modifications made to the frame in order to fit it inside the PEPT camera. In order to focus on the effects of the design modifications, only one superficial gas velocity was investigated for each of the design modifications and tracers. This was chosen to be $0.82\,\mathrm{cm\,s^{-1}}$, as this superficial gas velocity was shown, in chapter 5, to result in the optimal performance for the unmodified cell and for the basic mesh, this superficial gas velocity also yielded an optimal recovery of coarser particles for both meshes.

When processing the PEPT data it was important to check the integrity of the tracer throughout the duration of the experiment. In order to do this, the location of the tracer was plotted against time for each experiment and inspected to see if there was a change in behaviour. For experiments where there was a clear change in behaviour, indicating that the coating of the tracer broke during the experiment, only the first portion of the data was used in the analysis. Plots of tracer height in the cell versus time, for all experiments, can be found in appendix C.

For analysis of the PEPT data, the cylindrical volume of the flotation cell was divided into 6480 voxels measuring $10\,\mathrm{mm}$ by $10\,\mathrm{mm}$ by $10^{\circ}$. For each of the voxels, the average velocity components and the occupancy of the tracer were calculated. The velocity components were also used to calculate and plot streamlines in 2D slices through the cell. The density of the streamlines was chosen to best match the resolution of the averaged data. In other flotation studies using PEPT, occupancy is often defined as the number of tracer locations in a voxel (Boucher et al., 2017; Cole et al., 2014; Norori-McCormac, 2015), however over long time scales this is inappropriate due to the fact that the tracer activity decays, and so one location at the end of the experiment corresponds to a longer time than at the beginning of the experiment (Parker, 2017). In this study, occupancy is defined as

the total time the tracer spent in each cell voxel as a percentage of the total time the tracer spent in the flotation cell (Parker, 2017). As the flotation cell was divided into voxels in a cylindrical grid, the volume of the voxels varies and so the occupancy was also normalised by the volume of the voxel.

The tracer data can then be presented in different slices throughout the cell, both horizontally and vertically. For vertical slices, 6 evenly spaced wedges were taken through the cell, indicated by the shaded areas in figure 6.1(a), and the data in each were averaged to account for variation from different areas of the cell. These wedges were chosen such that they cut through the centre of the mesh holes, as illustrated in figure 6.1(b) & (c). Horizontal slices were simply taken at a set height through the cell; the height quoted is the height of the top of the voxels being presented. For example, a height of $120\,\mathrm{mm}$ corresponds to the voxel at 110-120 $\mathrm{mm}$, unless otherwise stated. To aid in the clarity of the discussion, the holes in the mesh shall be referred to as $A$, $B$, $C$, and $D$ from the centre of the cell, with $A$ being the hole that the impeller goes through and $D$ being the hole closest to the wall (figure 6.1). Holes $D$ are the ones that are blocked in the blocked mesh. It is important to note that the meshes did not fit exactly flush with the wall of the cell (to facilitate with their insertion) and there was a small gap between the edge of the mesh and the wall of the cell where the tracers may have been able to bypass the mesh.




(a) Division of the cell for PEPT data processing (b) Basic Mesh (c) Blocked Mesh

**Figure 6.1:** (a) Illustration of how the flotation cell volume is divided into voxels for processing, wedges averaged to create vertical slices are indicated by the shaded regions. The two different mesh designs used in this chapter: (b) basic mesh and (c) blocked mesh, with holes labelled $A - D$. Red arrows indicate the location of the six wedges averaged to create the vertical slices.

In this chapter, the streamlines, velocity components and the occupancy of two types of tracer (one coated in silica, rendering it hydrophobic, and the other coated in magnetite, rendering it hydrophilic) were used to investigate the effects that the different design modifications had on particle behaviour. Both tracers had the same diameter of $500\,\mu\mathrm{m}$.

## 6.2 Bulk Tracer Flow

Figures 6.2(a) and 6.2(b) show the streamlines of the tracer flow through vertical slices of the cell for all three design cases (the unmodified cell, the basic mesh and the blocked mesh) for the hydrophobic and the hydrophilic tracers respectively. Figures 6.3 and 6.4 show the streamlines of the hydrophobic and hydrophilic tracers, respectively, at varying heights through the unmodified cell. The plane of the impeller is at a height of $60\,\mathrm{mm}$ and the lip of the cell is at a height of $180\,\mathrm{mm}$. Horizontal slices of the tracer motion for each of the tracers and design modifications are presented in figures 6.5 and 6.6, with figure 6.5 showing the motion in the mesh and figure 6.6 showing the motion at the approximate height of the pulp-froth interface for each design.

The streamlines for the unmodified cell, for both the hydrophobic and hydrophilic tracers (figure 6.2), show that the pulp-froth interface sits at approximately a height of $140\,\mathrm{mm}$. The pulp is clearly made up of two mixing loops, anticlockwise above the impeller and clockwise below the impeller. The streamlines for the hydrophobic tracer (figure 6.2(a)) show good upwards tracer motion, that is close to vertical through the froth and then towards the lip of the cell, in a good overflowing motion, indicating that there was a good recovery of the hydrophobic tracer. There is some evidence of particle drop off at the top of the froth, close to the impeller, where there is a well known stagnant area of froth that does not overflow.

The hydrophilic tracer (figure 6.2(b)) shows slightly more chaotic motion in the froth, suggesting that, although there was clearly some recovery of this tracer, it did not take the most efficient path to the overflow. There is also evidence of the hydrophilic tracer flowing at the wall of the cell, which is indicative of a high water content at the cell wall (as the hydrophilic particle is entrained in the liquid).

The horizontal slices for the hydrophobic and hydrophilic tracers in the unmodified cell (figures 6.3 and 6.4), show that there was little difference between the motion of the

two tracers through the bulk of the cell, with only some differences seen in the froth. The majority of the slices, for both tracers, show a swirling motion, in the same direction as the impeller flow. This is something that is expected in the pulp of the froth, however this is still the case at $h = 150\,\mathrm{mm}$ which is above the pulp-froth interface. This phenomenon was observed for the first time by Norori-McCormac (2015) and is expected to detrimentally impact the particle recovery as it is indicative of a non-quiescent environment. The slice at a height of $180\,\mathrm{mm}$ for the hydrophobic tracer (figure 6.3) shows that the tracer generally flowed from the centre towards the lip of the cell, as is expected for attached particles moving with the froth. The horizontal slice for the hydrophilic tracer at the same height (figure 6.4), however, only shows some evidence of flow towards the lip close to the cell wall, which can be linked to trade off between hydrophilic particles following the net upwards liquid motion whilst also settling through the plateau borders. Closer to the centre there is either no data, which indicates that there was no presence of the hydrophilic tracer in this region, or the motion was rotational indicating that it was not recovered as easily.

The presence of either of the meshes in the cell had a clear effect on the streamlines of both the hydrophobic and hydrophilic tracers (figure 6.2). The key differences are that the upper mixing loop is compressed and that the froth depth is shallower, with the pulp-froth interface approximately at a height of $160\,\mathrm{mm}$, as indicated by the data from the hydrophilic tracer by the upwards motion of the streamlines (figure 6.2(b)). Interestingly, it is noted that the presence of the meshes created a secondary pulp zone above the mesh that is more quiescent than the pulp below the mesh.

The streamlines of the hydrophobic tracer, with the basic mesh (figure 6.2(a)), show that the tracer flows up through holes $A$, $B$ and $D$ yet flows down through holes $C$. Above the mesh there is a small, third mixing loop, in the secondary pulp zone above holes $C$, which leads into the downwards motion through the hole. This indicates that the tracer drops off from the pulp-froth interface and through holes $C$, however, the presence of the third mixing loop may help promote reattachment of detached particles. The streamlines for the hydrophobic tracer in the froth are much more chaotic than in the unmodified cell, suggesting that the presence of the mesh was creating a more chaotic froth and reducing the chance of the particle being recovered to the concentrate.

The streamlines for the hydrophilic tracer, with the basic mesh (figure 6.2(b)) also show that the tracer moves up through holes $A$, $B$ and $D$ and down through holes $C$,

however there is less clear upward flow and the downward motion more commonly links back to the upper mixing loop below the mesh. This indicates that the hydrophilic particle was less easily recovered to the froth. There is also no evidence of a third mixing loop in the secondary pulp zone indicating that there was less chance of the hydrophilic tracer being reattached in this zone. The horizontal slices through the mesh for the hydrophilic tracer (figure 6.5(b)) show that the tracer will occasionally circulate within a hole of the mesh indicating that there was less upwards motion of the hydrophilic tracer through the holes of the mesh than the hydrophobic tracer.

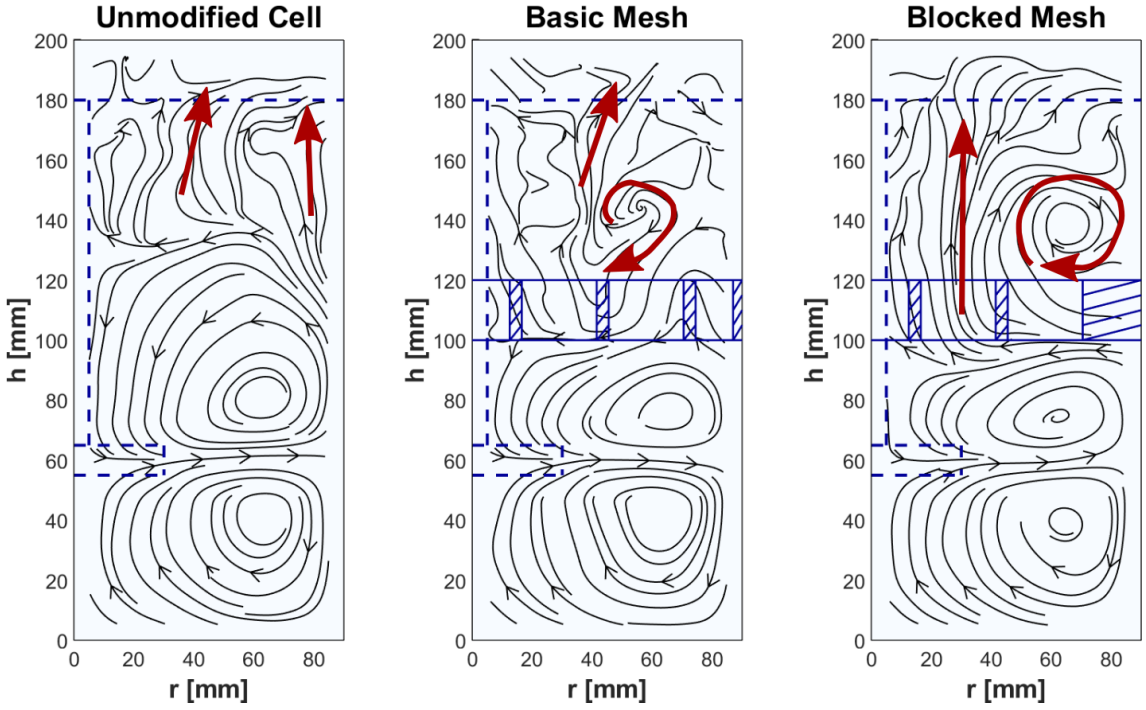
With the blocked mesh inserted in the cell, the hydrophobic tracer streamlines (figure 6.2(a)) show that there is no downwards motion of the tracer through any of the holes in the mesh, instead the tracer moves vertically upwards through holes $A$ and $B$ and diagonally upwards and away from the wall of the cell in holes $C$. This is due to the fact that holes $D$ is blocked and the tracer has to move laterally to get to a mesh hole in order to move vertically. In this case, there is a more well defined mixing loop in the secondary pulp zone than with the basic mesh. This mixing loop is located above the blocked section of the mesh and so detached particles move laterally along the top of the mesh. The fact that these particles do not then drop back through the mesh suggests that the mesh promotes a good environment for particle reattachment. The flow of the tracer in the froth is good and mainly vertical leading to a good overflow.

For the streamlines of the hydrophilic tracer, with the blocked mesh (figure 6.2(b)), there is a much larger mixing loop in the secondary pulp zone that extends through holes $B$ and $C$ of the mesh, with the tracer moving up through holes $B$ and then dropping down into the pulp below the mesh through holes $C$. This mixing loop in the secondary pulp zone is similar to the mixing loops in the primary pulp zone. There is a low recovery of the tracer from the mixing loop in the secondary pulp zone to the froth.

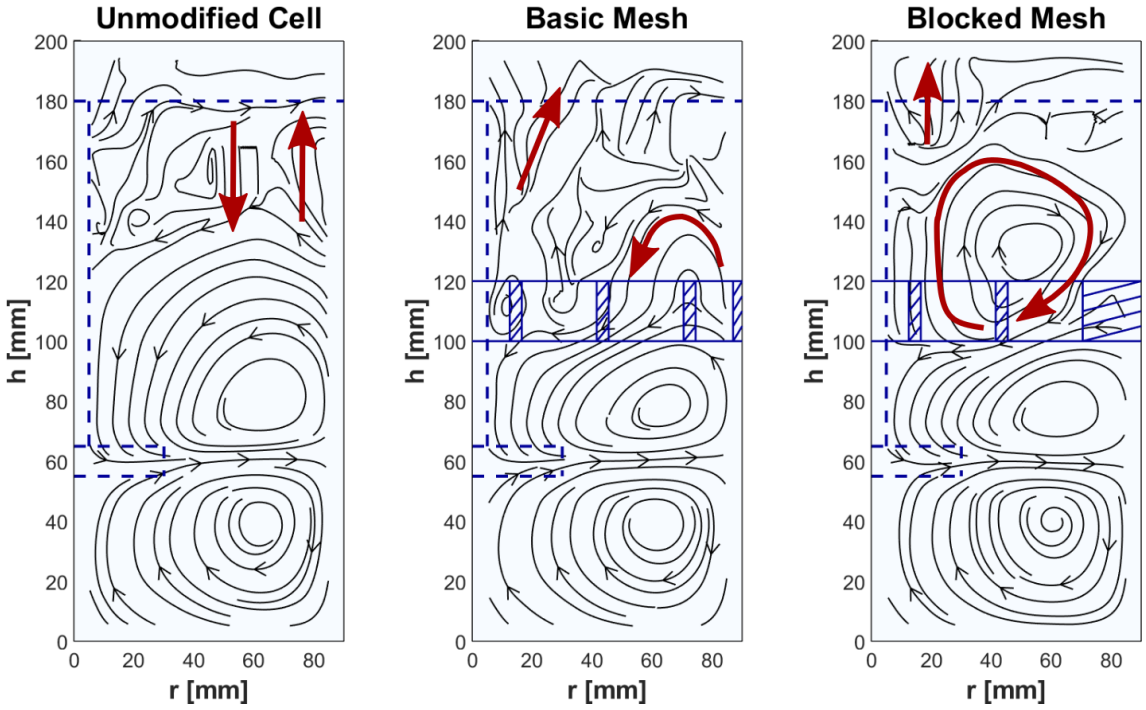
The horizontal slices through the mesh (figure 6.5), show that there are some areas where both the hydrophobic and the the hydrophilic tracers circulate within a hole of the blocked mesh. This happens in more areas with the hydrophilic tracer. At a height of $140\,\mathrm{mm}$ (figure 6.6) the hydrophilic tracer also circulates above the blocked holes of the mesh close the wall. This suggests that there was less vertical motion of the tracer here and therefore a lower water flowrate to the froth at the wall of the cell.

Whilst the streamlines give a good indication of the direction of the tracer motion, they

do not provide any information about magnitude, it is thus important to investigate other variables for the tracer such as velocity components and the occupancy to understand more about how the design modifications influence the flow of the tracer.




(a) Hydrophobic tracer




(b) Hydrophilic tracer

**Figure 6.2:** Streamlines within the cell, with each of the design types, for (a) the hydrophobic and (b) hydrophilic tracers. Both tracer types are $500\,\mu\mathrm{m}$ in diameter. Red arrows are added to highlight some flow patterns and are indicative only. The impeller and the level of the overflowing lip are shown in dashed blue lines and the position of the mesh shown in solid blue lines.

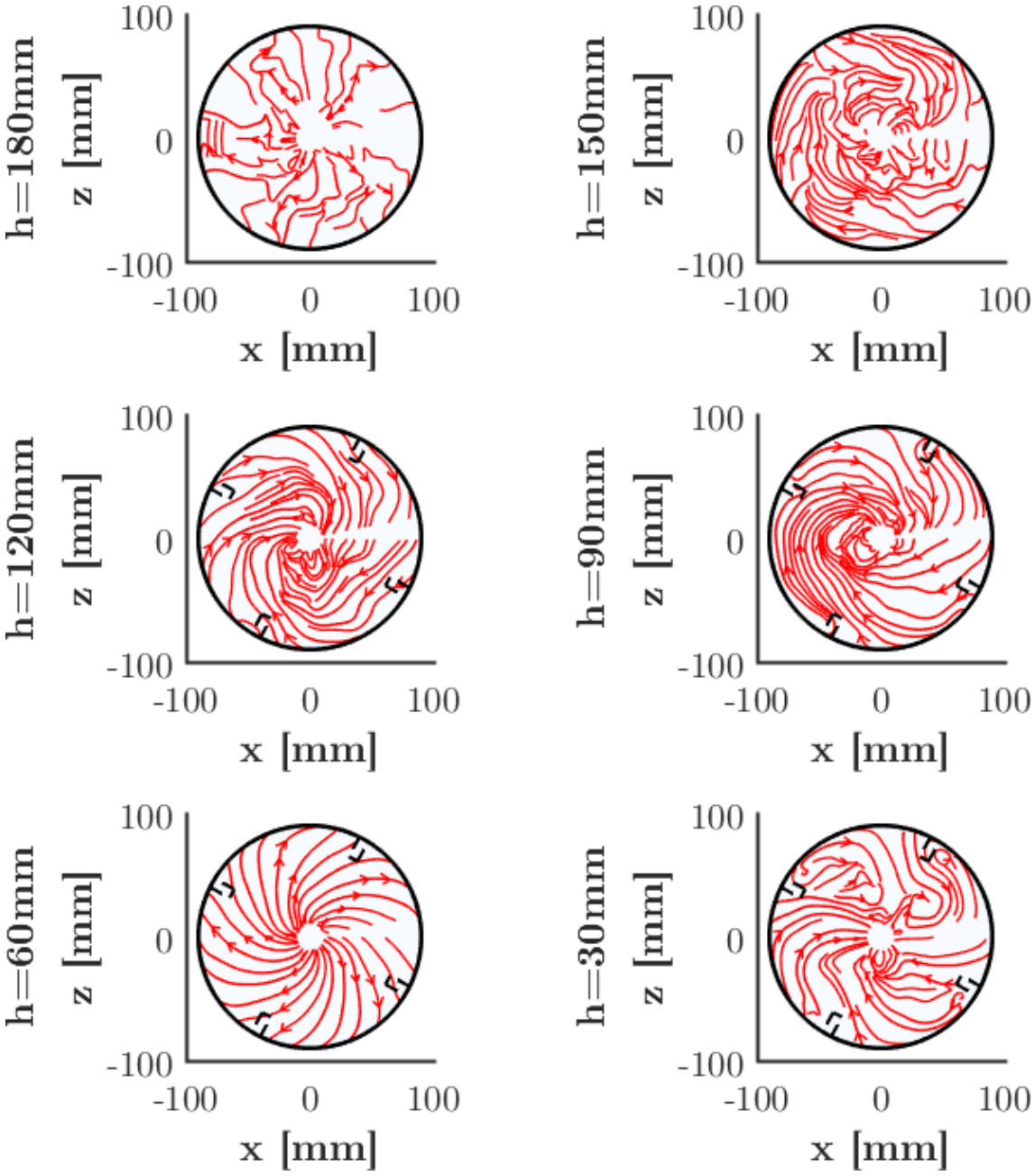



**Figure 6.3:** Bulk flow of the hydrophobic tracer, in the unmodified cell, at different heights through the cell.

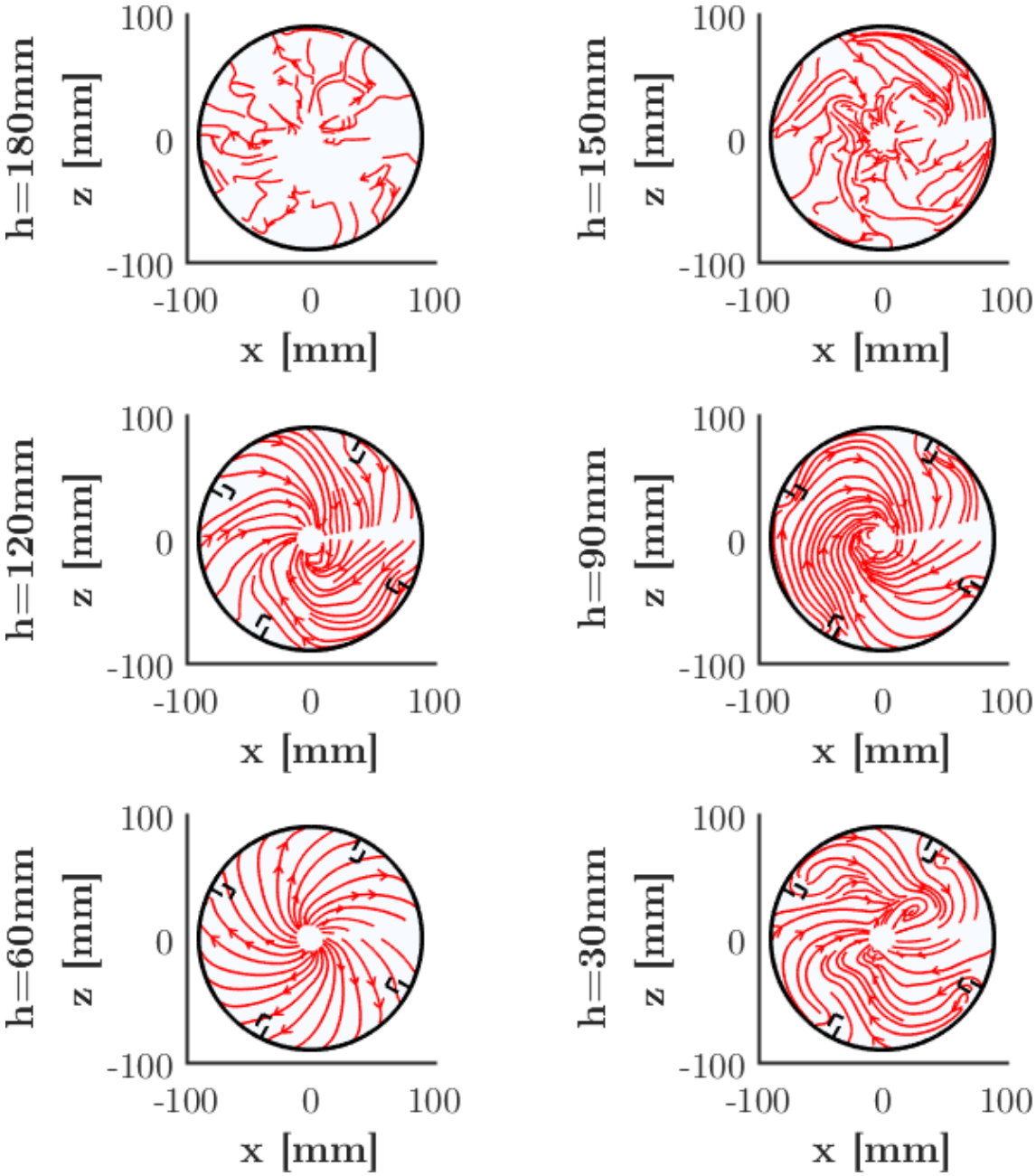
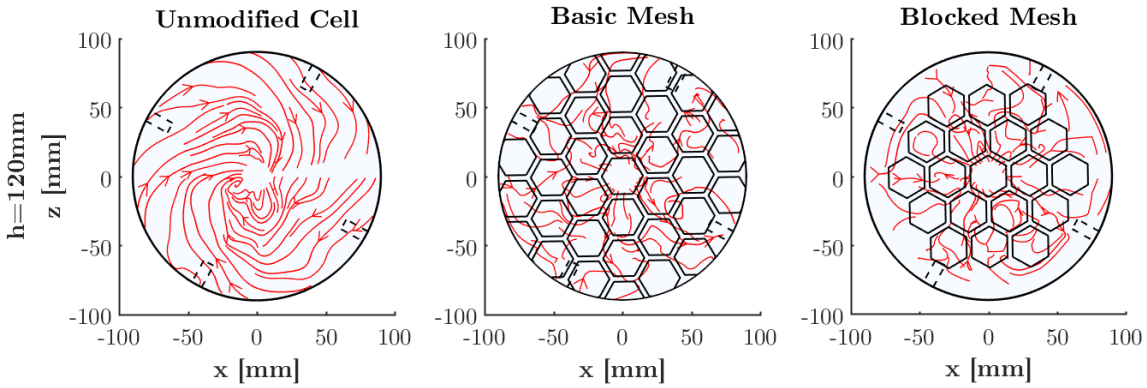
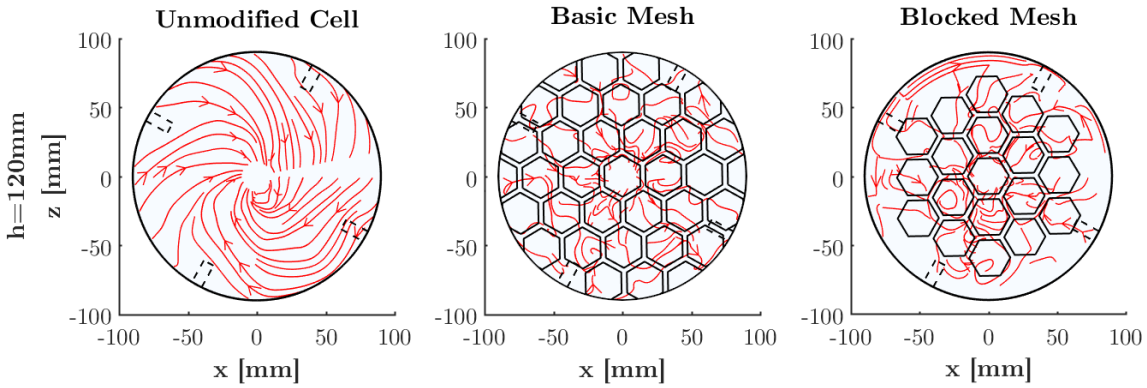



**Figure 6.4:** Bulk flow of the hydrophilic tracer, in the unmodified cell, at different heights through the cell.

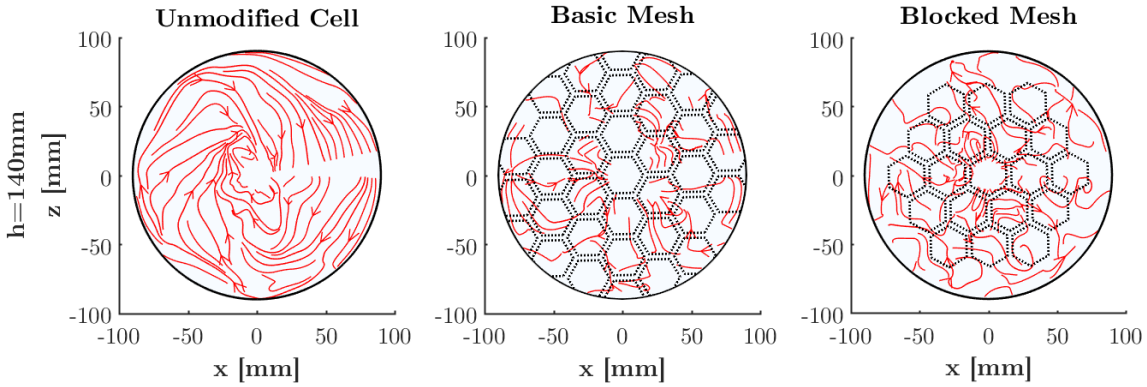



(a) Hydrophobic tracer

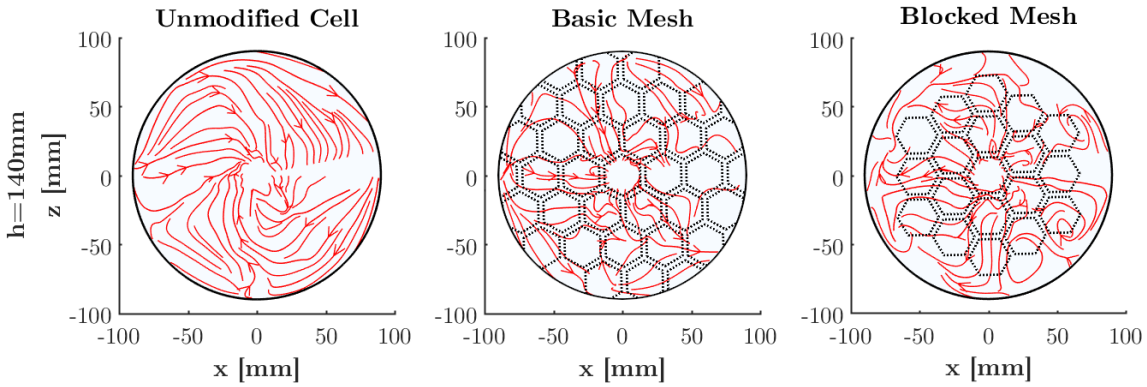



(b) Hydrophilic tracer

**Figure 6.5:** Horizontal slices of streamlines of the (a) hydrophobic and (b) hydrophilic tracer in the different cell designs at a height of 120 mm. The location of the mesh is outlined in black.




(a) Hydrophobic tracer




(b) hydrophilic tracer

**Figure 6.6:** Horizontal slices of streamlines of the (a) hydrophobic and (b) hydrophilic tracer in the different cell designs at a height of 140 mm. The location of the mesh is outlined in black.

## 6.3 Velocities

The average vertical velocity component of the hydrophobic and hydrophillic tracers in a vertical slice through the cell, for each of the three design cases, is shown in figure 6.7. In order to better understand how the vertical velocities varies in the cross section of the cell, figures 6.8 and 6.9 show horizontal slices taken at different heights through the unmodified cell for the hydrophobic and hydrophilic tracers respectively. Figures 6.10 and 6.11 show the values of the velocities of the different tracers at different points through the cell, allowing for direct comparison between tracers and design modifications. Figure 6.10 shows the variation in velocity from the centre of the cell to the wall, at different heights. Figure 6.11 shows the variation in velocity with height, at different locations along the radius of the cell; these locations are chosen to go through the centre of each of the holes of the mesh. The error bars presented on both of these figures are the standard error after averaging across the six slices. In addition, horizontal slices of vertical velocity through the mesh are shown in figure 6.12.

The vertical velocity of the hydrophobic tracer in the unmodified cell (figure 6.7(a) and figure 6.8) is much higher in the pulp zone of the cell than in the froth zone. This is as expected, as the bubbles in the froth will move more slowly than the pulp. Whilst the magnitude of the tracer velocity is low in the froth, the slices at $150\,\mathrm{mm}$ and $180\,\mathrm{mm}$ in figure 6.8 show that the velocity it is mostly positive throughout, especially just below the lip of the cell. This indicates that there was very little drop off of the hydrophobic particle from the froth and that there was good recovery to the concentrate. There are, however, negative velocities at the top of the overflowing froth (figure 6.7(a)), especially close to the centre of the cell, suggesting that bubble bursting us occurring and particles are being lost. In comparison, the hydrophilic tracer (figure 6.7(b)), shows some downward motion of the tracer in the froth, especially at $r = 50$-$70\,\mathrm{mm}$. This is especially clear in the slice at $150\,\mathrm{mm}$ in figure 6.9, where there are many more areas with a negative vertical velocity than for the same slice with the hydrophobic tracer, and these negative velocities are also a higher magnitude. This indicates that the hydrophilic tracer was less easily recovered than the hydrophobic. Figures 6.8 and 6.9 show that the vertical velocity in the pulp of the unmodified cell, for both tracers, are very similar, however the vertical profile of the vertical velocity (figure 6.11) shows that the average velocity of the hydrophobic tracer becomes positive at a height of approximately $120\,\mathrm{mm}$, indicating that the tracer was

attached to a bubble and moving upwards before it reached the froth. On the other hand, the vertical velocity hydrophilic tracer does not become positive until a height of $150\,\mathrm{mm}$, indicating that the hydrophilic tracer was behaving as expected for an entrained particle. The horizontal slices, at a height of $120\,\mathrm{m}$, (figure 6.12) show that the velocity of the tracer is not constant around the cell, instead there are high positive vertical velocities behind the baffles.

The vertical velocity of the hydrophobic tracer, with the basic mesh, in the pulp, is similar to that of the unmodified cell (figure 6.7(a)). However, due to the compression of the upper mixing loop by the mesh, figure 6.11(a) shows that at heights of $80$-$100\,\mathrm{mm}$ the negative velocities below holes $B$ and the positive velocities below holes $D$ have a lower magnitude than for the same place in the unmodified cell. As mentioned when discussing the streamlines of the tracer in section 6.2, the tracer moves down through holes $C$ and up through the other holes of the mesh. Figure 6.11(a) shows that the negative vertical velocity in holes $C$ has a higher magnitude than the positive vertical velocities through holes $A$ and $B$, however it is of a similar order of magnitude to the positive vertical velocity through holes $D$. This indicates that the higher velocity of the tracer through holes $D$, compared to $A$ and $B$, was due to the higher liquid content at the cell wall.

The vertical velocity of the hydrophobic tracer in the horizontal slice through the basic mesh (figure 6.12(a)), shows that the high positive velocities in holes $D$ are higher behind the baffles. This slice also shows that whilst the average vertical velocity of the hydrophobic tracer, in holes $B$, is positive in the vertical slice, there are still many areas where the vertical velocity is negative suggesting that the recovery of the tracer through the mesh is reduced.

In section 6.2, it was shown that there is a small mixing loop in the secondary pulp zone, for the hydrophobic tracer with the basic mesh. Figure 6.7(a) shows that the negative vertical velocities in this loop have a higher magnitude than the positive velocities. This indicates that there is reduced reattachment within the mixing loop. In the froth, the vertical velocities are generally positive (figure 6.10(a)), however there are negative velocities close to the lip of the cell, indicating that the tracer was detached from a bubble and lost to the pulp rather than being recovered to the concentrate. This is consistent with the results shown in 5 as the experiments with the basic mesh showed a lower recovery.

In general, with the basic mesh, the vertical velocities of the hydrophilic tracer are

similar to those of the hydrophobic tracer (figure 6.7(b)). The velocity through the mesh in the horizontal slice (6.12(b)), shows that the tracer again moves upwards through holes $D$, however with a lower magnitude than for the hydrophobic tracer. The hydrophilic tracer also has far fewer locations where it moves with a positive vertical velocity through the mesh, indicating that the particle drops more easily through the mesh than it moves upwards. In the froth, the tracer motion is generally positive (figure 6.10(a)), with less indication that the tracer drops off at the lip of the cell than the hydrophobic tracer. This suggests that, although the tracer often dropped from the pulp-froth interface, when it did enter the froth it is recovered to the concentrate. As this tracer is hydrophilic, the recovery of the tracer to the concentrate was through entrainment. In the unmodified cell, the hydrophilic tracer moves up the wall of the cell, but this is not the case with the basic mesh, the main positive motion of the hydrophilic tracer from the pulp to the froth occurs at the impeller and above holes $B$ (figure 6.7).

When the blocked mesh is used, the vertical velocity of the hydrophobic tracer in the pulp is very similar to that of the same tracer with the basic mesh (figure 6.7(a)), although again the mesh decreases the magnitude of the positive and negative velocities in the upper mixing loop relative to the unmodified cell. However, at $r = 25\,\mathrm{mm}$ the hydrophobic tracer velocity is positive, with the blocked mesh, just below holes $B$, whilst in the basic mesh it is still negative (figure 6.11(a)). This indicates that the blocked mesh improved the transfer of the hydrophobic particle through the mesh and into the froth and therefore to be recovered to the concentrate.

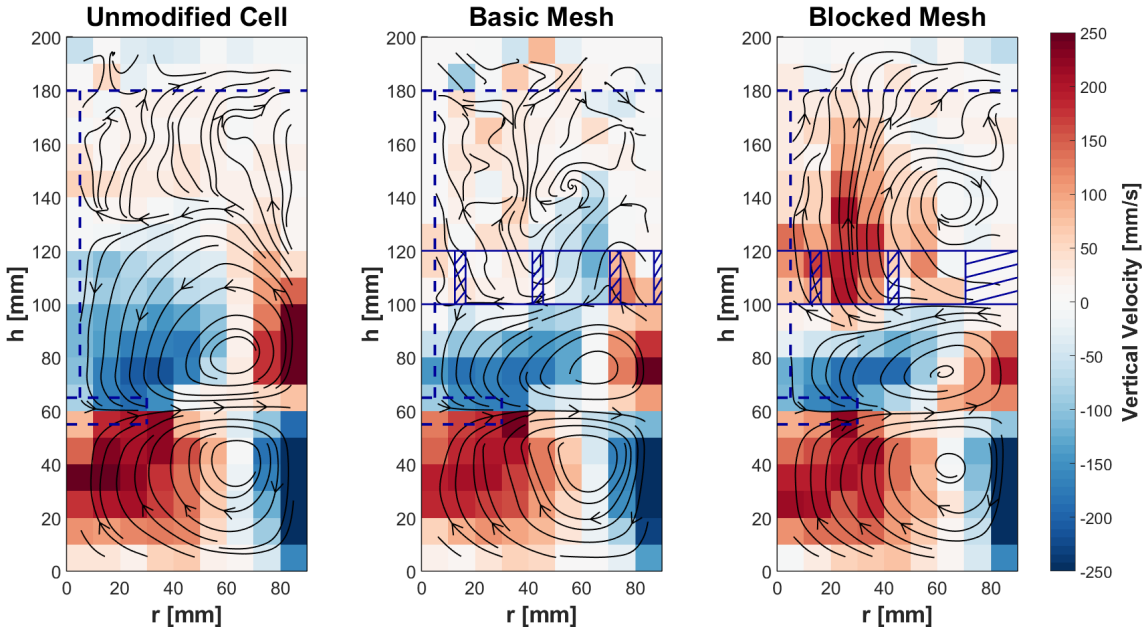
Unlike with the basic mesh, the hydrophobic tracer has a high positive vertical velocity through the majority of the holes of the mesh, with only occasional negative velocities towards the edge of holes $C$ (6.12(a)), this corresponds to the downwards motion of the third mixing loop above that hole. The lack of negative velocity of the tracer suggests that the blocked mesh substantially improved the chance that detached particles are reattached and subsequently recovered to the froth. Through the froth, the vertical velocity of the tracer is generally positive and high compared to the other two design cases (figure 6.10(a)). There is also not much evidence of negative motion close to the lip, suggesting good particle recovery. There is some negative velocity on top of the froth, however, this is close to the lip of the cell and so is unlikely to reduce recovery. This is consistent with the improved recovery relative to the basic mesh shown in chapter 5.

As previously discussed in section 6.2, the hydrophilic tracer with the blocked mesh

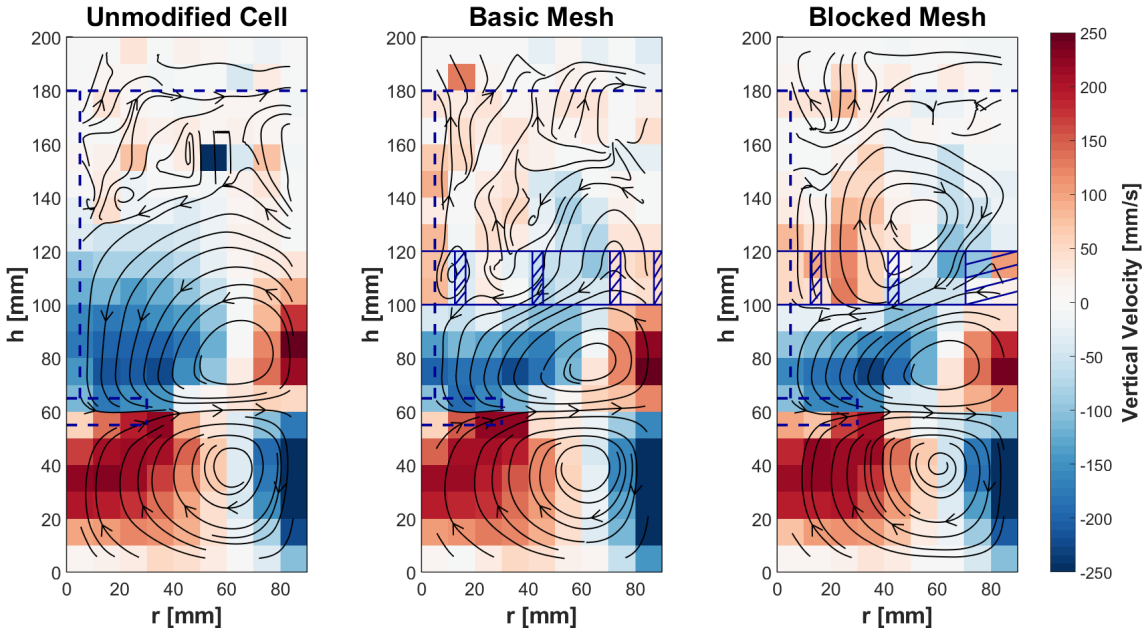
has a large third mixing loop above and through the mesh (figure 6.7(b)). This indicates that tracer rises through holes $B$ but is not easily recovered to the froth and so then drops back down into the pulp through holes $C$. The magnitude of the vertical velocities through holes $B$ and $C$ are generally similar (figure 6.12(b)), but the positive vertical velocities have a much lower magnitude than with the hydrophobic tracer suggesting that the recovery of the hydrophilic tracer through the blocked mesh was lower than for the hydrophobic.

The mixing loop in the secondary pulp zone, for the hydrophilic tracer, has similar streamlines to the ones in the primary pulp zone, however the vertical velocities are of a lower magnitude, suggesting that the secondary pulp zone is more quiescent than the primary. In the froth, the vertical velocity of the hydrophilic tracer is positive at $r = 25\,\mathrm{mm}$, however it is negative closer to the wall of the cell and in the overflow at the lip (figure 6.10(a)), the same tracer with the basic mesh has a positive velocity here. This indicates that the blocked mesh was better at preventing the recovery of the hydrophilic particle than the basic mesh.

It was shown in section 6.2, that both the hydrophobic and hydrophilic tracers in the unmodified cell showed swirl at the pulp-froth interface. In order to understand this further, figure 6.13 shows the azimuthal velocity component in the vertical slice for the different tracers and design cases. In this figure, positive is defined as the same direction in which the impeller was rotating. With either mesh inserted into the cell the azimuthal component of the velocity was very close to zero, showing that the secondary pulp zone, above both meshes, was more quiescent than the primary pulp zone, this demonstrates that the presence of the meshes helped to break down the swirl at the interface and therefore provide a more quiescent environment for particle transfer from the pulp to the froth.




(a) Hydrophobic tracer




(b) Hydrophilic tracer

**Figure 6.7:** Tracer vertical velocity within the cell for (a) the hydrophobic and (b) hydrophilic tracers. Blue shades are negative velocities, red are positive and the darker the colour represents high magnitudes. White corresponds to 0 vertical velocity.

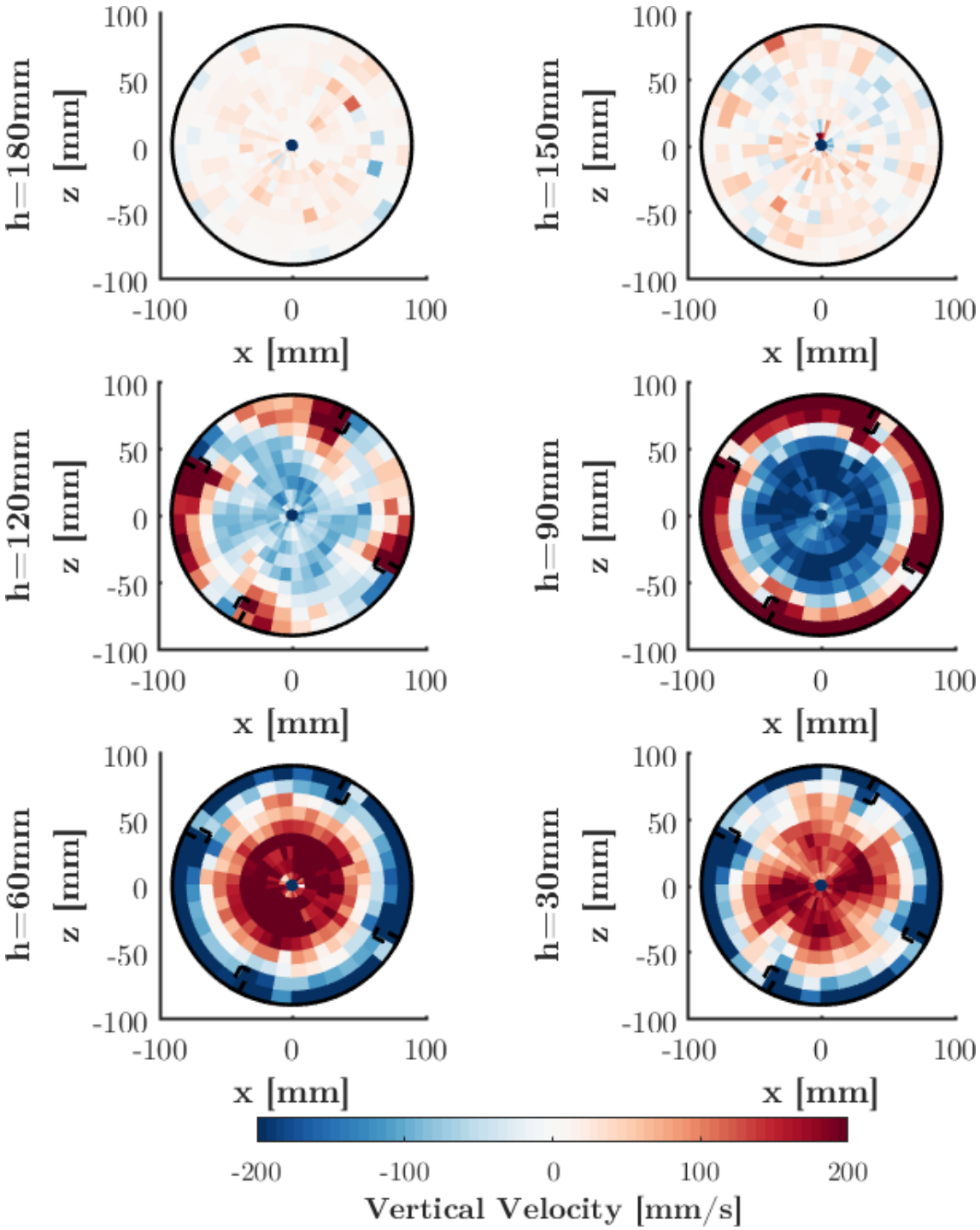



**Figure 6.8:** Vertical velocity of the hydrophobic tracer, in the unmodified cell, at different heights through the cell.

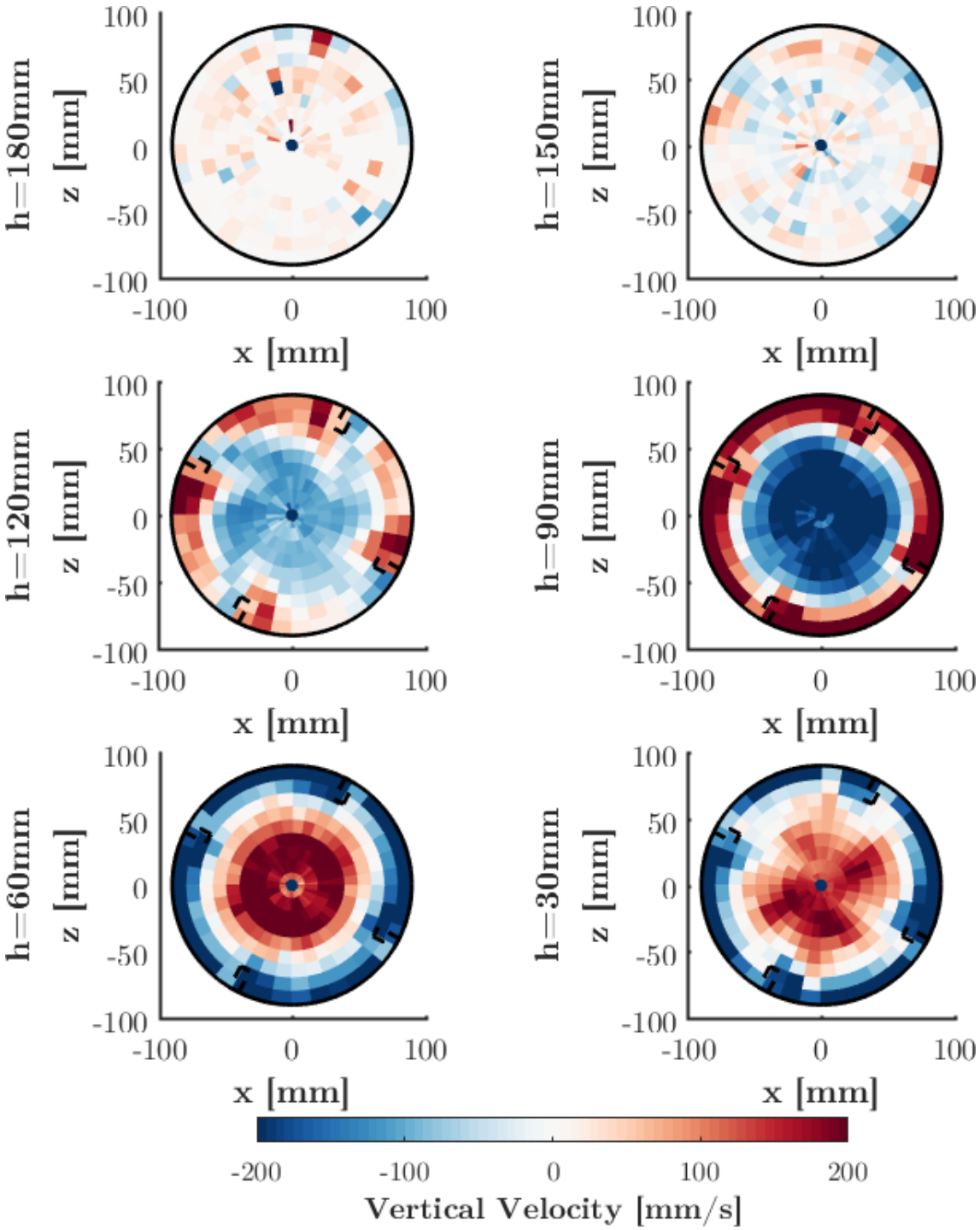
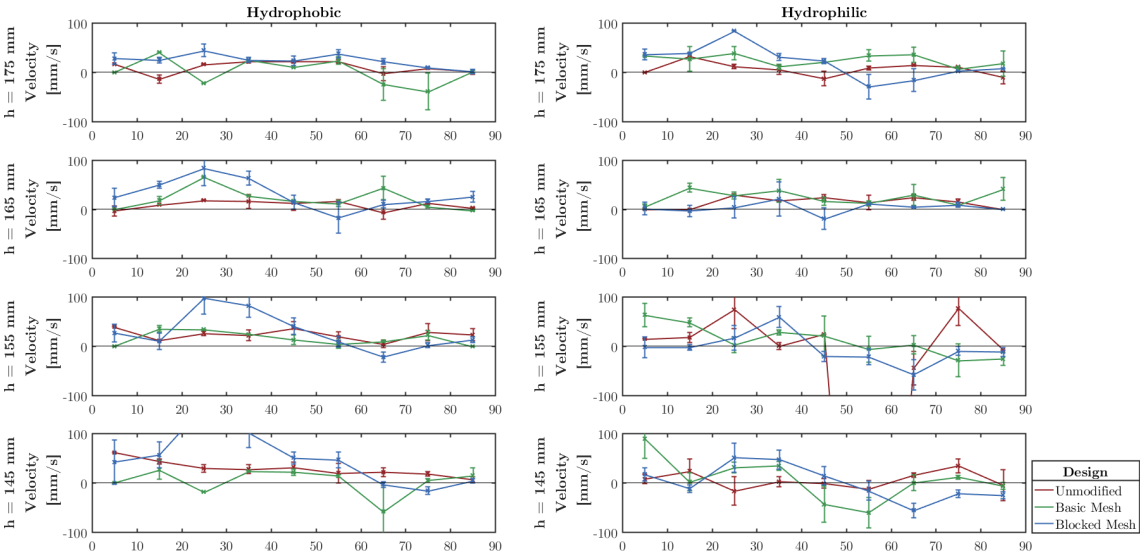
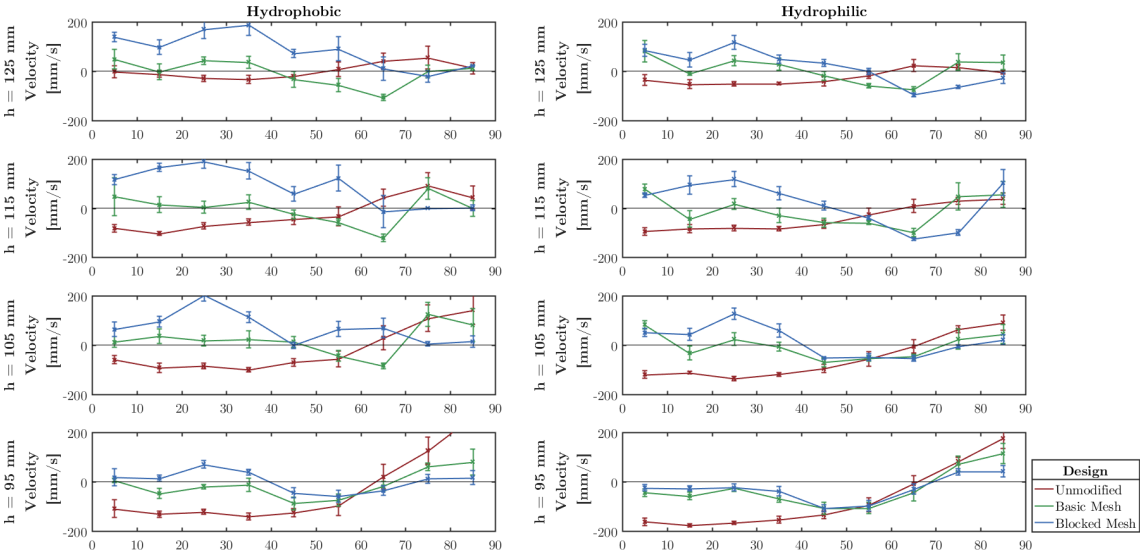



**Figure 6.9:** Vertical velocity of the hydrophilic tracer, in the unmodified cell, at different heights through the cell.

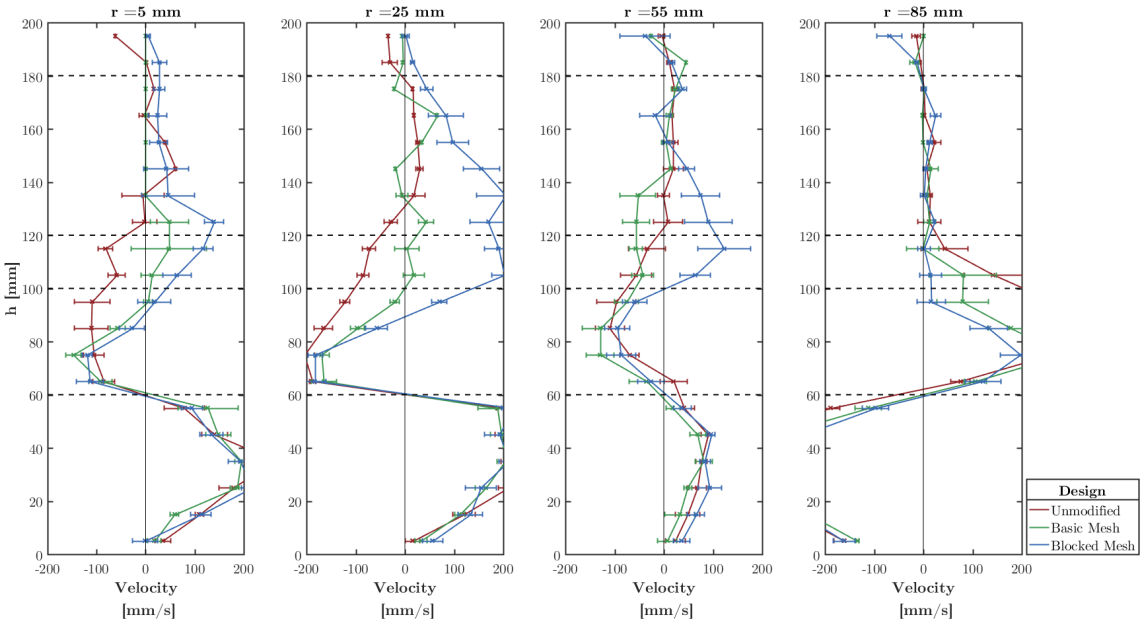



(a) Vertical velocity in the froth

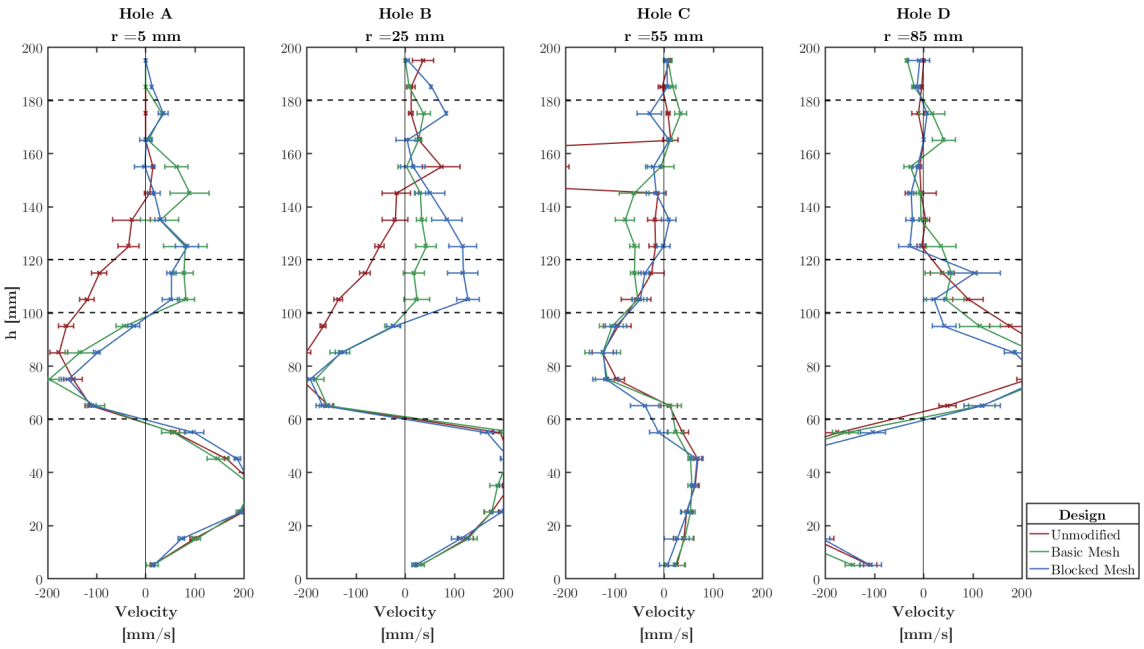



(b) Vertical velocity at the mesh

**Figure 6.10:** Plot of vertical velocity with radial location for different heights within the froth of the cell. Error bars are the standard error after averaging the value across 6 slices. The mesh is located between h=100 and h=120.

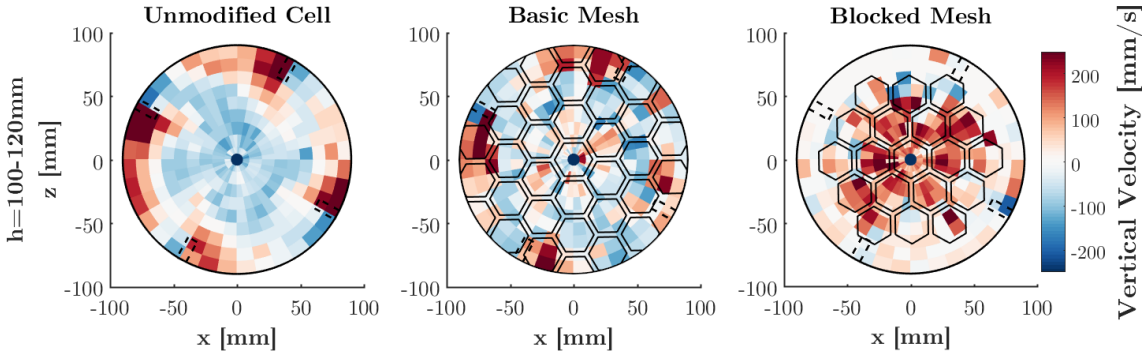



(a) Hydrophobic tracer

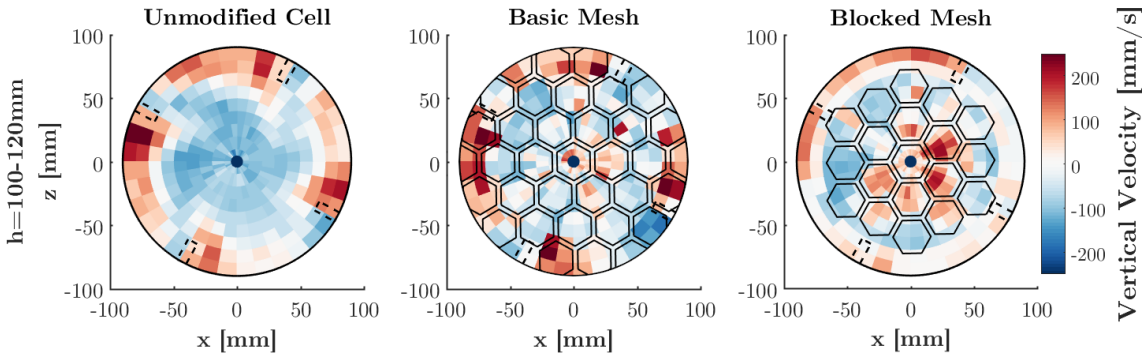



(b) Hydrophilic tracer

**Figure 6.11:** Plot of vertical velocity with height at different radii from the centre of the cell. Error bars are the standard error after averaging the value across 6 slices. The mesh is located between h=100 and h=120 mm.

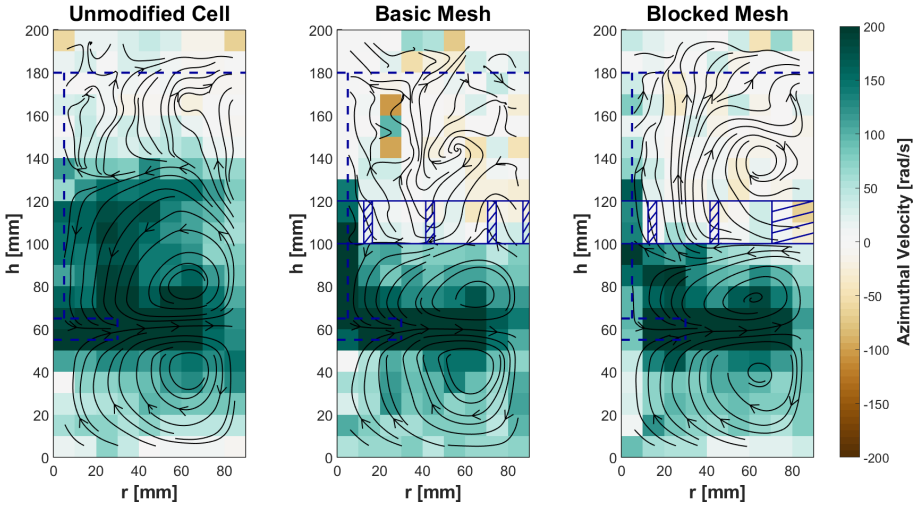



(a) Hydrophobic tracer

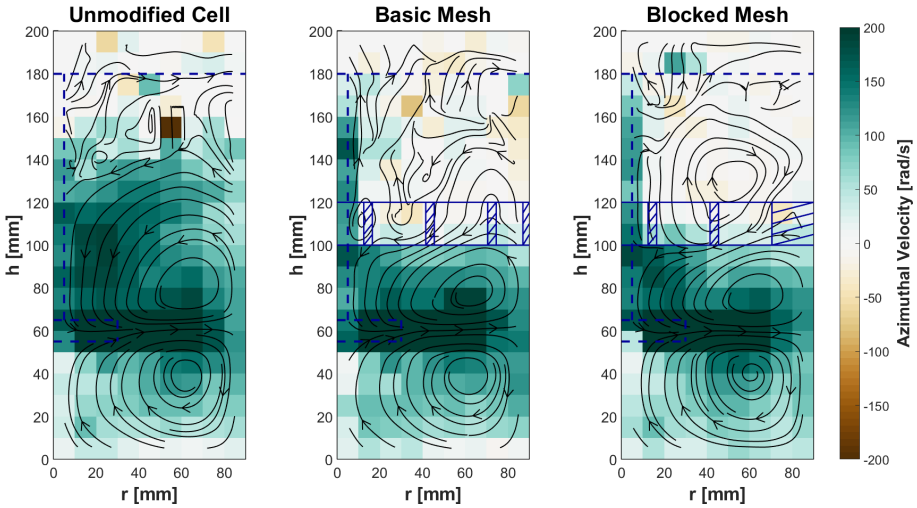



(b) Hydrophilic tracer

**Figure 6.12:** Horizontal slices of vertical velocity of different tracers though the meshes for the (a) hydrophobic tracer and (b) hydrophilic tracer. The location of the mesh is outlined in black.




(a) Hydrophobic tracer




(b) Hydrophilic tracer

**Figure 6.13:** Azimuthal velocity component of the tracer in the froth for the (a) hydrophobic and (b) hydrophilic. Positive is defined as the same direction as the impeller rotation.

## 6.4 Occupancy

The occupancy of the hydrophobic tracer and hydrophilic tracer for each of the three design cases is shown in figure 6.14. As mentioned in section 3.7.3, in this work occupancy is calculated as the total length of time the tracer spent in a voxel as a proportion of the total length of time the tracer spent in the cell normalised for the volume of the voxel. A higher occupancy indicates areas where the tracer spent a larger proportion of time, and hence shows paths the tracer took more frequently, or where the tracer moved more slowly. The difference between the two can be determined by looking at the data in conjunction with the velocities discussed in section 6.3. In a similar way to the vertical velocities, profiles of the change in occupancy with radius and height are shown in figures 6.15 and 6.16. The horizontal slices of occupancy at a height of $120\,\mathrm{mm}$ are shown in figure 6.17; this occupancy is calculated as a proportion of the total time the tracer spends in this slice, rather than the whole cell, to obtain a better understanding of how the tracer is moving through different holes in the mesh.

In figure 6.14(a), the occupancy of the hydrophobic tracer, in the unmodified cell, is seen to be relatively constant throughout the pulp (below a height of $140\,\mathrm{mm}$). There is a higher occupancy at the bottom of the cell below the impeller, this is expected as this is a dead zone in the mixing loops. In the froth, there are two distinct tracks through the froth, at $r = 20{-}40\,\mathrm{mm}$ and $r = 70{-}90\,\mathrm{mm}$, where there is a higher occupancy (figure 6.15(a)). The first of these two areas is similar in velocity to the majority of the froth, suggesting that this was a path that the tracer more frequently took through the froth to overflow. The high occupancy at the wall, however, corresponds to a very slow velocity suggesting that the velocity was the cause of the increased occupancy.

In the unmodified cell (figure 6.14(b)), the hydrophilic tracer clearly spends more time in the lower mixing loop, especially below the impeller, than the hydrophobic tracer. The hydrophilic tracer has a much lower occupancy in the froth zone of the cell than the hydrophobic tracer (figure 6.15(a)). The lower occupancy in the froth and higher occupancy in the pulp indicate that the hydrophilic tracer was far less easily recovered than the hydrophobic one. Figure 6.15(a) shows that there is a small increase in occupancy at radii greater than $60\,\mathrm{mm}$, where there are also positive velocities. This indicates that the hydrophilic tracer was recovered more frequently at the wall of the cell showing that there was an increased water flowrate here.

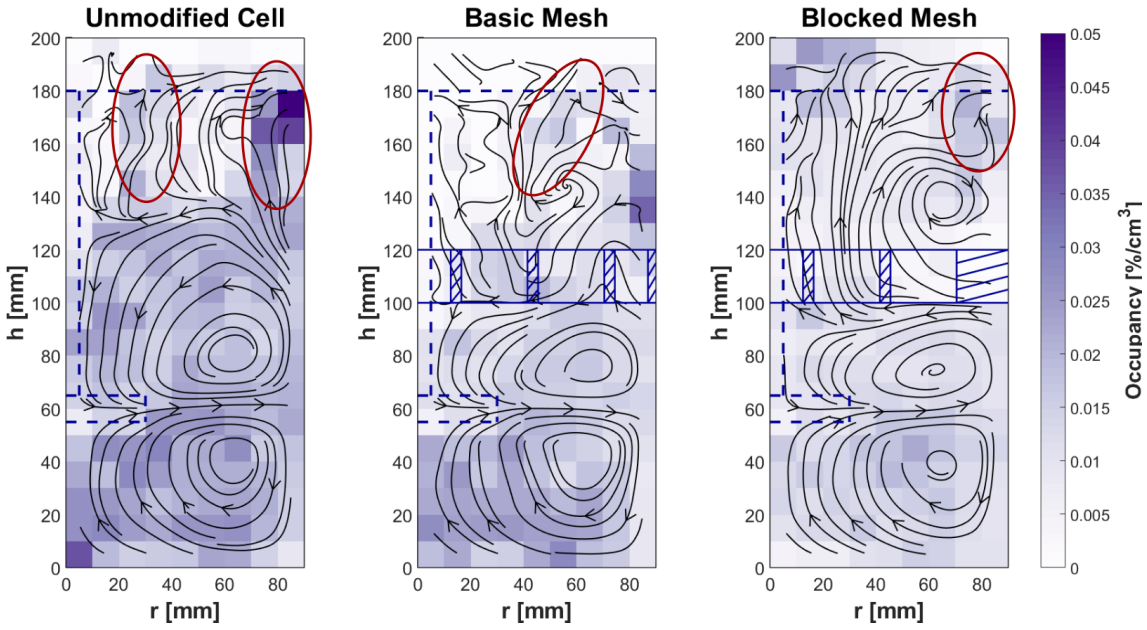
Figure 6.14(a) shows the occupancy of the hydrophobic tracer when the basic mesh was inserted into the cell. The occupancy in the primary pulp zone is slightly lower than in the pulp of the unmodified cell (figure 6.15(b)), suggesting that the hydrophobic tracer spent less time in the primary pulp zone with the basic mesh than in the unmodified cell. When travelling through the mesh, the tracer has a slightly lower occupancy through holes $D$ than the other holes of the basic mesh, however this is probably due to the increased velocity through this hole (figure 6.15(b)). The horizontal slice of occupancy, for the hydrophobic tracer, through the basic mesh (figure 6.17(a)) shows that there is a slight increase in occupancy through some holes in ring $C$, where the tracer motion is negative, however the majority of the holes have similar occupancy values. This indicates that the tracer moved up through the mesh as frequently as it moved down. Above holes $D$ there is an increase occupancy (figure 6.14(a)), however this corresponds to a very slow velocity so suggests that the tracer may have got stuck in this area. In the froth, the tracer moves through a clear path at a radius of approximately $40\,\mathrm{mm}$ (figure 6.14(a)), showing that there was a preferential path that the tracer takes through the froth. This path starts at the top of the third mixing loop, suggesting that this loop was promoting transfer from the pulp to the froth.

The hydrophilic tracer, with the basic mesh, has similar levels of occupancy in the pulp as the hydrophobic tracer with the same mesh (figure 6.14(b)), suggesting that both tracers have similar recoveries through the mesh. The horizontal slice through the mesh (figure 6.17(b)) shows little variation in occupancy across the different mesh holes, with only some higher values in ring $C$, corresponding to locations where there was negative vertical velocity. There are two areas of high occupancy in the froth (figure 6.15(a)), the first is at a radius of approximately $30\,\mathrm{mm}$ which shows a clear path from the secondary pulp zone to the froth and the overflow. The second area is at a radius of approximately $70\,\mathrm{mm}$ and is slightly higher than the first, this shows another path the tracer commonly took to the overflow, unlike with the hydrophobic tracer this high occupancy close to the wall was not caused by slow velocities. This suggests increased water flow at the wall of the cell. There is much less difference in the occupancy of the hydrophobic and hydrophilic tracers for the basic mesh than in the unmodified cell.

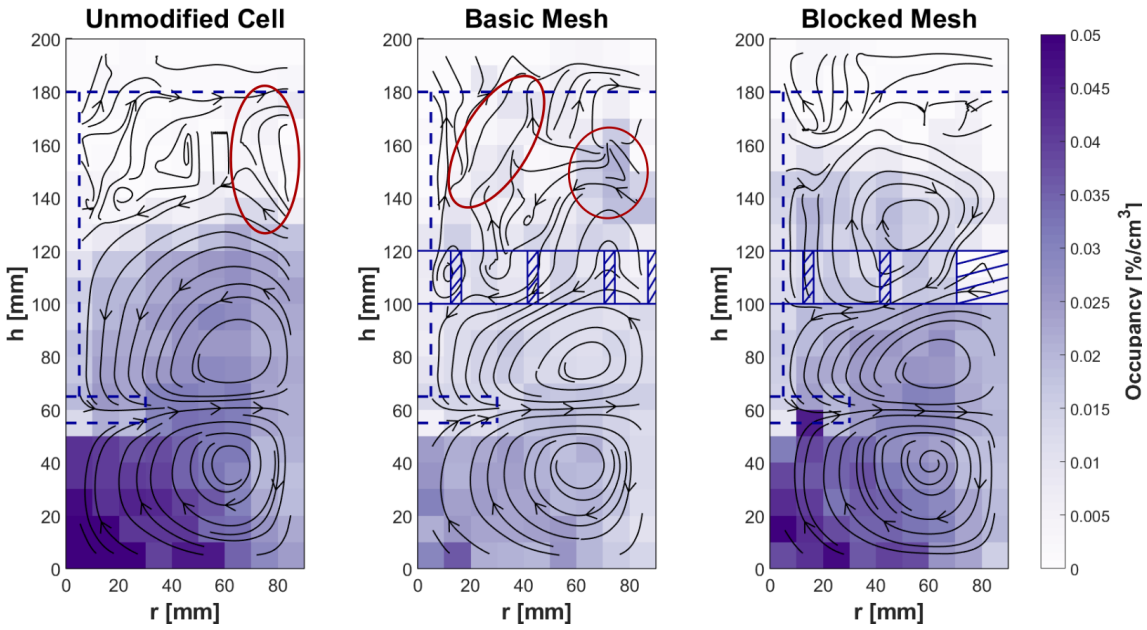
The occupancy of the hydrophobic tracer, with the blocked mesh, is relatively constant throughout the cell (figure 6.14(a)). The occupancy of this tracer in the primary pulp zone, below the mesh, is generally lower than in both of the other designs (figure 6.16),

indicating that the tracer spends less time in the pulp. The horizontal slice through the mesh (figure 6.17(a)), shows that the occupancy is significantly higher in holes $B$ than it is through holes $C$. The high occupancy in holes $B$ corresponds to a high velocity, indicating that the tracer moved more frequently through this hole. In comparison to figure 6.12, the tracer often had negative vertical velocities in holes $C$ and so the low occupancy in this hole indicates that there is a good recovery of the tracer from the pulp to the froth and that if the tracer drops through the mesh it does not happen frequently. The occupancy of the hydrophobic tracer, with the blocked mesh, is fairly constant throughout the froth (figure 6.15(a)) and there is no preferential path that the tracer moves through the froth. There is, however, a slight dip in occupancy at $R = 45\,\mathrm{mm}$, which corresponds to a higher vertical velocity. There is a slight increase in occupancy just below the lip of the cell, close to the wall, but this is caused by a slightly lower velocity. There is also a high occupancy at the top of the froth, close to the impeller which indicates that this tracer often got stuck in the stagnant zone around the impeller.

Interestingly, the occupancy of the hydrophilic tracer with the blocked mesh is very similar to the unmodified cell (figure 6.14(b)), with a high occupancy in the pulp and extremely low occupancy in the froth. The horizontal slice through the mesh (figure 6.17(b)) shows that the occupancy is constant across all the holes, with no clear preference for a particular ring of holes. The occupancy is also fairly constant throughout the whole of the third mixing loop, in the quiescent secondary pulp zone, indicating that the tracer was equally likely to be moving upwards as it was downwards. The occupancy in the froth is low, very similar to that of the unmodified cell (figure 6.15(a)), with a small increase at a radius of approximately $70\,\mathrm{mm}$, however, unlike in the unmodified cell this increase in occupancy corresponds to a negative velocity and therefore suggests that the tracer frequently dropped from the top of the froth back into the cell rather than overflowing the cell. It is important to note that the large difference in tracer occupancy in the froth between the hydrophobic and the hydrophilic tracers explains the low magnetite entrainment factor with the presence of the blocked mesh shown in chapter 5.

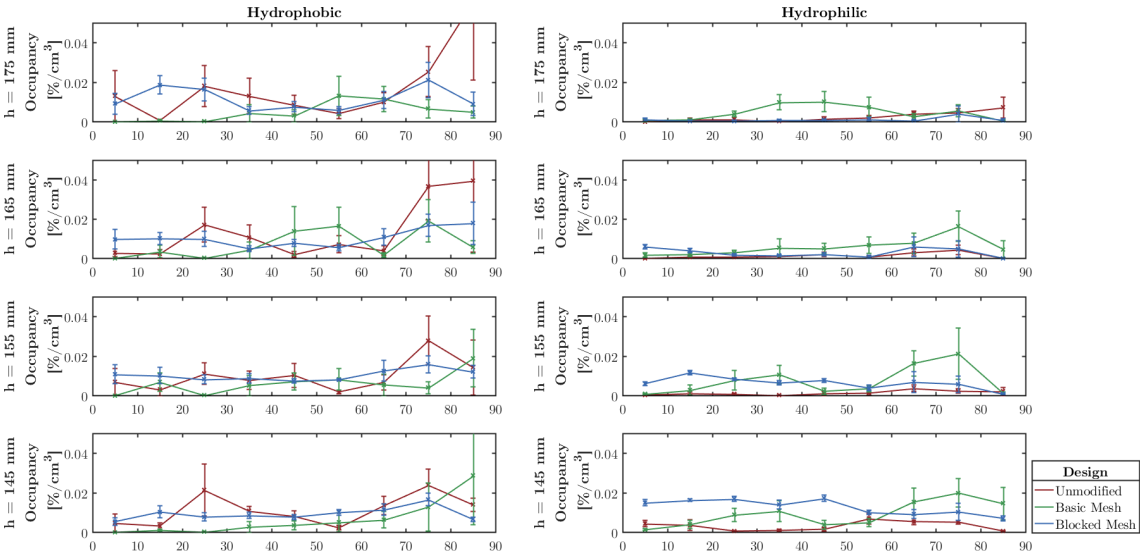



(a) Hydrophobic tracer

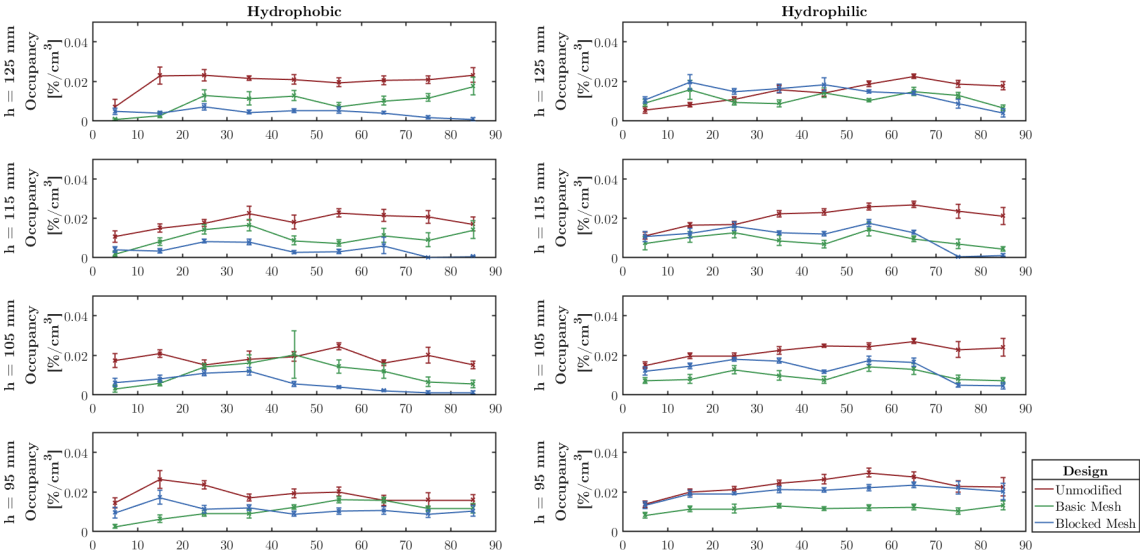



(b) Hydrophilic tracer

**Figure 6.14:** Tracer occupancy within the cell for (a) the hydrophobic and (b) hydrophilic tracers. Both tracer types are $500\,\mu\mathrm{m}$ in diameter.occupancy calculated by totalling the time the tracer spent each voxel then normalising by total length of time the tracer spent in that slice and normalised by the volume of the voxel. Darker blue shades represent higher occupancys i.e. voxels where the tracer spent a higher proportion of time.

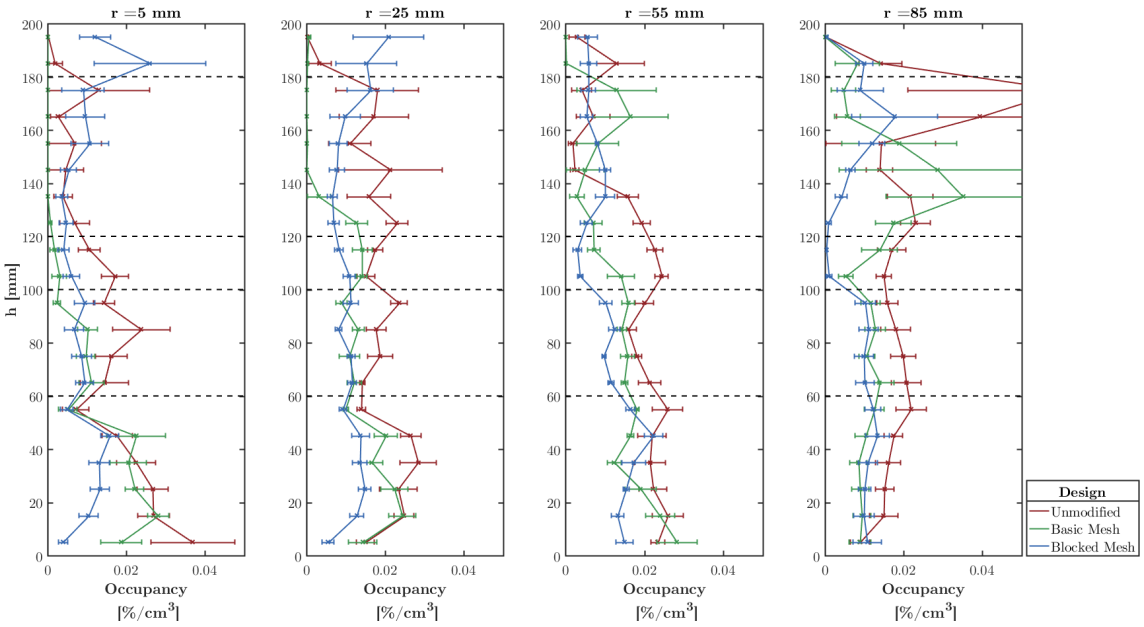



(a) Froth occupancy

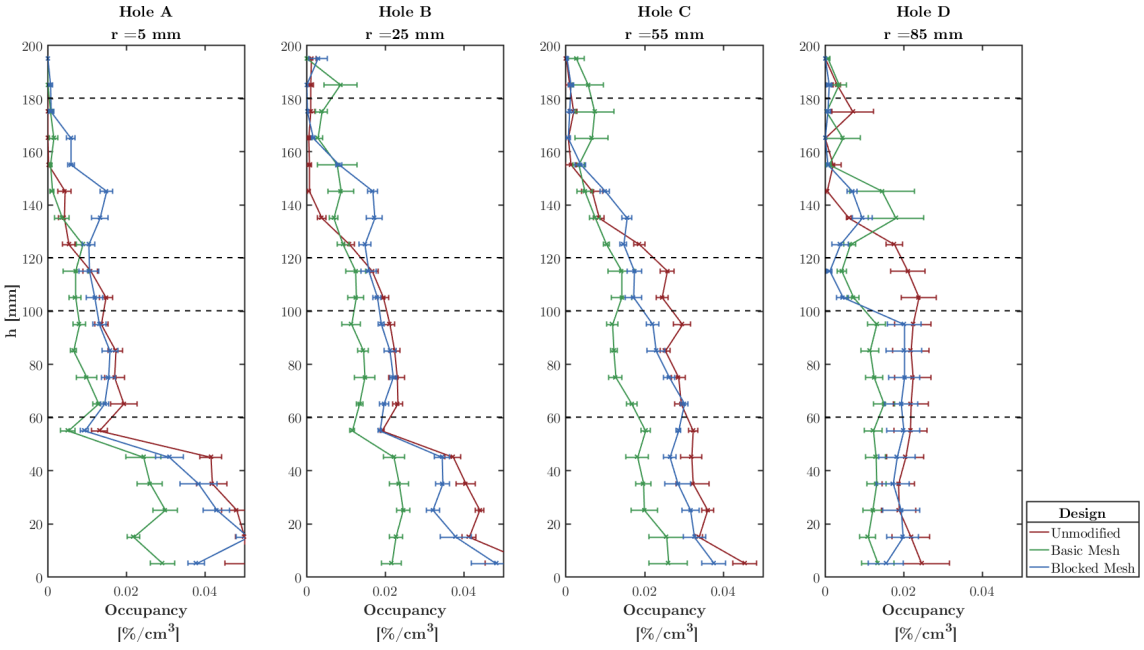



(b) Mesh occupancy

**Figure 6.15:** Plot of occupancy with radial location for different heights within the froth of the cell. Error bars are the standard error after averaging the value across 6 slices. The mesh is located between h=100 and h=120 mm.

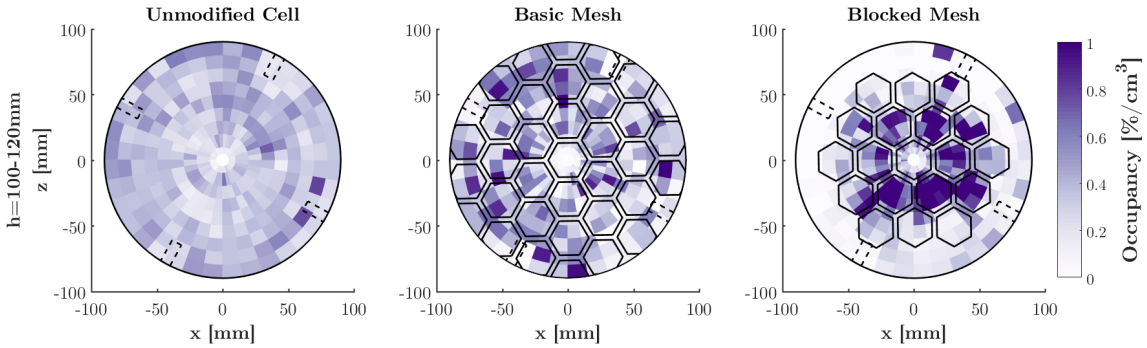



(a) Hydrophobic tracer

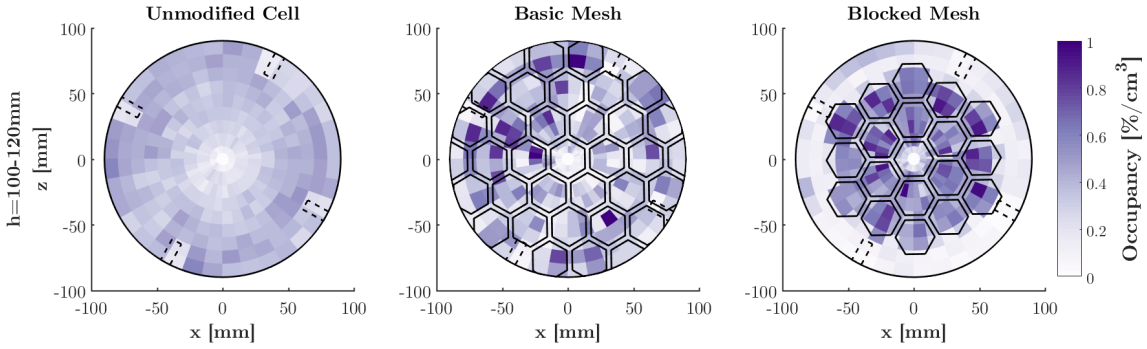



(b) hydrophilic tracer

**Figure 6.16:** Plot of occupancy with height at different radii from the centre of the cell. Error bars are the standard error after averaging the value across 6 slices. The mesh is located between h=100 and h=120.




(a) Hydrophobic tracer, $500\,\mu$m




(b) Hydrophilic tracer, $500\,\mu$m

**Figure 6.17:** Horizontal slices of occupancy of different tracers though the meshes; (a) hydrophobic tracer, (b) hydrophilic tracer. The location of the mesh is outlined in black.

## 6.5 Discussion

Investigating the flow of both a hydrophobic and a hydrophilic tracer in the unmodified cell allowed an understanding of hydrodynamic behaviour of both valuable and gangue minerals in this system. The streamlines of the tracers showed that the motion of both tracers was very similar in the pulp. It was clear from the streamlines of the hydrophilic tracer that the pulp-froth interface in the unmodified cell was located at a height of approximately $140\,\mathrm{mm}$. In the froth, however, there was a clear difference in flow patterns between the two tracers. These show that the hydrophobic tracer had good upwards motion through the froth and towards the launder into the overflow of the cell, yet this was not the case for the hydrophilic tracer. The difference between the two tracers was also clear from the vertical velocity data, where the hydrophobic tracer had positive vertical velocities throughout the froth, yet the hydrophilic data only had positive velocities close to the impeller and the wall of the cell. The occupancy data showed that the hydrophobic tracer occupied the pulp less frequently than the hydrophilic and is therefore floating more frequently. The hydrophobic tracer showed a clear path through the froth, that was frequently taken by the tracer. The occupancy of the hydrophilic tracer, however, was generally low across the froth, as would be expected for gangue material. The hydrophilic tracer had a slight increase in occupancy close to the wall of the cell which indicates that there was an increased water flowrate here. The differences in the velocities and occupancy of particles in the froth between the hydrophobic and hydrophilic tracers indicate that there was a good separation efficiency in the unmodified cell. The streamlines observed in the horizontal slice, and the azimuthal velocity component, showed that there was a high level of swirl, for both tracers, at the pulp-froth interface. The swirl is indicative of a non-quiescent environment which is not conducive to good recovery.

The presence of either mesh in the cell was shown to have the effect of compressing the upper mixing loop. In addition, the velocities of the tracers in this loop had a lower magnitude in comparison to the unmodified cell. Both meshes also resulted in a shallower froth, with the pulp-froth interface at a height of $160\,\mathrm{mm}$, and reduced evidence of the swirl at the pulp-froth interface. This resulted in a secondary pulp zone above the meshes that was more quiescent than the pulp below the meshes, which would be expected to translate into an improved recovery from the pulp to the froth. These different zones can be seen in the schematic in figure 6.18. This change in froth depth explains the air recovery

results presented in chapter 5 where, with either mesh in the cell the highest air recoveries were observed at the lowest air rate, yet in the unmodified cell the highest air recovery was observed at the highest air rate. This is because with shallow froths, higher air recoveries are expected at lower air rates, yet with deeper froths, higher air recoveries are expected at higher air rates (Hadler et al., 2012). As well as the effect that froth depth has on the air recovery, it also has an impact on the grade and recovery of the concentrate. A shallower froth will be less efficient at "cleaning" the concentrate and will therefore result in an improved recovery over a deeper froth yet a lower grade. However, this is not what the flotation performance results from chapter 5 indicated. In fact for the results from the basic mesh compared to the unmodified cell the opposite was true, in that whilst the froth depth decreased, the grade increased and the recovery decreased. In addition, for the results from the blocked mesh compared to the unmodified cell, despite the reduction in froth depth, there was little impact in flotation performance at the superficial gas velocity used for these PEPT studies. This indicates that it was not the effect of reducing the froth depth that impacted on flotation performance, but that the design of the mesh itself was the key influence and that therefore the secondary pulp zone was instrumental in altering the flotation performance in the cell. It would be interesting to investigate this further by directly measuring froth depth during experimentation potentially using a guided radar level sensor. However, consideration would need to be taken of how, at the small scale of this cell, inserting instruments into the froth would alter the properties of the froth. It would also not be possible to measure in this way during PEPT experimentation. An alternative would be attempting to measure the froth depth by measuring with a ruler from the outside of the cell, but there would be a lack of precision in this method.

The use of the basic mesh had a detrimental effect on the flow of the hydrophobic tracer. The streamlines were more chaotic than in the unmodified cell and there were negative velocities close to the lip of the cell, indicating that the tracer tended to drop off, back into the pulp rather than being recovered to the concentrate. There was a small mixing loop in the secondary pulp zone for the hydrophobic tracer, however this was not well developed. This loop, however, was not present for the hydrophilic tracer as there is no reattachment. Both tracers moved up through holes $A$, $B$ and $D$ and down through holes $C$, with the negative velocity being faster than the positive velocities. The velocity in holes $D$ was also a higher magnitude than the other positive velocities in the mesh, suggesting that there was a higher flowrate here. There was very little variation in

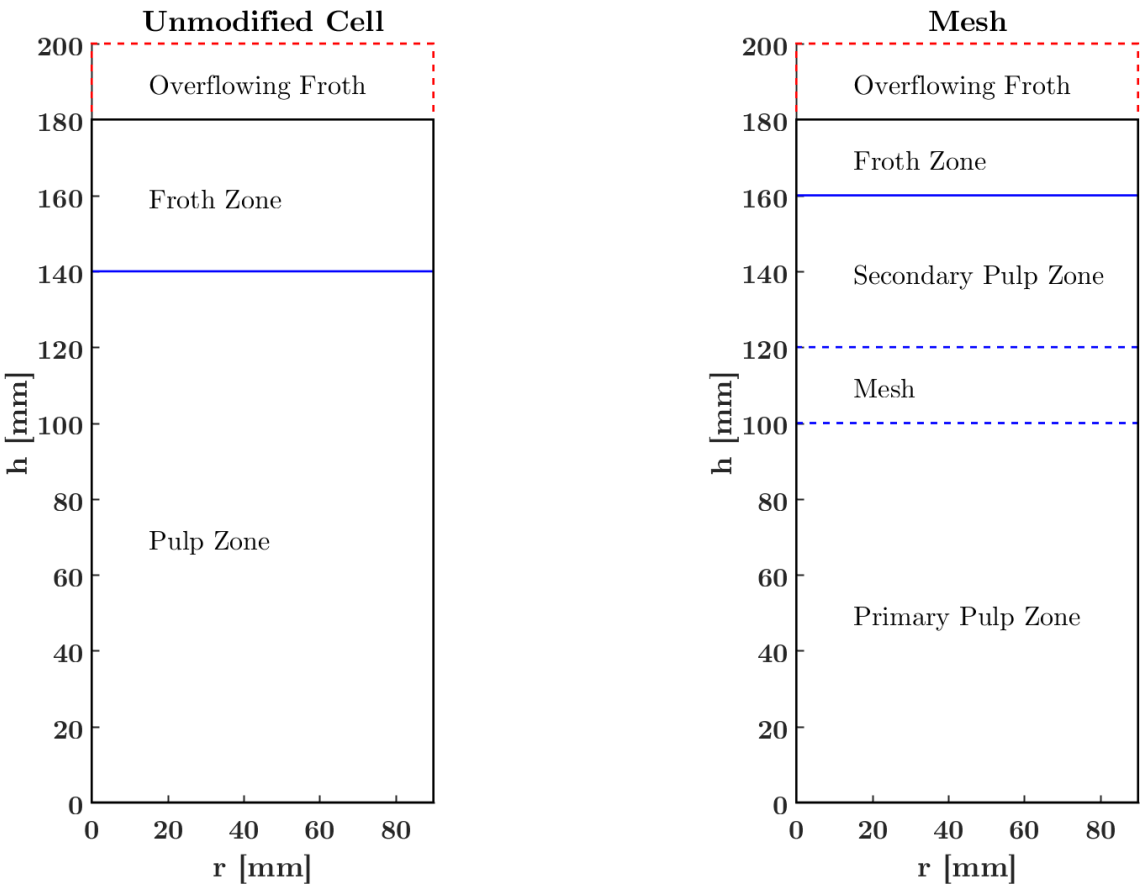



**Figure 6.18:** Schematics of the different zones in the unmodified cell and when a mesh is inserted.

occupancy, of either tracer, across the holes of the basic mesh, indicating that there was no preferred path through the mesh. The occupancy indicated that there was a clear path that the hydrophobic tracer preferentially moved along, through the centre of the froth. The hydrophilic tracer, however, had a high occupancy close to the wall of the cell, indicating that there was preferential flow here.

Blocking in the outer holes ($D$) of the mesh resulted in a well developed third mixing loop, in the secondary pulp zone, for both the hydrophobic and the hydrophilic tracers. For the hydrophobic tracer this was a medium sized loop above the blocked part of the mesh and holes $C$. This mixing loop promoted reattachment of any detached particles, as there were very few instances of particles having negative vertical velocities through the mesh. There was also a good positive flow of the hydrophobic tracer up through holes $B$, where there was also a higher occupancy, to the froth and then to the overflow. The positive vertical velocity of the tracer actually started at the top of the second mixing loop, below holes $B$, indicating that the blocked mesh was strongly aiding in the recovery of the hydrophobic tracer. Unlike in the unmodified cell or with the basic mesh, there was

no clear path that this tracer takes through the froth; instead the occupancy was constant throughout. There was, however, an increase in occupancy at the top of the froth, close to the impeller, where the tracer was likely stuck in a stagnant section of the froth.

For the hydrophilic tracer with the blocked mesh, the third mixing loop was much larger and more developed than for the hydrophobic tracer, and it extended through holes $B$ and $C$ of the mesh. This loop was similar to the mixing loops in the primary pulp zone, however the velocities were much lower. There was a low occupancy of the hydrophilic tracer in the froth suggesting that there was little transfer from this mixing loop into the froth, and therefore a reduced recovery of the hydrophilic tracer. There was an area of slightly higher occupancy just below the lip of the cell, for the hydrophilic tracer, which corresponds to negative vertical velocities. This indicates that the tracer was lost to the pulp rather than being recovered to the concentrate by entrainment , despite the increased water recovery shown in chapter 5. This is a very important finding, since it explains the relatively low entrainment factor for this design in chapter 5. Like for the unmodified cell, there was a clear difference in the flow of the hydrophobic and hydrophilic tracers with the blocked mesh indicating that there is a good separation efficiency. This has important implications for industry, as being able to implement a design modification similar to the blocked mesh would potentially improve the flotation performance and reducing entrainment with an easy to implement and low capital cost design. The presence of the quiescent secondary pulp is also significant as that is likely to be conducive to successful coarse particle flotation.

In chapter 5, it was seen that when using the blocked mesh there was a substantial increase in water recovery to the concentrate, yet there was a lower entrainment factor. Whilst the PEPT data analysis has provided an explanation for the reduced entrainment, it is not as clear what caused the increased water recovery. Potentially it is due to the reduced froth depth, as shallower froths are known to be wetter than deeper froths. However, it would therefore be expected that the use of both mesh designs would have resulted in increased water recovery relative to the unmodified case, yet this was not seen to be the case for the basic mesh. It is possible that this was caused by the physical barrier introduced by blocking in the holes directing the flow of water from the pulp upwards at the centre of the cell and then preventing the water draining through the froth and back into the pulp zone. It would therefore be interesting to investigate this further to fully understand how the blocked mesh is altering the flow within the flotation cell and to use this information

to develop the mesh design further. This could be done using numerical simulations with the data already collected from PEPT and from other more fundamental studies on froth flotation. In addition it would be beneficial to conduct more PEPT experimentation with the design modifications using a neutrally buoyant and uncoated, naturally hydrophilic tracer that would provide a better more direct analogy to the water movement within the flotation cell than the magnetite coated tracer used in this study. Performing positron emission tomography (PET) experiments, with a liquid tracer would also be valuable to directly assess liquid behaviour to understand this phenomenon further.

## 6.6 Conclusions

This chapter has presented the results from using positron emission particle tracking (PEPT) to investigate the effects that two design modifications have on the flow patterns of a hydrophobic and a hydrophilic tracer in a two-species flotation system. These experiments have been instrumental in furthering the understanding of how the different design modifications affect flotation performance.

The analysis of PEPT data for both a hydrophobic and a hydrophilic tracer of the same size, for each of the design modifications, has shown that the presence of the meshes compresses the mixing loops in the pulp and reduces the froth depth, resulting in a secondary pulp zone above the mesh, which has been shown to be more quiescent. A third mixing loop was seen in this secondary pulp zone, which was better developed for the blocked mesh than for the basic mesh. The presence of the basic mesh has a detrimental effect on the flow of the hydrophobic particle, which reduces the recovery. On the other hand, the blocked mesh has been shown to actively improve the reattachment of detached hydrophobic particles and to prevent the transfer of the hydrophilic tracer to the froth, therefore improving the valuable recovery with a good separation efficiency. The data from the hydrophilic tracer show that blocking in the outside holes of the mesh also has a good effect on reducing the water flowrate at the cell wall. This highlights that whilst the basic mesh is not an optimal design for improving flotation in this system, the design can easily be improved, simply by blocking in the outside holes of the mesh.

One of the key purposes of the meshes was to provide a more quiescent environment at the pulp-froth interface with the aim of improving coarse particle recovery. The reduction of swirl at the interface demonstrates that the meshes were creating a quiescent

environment, however there is no indication of the effects of particle size. This has previously been shown, from the literature and the results from chapter 4, to be an important consideration. The tracers investigated so far, in this work and in other PEPT flotation research in the literature, have all been one size. It is therefore interesting to further investigate these design modifications with differently sized tracers.

# Chapter 7

# Analysing the effect of different flotation cell retrofit design modifications on different particle sizes

## 7.1 Introduction

In Chapter 6, two design modifications: the basic mesh and the blocked mesh, were investigated using positron emission particle tracking (PEPT) with two different tracers: one hydrophobic and one hydrophilic. The results from the analysis of the PEPT data showed that the presence of either mesh design compressed the upper mixing loop in the primary pulp zone and created a secondary, more quiescent, pulp zone above the mesh which reduced the swirl at the pulp-froth interface. The use of the blocked mesh was also shown to result in a well formed third mixing loop forming above the mesh, in the secondary pulp zone, for both tracers. This extra mixing loop resulted in better reattachment of the hydrophobic tracer, and prevented the hydrophilic tracer from being recovered. This improved the separation efficiency of the system relative to the basic mesh and also reduced the entrainment of the hydrophilic tracer. A similar mixing loop was also seen for the hydrophobic tracer with the basic mesh, however it was not as well developed as with the blocked mesh.

The primary purpose of the retrofit design modifications is to introduce a quiescent

zone in the pulp, which results in a reduction in particle detachment. Whilst the results from chapter 6 showed that this was the case, only one size of tracer was used. The meshes have been designed with the purpose of coarse particle flotation in mind, and so it is interesting to understand how the design modifications affect the flow of different particle sizes.

In chapter 5 the particle size distributions of the concentrate were analysed to gain an initial understanding on the effect that the design modifications were having on the flotation performance of different particle sizes. This understanding can be developed further by utilising PEPT with different sizes of hydrophobic tracer. This thesis is the first time the different sizes of PEPT tracers have been used. In this chapter, the results from PEPT experiments with three different sizes of tracer ($400\,\mu\mathrm{m}$, $500\,\mu\mathrm{m}$ and $600\,\mu\mathrm{m}$) are discussed, in order to provide an understanding of how the quiescent secondary pulp zone, shown in chapter 6, affects the flotation of coarse particles of varying sizes.

The method for analysing the PEPT data is the same as was used in chapter 6 and is described in detail in section 3.7.3. As with the discussion in chapter 6, the holes shall be referred to as $A$, $B$, $C$ and $D$ from the centre of the cell to the wall (figure 6.1). The data from PEPT experiments using the $500\,\mu\mathrm{m}$ tracer are discussed in extensive detail in chapter 6 and so are only discussed in the present chapter as a comparison to the other two tracer sizes.

## 7.2 Bulk Tracer Flow

The streamlines of the different tracers for each of the design cases in a vertical slice through the cell (figure 7.1) give an understanding of the bulk flow of the tracer throughout the cell. The horizontal slices throughout the unmodified cell, for all three tracers, are shown in figures 7.2 - 7.4, and horizontal slices of streamlines through the mesh, and just above the mesh are shown in figures 7.5 and 7.6.

In the unmodified cell, the flow of the $400\,\mu\mathrm{m}$ tracer (figure 7.1(a)) is mostly similar to that of the $500\,\mu\mathrm{m}$ tracer (figure 7.1(b)). For both of these tracers the motion in the bulk of the froth (above a height of $140\,\mathrm{mm}$) is generally upwards with little evidence of tracer drop off or lateral motion of the tracer. This indicates that, in both cases, there is a good recovery of the particle from the pulp to the froth. On the other hand, the flow of the

$600\,\mu\mathrm{m}$ tracer (figure 7.1(c)) is remarkably different to the other two tracer sizes. There are fewer locations in the froth and the streamlines show the tracer dropping off from the pulp-froth interface back into the pulp of the cell indicating that the $600\,\mu\mathrm{m}$ tracer had a worse recovery than the other two tracer sizes.

The streamlines in horizontal slices through the unmodified cell for each of the three tracer sizes (figures 7.2 - 7.4) show that there is little variation in the motion of the different tracer sizes in the pulp. As was previously discussed in chapter 6, the $500\,\mu\mathrm{m}$ tracer shows swirl well into the froth phase at a height of $150\,\mathrm{mm}$ (figure 7.3). Figure 7.2 shows that this is also the case for the $400\,\mu\mathrm{m}$ tracer, however to a lesser extent. On the other hand, figure 7.4 shows that there is very little presence of the $600\,\mu\mathrm{m}$ tracer in the froth at all.

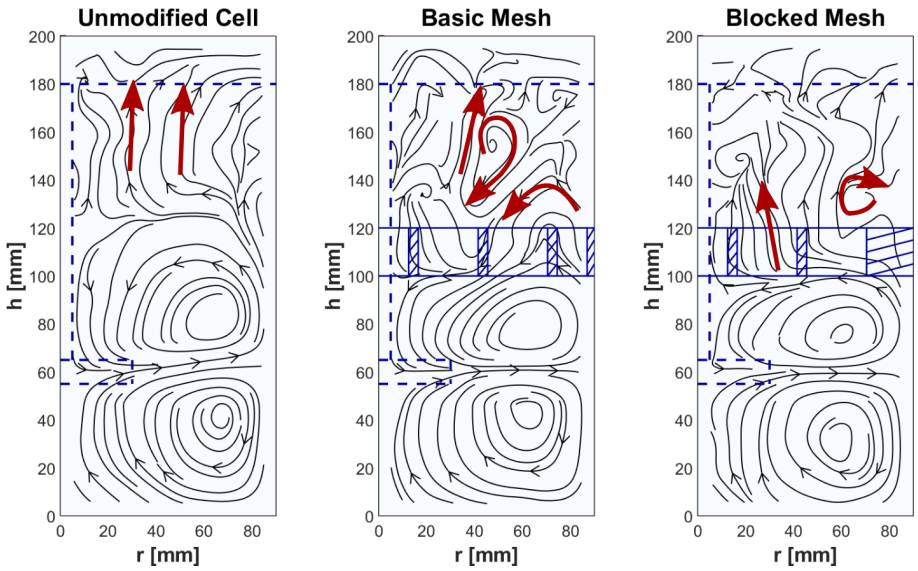
With the basic mesh, the $400\,\mu\mathrm{m}$ tracer (figure7.1(a)) generally shows similar flow to that of the $500\,\mu\mathrm{m}$ tracer (figure 7.1(b)). The tracer moves up through holes $A$, $B$ and $D$ of the basic mesh and moves down through holes $C$. There is also a small mixing loop in the quiescent pulp zone suggesting that some of the particles which drop off from the froth are recaptured and recovered, however as with the $500\,\mu\mathrm{m}$ tracer, this loop is not well developed.

The $600\,\mu\mathrm{m}$ tracer (figure 7.1(c)) shows similar motion through the holes of the basic mesh to the other two tracers, however there is no mixing loop in the quiescent pulp zone. Instead, the streamlines show that the particle generally moves upwards into the froth and the overflow, this suggests that the larger tracer shows less detachment than the smaller tracers. This indicates that the quiescent pulp zone is beneficial for coarse particle recovery. However, the lack of a mixing loop indicates that if the $600\,\mu\mathrm{m}$ tracer was detached then it was not so easily recaptured. The horizontal slices through the mesh for all tracers (figure 7.5) show that with the basic mesh there is azimuthal flow along the cell wall in holes $D$ and that there is clear motion of the tracer towards the impeller, indicating that the motion of the tracer was not just vertical through the mesh. For all three tracer sizes there is no evidence of swirl above the mesh, as can be seen from figure 7.6, indicating that the presence of the mesh helped to break down the swirl and reduce the turbulence. However, the streamlines in this slice show that the tracer commonly moves towards the impeller rather than towards the outside of the cell.

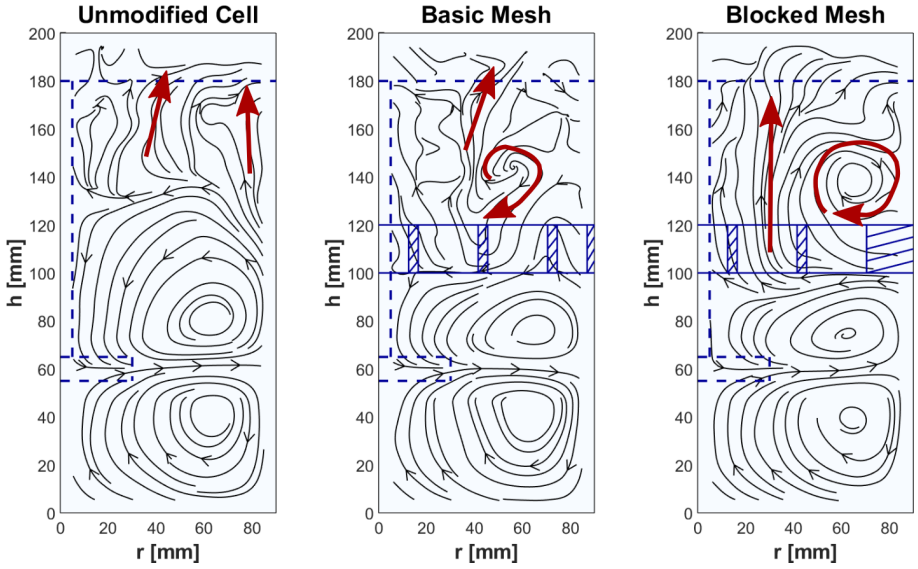
With the blocked mesh, the differences between the motion of the $400\,\mu\mathrm{m}$ tracer (fig-

ure 7.1(a)) and the $500\,\mu\mathrm{m}$ tracer (figure 7.1(b)) are greater than in both the unmodified cell and with the basic mesh. For both tracers there is generally only upwards flow through all holes of the mesh, unlike in the basic mesh, indicating that blocking holes $D$ helped to reduce the drop off of the tracer into the primary pulp zone and promote its recapture. The flow of the $400\,\mu\mathrm{m}$ tracer is more chaotic than the $500\,\mu\mathrm{m}$ tracer and the flow of the smaller tracer at the pulp-froth interface is more generally directed into the centre of the cell, which is not desirable. The mixing loop in the quiescent pulp zone is not as well developed as for the $500\,\mu\mathrm{m}$ tracer, however there is little indication of the tracer moving down at the cell wall. Instead, the majority of the downwards motion of the $400\,\mu\mathrm{m}$ tracer is concentrated close to the impeller.

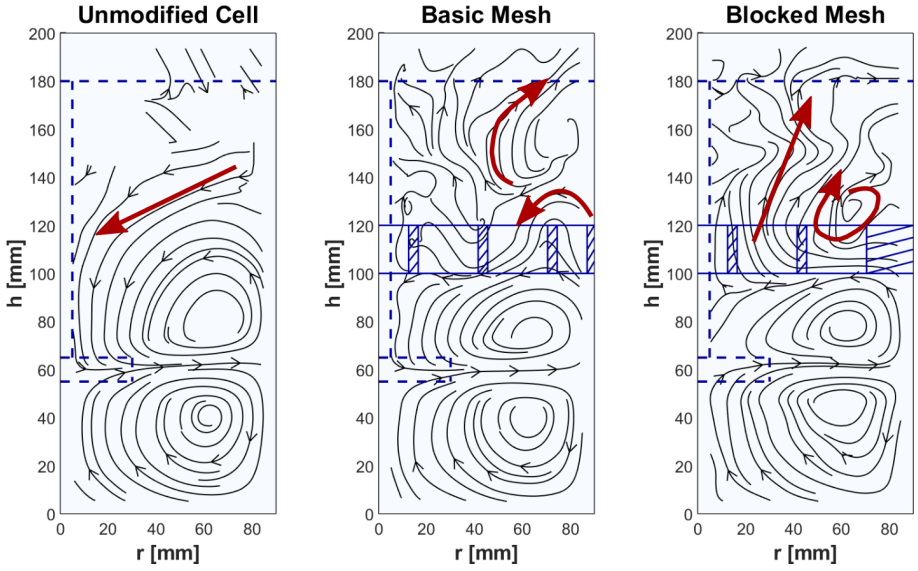
The $600\,\mu\mathrm{m}$ tracer also shows upwards motion through the holes of the blocked mesh (figure 7.1(c)), indicating again that the blocked mesh helped to reduce the tracer drop off to the pulp of the cell. There is a slightly larger mixing loop above the blocked hole for the $600\,\mu\mathrm{m}$ tracer than for the $400\,\mu\mathrm{m}$ tracer, however it is still small in comparison to the $500\,\mu\mathrm{m}$ tracer. This mixing loop dips into the top of holes $C$, suggesting that there was a tendency for the tracer to drop off and start moving back through the mesh, however it was often recaptured. The motion of the $600\,\mu\mathrm{m}$ tracer above the blocked mesh is initially towards the cell wall, however at a height of around $150\,\mathrm{mm}$, approximately where the pulp-froth interface sits, the direction shifts towards the impeller. This would suggest that there was a less quiescent environment here in comparison to the basic mesh. Towards the top of the froth the tracer again moves to flow towards the outside of the cell, aiding recovery. The streamlines through the blocked mesh, for all three tracer sizes, (figure 7.5) are broken, suggesting that the tracer motion through the mesh was predominantly vertical. Figure 7.6 shows that there is little evidence of swirl above the blocked mesh for all three tracers, similarly to the basic mesh, demonstrating that the presence of the mesh provided a more quiescent environment at the pulp-froth interface than the unmodified cell.




(a) $400\,\mu\mathrm{m}$




(b) $500\,\mu\mathrm{m}$




(c) $600\,\mu\mathrm{m}$

**Figure 7.1:** Streamlines of the tracer in the froth, with each of the cell designs, for hydrophobic tracers of different sizes (a) $400\,\mu\mathrm{m}$ and (b) $500\,\mu\mathrm{m}$ and (c) $600\,\mu\mathrm{m}$. Red arrows are added to highlight some flow patterns and are indicative only. The impeller and the level of the overflowing lip are shown in dashed blue lines and the position of the mesh shown in solid blue lines.

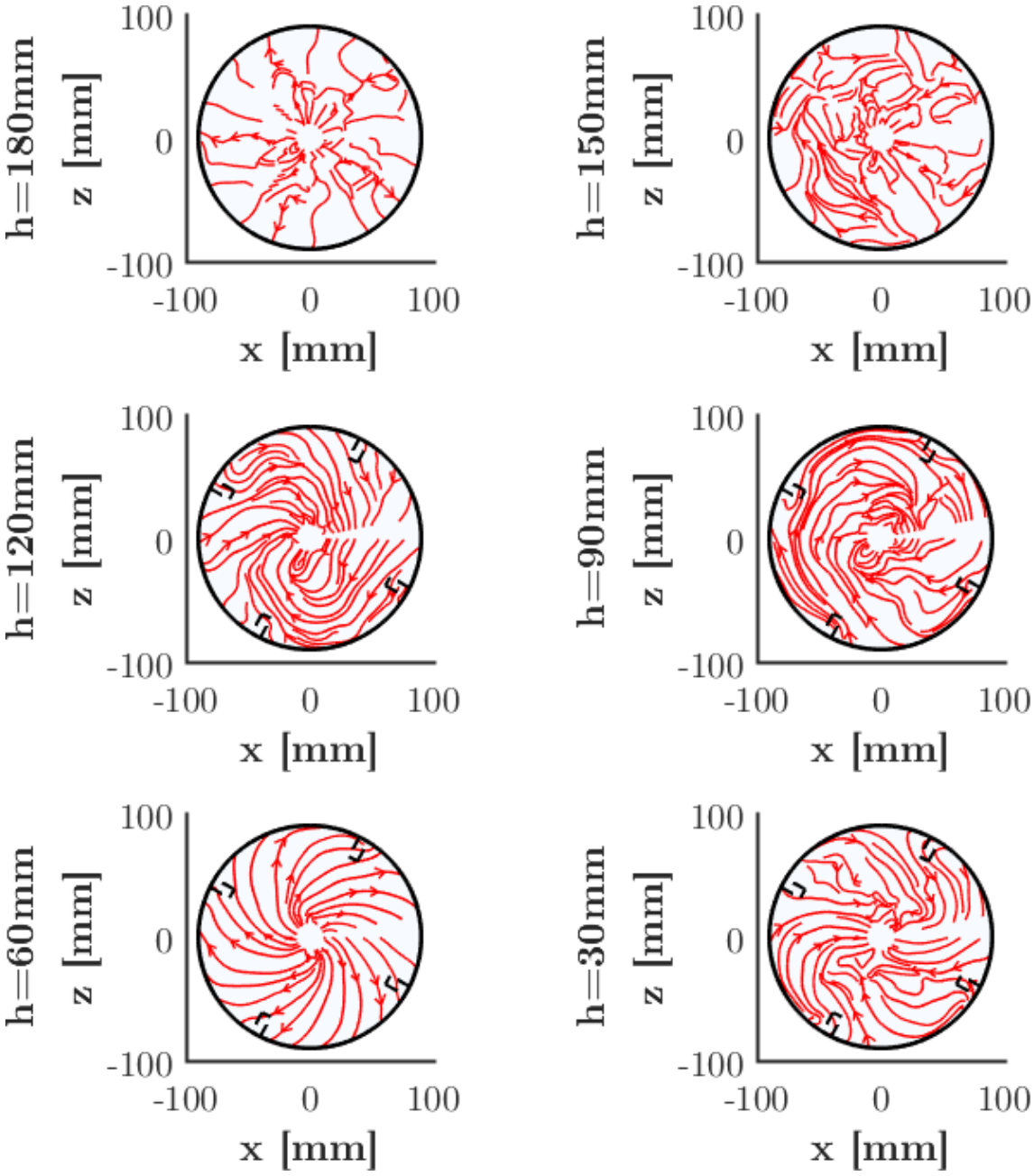



**Figure 7.2:** Bulk flow of the $400\,\mu\mathrm{m}$ tracer at different heights through the unmodified cell.

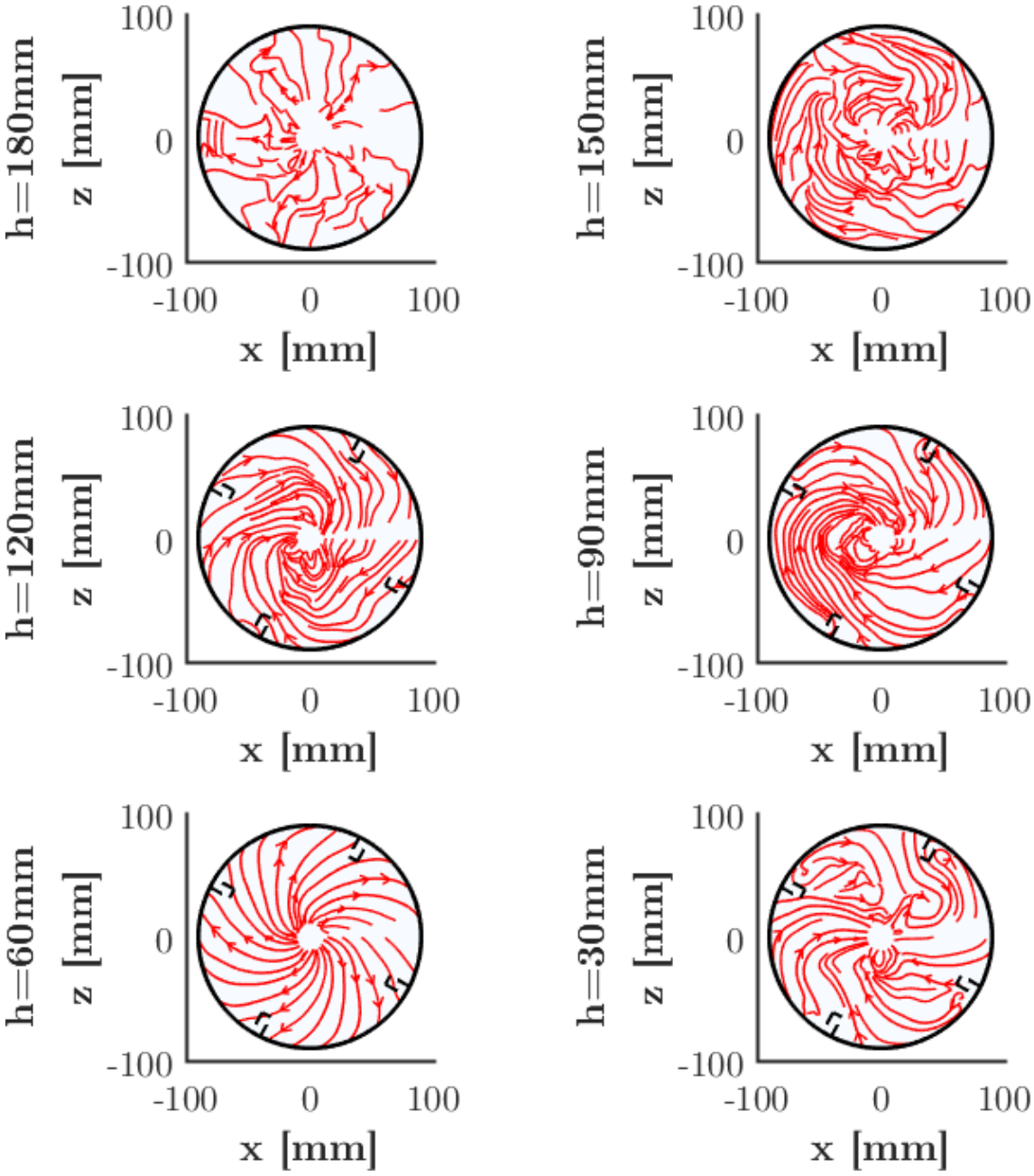



**Figure 7.3:** Bulk flow of the $500\,\mu\mathrm{m}$ tracer at different heights through the unmodified cell.

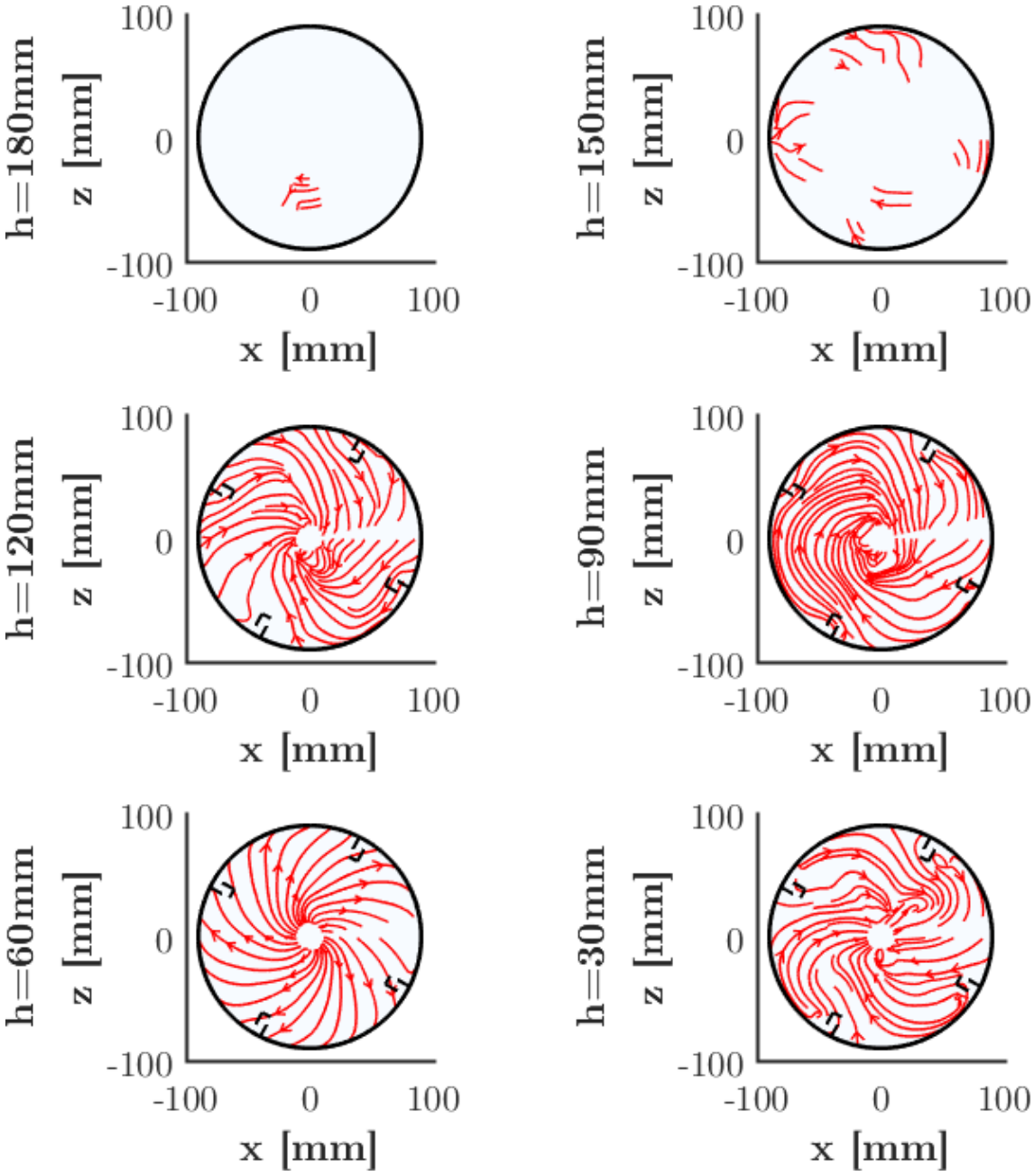
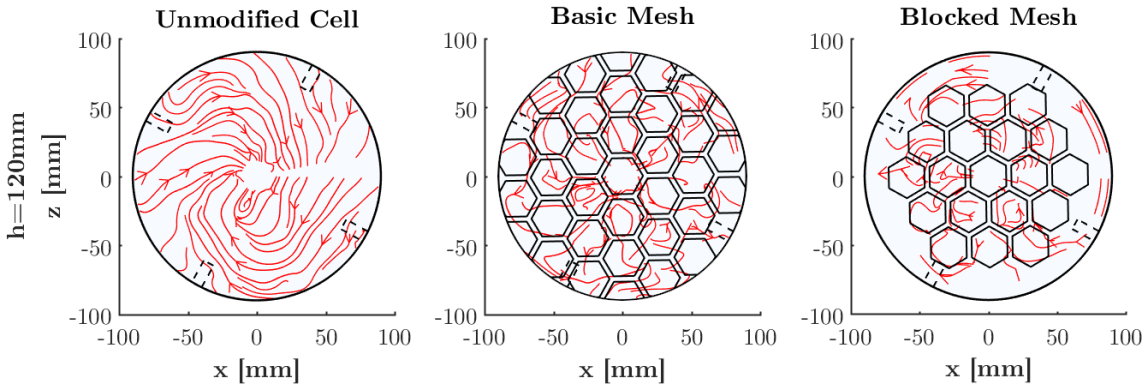
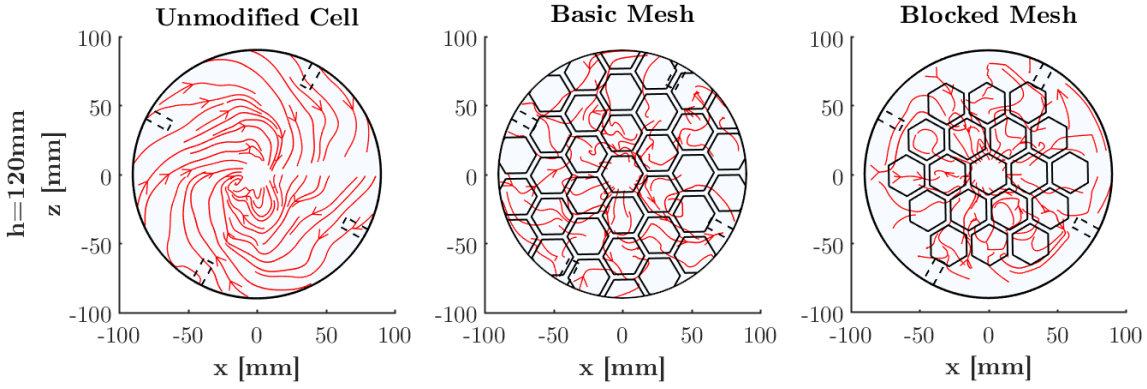


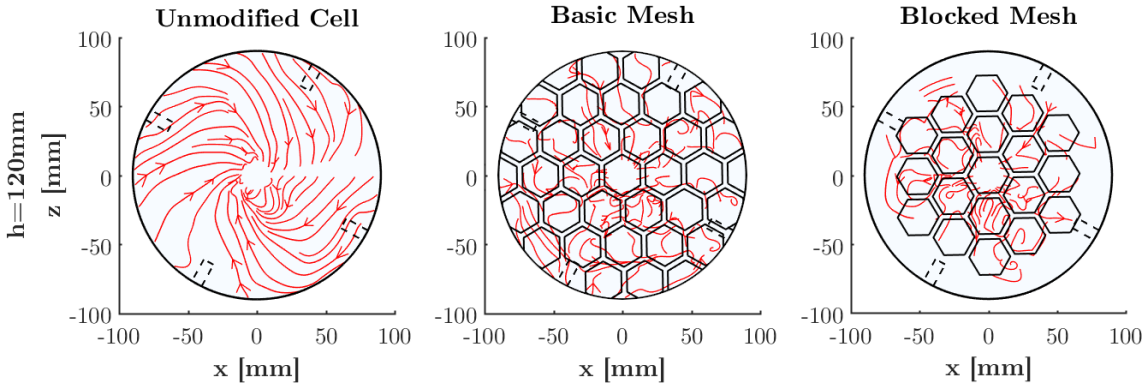

**Figure 7.4:** Bulk flow of the $600\,\mu\mathrm{m}$ tracer at different heights through the unmodified cell.




(a) 400 $\mu$m tracer

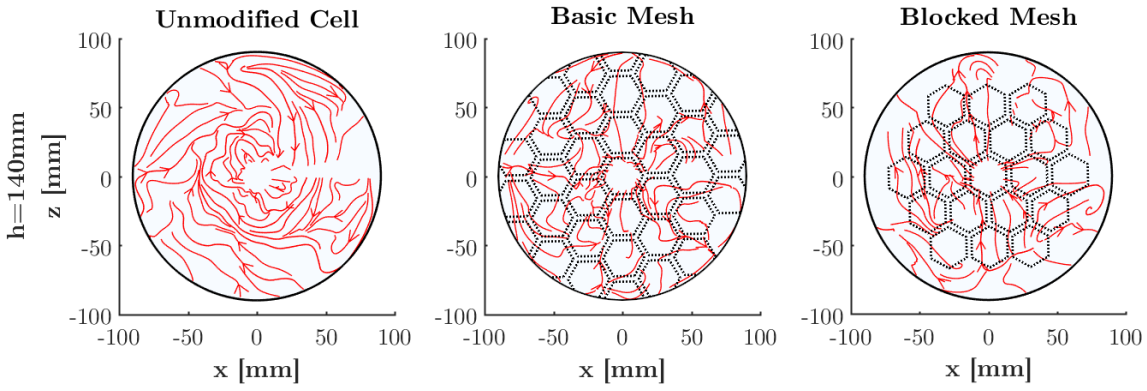



(b) 500 $\mu$m tracer

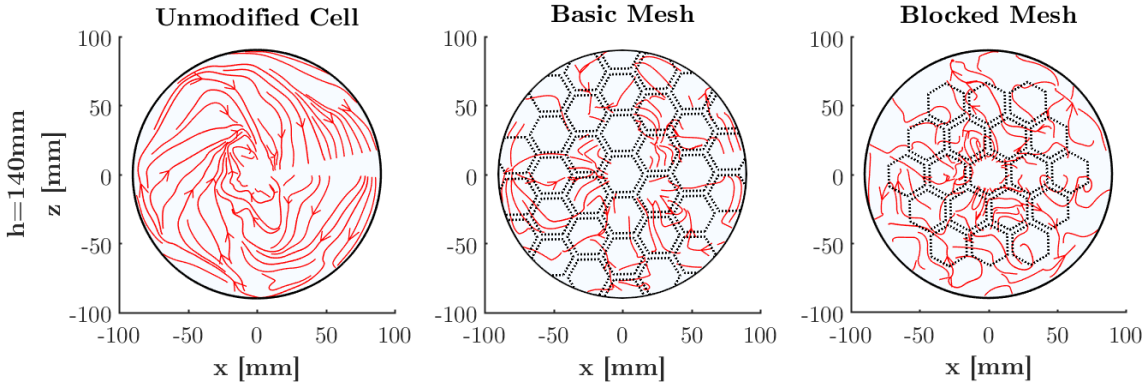



(c) 600 $\mu$m tracer

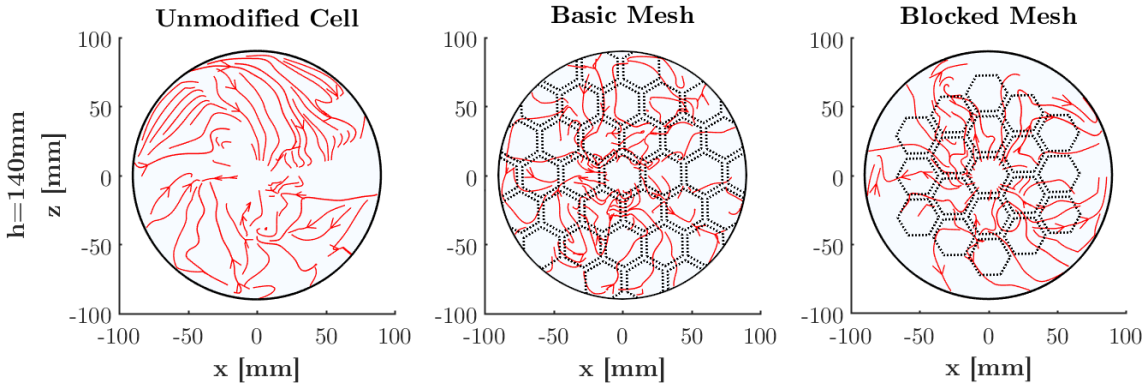
**Figure 7.5:** Horizontal slices of streamlines through the meshes at a height of 120 mm for the (a) 400 $\mu$m, (b) 500 $\mu$m and (c) 600 $\mu$m tracers. The location of the mesh is outlined in black.




(a) 400 $\mu$m tracer




(b) 500 $\mu$m tracer




(c) 600 $\mu$m tracer

**Figure 7.6:** Horizontal slices of streamlines above the meshes at a height of 140 mm for the (a) 400 $\mu$m, (b) 500 $\mu$m and (c) 600 $\mu$m tracers. The location of the mesh is outlined in black.

## 7.3 Velocities

The vertical velocities of the three differently sized tracers in each of the design modifications are shown in figure 7.7. In order to better understand how the vertical velocity varies in the cross section of the cell, figures 7.8, 7.9 and 7.10 show horizontal slices taken at different heights through the unmodified cell for the $400\,\mu\mathrm{m}$, $500\,\mu\mathrm{m}$ and $600\,\mu\mathrm{m}$ tracers respectively. Figures 7.11 and 7.12 show the values of the velocities of the different tracers at different points through the cell allowing for direct comparison between tracers and design modifications. The error bars presented on both of these figures are the standard error after averaging across the six slices. The horizontal slices of vertical velocity, through the mesh are shown in figure 7.13.

The vertical velocities in the pulp of the unmodified cell are similar for all three tracer sizes (figure 7.7), indicating that all three tracers were equally well suspended in the bulk of the pulp. Figures 7.8, 7.9 and 7.10 show this in more detail in horizontal slices at various heights through the unmodified cell. It is clear from these figures that the positive velocity beneath the impeller (i.e. at a height of $30\,\mathrm{mm}$) slightly decreases in magnitude as the trace size increase. This is inline with what would be expected as there would be lower energy in this zone and this impacts on the ability to lift larger particles. The vertical velocity of the $400\,\mu\mathrm{m}$ tracer, in the froth of the unmodified cell, is mainly positive; there are, however, negative velocities on the top of the froth close to the impeller (figure 7.7(a)). This suggests that the $400\,\mu\mathrm{m}$ tracer was lost from the froth due to bubble bursting, however, this was less common than for the $500\,\mu\mathrm{m}$ tracer. In general, figures 7.12(a) and 7.12(b) show that the vertical velocity of the $400\,\mu\mathrm{m}$ tracer in the froth is similar to that that of the $500\,\mu\mathrm{m}$ tracer. On the other hand, the $600\,\mu\mathrm{m}$ clearly does not float well in the unmodified cell with mostly negative velocities at a height of $150\,\mathrm{mm}$ in figure 7.10. Figures 7.11(b) and 7.12(c) show that, where the vertical velocity of the tracer is negative, the $600\,\mu\mathrm{m}$ has a higher magnitude velocity than the other two tracers suggesting that when the $600\,\mu\mathrm{m}$ tracer is detached it will drop back into the pulp faster than the other two tracer sizes.

The flow of the $400\,\mu\mathrm{m}$ tracer in the froth zone with the basic mesh is quite chaotic (figure 7.7(a)). There are only a few areas of the cell where the tracer has a positive vertical velocity and the majority of these are concentrated close to the impeller. In general, the tracer has a negative vertical velocity through the froth and at the top of the froth, which

is not conducive to successful recovery of the particle. As was shown with the streamlines, for all three tracer sizes, the tracer moves up through holes $A$, $B$ and $D$ of the basic mesh and down through holes $C$. All three tracers have higher magnitude vertical velocities through holes $D$ than the other holes in the basic mesh (figure 7.7). This indicates that there was a higher flowrate at the wall of the cell. The positive vertical velocity of the $400\,\mu\mathrm{m}$ tracer through holes $B$ is higher than for the $500\,\mu\mathrm{m}$ tracer (figure 7.11(b)) which was potentially due to the smaller size. In addition the $400\,\mu\mathrm{m}$ tracer has more positive vertical velocities through holes $D$ than the $500\,\mu\mathrm{m}$ tracer (figure 7.13) indicating that the smaller tracer dropped through the basic mesh less frequently than the larger tracer.

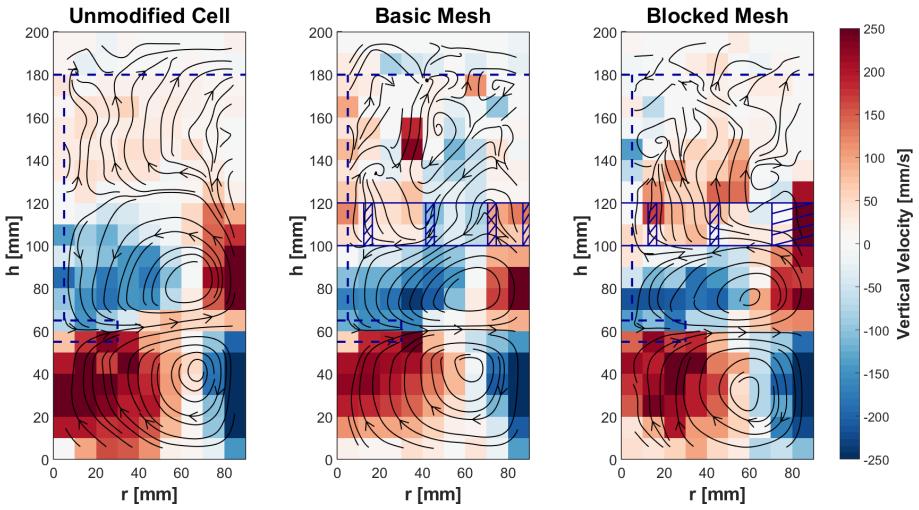
The vertical velocity of the $600\,\mu\mathrm{m}$ tracer (figure 7.7(c)) is more generally positive above the basic mesh than the other two tracer sizes, suggesting that the largest tracer was more easily recovered than the other two. Through the mesh itself (figure 7.11(b)), the positive vertical velocity velocity of the $600\,\mu\mathrm{m}$ tracer through holes $B$ is higher than the $500\,\mu\mathrm{m}$ tracer, and the negative vertical velocities are lower, indicating that the larger tracer remained in the froth longer than the other tracer sizes.

With the blocked mesh, the $400\,\mu\mathrm{m}$ tracer has more positive vertical velocities in the quiescent pulp zone, and in the froth, than with the basic mesh (figure 7.7(a)). Figure 7.12 shows that these velocities are also of a higher magnitude, suggesting that the blocked mesh is aiding the recovery of the $400\,\mu\mathrm{m}$ tracer. However, the flow is much more chaotic than in the unmodified cell and there are areas where there are very low velocities, especially close to the cell wall. While the average vertical velocity of the $400\,\mu\mathrm{m}$ tracer in the holes of the blocked mesh is positive, there are still areas of the mesh with negative vertical velocities (figure 7.13(a)). This indicates that the $400\,\mu\mathrm{m}$ tracer was being lost through the blocked mesh and was not as well recovered as the $500\,\mu\mathrm{m}$ tracer, however the magnitude of the positive velocities was higher than the negative velocities and the flow through the blocked mesh was still improved relative to the basic mesh. There are areas at the wall with very high velocities; this is where the mesh did not fit flush with the wall of the cell and the tracer was able to pass through the gap between the two.

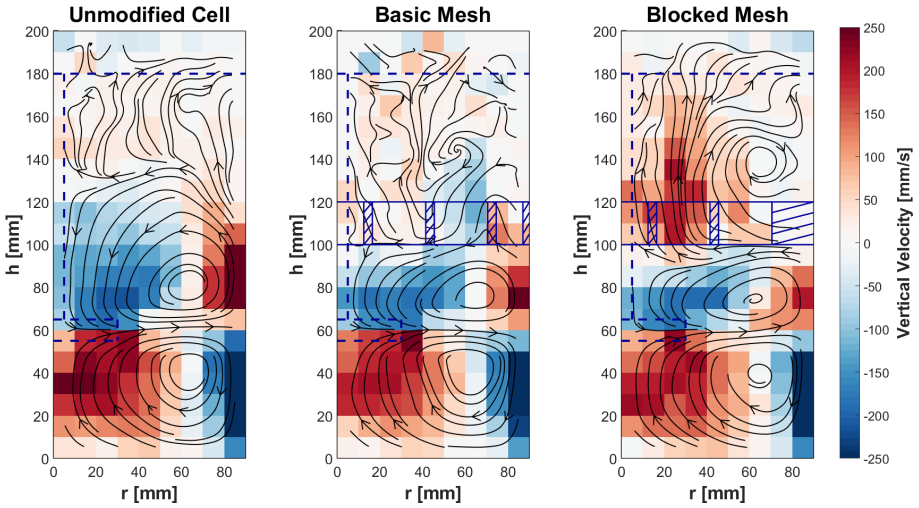
Whilst both the $600\,\mu\mathrm{m}$ tracer and the $500\,\mu\mathrm{m}$ tracer have high vertical velocities in holes $B$ (figures 7.7(a) and (b)), the $600\,\mu\mathrm{m}$ tracer slows down above the mesh, at a height of $140\,\mu\mathrm{m}$. This is shown clearly in figure 7.12(c) where the "peak" in velocity for the $600\,\mu\mathrm{m}$ with the blocked mesh is narrower, at $r = 25\,\mathrm{mm}$, in comparison to the other two tracer sizes with this design. Figure 7.11(a) also indicates that the vertical velocities

of the $600\,\mu\mathrm{m}$ tracer, through the blocked mesh and above, are higher than with the basic mesh, especially close to the lip of the cell, showing that the blocked mesh improved recovery compared to the basic mesh. The velocity of the tracer through the different holes in the blocked mesh (figure 7.13(c)) shows some areas with negative velocities, however there are fewer than for the $400\,\mu\mathrm{m}$ tracer. The velocities of the $600\,\mu\mathrm{m}$ tracer are similar to those of the $500\,\mu\mathrm{m}$ tracer and higher than those of the $400\,\mu\mathrm{m}$ tracer, suggesting that the blocked mesh improved the flotation of the coarser particles.

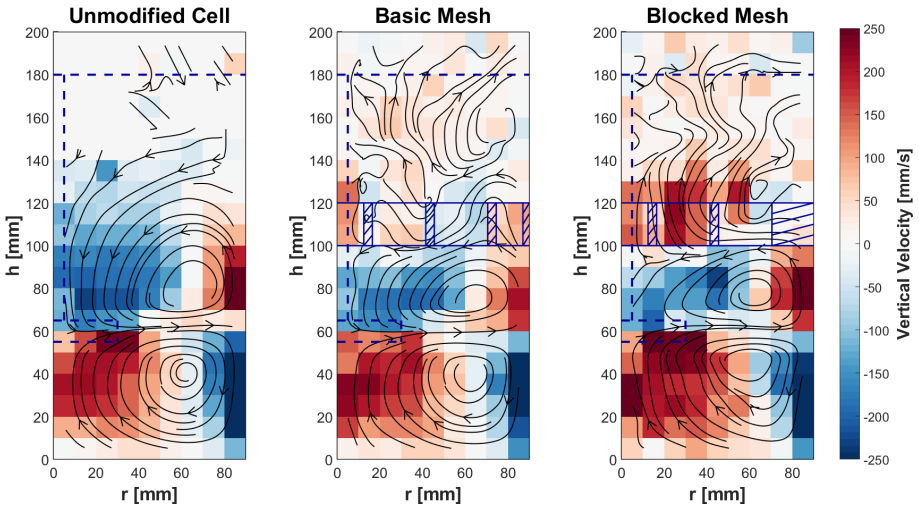
As was previously discussed in section 7.2, there is evidence from streamlines that there is swirl occurring at the pulp-froth interface. This was a phenomenon first seen in PEPT results from Norori-McCormac (2015) and is thought to be detrimental to particle recovery, as it indicates a non-quiescent environment. In order to get a better understanding of this phenomenon, and how the different mesh designs affect it, the azimuthal velocity component is shown in figure 7.14. Here, positive is defined as the same direction the impeller is rotating. For the unmodified cell the pulp-froth interface sits at approximately a height of $140\,\mathrm{mm}$. Figure 7.14 shows that, for all three tracer sizes, in the unmodified cell, there are very high azimuthal velocities at the pulp-froth interface suggesting a non-quiescent environment. In general, with both meshes, the azimuthal velocities through the mesh and above it are lower and show no evidence of swirl. This indicates that the presence of the mesh in the cell helped to break down the swirl at the interface, however there is no clear difference between the two meshes or the different tracer sizes.




(a) $400\,\mu\mathrm{m}$




(b) $500\,\mu\mathrm{m}$




(c) $600\,\mu\mathrm{m}$

**Figure 7.7:** Vertical velocity component of the tracer in the froth for hydrophobic tracers of different sizes (a) $400\,\mu\mathrm{m}$ and (b) $500\,\mu\mathrm{m}$ and (c) $600\,\mu\mathrm{m}$.

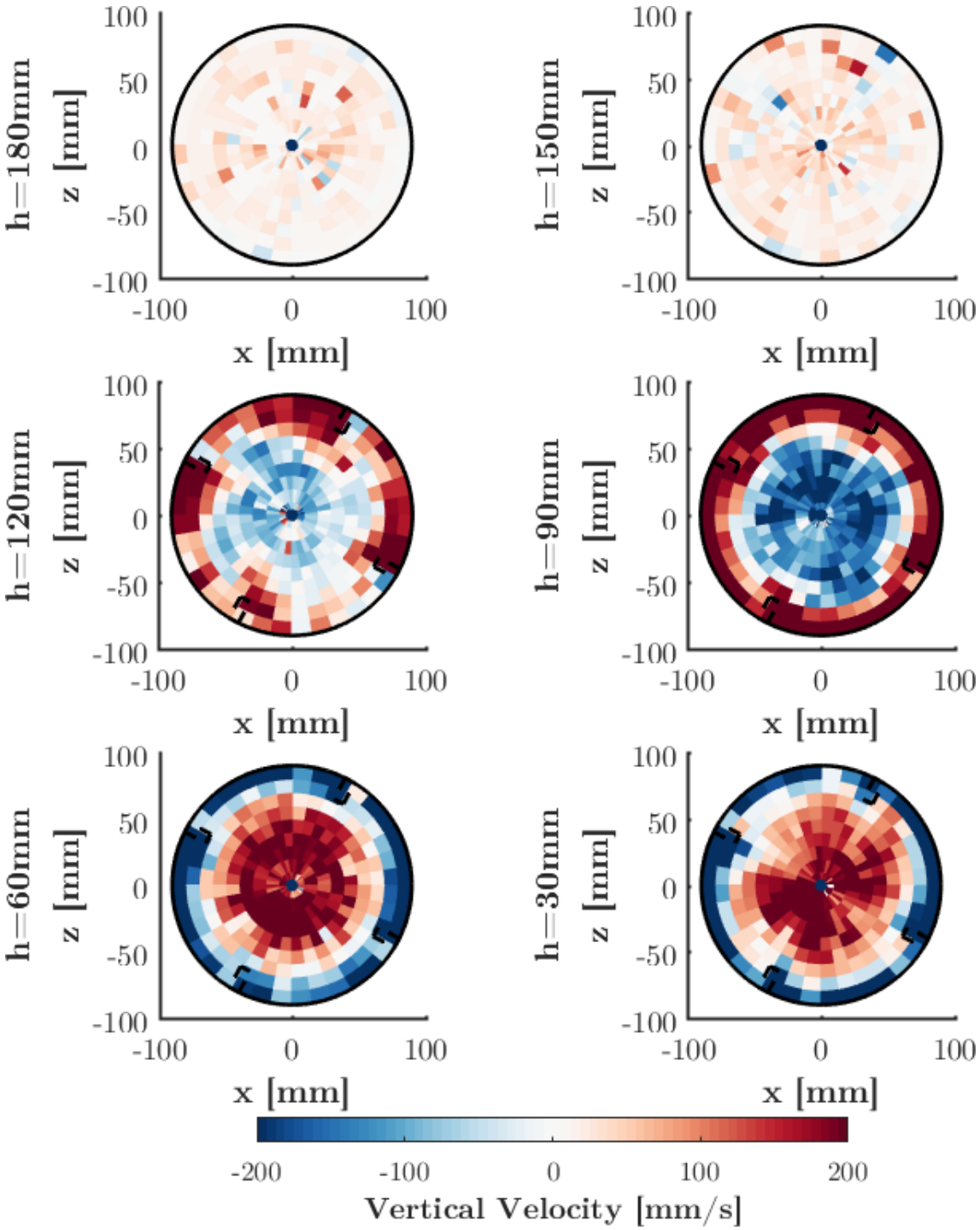



**Figure 7.8:** Vertical velocity of the $400\,\mu\mathrm{m}$ tracer at different heights through the unmodified cell.

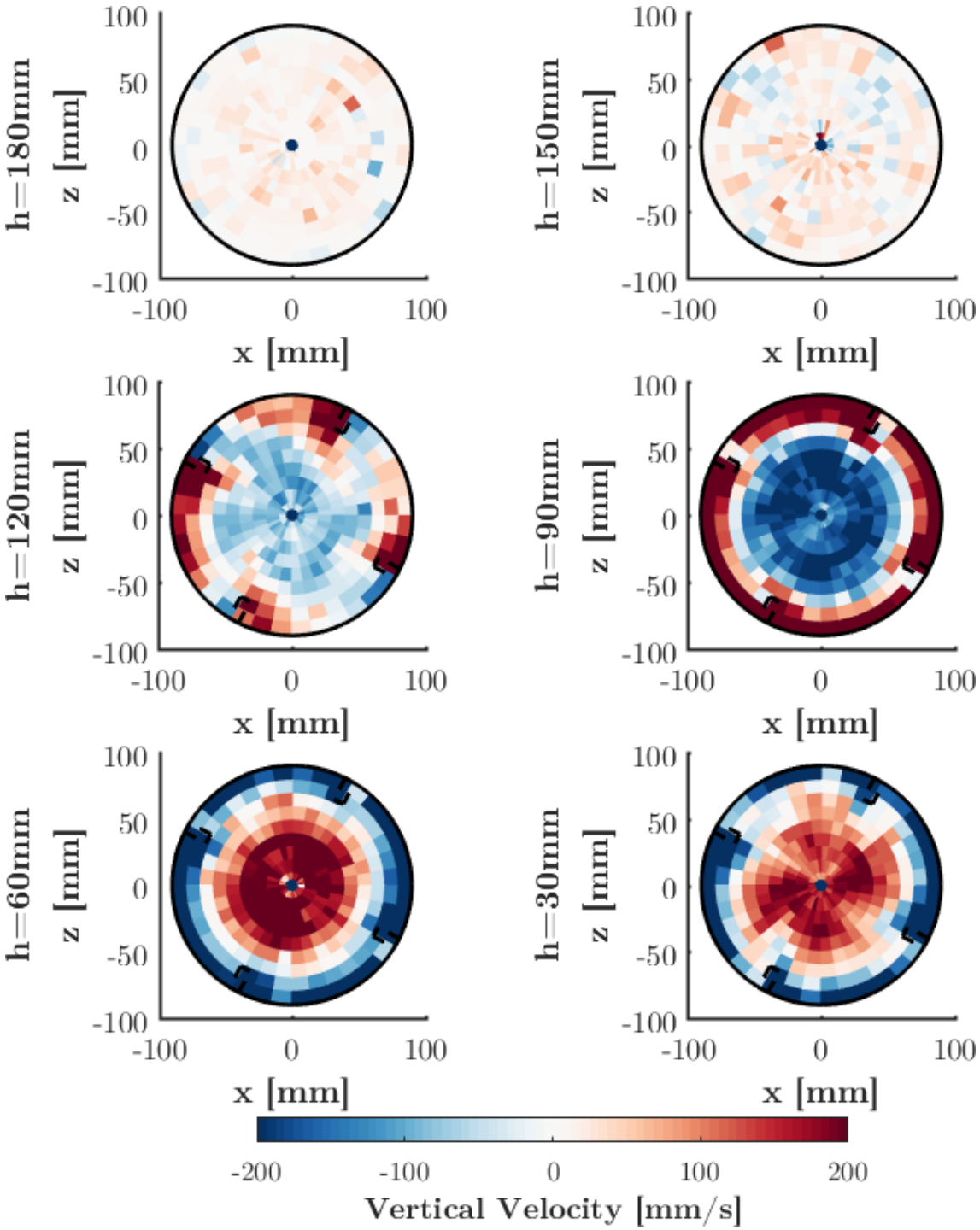



**Figure 7.9:** Vertical velocity of the $500\,\mu\mathrm{m}$ tracer at different heights through the unmodified cell.

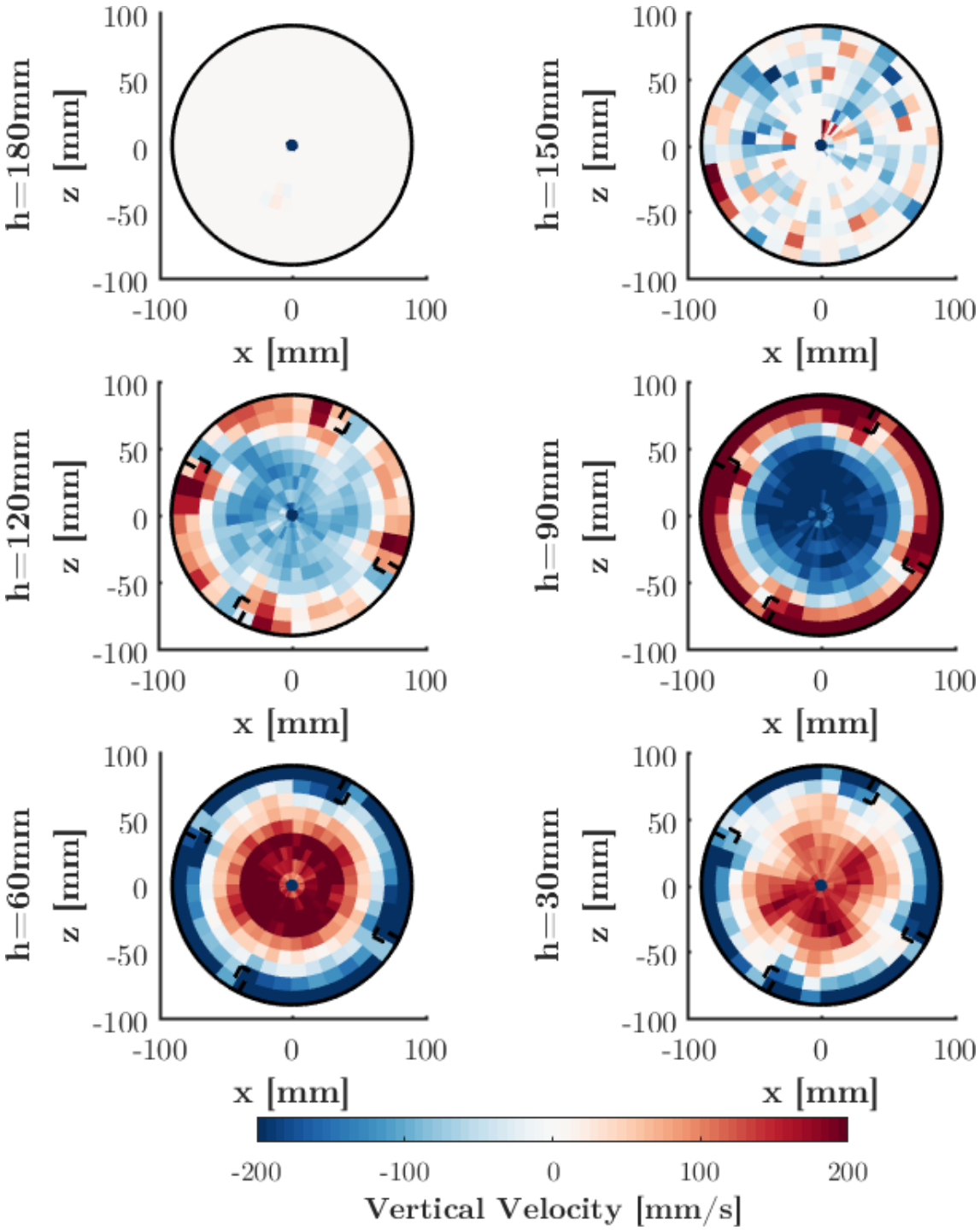
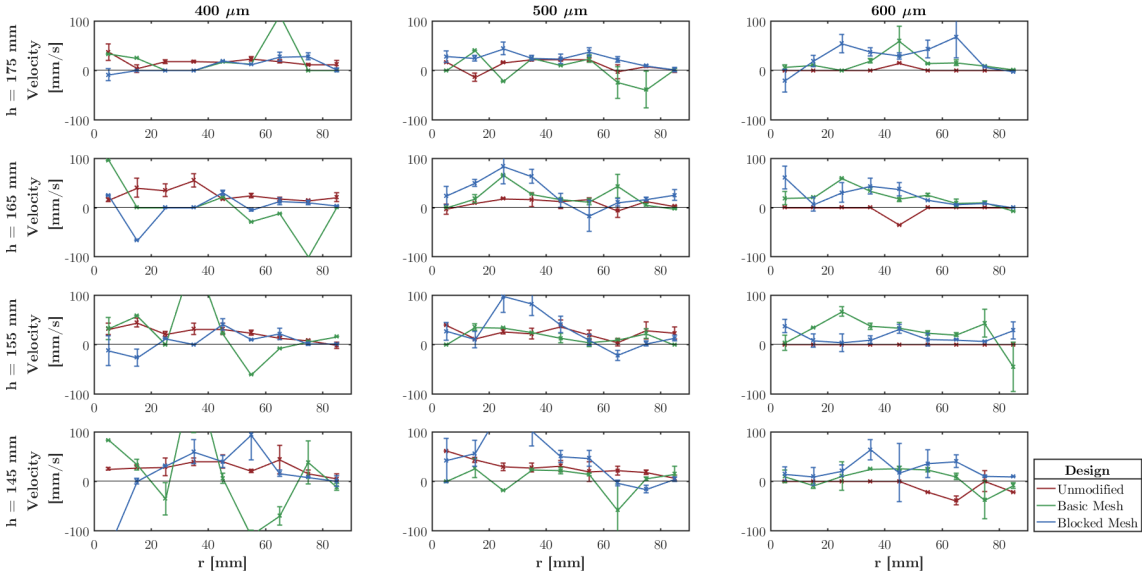
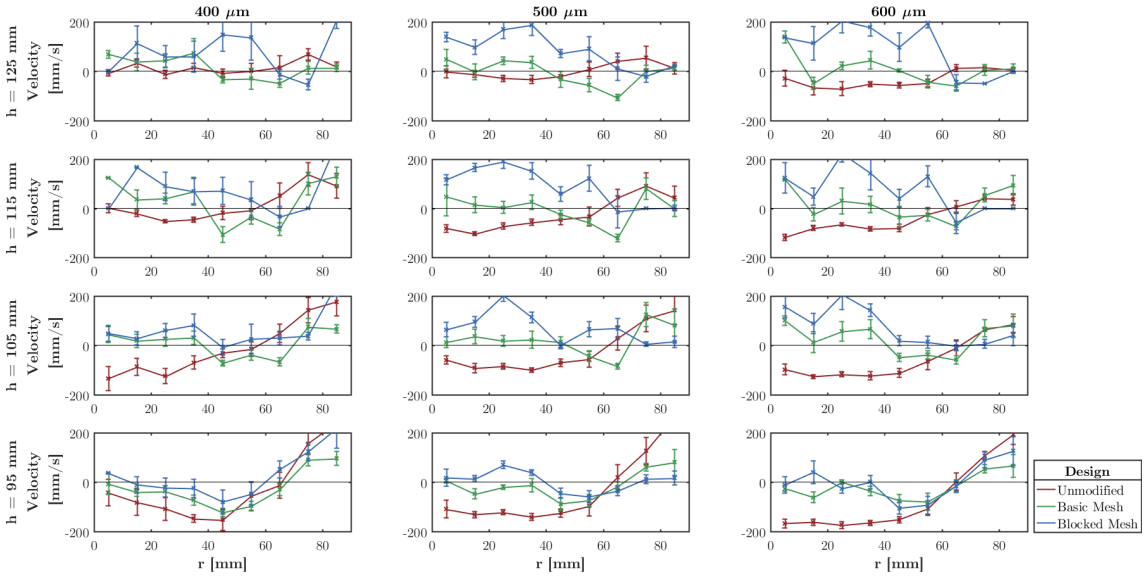



**Figure 7.10:** Vertical velocity of the $600\,\mu\mathrm{m}$ tracer at different heights through the unmodified cell.

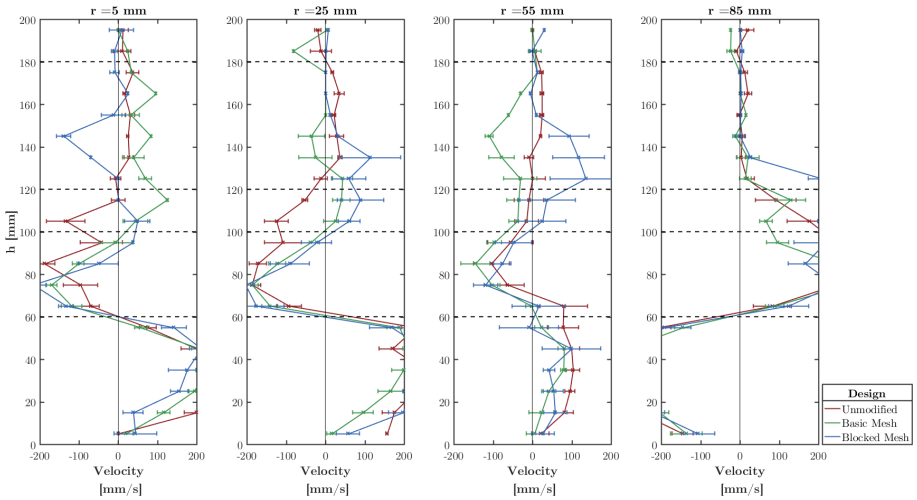



(a) Froth

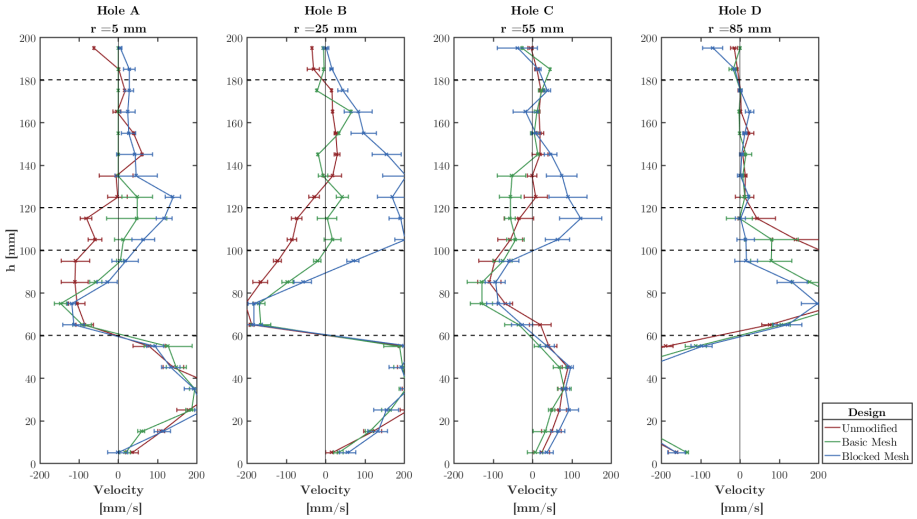



(b) Mesh

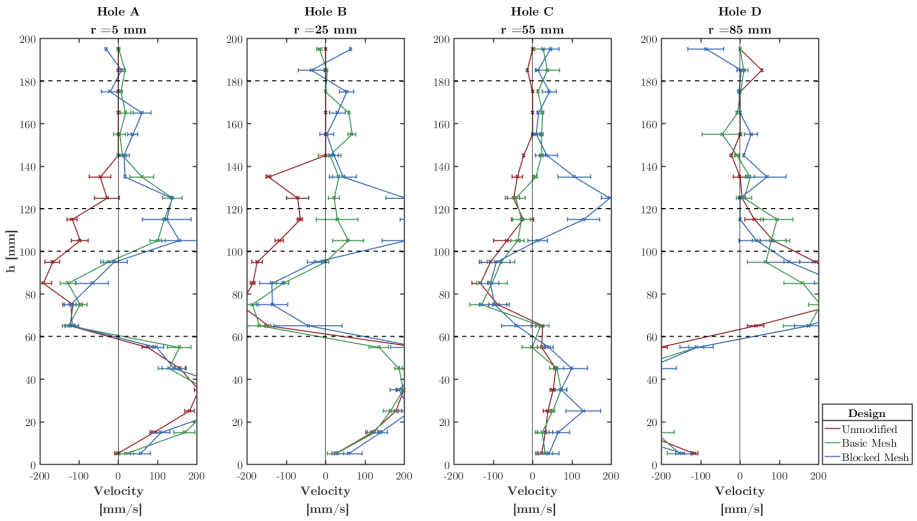
**Figure 7.11:** Plot of Vertical Velocity with radial location for different heights within the froth of the cell. Error bars are the standard error after averaging the value across 6 slices. The mesh is located between h=100 and h=120.




(a) 400 $\mu$m tracer

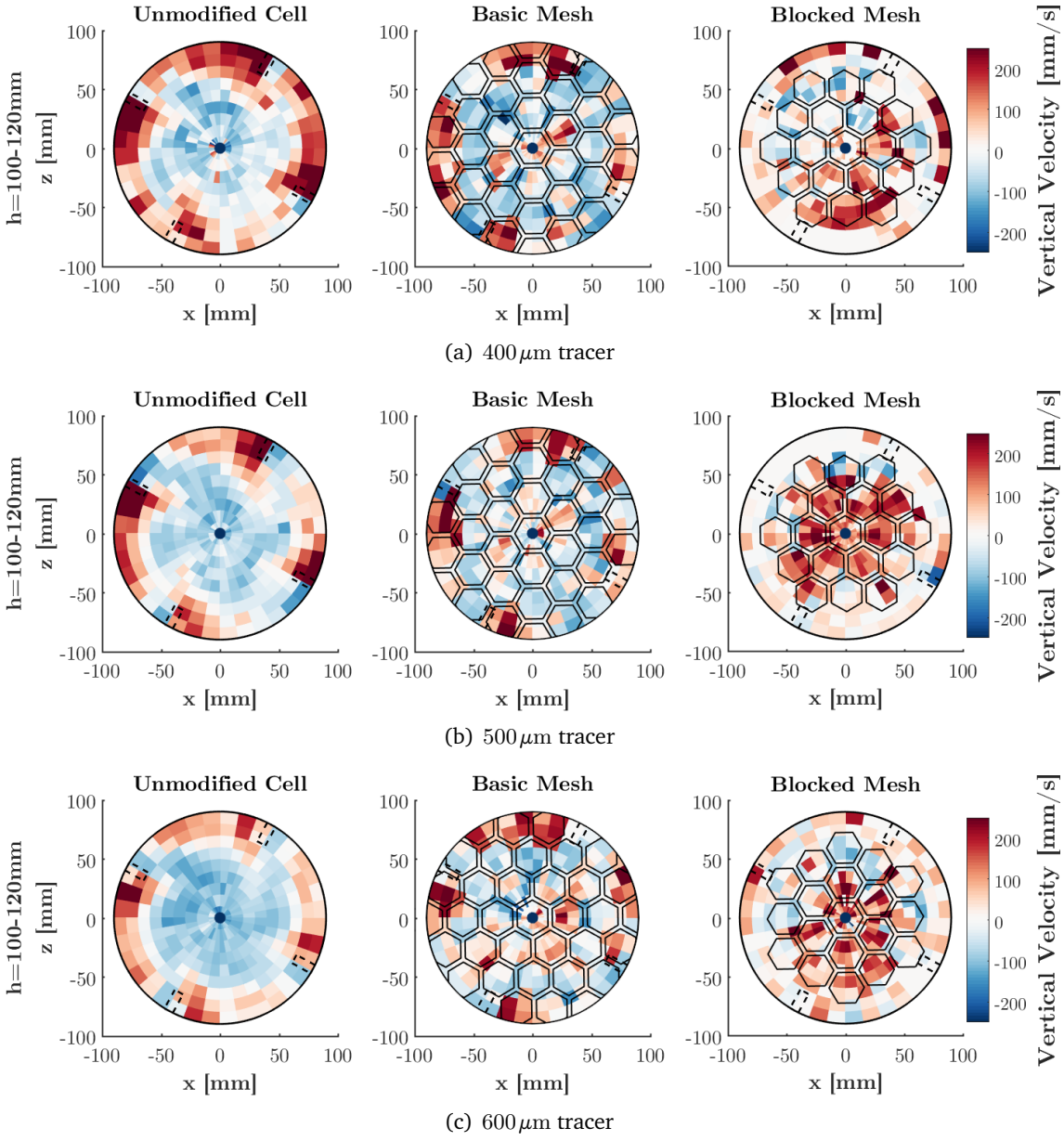



(b) 500 $\mu$m tracer




(c) 600 $\mu$m tracer

**Figure 7.12:** Plot of Vertical Velocity with height at different radii from the centre of the cell. Error bars are the standard error after averaging the value across 6 slices. The mesh is located between h=100 and h=120 mm.

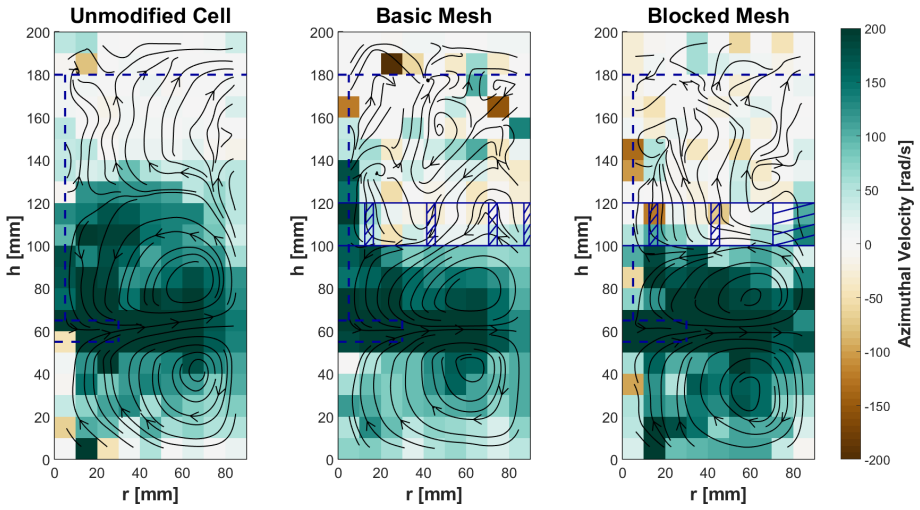



(a) 400 $\mu$m tracer

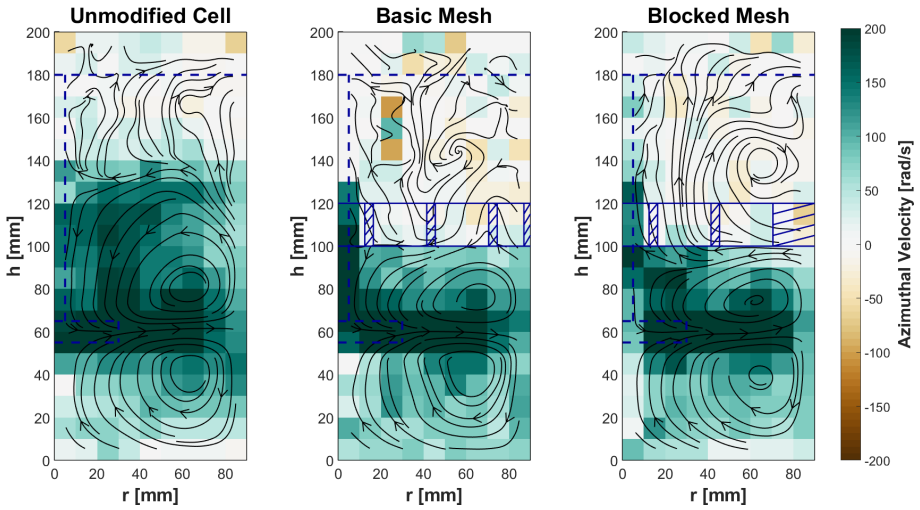
(b) 500 $\mu$m tracer

(c) 600 $\mu$m tracer

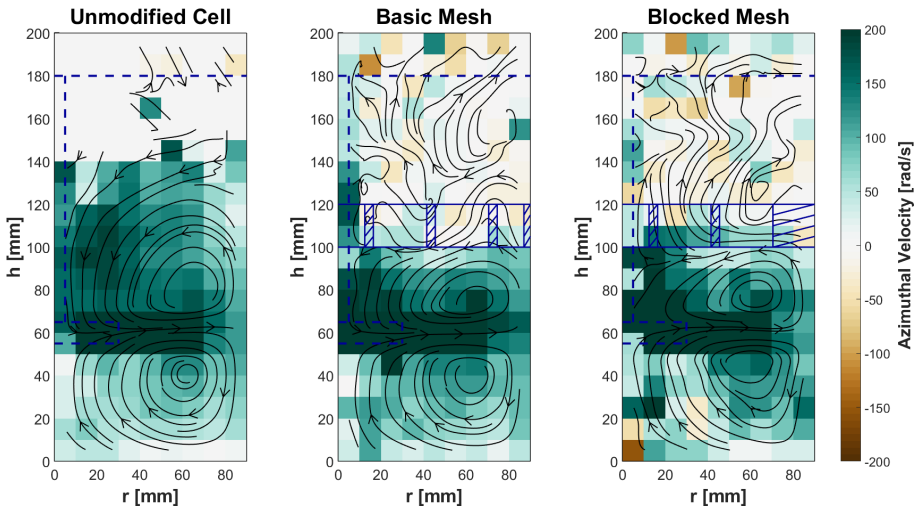
**Figure 7.13:** Horizontal slices of Vertical Velocity of the different tracers through the mesh; (a) 400 $\mu$m tracer, (b) 500 $\mu$m tracer, (c) 600 $\mu$m tracer. The location of the mesh is outlined in black.




(a) $400\,\mu\mathrm{m}$




(b) $500\,\mu\mathrm{m}$




(c) $600\,\mu\mathrm{m}$

**Figure 7.14:** Azimuthal velocity component of the tracer in the froth for hydrophobic tracers of different sizes (a) $400\,\mu\mathrm{m}$ and (b) $500\,\mu\mathrm{m}$ and (c) $600\,\mu\mathrm{m}$. Positive is defined as the same direction as the impeller rotation.

## 7.4 Occupancy

The occupancy of each of the tracers and design cases, through a vertical slice in the cell is shown in figure 7.15. This is calculated as the length of time the tracer spent in each voxel as a proportion of the total time the tracer spent in the cell during the experiment and then normalised for voxel volume. Occupancy is useful to determine where the tracer spent the most time, as this can indicate how well the tracer was recovered and if there are any preferential paths through the froth that the tracer took. It is important to note that a high occupancy can be attributed to one of two things, firstly that the tracer entered a particular voxel multiple times and secondly that the tracer was moving slowly. It is therefore important to look at the occupancy in conjunction with the velocity to determine which of the two is the case. As with the vertical velocities through the cell, figures 7.16 and 7.17 show the variation in occupancy at different points in the cell. The occupancy in the horizontal slices through the mesh (figure 7.18) is calculated as a proportion of the total time the tracer spent in the slice. This highlights how the tracer preferentially moves through different holes of the mesh.

The occupancy of the $400\,\mu\mathrm{m}$ tracer, in the unmodified cell (figure 7.15(a)), is low throughout the pulp zone, indicating that it spent a larger proportion of time in the froth. In the froth zone the occupancy is quite high, especially towards the edge of the cell, at radii greater than $60\,\mathrm{mm}$. The tracer velocity in this area is not significantly different to the rest of the froth (figure 7.7(a)), suggesting that the tracer preferentially flowed through the froth close to the wall of the cell. The occupancy is also high on top of the froth close to the impeller, suggesting that the tracer made it to the froth but not into the overflowing section. On the other hand, the $600\,\mu\mathrm{m}$ tracer has a very low occupancy in the areas where it did enter the froth, and much higher in the pulp, especially at the bottom of the cell towards the centre, indicating that it was not floating.

The $400\,\mu\mathrm{m}$ tracer, for the basic mesh, has a higher occupancy in the pulp than for the unmodified cell, and also a lower occupancy in the froth (figure 7.15(a)). The occupancy in the pulp is also higher than for the $500\,\mu\mathrm{m}$ tracer with the basic mesh, this indicates that the basic mesh was inhibiting the flotation of the smaller tracer. The occupancy of the tracer in the overflowing froth is higher close to the impeller for the $400\,\mu\mathrm{m}$ tracer than for the $500\,\mu\mathrm{m}$ tracer, suggesting that the tracer gets stuck in the stagnant, non-overflowing froth, however, this is less than for the same tracer in the unmodified cell. Although there

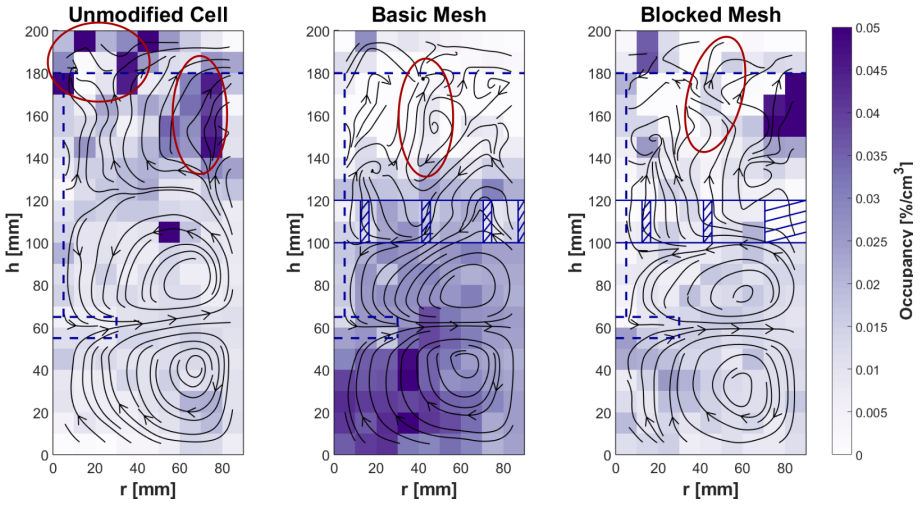
is a path of increased occupancy in the froth for the $400\,\mu\mathrm{m}$ tracer at $r$ =40 mm, figure 7.16(a) shows that there is a slight decrease in occupancy at this radius at a height of $180\,\mathrm{mm}$, suggesting that the tracer was not always recovered to the concentrate. In the holes of the basic mesh, the occupancy of the $400\,\mu\mathrm{m}$ tracer is similar in holes $B$ and $C$, and a little lower in holes $A$ and $D$ (figure 7.16(b)), indicating that the tracer preferentially entered these holes. The drop in occupancy through holes $D$ corresponds to an increased velocity. The occupancy of the $400\,\mu\mathrm{m}$ tracer through the basic mesh is higher than the $500\,\mu\mathrm{m}$ tracer (figure 7.16(b)), this indicates that the $400\,\mu\mathrm{m}$ tracer was not passing into the froth as much as the $500\,\mu\mathrm{m}$ tracer. Figure 7.18 shows the occupancy in the horizontal slice of the mesh, this is the occupancy as a proportion of the total time the tracer spends in the mesh, and not the whole cell, in order to highlight difference between the different holes of the mesh. The $400\,\mu\mathrm{m}$ tracer, with the basic mesh, has a very low occupancy in several of the holes of the mesh, however the occupancy is relatively constant across the rest of the holes in $B$ and $C$. In the holes $D$, there are areas with higher occupancy, however these correspond to lower velocities.

The behaviour of the $600\,\mu\mathrm{m}$ tracer, with the basic mesh, is much improved in comparison to the unmodified cell (figure 7.15(c)). The occupancy in the pulp is a lot lower, suggesting that the tracer was recovered to the froth more easily. There is a high occupancy path for the $600\,\mu\mathrm{m}$ tracer close to the wall where there are also slow negative velocities suggesting that the tracer became detached and slowly drained through the froth. Comparing the occupancy (figure 7.18(c)) and the vertical velocity (figure 7.13(c)), areas where there is higher tracer occupancy through the mesh correspond to lower velocities, and visa-versa, indicating that there was no preference of flow through any of the holes of the mesh.

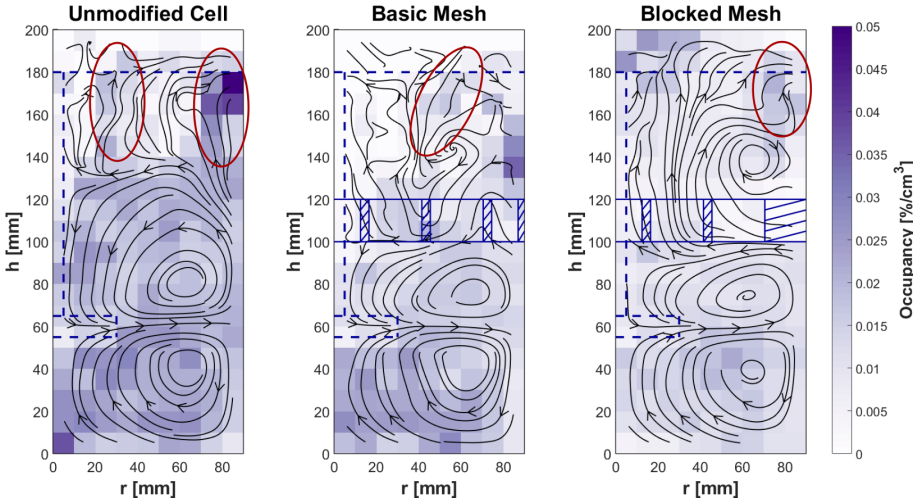
The occupancy of the $400\,\mu\mathrm{m}$ tracer in the pulp, with the blocked mesh, is similar to the unmodified cell and lower than the basic mesh (figure 7.15(a)), showing that this tracer is recovered better with the presence of the blocked mesh than the basic mesh. As for the other two designs, this tracer has a high occupancy in the overflowing froth close to the impeller, suggesting that it was stuck in the stagnant zone of the froth. There is also a high occupancy zone just below the lip at the wall of the cell, however this corresponds to an area of extremely low velocity suggesting that the tracer may have got stuck here. There are many areas of the froth, with the blocked mesh, where the $400\,\mu\mathrm{m}$ tracer has a very low occupancy, however there is a clear path through the froth at $r$ =40 mm. Unlike with the

basic mesh, this follows with a higher occupancy in the overflowing froth indicating that the $400\,\mu\mathrm{m}$ tracer was more successfully recovered with the blocked mesh. Figure 7.18(a) shows that the occupancy does not change hugely through the different holes of the mesh, however there is a slight preference for the tracer to be in holes $C$. In comparison to the vertical velocities (figure 7.13(a)) this is where there are often negative velocities which indicates that the $400\,\mu\mathrm{m}$ tracer frequently drops through the mesh.

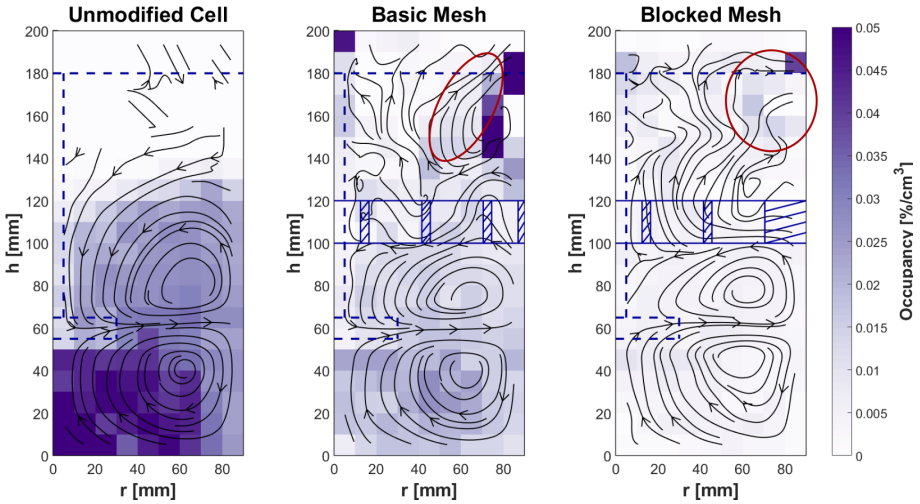
The occupancy of the $600\,\mu\mathrm{m}$ tracer with the blocked mesh, throughout the whole cell, is much lower than the other tracers and designs (figure 7.17(c)). This indicates that the residence time of this tracer was much lower than the other tracers. Through the mesh, the occupancy of the $600\,\mu\mathrm{m}$ tracer (figure 7.18(c)) is similar to the $500\,\mu\mathrm{m}$ where the tracer preferentially moves through holes $B$. There is also a high positive velocity through holes $B$ (figure 7.13) showing that the tracer was recovered from the pulp to the froth well. Figure 7.16(a) indicates that, in the majority of the froth, the occupancy of the $600\,\mu\mathrm{m}$ tracer is similar for both mesh designs. This suggests that both designs improved the flotation of this tracer, compared to the unmodified cell.




(a) $400\,\mu$m

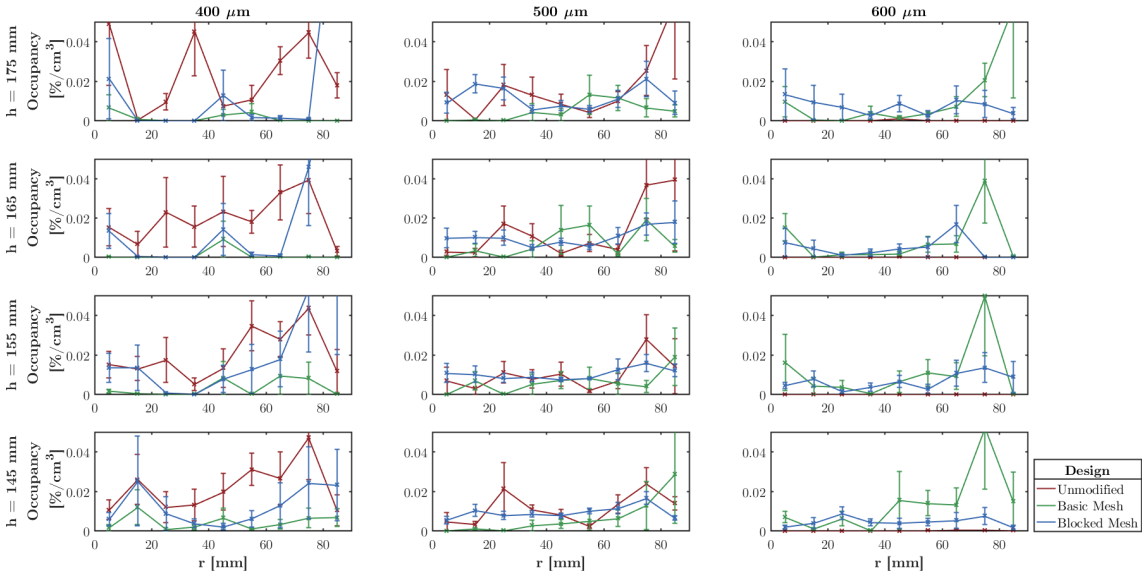



(b) $500\,\mu$m

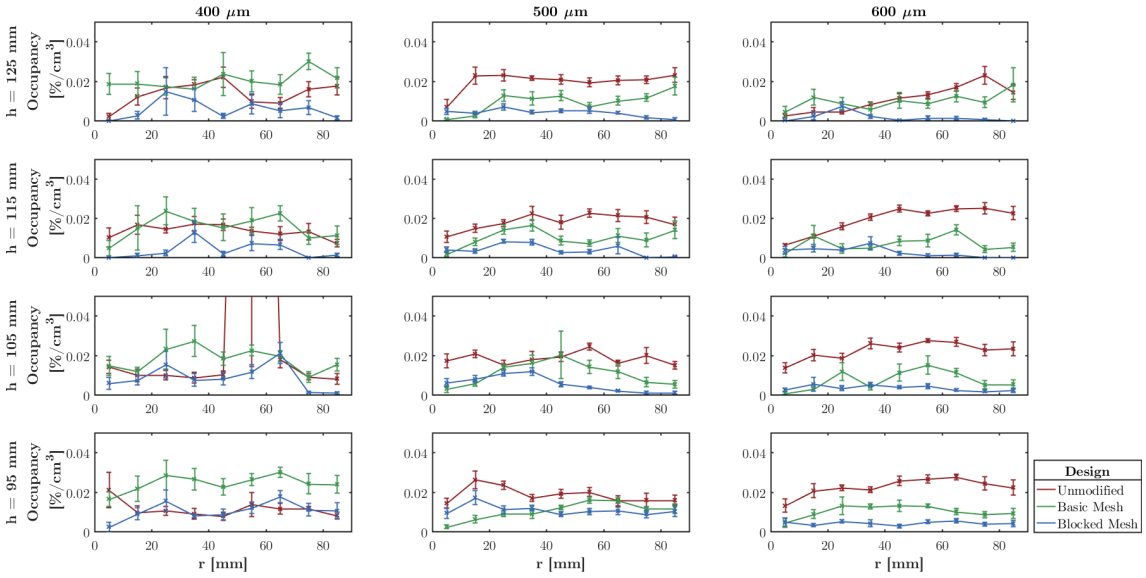



(c) $600\,\mu$m

**Figure 7.15:** occupancy of the tracer in the froth for hydrophobic tracers of different sizes (a) $400\,\mu$m and (b) $500\,\mu$m and (c) $600\,\mu$m.

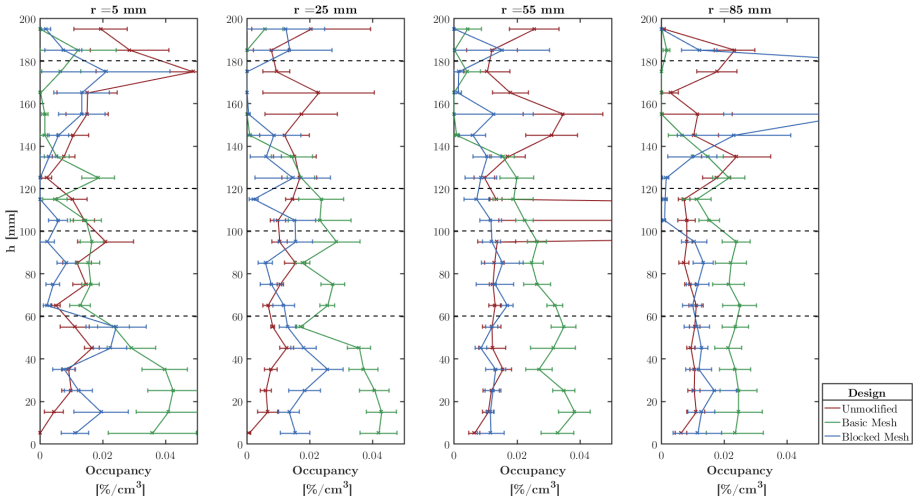



(a) Froth

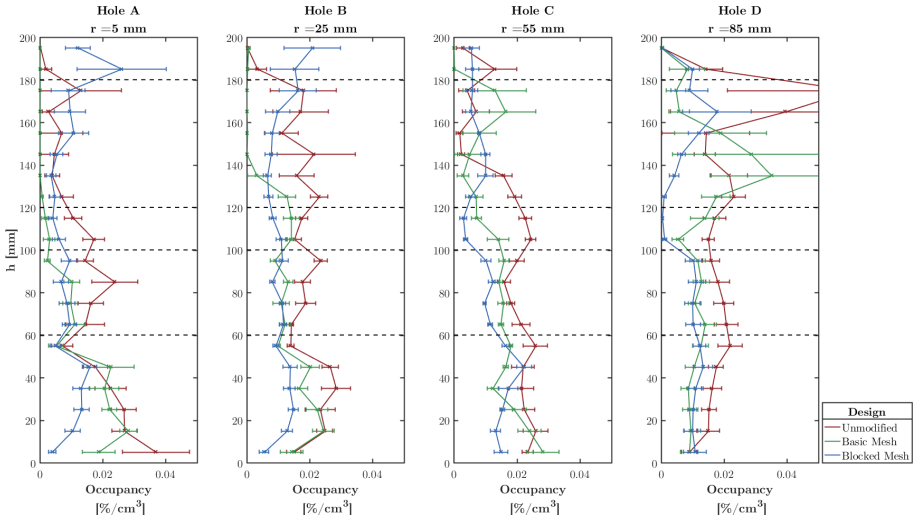



(b) Mesh

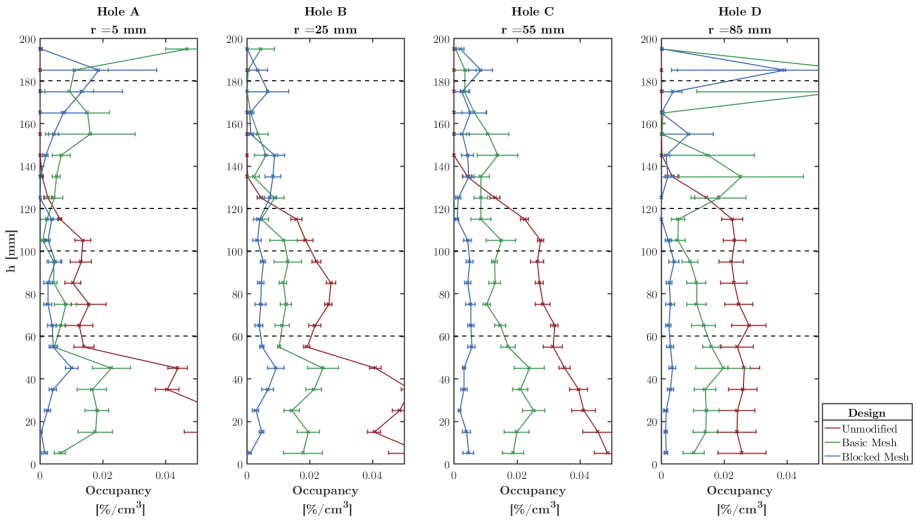
**Figure 7.16:** Plot of occupancy with radial location for different heights within the froth of the cell. Error bars are the standard error after averaging the value across 6 slices. The mesh is located between h=100 and h=120 mm




(a) 400 $\mu$m tracer

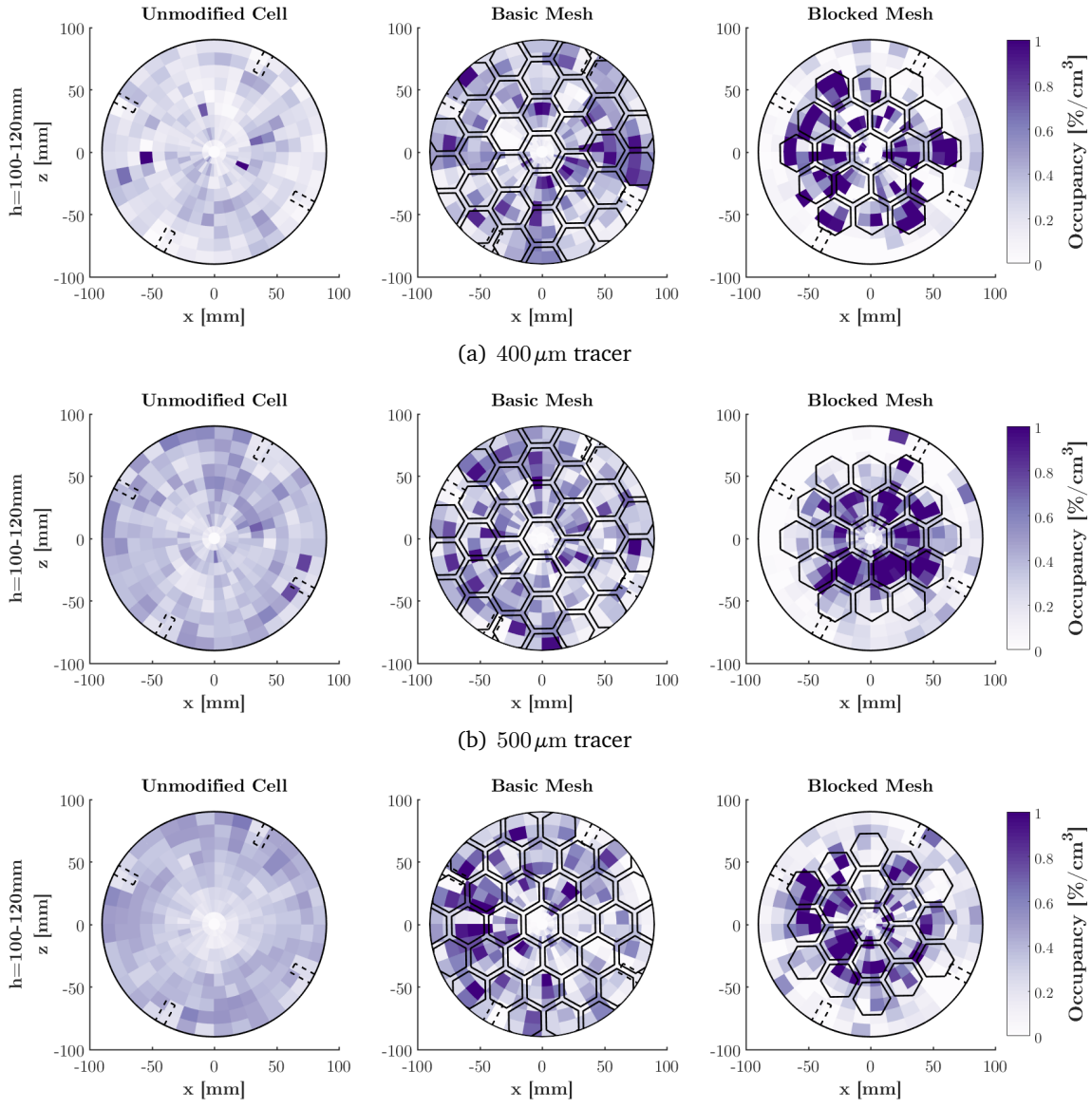



(b) 500 $\mu$m tracer




(c) 600 $\mu$m tracer

**Figure 7.17:** Plot of occupancy with height at different radii from the centre of the cell. Error bars are the standard error after averaging the value across 6 slices. The mesh is located between h=100 and h=120 mm.




(a) 400 $\mu$m tracer

(b) 500 $\mu$m tracer

(c) 600 $\mu$m tracer

**Figure 7.18:** Horizontal slices of occupancy of the different tracers through the mesh; (a) 400 $\mu$m tracer, (b) 500 $\mu$m tracer, (c) 600 $\mu$m tracer. The location of the mesh is outlined in black.

## 7.5 Discussion

The streamlines and vertical velocities, in the unmodified cell, show that the $400\,\mu\mathrm{m}$ tracer behaved in a similar way to the $500\,\mu\mathrm{m}$ tracer, both showed good positive flow from the pulp to the overflowing froth. The occupancy of the $400\,\mu\mathrm{m}$ tracer was higher in the froth and lower in the pulp than the $500\,\mu\mathrm{m}$ tracer, indicating that it was recovered more easily. As with the $500\,\mu\mathrm{m}$ tracer, there was evidence of swirl at the pulp-froth interface for the $400\,\mu\mathrm{m}$ tracer. On the other hand, the $600\,\mu\mathrm{m}$ tracer had a very different flow to the other two tracers; the tracer very rarely entered the froth and when it did there was mainly a negative vertical velocity, suggesting it dropped back into the pulp. The occupancy of this tracer was very high in the bottom of the pulp, close to the centre of the cell, suggesting that it was too large to float successfully.

With the basic mesh in the cell, the flow of the $400\,\mu\mathrm{m}$ tracer was again similar to the $500\,\mu\mathrm{m}$ tracer; they both showed the tracer moving up through holes $A$, $B$ and $D$ and down through holes $C$. The positive velocities in holes $D$ had a higher magnitude than in the other holes of the basic mesh, indicating that there was a high liquid content near the cell wall. Both tracers also had a similarly chaotic flow in the froth, in comparison to the unmodified cell, with several areas of negative vertical velocity where the tracer was inferred to be detached. The occupancy in the pulp was much higher for the $400\,\mu\mathrm{m}$ tracer than the $500\,\mu\mathrm{m}$ tracer with the basic mesh, and also than the unmodified cell. This indicates that the basic mesh reduced the recovery of the smaller, $400\,\mu\mathrm{m}$ tracer. On the other hand, the presence of the basic mesh greatly improved the flotation of the $600\,\mu\mathrm{m}$ tracer, relative to the unmodified cell, however, the motion in the froth and above the mesh was still quite chaotic. The $600\,\mu\mathrm{m}$ tracer moved through the basic mesh in the same way as the other two tracers, however with a higher magnitude positive vertical velocity and lower magnitude negative vertical velocity, indicating that it was recovered more easily. The occupancy of the $600\,\mu\mathrm{m}$ tracer in the froth was higher than that of the $400\,\mu\mathrm{m}$ tracer, suggesting that the basic mesh promoted the flotation and recovery of the larger tracer better than for the smaller tracer.

The blocked mesh resulted in an improvement of the flow of the $400\,\mu\mathrm{m}$ tracer relative to the basic mesh, as there were very few areas where it had a negative vertical velocity. In addition, the streamlines were a little less chaotic. The positive velocities were also a higher magnitude than for the same tracer with the basic mesh. The vertical velocities

of the $400\,\mu\mathrm{m}$ tracer were more often positive through the blocked mesh than the basic mesh, again with a higher magnitude, however they were lower than for the $500\,\mu\mathrm{m}$ tracer with the blocked mesh. This indicates that the presence of the blocked mesh improved the recovery of the $400\,\mu\mathrm{m}$ tracer relative to the basic mesh, but it was reduced compared to the $500\,\mu\mathrm{m}$ tracer as well as the $400\,\mu\mathrm{m}$ tracer in the unmodified cell. There was a small mixing loop above holes $C$ for the $400\,\mu\mathrm{m}$ tracer, however this was not as well developed as for the $500\,\mu\mathrm{m}$ tracer. As a result, there were more negative velocities through holes $C$ of the blocked mesh. The occupancy of the $400\,\mu\mathrm{m}$ tracer in the froth, with the blocked mesh, was slightly higher than with the basic mesh, and it showed a similar path through the froth. There was also a higher occupancy in the overflow, indicating that the blocked mesh improved the recovery of the $400\,\mu\mathrm{m}$ tracer relative to the basic mesh.

The flow of the $600\,\mu\mathrm{m}$ tracer with the blocked mesh was, again, much improved compared to the unmodified cell. Compared to the basic mesh there were fewer areas of negative vertical velocity suggesting that the blocked mesh improved the recovery of the tracer. As for the $400\,\mu\mathrm{m}$ tracer, there was a small mixing loop above holes $C$, where the $600\,\mu\mathrm{m}$ tracer drops towards the top of the mesh, before moving up towards the froth again, inferring that the tracer was recaptured. There were also fewer negative velocities for the $600\,\mu\mathrm{m}$ tracer in the blocked mesh than for the $400\,\mu\mathrm{m}$ tracer, indicating that it was recovered better. The fact that the occupancy of this tracer was concentrated in holes $B$, where there are high positive velocities, also indicates a good recovery, however this was still lower than for the $500\,\mu\mathrm{m}$ tracer. The vertical velocity of the $600\,\mu\mathrm{m}$ tracer suddenly drops at the pulp-froth interface and instead there is lateral motion towards the impeller, this may indicate a slightly less quiescent environment than for the other tracers. This would therefore need to be investigated further to improve the understanding of how different sizes of particles are affected by the quiescent zone, and what implications this would have for recovery and in an industrial application of this design.

## 7.6 Conclusions

This chapter presented the results from using PEPT to investigate the effect that the design modifications investigated in chapters 5 and 6 have on the flotation of three sizes ($400\,\mu\mathrm{m}$, $500\,\mu\mathrm{m}$ and $600\,\mu\mathrm{m}$) of radioactive labelled tracers with hydrophobic surfaces. The analysis of the PEPT data for the $500\,\mu\mathrm{m}$ tracer has been discussed in detail in chapter

6, and was used here as a reference for the other two tracer sizes. This was the first time different sized tracers have been used in a PEPT study with a continuous flotation cell. It is important to note that the tracers used in this study were much larger than the particle size of the feed, due to limitations in the tracer manufacture procedure. However, as the tracers were coated with the same particles used in the feed the results give a good indication as to the flotation behaviour of the different particles, as well as showing the relative difference between floating different particle sizes. The size of these tracers, however, are similar to the very top end of current coarse particle flotation so these results show good promise for industrial applications.

The analysis of the PEPT data for the different tracer sizes with the different design modifications shows that the presence of a mesh greatly improves the flotation performance of the coarsest tracer ($600\,\mu\mathrm{m}$). Both meshes were shown to inhibit the flotation of the $400\,\mu\mathrm{m}$ relative to the unmodified cell, however the blocked mesh showed better flotation of this tracer than the basic mesh. The presence of the blocked mesh also improved the positive velocities of the $600\,\mu\mathrm{m}$ tracer relative to the basic mesh, again indicating that it promoted an improved recovery. Overall, the blocked mesh resulted in an improvement in flotation of all three tracer sizes relative to the basic mesh, and only the $400\,\mu\mathrm{m}$ tracer showed a slight decrease in flotation compared to the unmodified cell, indicating that the blocked mesh successfully improved the flotation of coarse particles.

Whilst these results are promising for the future of coarse particle flotation, showing that introducing a blocked mesh into the cell can improve the flotation of coarser particles, these results are from experiments performed at a much smaller scale than industrial experiments. It is therefore important to follow up this work with more investigations into how the design modifications will scale up. These investigations should be varied, including different laboratory and industrial scales combined with numerical simulations for developing design.

# Chapter 8

# Conclusions

The aim of this thesis was to improve the understanding of the relationships between particle size, froth stability and flotation performance in flotation. This thesis also investigated how different retrofit design modifications affected the flotation performance and behaviour of different particle types.

This aim was achieved in three key ways, by using a continuously overflowing, bench-scale, flotation cell with systems that were more complex than had previously been used. The first way this aim was achieved was by using the flotation cell to investigate the effect that altering the feed particle size distribution of a copper tailings ore had on the froth stability and flotation performance with a view to improving the reprocessing of tailings material. The second way was by developing retrofit design modifications for use in the continuous flotation cell to alter the flow conditions and improve flotation performance. Finally the aim was achieved by using positron emission particle tracking (PEPT) to investigate how these retrofit design modification alter the flow of different particle types (hydrophobic and hydrophilic) and different particle sizes.

## 8.1 Key findings

This thesis provided a direct comparison between two measures of froth stability: air recovery and dynamic froth stability, and showed a good correlation between the two. it was shown that there was an optimum in froth stability, at an intermediate particle size distribution, which also corresponded to an improvement in mineral recovery. This work has improved our understanding of the relationship between feed particle size, froth

stability and flotation performance. In addition it has been shown that simple changes can be made to industrial flowsheets in order to improve recovery of valuable material, especially when reprocessing tailings material via froth flotation. This work also showed that the continuous flotation cell can be successfully used to investigate a real and complex ore.

Whilst it was possible to use a real ore with the continuous flotation cell, it was decided that a synthetic two-species ore would be used for the remaining experiments in this thesis. This decision was taken as a two-species ore is easier to analyse and therefore better facilitates the assessment of different design modifications. In addition, a two-species ore still gives a better representation of true flotation than had previously been studied in the continuous flotation cell.

The continuously overflowing, bench scale flotation cell was then used to investigate the effects that inserting two retrofit design modifications, into the top of the pulp zone, had on flotation performance and froth stability of the two-species system. The first mesh design was the same as was shown to be optimal for Norori-McCormac (2015), the second was based on this design, however it was altered so that the outer holes of the mesh are blocked in. The rationale was to reduce the liquid flowrate at the walls of the cell and reduce the entrained gangue material.

In terms of froth stability, for a given superficial gas velocity there was no statistically significant difference between the three designs (the unmodified cell, the basic mesh and the blocked mesh). However, the relationship between changing superficial gas velocity and the air recovery was statistically different between each design. None of the designs showed a peak in air recovery (PAR), however this is likely to do with the small range of superficial gas velocities investigated. The froth stability for the unmodified cell increased with an increase in superficial gas velocity, indicating that the PAR may have been at a higher superficial gas velocity. With either of the meshes inserted into the cell, the froth stability decreased with an increasing superficial gas velocity, but at different rates for the different mesh designs. This indicates that inserting one of these two meshes into the cell results in the PAR being achieved at a lower superficial gas velocity than in the unmodified cell. This caries interesting implications from an operational point of view.

In terms of flotation performance, using the basic mesh resulted in an improved concentrate, grade but a reduced indicative recovery relative to the unmodified cell. On

the other hand, the blocked mesh had little effect on the grade, yet greatly increased the indicative recovery, especially at the highest superficial gas velocity investigated. The presence of the blocked mesh also led to a substantial increase in water flowrate, which was unexpected, however the mesh also significantly reduce the entrainment factor indicating that it inhibits the recovery of gangue material via entrainment. This has important implications for fine particle flotation as, even if the problem of fine valuable attachment can be overcome, there will still be a high level of entrainment of fine gangue material, therefore, the blocked mesh may help to improve the grade of the concentrate with feeds that have a very fine particle size distribution, such as tailings.

The two retrofit design modifications were subsequently investigated using positron emission particle tracking (PEPT) with a range of tracer types and sizes. It is important to note that the tracers used in this these were much larger than the size of the particles in the system due to the limitations in the tracer manufacture process. However, they allow for a systematic investigation of particle size effects, while maintaining a representative particle size distribution of the feed and can be similar to the size of particles being investigated for "coarse particle flotation". The analysis of the PEPT data showed that the presence of either mesh in the cell resulted in a shallower froth, and a secondary pulp zone, which was more quiescent than the primary pulp zone. This can be seen in the schematics in figure 6.18. This quiescent secondary pulp zone helped to reduce particle drop off at the pulp-froth interface.

Further analysis of the PEPT data showed that the presence of the basic mesh was detrimental to the flow and recovery of the $400\,\mu\mathrm{m}$ and $500\,\mu\mathrm{m}$ hydrophobic tracers. On the other hand, the basic mesh did result in an improved recovery of the $600\,\mu\mathrm{m}$ hydrophobic tracer, which was not recovered well in the unmodified cell. The blocked mesh, however, resulted in a substantial improvement in the recovery of the $500\,\mu\mathrm{m}$ and $600\,\mu\mathrm{m}$ hydrophobic tracers relative to both the unmodified cell and the basic mesh. Whilst there was a slightly worse recovery of the $400\,\mu\mathrm{m}$ tracer relative to the unmodified case, it was still better relative to the basic mesh. The improved recovery was due to the presence of a mixing loop in the secondary pulp zone, which promoted reattachment of detached particles. A similar, but larger and more well developed, mixing loop was shown for the hydrophilic tracer with the blocked mesh, which prevented the recovery of the hydrophilic tracer to the froth and explains the reduced entrainment factor with this design.

This thesis has presented two methodologies for improvements in the froth flotation

process. Both have important implications for improving the sustainability of the mining industry. Firstly, it was shown that the recovery of valuable minerals from the reprocessing of material from tailings dams can be improved by optimising the particle size distribution of the feed to flotation. Secondly, a retrofit design modification has been proposed that will introduce a quiescent secondary pulp zone into the flotation cell, which resulted in an improvement in recovery and a reduction in entrained hydrophilic material. This design modification was also shown to result in an environment thought conducive to successful flotation of coarse particles. Implementing such design modifications at the industrial scale may result in substantial benefits by reducing energy consumption used in comminution.

These results have only been shown to be the case at the bench-scale, and so there is scope for further testing of these modifications in order to scale up for industrial operation. There are challenges involved with scaling up the physical characteristics of a cell, primarily the fact that there are stagnant areas of the froth towards the centre (Zheng et al., 2004). This is overcome in industry by altering the launders of the cell or introducing crowders (Mesa and Brito-Parada, 2019), and so it is imperative not only to consider how the results from this work translate into a larger flotation cell, but also how the horizontal mesh design would interact with launders and crowders. This can be done in stages with different size laboratory scale equipment, which allows more control, before moving to pilot scale and eventually plant scale. Numerical simulations would also be integral in improving the design modification with regards to scale up.

## 8.2 Further work

As was discussed in chapter 4, there are limitations to the current set up of the continuously overflowing flotation cell. Primarily that it is not possible to obtain large enough samples of the concentrate for a full mineralogical analysis. In addition to this, as the concentrate is pumped directly back into the pulp of the cell, there is no tailings stream and so a proxy for recovery needs to be used. Both of these limitations could be improved upon by introducing a sump. This will allow direct recovery to be calculated and should also allow large concentrate samples to be taken without affecting steady state operation. This may then make it easier to use a more complex ore than the two-species system.

Whilst the retrofit design modifications were shown to result in a quiescent pulp

zone, and improved the flotation of a $600\,\mu\mathrm{m}$ tracer, the particle size distribution of the magnetite-silica feed was not varied. It would be interesting to investigate how the effects that the retrofit design modifications had on flotation vary with different feeds, with a particular focus on very fine and very coarse material. One of the other key findings from the PEPT data was that with the design modifications inserted into the cell the froth depth appeared to be reduced, however this did not affect the flotation performance as was expected. The reasons for this could be investigated further by running experiments controlling and varying the froth depth with the different modifications. The froth depth could be monitored using a device like a guided radar level sensor, although this would come with the caveat of potentially altering the froth properties at such a small scale and being challenging to implement during PEPT studies.

In addition, it would be interesting to investigate the improvements shown by blocking in the outer mesh holes further. This could be done by producing a series of meshes with different areas blocked in, to determine if there is an optimum configuration, both in terms of flotation performance and also in PEPT experiments. Alongside this, it is important to understand the mechanism behind the increased water recovery with the blocked mesh to inform the design of future design modifications. This could be done with a combination of numerical simulations and the use of a neutrally buoyant naturally hydrophobic tracer to act as a better analogy to the water in the system rather than the hydrophobic particles.

There are limitations with the current tracer manufacture process which resulted in it being challenging to produce tracers of a similar size and density to the particles in the system. Further work needs to be done to refine the manufacture process to allow for smaller tracers to be created and for the density to be modified such that it is a closer match to the different particle types being used in the system.

Conducting experiments in a continuously overflowing flotation cell at the bench scale has many benefits. The cell has been specifically designed to fit within the field of view of the PEPT camera, and so can easily be used to investigate how different design modifications affect the behaviour of different particles. In addition to this, the size of the cell means that the design modifications can easily be prototyped with the use of 3D printing. This means that this bench scale cell is incredibly flexible and a good point for initially testing new designs. However, due to the small sample sizes that can be taken from the concentrate, it is challenging to gain a full understanding of how modifications affect flotation performance of different particles (e.g. varied size and mineralogy). For this

reason, it is important to also test the design modifications that are shown to be optimal at a larger laboratory scale, such as that used by Morrison et al. (2017). This will be the first step in the process of scaling-up these types of retrofit designs for industrial use. Future work would also include developing the mesh designs further with simulations at a variety of different scales and investigating how these new retrofit design modifications could potentially interact with those already used in industry such as different launders and crowders. This will be especially important for investigations at larger sizes, close to industrial flotation.

## References

Ahmed, N., Jameson, G., 1985. The effect of bubble size on the rate of flotation of fine particles. International Journal of Mineral Processing 14 (3), 195–215.

Ahmed, N., Jameson, G. J., 1989. Flotation Kinetics. Mineral Processing and Extractive Metallurgy Review 5 (1-4), 77–99.

Aktas, Z., Cilliers, J., Banford, A., 2008. Dynamic froth stability: Particle size, airflow rate and conditioning time effects. International Journal of Mineral Processing 87 (1-2), 65–71.

Ata, S., 2011. The role of frother on the detachment of particles from bubbles. Minerals Engineering 24 (5), 476–478.

Ata, S., 2012. Phenomena in the froth phase of flotation — A review. International Journal of Mineral Processing 102-103, 1–12.

Ata, S., Ahmed, N., Jameson, G. J., 2002. Collection of hydrophobic particles in the froth phase. International Journal of Mineral Processing 64 (2), 101–122.

Ata, S., Jameson, G., 2005. The formation of bubble clusters in flotation cells. International Journal of Mineral Processing 76 (1), 123–139.

Ata, S., Jameson, G. J., 2013. Recovery of coarse particles in the froth phase – A case study. Minerals Engineering 45, 121–127.

Awatey, B., Thanasekaran, H., Kohmuench, J. N., Skinner, W., Zanin, M., 2013. Optimization of operating parameters for coarse sphalerite flotation in the HydroFloat fluidised-bed separator. Minerals Engineering 50-51, 99–105.

Barbian, N., Hadler, K., Cilliers, J. J., 2006. The froth stability column: Measuring froth stability at an industrial scale. Minerals Engineering 19 (6), 713–718.

Barbian, N., Hadler, K., Ventura-Medina, E., Cilliers, J. J., 2005. The froth stability column: linking froth stability and flotation performance. Minerals Engineering 18 (3), 317–324.

Barbian, N., Ventura-Medina, E., Cilliers, J., 2003. Dynamic froth stability in froth flotation. Minerals Engineering 16 (11), 1111–1116.

Bemrose, C., Fowles, P., Hawkesworth, M., O'Dwyer, M., 1988. Application of positron emission tomography to particulate flow measurement in chemical engineering pro-

cesses. Nuclear Instruments and Methods in Physics Research Section A: Accelerators, Spectrometers, Detectors and Associated Equipment 273 (2-3), 874–880.

Bikerman, J., 1948. Surface chemistry for industiral research. Academic Press Inc., New York.

Bikerman, J., 1973. Formation and structure. In: Foams. Springer, pp. 33–64.

Boucher, D., Jordens, A., Sovechles, J., Langlois, R., Leadbeater, T. W., Rowson, N. A., Cilliers, J. J., Waters, K. E., 2017. Direct mineral tracer activation in positron emission particle tracking of a flotation cell. Minerals Engineering 100, 155–165.

Bournival, G., Ata, S., Jameson, G., 2014. The influence of submicron particles and salt on the recovery of coarse particles. Minerals Engineering 69, 146–153.

Buffler, A., Cole, K., Leadbeater, T. W., Van Heerden, M. R., 2018. Positron emission particle tracking: A powerful technique for flow studies 48, 1860113.

Bulatovic, S. M., 2007. Handbook of flotation reagents : chemistry, theory and practice. Elsevier.

Calvo, G., Mudd, G., Valero, A., Valero, A., 2016. Decreasing ore grades in global metallic mining: A theoretical issue or a global reality? Resources 5 (4), 36.

Chipfunhu, D., Zanin, M., Grano, S., 2011. The dependency of the critical contact angle for flotation on particle size - Modelling the limits of fine particle flotation. Minerals Engineering 24, 50–57.

Chiti, F., Bakalis, S., Bujalski, W., Barigou, M., Eaglesham, A., Nienow, A. W., 2011. Using positron emission particle tracking (PEPT) to study the turbulent flow in a baffled vessel agitated by a Rushton turbine: Improving data treatment and validation. Chemical Engineering Research and Design 89 (10), 1947–1960.

Cilek, E. C., Karaca, S., 2015. Effect of nanoparticles on froth stability and bubble size distribution in flotation. International Journal of Mineral Processing 138, 6–14.

Clayton, R., Jameson, G., Manlapig, E., 1991. The development and application of the Jameson cell. Minerals Engineering 4 (7-11), 925–933.

Cole, K., Buffler, A., Cilliers, J., Govender, I., Heng, J., Liu, C., Parker, D., Shah, U., van Heerden, M., Fan, X., 2014. A surface coating method to modify tracers for positron

emission particle tracking (PEPT) measurements of froth flotation. Powder Technology 263, 26–30.

Cole, K., Buffler, A., van der Meulen, N., Cilliers, J., Franzidis, J.-P., Govender, I., Liu, C., van Heerden, M., 2012. Positron emission particle tracking measurements with 50 micron tracers. Chemical Engineering Science 75, 235–242.

Cole, K., Waters, K., Parker, D., Neethling, S., Cilliers, J., 2010. PEPT combined with high speed digital imaging for particle tracking in dynamic foams. Chemical Engineering Science 65 (5), 1887–1890.

Coleman, R., Rinne, A., 2011. Flotation Mechanism Design for Improved Metallurgical and Energy Performance. Tech. rep.

Costes, J., Couderc, J., 1988. Study by laser Doppler anemometry of the turbulent flow induced by a Rushton turbine in a stirred tank: Influence of the size of the units—I. Mean flow and turbulence. Chemical Engineering Science 43 (10), 2751–2764.

Crawford, R., Ralston, J., 1988. The influence of particle size and contact angle in mineral flotation. International Journal of Mineral Processing 23 (1-2), 1–24.

Dippenaar, A., 1982. The destabilization of froth by solids. II. The rate-determining step. International Journal of Mineral Processing 9 (1), 15–22.

Feng, D., Aldrich, C., 1999. Effect of particle size on flotation performance of complex sulphide ores. Minerals Engineering 12 (7), 721–731.

Filippov, L., Filippova, I., Severov, V., 2010. The use of collectors mixture in the reverse cationic flotation of magnetite ore: The role of Fe-bearing silicates. Minerals Engineering 23 (2), 91–98.

Fuerstenau, M. C., Jameson, G. J., Yoon, R.-H., 2007. Froth Flotation: A Century of Innovation. SME.

Gontijo, C. d. F., Fornasiero, D., Ralston, J., 2008. The Limits of Fine and Coarse Particle Flotation. The Canadian Journal of Chemical Engineering 85 (5), 739–747.

Gordon, R. B., 2002. Production residues in copper technological cycles. Resources, Conservation and Recycling 36 (2), 87–106.

Govender, I., Morrison, A. J., Mainza, A., Van Der Westuien, A., Franzidis, J.-P., Powell, M.,

2010. Using positron emission particle tracking (PEPT) to investigate industrial systmes. Tech. rep.

Gulsoy, O. Y., 2005. A simple model for the calculation of entrainment in flotation. Korean Journal of Chemical Engineering 22 (4), 628–634.

Gupta, A., Yan, D., 2006. Mineral Processing Design and Operation. Elsevier.

Hadler, K., Cilliers, J., 2009. The relationship between the peak in air recovery and flotation bank performance. Minerals Engineering 22 (5), 451–455.

Hadler, K., Greyling, M., Plint, N., Cilliers, J., 2012. The effect of froth depth on air recovery and flotation performance. Minerals Engineering 36, 248–253.

Hadler, K., Smith, C., Cilliers, J., 2010. Recovery vs. mass pull: The link to air recovery. Minerals Engineering 23 (11), 994–1002.

Hemmati Chegeni, M., Abdollahy, M., Khalesi, M. R., 2016. Bubble loading measurement in a continuous flotation column. Minerals Engineering 85, 49–54.

Henderson, R. D., 2016. Minera valle central operation rancagua, region VI, Chile 43-101 Technical report prepared for : Amerigo Resources Ltd. Tech. Rep. December.

Hewitt, D., Fornasiero, D., Ralston, J., Fisher, L. R., 1993. Aqueous Film Drainage at the Quartz/Water/Air Interface. Tech. Rep. 5.

Ip, S., Wang, S., Toguri, J., 1999. Aluminum foam stabilization by solid particles. Canadian Metallurgical Quarterly 38 (1), 81–92.

Jameson, G. J., 2010. New directions in flotation machine design. Minerals Engineering 23 (11-13), 835–841.

Jameson, G. J., Emer, C., 2019. Coarse chalcopyrite recovery in a universal froth flotation machine. Minerals Engineering 134, 118–133.

Johansson, G., Pugh, R., 1992. The influence of particle size and hydrophobicity on the stability of mineralized froths. International Journal of Mineral Processing 34 (1-2), 1–21.

King, R., 2012. Modeling and simulation of mineral processing systems b. In: Modelling and simulation of mineral processing systems. Vol. XXXIII. p. 492.

Kohmuench, J., Mankosa, M., Thanasekaran, H., Hobert, A., 2018. Improving coarse particle flotation using the HydroFloat$^{TM}$ (raising the trunk of the elephant curve). Minerals Engineering 121, 137–145.

Leistner, T., Peuker, U. A., Rudolph, M., 2017. How gangue particle size can affect the recovery of ultrafine and fine particles during froth flotation. Minerals Engineering 109, 1–9.

Li, G., Deng, L., Cao, Y., Wang, B., Ran, J., Zhang, H., 2017. Effect of sodium chloride on fine coal flotation and discussion based on froth stability and particle coagulation. International Journal of Mineral Processing 169, 47–52.

Li, Y., Honaker, R., Chen, J., Shen, L., 2016. Effect of particle size on the reverse flotation of subbituminous coal. Powder Technology 301, 323–330.

Liang, L., Li, Z., Peng, Y., Tan, J., Xie, G., 2015. Influence of coal particles on froth stability and flotation performance. Minerals Engineering 81, 96–102.

Liu, Q., Wannas, D., 2004. The Role of polymeric-depressant-induced flocculation in fine particle flotation. Tech. rep.

Mackay, I., Mendez, E., Molina, I., Videla, A., Cilliers, J., Brito-Parada, P., 2018. Dynamic froth stability of copper flotation tailings. Minerals Engineering 124, 103–107.

Mackay, I., Videla, A., Brito-Parada, P., 2019. The link between particle size and froth stability - Implications for reprocessing of flotation tailings. Journal of Cleaner Production.

McFadzean, B., Achaye, I., Wiese, J., Chidzanira, T., Harris, M., 2016a. The effect of particle size on froth stabilities of different ores. XXVII International Mineral Processing Congress, 1–11.

McFadzean, B., Marozva, T., Wiese, J., 2016b. Flotation frother mixtures: Decoupling the sub-processes of froth stability, froth recovery and entrainment. Minerals Engineering 85, 72–79.

Mesa, D., Brito-Parada, P. R., 2019. Scale-up in froth flotation: A state-of-the-art review. Separation and Purification Technology 210, 950–962.

Miettinen, T., Ralston, J., Fornasiero, D., 2010. The limits of fine particle flotation. Minerals Engineering 23 (5), 420–437.

Molina, I., Martins, P., Videla, A., 2016. On the interaction effect between xanthate colletor, frothers and solids: Alaboratory characterization of copper sulfide flotation. Procemin2016, 12th International Mineral Processing Conference, Santiago, Chile.

Morrison, A., Brito-Parada, P., Cilliers, J., 2017. Tank design modifications for the improved performance of froth flotation equipment. Ph.D. thesis.

Morrison, A., Govender, I., Mainza, A., Parker, D., 2016. The shape and behaviour of a granular bed in a rotating drum using Eulerian flow fields obtained from PEPT. Chemical Engineering Science 152, 186–198.

Neethling, S., Cilliers, J., 2009. The entrainment factor in froth flotation: Model for particle size and other operating parameter effects. International Journal of Mineral Processing 93 (2), 141–148.

Neethling, S., Lee, H., Cilliers, J., 2003. Simple relationships for predicting the recovery of liquid from flowing foams and froths. Minerals Engineering 16 (11), 1123–1130.

Newcombe, B., Bradshaw, D., Wightman, E., 2012. Flash flotation... and the plight of the coarse particle. Minerals Engineering 34, 1–10.

Nguyen, A., Schulze, H., Ralston, J., 1997. Elementary steps in particle—bubble attachment. International Journal of Mineral Processing 51 (1-4), 183–195.

Norori-McCormac, A., 2015. The relationship between particle size, cell design and air recovery: the effect on flotation performance Alexander Norori-McCormac. Ph.D. thesis.

Norori-McCormac, A., Brito-Parada, P. R., Hadler, K., Cole, K., Cilliers, J. J., 2017. The effect of particle size distribution on froth stability in flotation. Separation and Purification Technology 184, 240–247.

Parker, D., Broadbent, C., Fowles, P., Hawkesworth, M., McNeil, P., 1993. Positron emission particle tracking - a technique for studying flow within engineering equipment. Nuclear Instruments and Methods in Physics Research Section A: Accelerators, Spectrometers, Detectors and Associated Equipment 326 (3), 592–607.

Parker, D., Forster, R., Fowles, P., Takhar, P., 2002. Positron emission particle tracking using the new Birmingham positron camera. Nuclear Instruments and Methods in Physics Research Section A: Accelerators, Spectrometers, Detectors and Associated Equipment 477 (1-3), 540–545.

Parker, D. J., 2017. Positron emission particle tracking and its application to granular media. Review of Scientific Instruments 88 (5), 051803.

Pianko-Oprych, P., Nienow, A., Barigou, M., 2009. Positron emission particle tracking (PEPT) compared to particle image velocimetry (PIV) for studying the flow generated by a pitched-blade turbine in single phase and multi-phase systems. Chemical Engineering Science 64 (23), 4955–4968.

Radman, J. R., Langlois, R., Leadbeater, T., Finch, J., Rowson, N., Waters, K., 2014. Particle flow visualization in quartz slurry inside a hydrocyclone using the positron emission particle tracking technique. Minerals Engineering 62, 142–145.

Rahman, R. M., Ata, S., Jameson, G. J., 2012. The effect of flotation variables on the recovery of different particle size fractions in the froth and the pulp. International Journal of Mineral Processing 106-109, 70–77.

Ralston, J., Fornasiero, D., Hayes, R., 1999. Bubble–particle attachment and detachment in flotation. International Journal of Mineral Processing 56 (1-4), 133–164.

Rubio, J., Capponi, F., Nunes, D. G., Guerrero, C. P., Berkowitz, G., 2003. Advances in flotation of minerals fines. Tech. rep.

Scheludko, A., Toshev, B., Bojadjiev, D., 1976. Attachment of particles to a liquid surface (capillary theory of flotation). Journal of the Chemical Society, Faraday Transactions 1: Physical Chemistry in Condensed Phases 72, 2815–2828.

Schulze, H., 1977. New theoretical and experimental investigations on stability of bubble/particle aggregates in flotation: A theory on the upper particle size of floatability. International Journal of Mineral Processing 4 (3), 241–259.

Schulze, H., Radoev, B., Geidel, T., Stechemesser, H., Töpfer, E., 1989. Investigations of the collision process between particles and gas bubbles in flotation — A theoretical analysis. International Journal of Mineral Processing 27 (3-4), 263–278.

Schwarz, S., Grano, S., 2005. Effect of particle hydrophobicity on particle and water transport across a flotation froth. Colloids and Surfaces A: Physicochemical and Engineering Aspects 256 (2), 157–164.

Tao, D., Luttrell, G., Yoon, R.-H., 2000. A parametric study of froth stability and its effect

on column flotation of fine particles. International Journal of Mineral Processing 59 (1), 25–43.

Trahar, W., 1981. A rational interpretation of the role of particle size in flotation. International Journal of Mineral Processing 8 (4), 289–327.

Vieira, A. M., Peres, A. E., 2007. The effect of amine type, pH, and size range in the flotation of quartz. Minerals Engineering 20 (10), 1008–1013.

Wang, J., Wang, L., Hanotu, J., Zimmerman, W. B., 2017. Improving the performance of coal flotation using oscillatory air supply. Fuel Processing Technology 165, 131–137.

Waters, K., Rowson, N., Fan, X., Parker, D., Cilliers, J., 2008. Positron emission particle tracking as a method to map the movement of particles in the pulp and froth phases. Minerals Engineering 21 (12-14), 877–882.

Waters, K. E., Rowson, N. A., Fan, X. F., Parker, D. J., Cilliers, J. J., 2009. The use of positron emission particle tracking as a method for tracking particles in flotation froths. Philosophical Magazine Letters 88 (910), 735–739.

Wills, B. A., Finch, J., 2015. Wills' mineral processing technology: an introduction to the practical aspects of ore treatment and mineral recovery. Butterworth-Heinemann.

Xia, J., Rinne, A., Myllykangas, H., Gronstrand, S., 2010. Performance of outotec floatforce® flotation mechanism - a study in both computational fluid dynamics and industrial scale measurement. Tech. rep.

Yianatos, J. B., Bergh, L. G., Díaz, F., Rodríguez, J., 2005. Mixing characteristics of industrial flotation equipment. Chemical Engineering Science 60 (8-9), 2273–2282.

Zheng, X., Franzidis, J.-P., Manlapig, E., 2004. Modelling of froth transportation in industrial flotation cells: Part I. Development of froth transportation models for attached particles. Minerals Engineering 17 (9-10), 981–988.

# Appendix A

# Publications

## A.1 Dynamic froth stability of copper flotation tailings

**(Minerals Engineering - *published May 2018*)**

The results from the dynamic froth stability experiments in chapter 4 were published as a paper in Minerals Engineering in May 2018. This is an open access paper and can be found here: https://doi.org/10.1016/j.mineng.2018.05.005

## A.2 The link between particle size and froth stability - implications for reprocessing of flotation tailings

**(Journal of cleaner production - *published September 2019*)**

The results from the air recovery experiments, as well as the comparison between the two stability measures in chapter 4 were published as a paper in the Journal of Cleaner Production in September 2019 and can be found here: https://doi.org/10.1016/j.jclepro.2019.118436

Minerals Engineering 124 (2018) 103–107

Contents lists available at ScienceDirect

Minerals Engineering

journal homepage: www.elsevier.com/locate/mineng

# Dynamic froth stability of copper flotation tailings

I. Mackay[a,*], E. Mendez[b], I. Molina[b], A.R. Videla[b], J.J. Cilliers[a], P.R. Brito-Parada[a]

[a] Department of Earth Science and Engineering, Imperial College London, SW7 2AZ, United Kingdom
[b] Department of Mining Engineering, Pontificia Universidad Catolica de Chile, 7820436, Chile

ARTICLE INFO

*Keywords:*
Particle size
Column flotation
Copper tailings
Dynamic froth stability

ABSTRACT

In this work, dynamic froth stability is used for the first time to investigate the flotation behaviour of copper tailings. Reprocessing of material from tailings dams is not only environmentally desirable, but also increasingly economically feasible as head grades can be high compared to new deposits. Flotation tailings, however, usually contain a large proportion of fine (10–50 μm) and ultra fine (< 10μm) material and the effect of these particle sizes on froth stability is not yet fully understood.

For this study, samples were obtained from the overflow and underflow streams of the primary hydrocyclone at a concentrator that reprocesses copper flotation tailings. These samples were combined in different ratios to assess the dynamic froth stabilities at a wide range of particle size distributions and superficial gas velocities. The findings have shown that the effect of particle size on dynamic froth stability can be more complex than previously thought, with a local maximum in dynamic froth stability found at each air rate. Moreover, batch tests suggest that a local maximum in stability can be linked to improvements in flotation performance. Thus this work demonstrates that the dynamic froth stability can be used to find an optimum particle size distribution required to enhance flotation. This also has important implications for the reprocessing of copper tailings as it could inform the selection of the cut size for the hydrocyclones.

## 1. Introduction

One of the key challenges currently facing the mining industry is the decreasing head grades whilst the global demand for metals is ever increasing. It is therefore becoming more important for the industry to look to other potential sources to meet the demand. One such source is tailings dams. Historically, processing efficiency was much lower than it is today, resulting in tailings being higher grade (Falagán et al., 2017). For example, over the 20th century the copper grade of tailings has fallen from 0.75% to 0.14% (Gordon, 2002). In some cases historic tailings dams can therefore be higher grade than current deposits. Reprocessing this material is beneficial to industry for several reasons. Firstly, there are lower costs involved compared to a new mine as the ore has already been mined and milled. Secondly, tailings dams present a significant environmental problem, so reprocessing can help to reduce environmental contamination (Chen et al., 2014). However, there is no blanket approach to reprocessing tailings as there will be different requirements associated to each individual dam (Edraki et al., 2014). Another problem is that the majority of material held in tailings dams is fine grained, < 50 μm.

### 1.1. Fine particle flotation

There are several challenges in the flotation of fine particles, generally those less than 50 μm in size. Firstly, the probability of bubble particle attachment occurring is low (Miettinen et al., 2010). Secondly, they are more easily entrained due to the low particle diameter to Plateau border size ratio (Trahar, 1981) and thirdly, they can require higher quantities of reagents in order to increase the contact angle caused by a higher specific surface area (Chipfunhu et al., 2011).

Whilst there has been a significant body of work in fine particle flotation, it is not yet fully understood whether fine particles stabilise or destabilise the froth. Johansson and Pugh (1992) studied the effects of different contact angles and different particle sizes of quartz on the dynamic froth stability in a laboratory scale, stirred flotation column. For the finest particle size investigated, 26–44 μm, it was found that particles stabilised the froth when they were moderately hydrophobic (Contact Angle ≈50–65°), however at lower contact angles they had little effect on the stability and at higher contact angles they destabilised the froth. Tao et al. (2000) showed that a small increment in the solids concentration of very fine coal particles (10 μm), also in a laboratory scale flotation column, lead to a large decrease in water recovery and this suggested that the fine particles had a destabilising

* Corresponding author.
*E-mail address:* isobel.mackay11@imperial.ac.uk (I. Mackay).

https://doi.org/10.1016/j.mineng.2018.05.005
Received 21 December 2017; Received in revised form 18 April 2018; Accepted 4 May 2018
Available online 21 May 2018
0892-6875/ © 2018 The Authors. Published by Elsevier Ltd. This is an open access article under the CC BY license (http://creativecommons.org/licenses/BY/4.0/).

effect on the froth.

Ahmed and Jameson (1985) suggested that a potential way to achieve the flotation of fine and coarse particles is to split the feed and use different operating conditions to treat each size. However, this requires a more complex flowsheet and so it is also important to understand if there are techniques for treating different sizes together. The interaction between fine particles and coarse particles of pure silica has been studied by Vieira and Peres (2007) and Rahman et al. (2012). The work by Vieira and Peres (2007) investigated the effects that changing the amount of fine material (38–74 μm) in the feed had on the flotation recovery of different particle sizes using a Denver cell. The results showed that there is an intermediate amount of fines required in the feed to optimise the solids recovery of all particle sizes investigated. They suggested that this can be attributed to an improvement in froth stability. Rahman et al. (2012) also studied the effects of changing feed size (with d80s ranging from 80 to 240 μm) on solids recovery in a laboratory scale flotation column. They found that an increase in the amount of fine material (i.e. a decrease in d80) resulted in increased recoveries. Contrary to Vieira and Peres (2007),Rahman et al. (2012) did not observe that an intermediate amount of fines in the feed produced the best results.

Work by Leistner et al. (2017) investigated the effect that the size of gangue material, quartz, had on the recovery of ultrafine (< 10 μm) and fine (10–50 μm) particles of the target mineral, magnetite. These experiments were conducted in a mechanical laboratory scale flotation cell. The results indicated that using fine quartz increases magnetite recovery for both size fractions whilst using ultrafine quartz particles has the opposite effect. This indicates that the recovery of ultrafine valuable particles can be improved in the presence of coarser gangue particles.

Froth stability is not only dependent on particle size or hydrophobicity, as already discussed, but the superficial gas velocity also plays an important role. Recently, Norori-McCormac et al. (2017) used a novel laboratory scale mechanical flotation cell to investigate the effects of superficial gas velocity and particle size on froth stability, measured using air recovery. They found that at high air rates a relatively fine feed, d80 of 89.6 μm, resulted in higher froth stabilities, yet at lower air rates it was an intermediate feed size that yielded the higher froth stabilities. This suggests that the relationship is more complex than previously thought.

### 1.2. Dynamic froth stability

The Bikerman test was developed to investigate the foam stability of dynamic systems using a flotation column (Bikerman, 1948). In this test gas is bubbled through a porous membrane into liquid in the column, allowing a foam layer to form at the top. This foam will rise until it reaches a steady state where the volume of gas entering the system, as bubbles, is equal to the volume of gas escaping when the bubbles burst (Bikerman, 1948). Many studies have shown that the height of the column of foam is proportional to the rate of flow of gas in the system and Bikerman (1948) defines the rate of proportionality as the dynamic foam stability (Σ):

$$\Sigma = \frac{V_f}{Q} = \frac{H}{J_g}, \tag{1}$$

where $V_f$ is the volume of the foam, $Q$ is the volumetric flow rate of the gas, $H$ is the foam height of the system at steady state and $J_g$ is the superficial gas velocity. This rate of proportionality does not only apply to foams but also to froths and can also be described as the average lifetime of a bubble in the froth (Bikerman, 1973).

There have been several studies looking at the effects of particle size and superficial gas velocity on froth stability. Ip et al. (1999) investigated the relationship between froth stability and particle size, using a silica, water, air system. Although the results showed a general decrease in stability with an increase in mean particle size, this was not a smooth change; between a size of 60 μm and 90 μm there was little variation in froth stability. Barbian et al. (2003) used a modified Denver cell with a Platinum Group Metal (PGM) ore and observed that the dynamic froth stability factor decreased with an increase in superficial gas velocities. However, the superficial gas velocities in their work ranged between 0.13 cm $s^{-1}$ and 0.66 cm $s^{-1}$ and were therefore low compared to industrial flotation cells. Aktas et al. (2008) used a similar cell, again with a PGM ore, and observed the same relationship between dynamic froth stability and superficial gas velocity, again investigating the effects at low superficial gas velocities, between 0.26 cm $s^{-1}$ and 0.53 cm $s^{-1}$. In addition to varying the gas velocity (Aktas et al., 2008) also varied the particle size and found that as the particle size increased the dynamic froth stability decreased, however, only four different sizes were used and these were coarse (d90 of 118 μm to 306 μm) and so the study doesn't give information about a broad range of both fine and coarse particles. More recently, Liang et al. (2015) investigated the effects of coal particles of different sizes on the froth stability again using a modified stability column. Four different size fractions were used here, namely −74 μm, −125 + 74 μm, −250 + 125 μm and −500 + 250 μm. Whilst these sizes consider a wider overall distribution than other studies, each of the size ranges tested was quite broad. These experiments were also run at low gas velocities of 0.2 cm $s^{-1}$. McFadzean et al. (2016a) studied the effects of particle size on dynamic froth stability for three different ores: a synthetic silica and pyrite ore, a PGM ore, and an Itabirite ore. The results for all three ores showed a smooth decreasing power law relationship when increasing the average feed particle size. Whilst the particle size of the synthetic ore ranges from around 16 μm to 210 μm the other two ores had smaller size ranges, between 29 μm and 71 μm. These experiments were run at a superficial gas velocity of 0.98 cm $s^{-1}$.

Barbian et al. (2005) developed a froth stability column to be used at industrial scale, allowing froth stability to be correlated to flotation performance. The results, from a copper sulphide ore, showed that the highest dynamic froth stability resulted in the highest copper grade but lowest recovery. McFadzean et al. (2016b) also showed a link between dynamic froth stability and flotation performance in their work. Their study investigated the effects of different frother blends on the froth stability of a PGM ore with an agitated laboratory scale column. The results showed that a higher froth stability resulted in higher recovery, but that there was little correlation with grade. The results from these two studies are contradictory suggesting that the relationship between froth stability and flotation performance is more complicated.

Whilst there have been various studies investigating the dynamic froth stability and the link to particle size, different gas velocities and flotation performance, there has been no attempt to link all three aspects. This work fills this gap by determining the dynamic froth stability of copper flotation tailings, considering different particle size distributions and at a range of superficial gas velocities. In addition, batch flotation tests were performed for selected conditions to obtain a preliminary assessment of flotation performance. The range of particle sizes investigated here are wider than have previously been studied and the superficial gas velocities are higher, and closer to those encountered in industrial flotation cells.

## 2. Methodology and equipment

### 2.1. Case study: tailings reprocessing plant

A processing plant in Chile has been reprocessing copper flotation tailings from two historic and one fresh tailings dams since 1992. The grade ranges from 0.12% Cu for the fresh tailings to 0.27% Cu for the historic tailings. The feed from these tailings dams to the plant contains a high proportion of fines, approximately 50%, by mass, of the material passing 10 μm. Once the tailings feed has been transported to the plant it passes through the primary hydrocyclone for the different particle

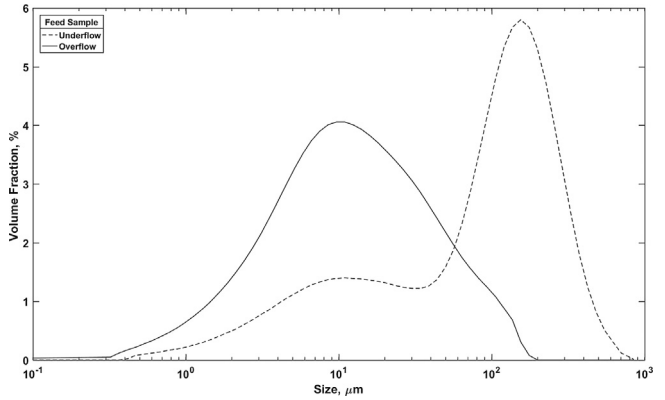



**Fig. 1.** Cumulative size distributions of the hydrocyclone overflow and underflow streams from the copper tailings reprocessing plant.

sizes to be treated separately. The underflow stream, with a d90 of 270 μm, is sent to the flotation circuit.

### 2.2. Materials

Samples of copper tailings were collected from the overflow and underflow streams of the primary hydrocyclone at the processing plant discussed in Section 2.1. The d90s of these samples were 63.7 μm and 279 μm respectively and the particle size distributions of each can be found in Fig. 1. The samples were obtained as slurry, which was subsequently dried and the two sizes combined in different proportions, by mass, to produce seven particle size distributions, which can be seen in Table 1. All experiments were conducted using the same batch of solids collected from the processing plant to minimize any effects due to mineralogy. The experiments were carried out using Sodium Isopropyl Xanthate, as a collector, at a concentration of 50 g $t^{-1}$ and DowFroth400 at a concentration of 20 g $t^{-1}$ as frother. The slurry was modified to pH9 using lime. This reagent environment was studied in previous work by Molina et al. (2016).

### 2.3. Froth stability experiments

A laboratory scale, unstirred flotation column (Fig. 2) was used for the dynamic froth stability experiments in a modified Bikerman test. This set up is similar to the systems used in a variety of other studies (Ip et al., 1999; Cilek and Karaca, 2015; Li et al., 2017). The column was 157 cm tall with graduations on the front wall and a square cross sectional area of 139.2 $cm^2$. Air was injected into a chamber at the base of the column where it then passed through a porous disk (porosity No. 1) of sintered glass, 8 cm in diameter in order to produce bubbles. Six liters of slurry were used with a solids content of 10% for all experiments (Molina et al., 2016). Between each experiment the column and frit were cleaned thoroughly by rinsing each wall with water and then ethanol twice and then finishing with a final rinse with water to ensure

**Table 1**
The proportions of overflow and underflow material in the seven different particle size distributions investigated and their corresponding d10, d50 and d90s

| Overflow | Underflow | d10, μm | d50, μm | d90 μm |
|---|---|---|---|---|
| 1 | 0 | 2.6 | 13 | 64 |
| 0.75 | 0.25 | 3.4 | 36 | 117 |
| 0.50 | 0.50 | 4.2 | 59 | 171 |
| 0.375 | 0.625 | 4.6 | 70 | 198 |
| 0.25 | 0.75 | 5.0 | 82 | 225 |
| 0.125 | 0.875 | 5.3 | 89 | 241 |
| 0 | 1 | 5.8 | 105 | 279 |

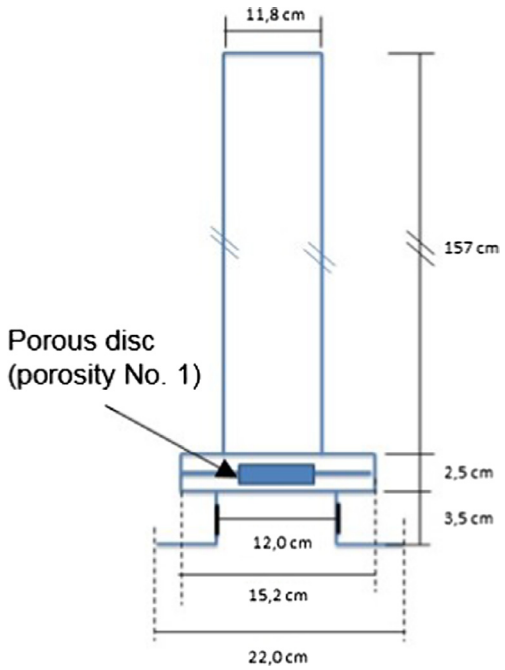



**Fig. 2.** Schematic of the laboratory scale flotation column. Adapted from Molina et al. (2016).

no ethanol remained on the walls.

The froth heights for each of the seven particle size distributions were investigated in the column, each at three different superficial gas velocities that ranged between 0.96 cm $s^{-1}$ and 1.92 cm $s^{-1}$. It is important to note that since a wide range of conditions were evaluated, not all cases could be run at the same three values of superficial gas velocity. For fine particles at high air rates the froth was very stable and would quickly reach the full height of the column and overflow. At the other extreme, coarse particles at low air rates did not produce a stable froth at all. Measurements of the froth height, to the nearest 0.5 cm, were recorded regularly over a 30 min period and each experiment was duplicated.

### 2.4. Flotation performance experiments

Preliminary flotation performance tests for selected particle size distributions were conducted in a 3L Denver cell with a cross-sectional area of 169 $cm^2$ at a superficial gas velocity of 1.44 cm $s^{-1}$. This air rate was chosen to match the air rate for which dynamic froth stability experiments were run for all seven of the particle size distributions. These tests were performed with the same reagent environment and solids concentration as in the column flotation tests. The Denver cell was operated with an agitation speed of 1200 rpm, a conditioning time of 5 min and a flotation time of 10 min. The performance of three particle size distributions were investigated in this set of experiments, those with d90s of 117 μm, 225 μm and 279 μm.

### 2.5. Sample analysis

The particle size distributions of the varying feeds were determined using a Malvern Mastersizer 2000 particle analyser. The concentrate samples from the flotation performance experiments were analysed chemically using atomic adsorption spectrometry to determine copper content.

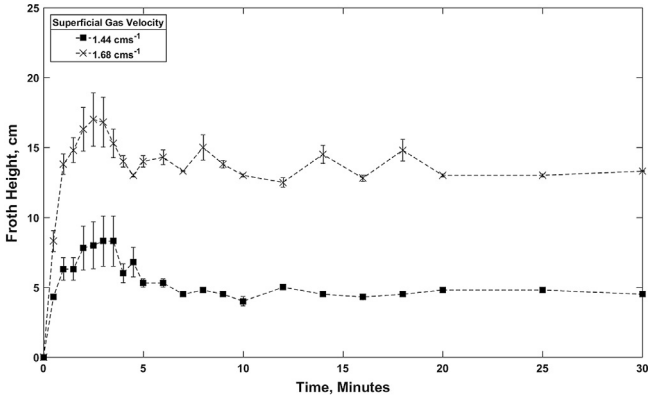



**Fig. 3.** Froth height growth for experiments with d90 of 279 μm over 30 min of operation at two different superficial gas velocities. Intervals represent one standard deviation.

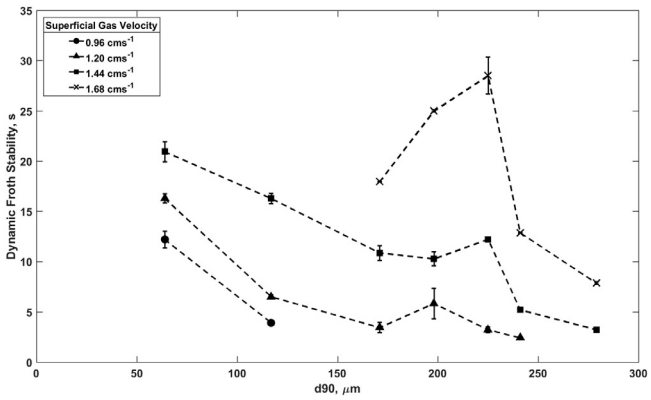



**Fig. 4.** Dynamic froth stability for different particle size distributions at a range of superficial gas velocities. Error bars represent one standard deviation.

## 3. Results & discussion

### 3.1. Particle size and dynamic froth stability

Fig. 3 shows froth height for the experiments at two different air rates for the coarsest particle size distribution, with a d90 of 279 μm. Each curve represents average data across duplicated experiments, with intervals representing one standard deviation. This illustrates that the froth height initially increased and after a period of 5 min slightly decreased again, reaching steady state. Previous work has referred to the maximum froth height, $H_{max}$, when calculating Σ, Eq. (1), however as can be seen from these experiments the maximum height the froth achieves is not the froth height at steady state. In this work, when calculating the dynamic froth stability we have used the equilibrium height, $H_{eq}$, which is the steady state froth height reached after approximately 30 min of operation.

The dynamic froth stability factor, Eq. (1), was calculated for each experiment using the equilibrium heights, which can be found in Table 2. Fig. 4 shows the dynamic froth stability factor, for different particle size distributions at constant air rates. For all particle size distributions, decreasing the superficial gas velocity will lead to a decrease in dynamic froth stability factor. This is contrary to what was found by Aktas et al. (2008). It is important to note that the superficial gas velocities used in this work are higher than those use in previous work and similar to industrial values.

**Table 2**
Average equilibrium heights, $H_{eq}$, and dynamic froth stability factors, Σ, for all particle size distributions and superficial gas velocities, $J_g$, investigated.

| Condition No. | d90, μm | $J_g$, cm s$^{-1}$ | $H_{eq}$, cm | Σ, s |
|---|---|---|---|---|
| 1 | 64 | 0.96 | 11.7 | 12.2 |
| 2 | 64 | 1.20 | 19.6 | 16.3 |
| 3 | 64 | 1.44 | 30.2 | 20.9 |
| 4 | 117 | 0.96 | 3.8 | 3.9 |
| 5 | 117 | 1.20 | 7.8 | 6.5 |
| 6 | 117 | 1.44 | 23.4 | 16.3 |
| 7 | 171 | 1.20 | 4.1 | 3.44 |
| 8 | 171 | 1.44 | 15.7 | 10.9 |
| 9 | 171 | 1.68 | 30.2 | 18.0 |
| 10 | 198 | 1.20 | 7.0 | 5.8 |
| 11 | 198 | 1.44 | 14.8 | 10.3 |
| 12 | 198 | 1.68 | 42.0 | 25.0 |
| 13 | 225 | 1.20 | 3.9 | 3.2 |
| 14 | 225 | 1.44 | 17.6 | 12.2 |
| 15 | 225 | 1.68 | 47.9 | 28.5 |
| 16 | 241 | 1.20 | 2.9 | 2.4 |
| 17 | 241 | 1.44 | 7.5 | 5.2 |
| 18 | 241 | 1.68 | 21.6 | 12.8 |
| 19 | 279 | 1.44 | 4.7 | 3.2 |
| 20 | 279 | 1.68 | 13.2 | 7.9 |
| 21 | 279 | 1.92 | 25.8 | 13.4 |

From the results in Fig. 4 there is an overall decrease in dynamic froth stability with increasing particle size. However, the decrease is not smooth and two stability regimes can be seen. The first is at finer particle size distributions, below 171 μm, where the dynamic froth stability factor decreases as d90 increases. At the coarser particle size distributions, above 171 μm, there is a local maximum in froth stability at a given superficial gas velocity. This maximum is much more pronounced at higher superficial gas velocities.

Previous work by Aktas et al. (2008),Liang et al. (2015) and McFadzean et al. (2016a) only reported a decrease in dynamic froth stability with an increase in particle size. However, there are several differences in experimental method (as discussed in detail in Section 1.2), such as the range of particle sizes considered and the superficial gas velocities used, meaning that a similar maximum may exist in those systems but was not encompassed by the data. At the lower of the two air rates investigated here the data is smoother. These air rates are similar to the one used in experiments by McFadzean et al. (2016a), 0.98 cm s$^{-1}$, suggesting that it is not just the particle size that plays an important role in froth stability but there is also a superficial gas velocity effect. These results also show that the relationship is more complex than previously thought. This is similar to the findings from Norori-McCormac et al. (2017) when investigated the effects particle size and superficial gas velocity have on the air recovery. Whilst Ip et al. (1999) discuss that their results illustrate the same decrease in froth stability with an increase in size, the relationship was not smooth. In fact, the data shows a plateau at a similar particle size to where there local maximum is seen in our data.

It is clear that, when operating towards the right hand side of the graph, there is an optimal particle size distribution that will improve the dynamic froth stability. This suggests that if the tailings reprocessing plant were to slightly lower the cut size of the primary hydrocyclone they could improve the froth stability in the flotation cells. As previously discussed a higher dynamic froth stability has been shown to correlate to an improvement in grade (Barbian et al., 2005) or recovery (McFadzean et al., 2016b).

### 3.2. Particle size and flotation performance

In order to understand the effect of particle size distribution, not only on dynamic froth stability but also on flotation performance, preliminary experiments were conducted using batch flotation tests.

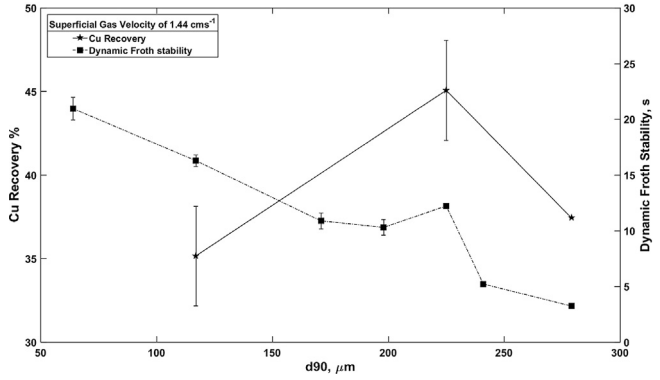



**Fig. 5.** Copper recovery from batch flotation tests and dynamic froth stability at a superficial gas velocity of 1.44 cm $s^{-1}$. Error bars represent one standard deviation.

These were performed on three particle size distributions with a superficial gas velocity of 1.44 cm $s^{-1}$, condition numbers 6, 14 and 19 (from Table 2). The three particle size distributions chosen were *i*) the closest to the feed to the primary hydrocyclone, *ii*) the local maximum in dynamic froth stability, and *iii*) the size currently being sent to the flotation circuit.

Fig. 5 shows the results of copper recovery as a function of particle size (d90) for these tests compared to the dynamic froth stability at the same air rate from Fig. 4. It is observed that at the particle size distribution where there is the local peak in dynamic froth stability, d90 of 225 μm, there is also a peak in copper recovery. It is also interesting to note that out of the three particle sizes the one with highest dynamic froth stability, d90 of 117 μm, actually corresponds to the lowest copper recovery. This indicates that there is not always a direct correlation between dynamic froth stability and copper recovery contrary to the results from McFadzean et al. (2016b). For the tests in this work, the highest copper grade was achieved at the lowest dynamic froth stability, with a d90 of 279 μm, which is the opposite of what was reported in Barbian et al. (2005). The results here show that dynamic froth stability alone cannot be used to determine an optimal particle size for performance, but it is also important to consider which of the two regimes is being investigated.

## 4. Conclusions

This work has investigated the effects of varying the particle size distribution on the dynamic froth stability of samples from a copper flotation tailings dam at different superficial gas velocities. Compared to previous work, this study has investigated a wider range of particle size distributions, and at superficial gas velocities that are more comparable to those used in industrial flotation cells. In all experiments, for the same feed particle size distribution, there was an increase in dynamic froth stability with an increase in superficial gas velocity.

When considering the relationship between particle size distribution and dynamic froth stability, we postulate the existence of two regimes. The first is at lower feed d90s, where there is a decrease in froth stability for an increase in particle size. The second is at higher feed d90s, where dynamic froth stability goes through a maximum as the d90 of the feed increases. A preliminary investigation of the relationship between dynamic froth stability and flotation performance was carried out using batch flotation tests for selected particle size distributions at one air rate. The results showed that the local peak in dynamic froth stability corresponded to a clear improvement in copper recovery for the system. This suggests that, when operating at coarser particle size distributions, the presence of fines in the system can, to some extent, improve the dynamic froth stability and flotation performance. However, if there is too high a proportion of fines the increase in dynamic froth stability does not necessarily correspond to improved performance. In the case of the reprocessing plant this work suggests that operations may be improved by lowering the cut size of the primary hydrocyclone. Future work will include testing the same ore in laboratory experiments that are more representative of plant scale flotation.

This work has shown that the relationship between froth stability, particle size and air rate is more complex than previously thought. Particularly, in order to use dynamic froth stability to determine the optimum particle size distribution for flotation, a wide range of particle sizes should be considered.

## Acknowledgments

This work was supported by the Engineering and Physical Sciences Research Council (award number 1661853); the Society for Chemical Industry and the Faculty of Engineering at Pontificia Universidad Catolica de Chile.

## References

Ahmed, N., Jameson, G., 1985. The effect of bubble size on the rate of flotation of fine particles. Int. J. Miner. Process. 14 (3), 195–215.
Aktas, Z., Cilliers, J., Banford, A., 2008. Dynamic froth stability: particle size, airflow rate and conditioning time effects. Int. J. Miner. Process. 87 (1-2), 65–71.
Barbian, N., Hadler, K., Ventura-Medina, E., Cilliers, J., 2005. The froth stability column: linking froth stability and flotation performance. Miner. Eng. 18 (3), 317–324.
Barbian, N., Ventura-Medina, E., Cilliers, J., 2003. Dynamic froth stability in froth flotation. Miner. Eng. 16 (11), 1111–1116.
Bikerman, J., 1973. Formation and structure. In: Foams. Springer, pp. 33–64.
Bikerman, J.J., 1948. Surface Chemistry for Industrial Research. Academic Press, Inc, Publishers., New York.
Chen, T., Lei, C., Yan, B., Xiao, X., 2014. Metal recovery from the copper sulfide tailing with leaching and fractional precipitation technology. Hydrometallurgy 147, 178–182.
Chipfunhu, D., Zanin, M., Grano, S., 2011. The dependency of the critical contact angle for flotation on particle size – modelling the limits of fine particle flotation. Miner. Eng. 24, 50–57.
Cilek, E.C., Karaca, S., 2015. Effect of nanoparticles on froth stability and bubble size distribution in flotation. Int. J. Miner. Process. 138, 6–14.
Edraki, M., Baumgartl, T., Manlapig, E., Bradshaw, D., Franks, D.M., Moran, C.J., 2014. Designing mine tailings for better environmental, social and economic outcomes: a review of alternative approaches. J. Cleaner Prod. 84, 411–420.
Falagán, C., Grail, B.M., Johnson, D.B., 2017. New approaches for extracting and recovering metals from mine tailings. Miner. Eng. 106, 71–78.
Gordon, R.B., 2002. Production residues in copper technological cycles. Resour. Conserv. Recycl. 36 (2), 87–106.
Ip, S., Wang, Y., Toguri, J., 1999. Aluminum foam stabilization by solid particles. Can. Metall. Q. 38 (1), 81–92.
Johansson, G., Pugh, R., 1992. The influence of particle size and hydrophobicity on the stability of mineralized froths. Int. J. Miner. Process. 34 (1-2), 1–21.
Leistner, T., Peuker, U.A., Rudolph, M., 2017. How gangue particle size can affect the recovery of ultrafine and fine particles during froth flotation. Miner. Eng. 109, 1–9.
Li, G., Deng, L., Cao, Y., Wang, B., Ran, J., Zhang, H., 2017. Effect of sodium chloride on fine coal flotation and discussion based on froth stability and particle coagulation. Int. J. Miner. Process. 169, 47–52.
Liang, L., Li, Z., Peng, Y., Tan, J., Xie, G., 2015. Influence of coal particles on froth stability and flotation performance. Miner. Eng. 81, 96–102.
McFadzean, B., Achaye, I., Chidzanira, T., Harris, M., 2016a. The effect of particle size on froth stabilities of different ores. In: IMPC 2016: XXVIII International Mineral Processing Congress Proceedings, Quebec, Canada.
McFadzean, B., Marozva, T., Wiese, J., 2016b. Flotation frother mixtures: decoupling the sub-processes of froth stability, froth recovery and entrainment. Miner. Eng. 85, 72–79.
Miettinen, T., Ralston, J., Fornasiero, D., 2010. The limits of fine particle flotation. Miner. Eng. 23 (5), 420–437.
Molina, I.A., Martins, P., Videla, A.R., 2016. On the interaction effect between xanthate collector, frothers and solids: A laboratory characerization of copper sulfide flotation. In: Procemin2016, 12th International Mineral Processing Conference, Santiago, Chile.
Norori-McCormac, A., Brito-Parada, P.R., Hadler, K., Cole, K., Cilliers, J.J., 2017. The effect of particle size distribution on froth stability in flotation. Sep. Purif. Technol..
Rahman, R.M., Ata, S., Jameson, G.J., 2012. The effect of flotation variables on the recovery of different particle size fractions in the froth and the pulp. Int. J. Miner. Process. 70–77.
Tao, D., Luttrell, G., Yoon, R.-H., 2000. A parametric study of froth stability and its effect on column flotation of fine particles. Int. J. Miner. Process. 59 (1), 25–43.
Trahar, W., 1981. A rational interpretation of the role of particle size in flotation. Int. J. Miner. Process. 8 (4), 289–327.
Vieira, A.M., Peres, A.E., 2007. The effect of amine type, ph, and size range in the flotation of quartz. Miner. Eng. 20 (10), 1008–1013.

# The link between particle size and froth stability - implications for reprocessing of flotation tailings

Mackay I.*[a], Videla A.R.[b], Brito-Parada P.R.*[a]

[a]*Department of Earth Science and Engineering, Imperial College London, SW7 2AZ, United Kingdom*
[b]*Department of Mining Engineering, Pontificia Universidad Catolica de Chile, 7820436, Chile*
**Corresponding Authors: isobel.mackay11@imperial.ac.uk and p.brito-parada@imperial.ac.uk*

**Abstract**

Historic tailings dams can often be considered as valuable mineral reserves due to the declining head grades of primary deposits. The reprocessing of such material is of great interest to the minerals processing industry, not only from an economic point of view, but also from an environmental one. However, tailings material is generally comprised of fine particles, which poses a challenge for its reprocessing using froth flotation due to reduced recoveries of these particle sizes. In addition, there is some debate as to the effect that these fine particles have on the froth stability, which in turn is linked to mineral recovery.

In this work, air recovery was used as a measure of froth stability to determine the flotation response of a copper tailings ore to changes in particle size distribution and superficial gas velocity. The system exhibited a maximum in air recovery, which correlates well with the local peak in dynamic froth stability presented in previous work. This maximum in froth stability is also shown to correspond to an improvement in flotation performance, thus highlighting the importance of considering the link between particle size, air rate and froth stability when determining the flotation strategy for tailings reprocessing. The results are discussed in terms of the implications for the reprocessing plant from where the ore samples were obtained and, more generally, for the efficient flotation reprocessing of tailings.

*Keywords:* Froth flotation, Stability, Air Recovery, Copper Tailings Reprocessing, Continuous Flotation

https://doi.org/10.1016/j.jclepro.2019.118436

Copyright © 2019. This manuscript version is made available under the CC-BY-NC-ND 4.0 license (http://creativecommons.org/licenses/by-nc-nd/4.0/)

## 1 Introduction

The global demand for metals, such as copper, is increasing, putting a strain on mining companies as head grades of deposits decrease. At the beginning of the 20$^{th}$ century copper tailings dams had an average copper content (or grade) of 0.75%, while today they are as low as 0.14% (Gordon, 2002). This drop is due to an improvement in processing efficiency (Falagán et al., 2017). Reprocessing historic tailings dams is therefore attractive to the mining industry, as they are relatively high grade in comparison to modern reserves. There are also other benefits, for instance, there is no comminution requirement. Added to this, by reprocessing the waste material, mining companies can reduce the significant environmental problems associated with tailings dams (Chen et al., 2014).

One of the most widely used separation techniques across the minerals processing industry is froth flotation, a technique that utilises the differences in surface properties to separate valuable minerals from the waste material (Fuerstenau et al., 2007). Due to the relative versatility of flotation, especially with regards to complex and low grade ores, this technique is commonly used for the reprocessing of tailings ma-

terial (Wills and Finch, 2015). However, one of the major challenges presented by reprocessing tailings material in this way is that it contains a large portion of fine and ultra-fine particles, which are harder to process using froth flotation (Edraki et al., 2014). It is therefore vital to carry out research into understanding the effects of different operating conditions on the flotation performance of tailings material.

There have been numerous recent studies investigating the potential for reprocessing tailings ores using froth flotation for a variety of different ore types such as copper (Lutandula and Maloba, 2013; Alcalde et al., 2018; Mackay et al., 2018; Yin et al., 2018), gold (Valderrama and Rubio, 2007), zinc (Yang et al., 2015; Babel et al., 2018) and cassiterite (Leistner et al., 2016). These studies have shown that there is good potential for the reprocessing of the various tailings types investigated. However, each of the aforementioned papers presents a different solution to the general problem that is specific to that ore. Due to the case-specific nature of tailings material, it is challenging to develop a generic framework for tailings management (Adiansyah et al., 2015). The present study will investigate the ability to improve the flotation recovery of valuable minerals from tailings materials by altering the feed particle size distribution.

### *1.1. Fine Particle Flotation*

Due to the fact that the majority of particles in tailings dams are fine (less than 50 µm), it is important to understand the challenges of successfully floating such material and what effects the presence of the fine particles has on froth stability and therefore flotation performance. The first major problem when recovering fine or ultrafine particles through froth flotation is that, due to their higher specific surface area, they consume larger quantities of reagents (Feng and Aldrich, 1999). The second problem is that there is a much lower probability of the particle attaching to the bubble (Miettinen et al., 2010). The third problem is that, the small size of the particles results in lower settling velocities and particles are therefore more easily entrained (Neethling and Cilliers, 2009). For more detail into the problems associated with fine particle flotation the reader is directed to Miettinen et al. (2010), which presents an in depth review paper on the matter.

Whilst it is well known that fine particle recovery in froth flotation is poor (Fuerstenau et al., 2007), there have also been several studies investigating the effects that the amount of fine particles in the feed has on the recovery of different particle sizes in the system. These studies have shown that the presence of fine particles, to some extent, can improve the flotation recoveries of other particles in the system. Vieira and Peres (2007) conducted laboratory experiments in a Denver flotation cell to investigate this, varying the proportion of fine (38-74 µm) quartz particles in the feed from none to 15.6%, and measuring the recoveries of the fine, medium and coarse quartz particles were measured. The results showed that the feed with and intermediate proportion of fine quartz particles (11.6 %) improved the recovery of all three size fractions. The authors proposed that this effect was due to the presence of fine particles stabilising the froth, however the froth stability was not quantified in this work. Conversely, flotation experiments conducted by Rahman et al. (2012) showed that when changing the feed size of silica particles in a laboratory scale flotation column, it was the finest feed (with a $d_{80}$ of 80 µm) that resulted in increased recoveries of the coarser particle sizes (>90 µm). The work by Rahman et al. (2012) also showed that an intermediate feed size (with a $d_{80}$ of 150 µm) resulted in improved recoveries of the finest three particle sizes (10 µm, 36 µm and 64 µm).

Both Vieira and Peres (2007) and Rahman et al. (2012) used single species systems in their flotation experiments. On the other hand, Leistner et al. (2017) investigated the effects of varying the particle size of both valuable and gangue minerals on the recovery using a laboratory scale flotation cell. Their study used fine (10-50 µm) and ultrafine (<10 µm) magnetite as the valuable material, in the presence of fine and ultrafine quartz as the gangue material. The results showed that the presence of fine quartz particles increased the recovery of both sizes of magnetite, whilst the presence of ultra fine quartz reduced the recovery of the magnetite. This indicates that the size of the gangue particles has a strong effect on the

Copyright © 2019.

recovery of the valuable ones. Ran et al. (2019) also performed experiments using a multi-species mineral system. These flotation experiments investigated the effect of particle size on flotation performance for the separation of copper, gold and lead. This study showed that the most favourable size fraction for improving the recovery was an intermediate size of $-74+59\,\mu m$.

As well as understanding the effect of particle size on recovery, it is also important to understand the effect that different particle sizes have on froth stability. There have been several different bodies of work on this topic(Johansson and Pugh, 1992; Ip et al., 1999; Aktas et al., 2008; McFadzean et al., 2016; Norori-Mccormac et al., 2017; Mackay et al., 2018), yet the results are not conclusive. The majority of the work measures the dynamic froth stability in non-overflowing laboratory scale columns. Johansson and Pugh (1992) showed that whether or not fine particles will destabilise the froth depends on the hydrophobicity of the particles. They varied the contact angles of the particles in the feed and measured the resulting dynamic froth stability. The results showed that at low contact angles ($< 40°$), fine particles (26-44 µm) had little effect on the stability, intermediate angles ($\sim 65°$) gave the best stability whilst higher angles ($> 80°$) destabilised the froth. Ip et al. (1999) measured the dynamic froth stability in a column with different particle sizes (from 45-130 µm) of a synthetic feed, consisting only of silica. They showed that, in general, smaller mean particle sizes led to higher froth stabilities. However, this was not a perfectly linear relationship; instead, there was a plateau at the intermediate particle sizes. Aktas et al. (2008) varied the particle size ($d_{50}$ between 28 µm and 75 µm) of a platinum group metal (PGM) ore in a froth stability column and showed a linear relationship where smaller feed sizes resulted in higher froth stabilities. A similar, inversely proportional relationship was presented by McFadzean et al. (2016), also using a synthetic ore ($d_{50}$ between 15 µm and 212 µm) in addition to several PGM ores ($d_{50}$ between 30 µm and 70 µm); the relationship obtained, however, was a power law rather than simply linear.

Unlike most of these studies, Norori-Mccormac et al. (2017) investigated the effects of particle size in a laboratory scale, continuously overflowing, mechanical flotation cell and used air recovery as the measure of froth stability (Moys, 1984). These results showed that the relationship between particle size and froth stability is not a simple one, but there is also a dependence on the superficial gas velocity in the system. At high superficial gas velocities the relationship is the same as those seen in Aktas et al. (2008) and McFadzean et al. (2016) in that smaller feed sizes result in an improved froth stability. However, at lower superficial gas velocities there is an intermediate feed size that results in the optimal stability. Most recently, Mackay et al. (2018) investigated the effects of varying the particle size on dynamic froth stability in a laboratory scale column for a copper tailings ore. These results showed that there were two stability regimes: the first was at finer particle sizes, where the relationship is the same as seen in other work, while at coarser particle sizes ($d_{90}$ greater than 170 µm) there was an optimal particle size for improved froth stability at $d_{90}$ of 220 µm. This was found to be the case for a range of superficial gas velocities that are similar to industrial values. It is important to point out that the majority of these studies are conducted using synthetic ores or in non-overflowing columns which are not necessarily representative of industrial flotation.

### *1.2. Bench scale flotation cells*

Due to the complexities involved with carrying out experiments in an industrial setting, a vast amount of flotation research is done at the laboratory scale. The majority of laboratory scale testing, for mechanically stirred flotation, uses batch tests, e.g. tests conducted in a Denver cell (Wills and Finch, 2015). Batch tests are relatively simple to conduct and are often used due to their suitability for optimising flotation chemistry. However, these cells are limited in their usefulness to study other aspects of flotation performance since they cannot be operated at steady state. A continuous, bench-scale, flotation cell was developed by Norori-Mccormac et al. (2017) and was shown to operate in a manner similar to industrial flotation cells. In this cell, the overflowing concentrate is pumped back into the pulp phase allowing steady state to be achieved and maintained for over

Copyright © 2019.

an hour. This is extremely beneficial to laboratory research as it provides a better comparison to industrial flotation froth behaviour than batch testing.

In order to relate experiments to industrial processes it is important to be able to quantify the flotation performance. There are various different metrics commonly used to do this, with concentrate grade and recovery being the most ubiquitous. Another valuable performance indicator is froth stability (Neethling and Brito-Parada, 2018). There are several different measures of stability depending on the type of system being investigated. When considering a continuous system, air recovery, or the fraction of air entering the cell that over flows the lip, has been shown to be a robust measure. It is defined in equation 1:

$$\alpha = \frac{Q_{out}}{Q_{in}} = \frac{v_f h w}{Q_{in}}, \tag{1}$$

where $\alpha$ is the air recovery, $Q_{out}$ is the air overflowing the cell in bubbles and not lost due to bursting, $Q_{in}$ is the flow rate of air into the cell, $v_f$ is the overflowing froth velocity, $h$ is the height of the overflowing froth over the cell lip, and $w$ is the length of the lip of the cell. Equation 1 considers that flotation froths are very dry, particularly at the top of the froth where liquid fractions are very low. It is important to note that the relationship between air recovery and air rate is non linear. Hadler and Cilliers (2009) established that, when increasing the air rate, a peak in air recovery (PAR) can be seen, which is due to a trade-off between froth stability and mobility. Hadler et al. (2010) demonstrated that, at industrial scale, changing the air flowrate into a flotation cell to the PAR resulted in an increased mineral recovery with only a small drop in the grade of the concentrate.

This work uses the continuously overflowing flotation cell first used by Norori-Mccormac et al. (2017) to investigate particle size effects on froth stability, using a copper tailings ore and thus allowing a closer comparison of the cell to industrial systems. It also makes it possible to understand better the relationships between different operating parameters, in particular the particle size of the feed and the superficial gas velocity, and froth stability for a copper tailings ore. In addition, this work expands on that done by Mackay et al. (2018) by using the same ore, from the same batch, but in a continuously overflowing system measuring air recovery as opposed to a non-overflowing column measuring dynamic froth stability. This allows a direct comparison between two different measures of stability. The results from Mackay et al. (2018) indicated that there were two stability regimes, one that follows the trends seen by other authors and a second that shows and optimum feed particle size for an improvement in froth stability and flotation performance. This paper focuses on this second region, with $d_{90}$ >150 µm, in order to investigate this trend further. This will have strong implications for furthering our understanding of the relationship between particle size, froth stability and flotation performance in order to improve the efficiency of tailings reprocessing by froth flotation.

## 2 Materials and Methods

### *2.1. Materials*

The samples used in this study were obtained from a Chilean processing plant that reprocesses both historic and fresh copper tailings with copper grades of 0.27 % and 0.12 %, respectively. Due to the nature of tailings, approximately 50 % of the material entering the plant is less than 10 µm. The plant uses a primary hydrocyclone to split the material for processing. The hydrocyclone overflow stream has a $d_{90}$ of 63.7 µm and the underflow stream has a $d_{90}$ of 279 µm. The underflow stream is then processed via flotation. Samples were obtained from the underflow and overflow streams of the primary hydrocyclone, as slurry, and then dried, resulting in two samples with different particle size distributions. This allowed the two samples to be combined in different ratios to produce the three different particle size distributions investigated in this work (table 1 and figure 1). The samples used for these experiments were obtained from the same batch that was used in Mackay et al. (2018) and the particle sizes were chosen in order to further investigate the local maximum in froth stability presented by Mackay et al. (2018). These particle size distributions were determined using a Malvern Mastersizer 3000e particle analyser. The Mastersizer

Copyright © 2019.

uses laser diffraction and applies the Mie theory of light scattering. The copper content of the different was determined by atomic absorption as described in section 2.3 and is presented in table 1.

Table 1: Particle size distributions and copper content for the three different feeds used.

| Feed | $d_{10}$, [µm] | $d_{50}$, [µm | $d_{90}$, [µm] | Cu, [%] |
|---|---|---|---|---|
| *A* | 2.6 | 23.0 | 179.3 | 0.27 |
| *B* | 2.9 | 30.2 | 219.1 | 0.27 |
| *C* | 3.3 | 47.1 | 253.4 | 0.32 |

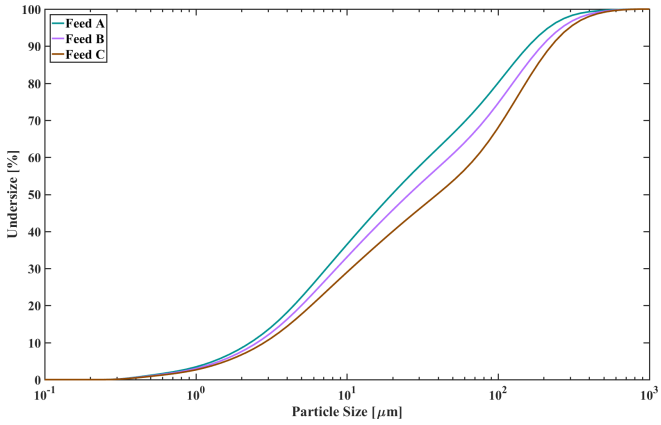


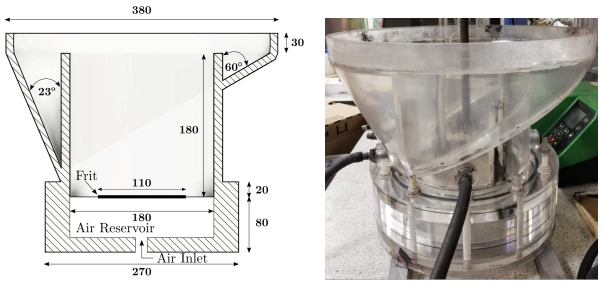

Figure 1: Cumulative size distributions of the four different feeds used.

The mineralogy of the feeds used in this study was analysed by QEMSCAN (quantitative evaluation of minerals by scanning electron microscopy). A QEMSCAN E430 in bulk mineralogical analysis measurement mode was used with a measurement time of 2.5 hrs and an acceleration voltage of 20kV. The software used were iMeasure v.4.3 for data acquisition and iDiscover v.4.3 for data processing. The QEMSCAN was calibrated using Quartz, Copper and Gold standards, with preset values of 44, 130 and 232 respectively.

The reagent environment used for these experiments was developed by Molina et al. (2016) and is the same as was used in Mackay et al. (2018). The collector used was Sodium Isopropyl Xanthate at $50\,\mathrm{g\,t^{-1}}$ and the frother was DowFroth 400 (supplied by Nasaco Ltd.) at $20\,\mathrm{g\,t^{-1}}$. Lime, *CaO* (supplied by Arcos Organics), was used to ensure a constant pH of 9 across all experiments.

### *2.2. Continuously overflowing flotation cell*

The experimental system used in this work is a four litre continuously overflowing flotation cell (shown in figure 2) developed by and described in Norori-Mccormac et al. (2017). The overflowing concentrate is pumped back into the cell allowing for continuous operation and for steady state conditions to be achieved.




(a) Schematic of the flotation cell (b) Photograph of the flotation cell

Figure 2: Details of the design of the continuously overflowing flotation cell. The concentrate is pumped from the launder back into the pulp zone of the cell. Measurements given in the schematic in (a) are in millimetres.

For each experiment, 900 g of copper tailings ore, with one of the three different size distributions in table 1, were combined with 2.9 L of deionised water to form the slurry. The slurry was then added to the cell along with the frother and collector and was then agitated, at 950 rpm, to condition for 15 minutes. This was the same process as was used by Norori-Mccormac et al. (2017). Four different superficial gas velocities ($J_g$) were used across the experiments, $0.92\,\mathrm{cm\,s^{-1}}$, $1.05\,\mathrm{cm\,s^{-1}}$, $1.18\,\mathrm{cm\,s^{-1}}$ and $1.31\,\mathrm{cm\,s^{-1}}$. These values of $J_g$ are similar to those used industrially (Mesa and Brito-Parada, 2019) as well as those used in Mackay et al. (2018).

For each experiment, 6 different conditions were run; conditions included each of the four superficial gas velocities, with two of them repeated. The order in which the conditions were performed was randomised. Each condition was run for 15 minutes, which was made up of 5 minutes without measurement to enable steady state to be achieved, and 10 minutes of measurement time. An on-line laser (ifm electronics, 01D300) was used to measure the over-

Copyright © 2019.

flowing froth height via LabVIEW. A web camera (Logitech, C525) was combined with FrothTracker, an in-house, block matching, image analysis program, and used to measure the overflowing froth velocity. The measured values of overflowing froth height and velocity allowed air recovery to be calculated using equation 1.

### *2.3. Sample Analysis*

Froth samples for each condition were collected using a 3D printed scoop that was inserted into the launder of the cell for 10 seconds. They were then weighed and dried in order to calculate the solids content of the concentrate and the solids flowrate to the concentrate. The samples were then analysed for copper content (Wheal Jane Laboratories, *Cornwall, UK*). The samples were first prepared by hydrochloric acid attack and then the copper content analysed using a Thermo Fisher Scientific iCE 3300 Atomic Absorption Spectrometer.

Due to the fact that the concentrate is recycled back into the pulp of the cell, effectively acting as the feed stream, there is no tailings stream in this cell. Copper recovery was therefore not calculated in the traditional way, instead the copper grade of the concentrate and the solids flowrate over the lip of the cell were used to calculate the copper recovery per minute. This can be done using equation 2,

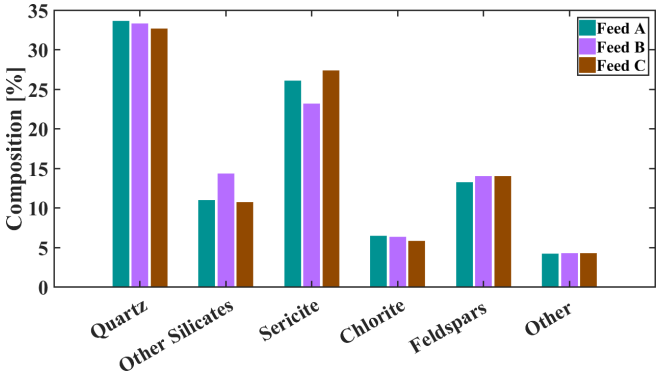
$$Recovery = \frac{G_c F_c}{G_f M_f}, \tag{2}$$

where $G$, $F$ and $M$ represent the grade, flowrate and mass, while the subscripts $c$ and $f$ correspond to the concentrate and feed streams. The mass of the feed is used as the mass of solids used in the experiments (900 g) and the flowrate to the concentrate is measured in grams per minute.

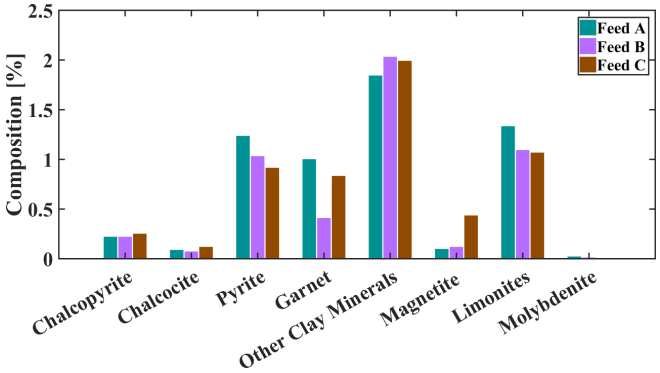
## 3 Results & Discussion

### *3.1. Sample Characterisation*

The detailed mineralogy of each of the different feeds can be seen in figure 3. The mineralogy shows that, in general, there is no large difference in the mineralogy of the different feeds used. The liberation by size of the chalcopyrite, for particles greater than 75 µm and less than 75 µm, is shown figure 4. For all three feeds, the majority of the chalcopyrite has a liberation of lower than 50% and this poorly liberated chalcopyrite is mostly over 75 µm. Feeds $A$ and $B$ contain no chalcopyrite that is more than 50% liberated and over 75 µm, whereas feed $C$ contains a large proportion of chalcopyrite that fits into this category. The chalcopyrite in feeds $B$ and $C$ is better liberated than feed $A$, with a higher proportion of the chalcopyrite being over 50% liberated.




(a) Mineralogy for high value minerals




(b) Mineralogy for low value minerals

Figure 3: Mineral composition of the different feeds, from the QEMSCAN analysis, split into (a) minerals that comprise more than 5% of the feed and (b) minerals that are less than 2.5% of the feed.

### *3.2. Froth Stability*

In order to verify that the changes in air recovery are caused by changes in operating conditions and

Copyright © 2019.

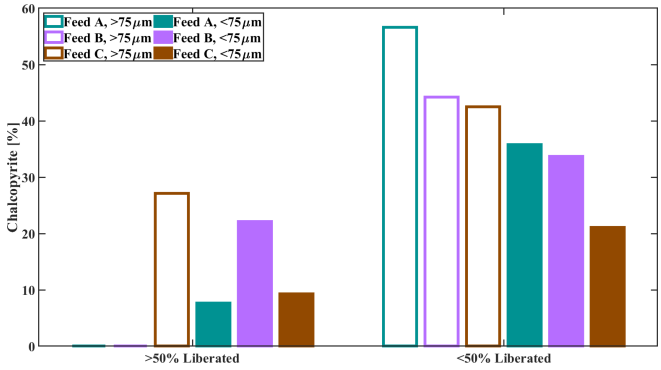



Figure 4: Chalcopyrite liberation by size from QEMSCAN analysis of the three different feeds.

not by changes in the system with time, tests were run for an hour and a half to ensure the operation remained at steady state. Figure 5 shows the moving average of the air recovery over 90 minutes for an experiment at a $J_g$ =0.92 cm s$^{-1}$. The data was divided into six, 15 minute windows and the data in the last 10 minutes of each window were averaged (the data in the light grey vertical bands) to analyse the change in air recovery over time. The average value for each of these 10 minute windows is presented in figure 5, with black dots and error bars representing a 95% confidence interval. The overall 95% confidence interval is presented in figure 5 with a horizontal dark grey band.

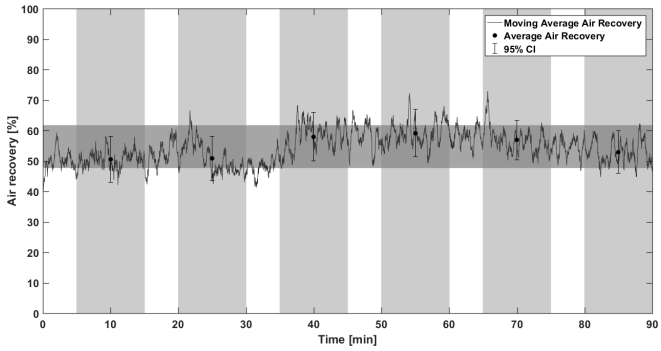



Figure 5: The variation in air recovery over time at a constant condition, with 10 minute measurement windows highlighted by light grey vertical bands and a confidence band for the average value of air recovery represented by the dark grey horizontal band. Error bars represent a 95% confidence interval.

A heat map of the air recovery data for varying feed size distributions and superficial gas velocities can be seen in figure 6. When investigating the effects of varying superficial gas velocity for a constant feed size (the rows of the heat map) only feed $A$ displays a peak in air recovery which is at a superficial gas velocity of 1.18 cm s$^{-1}$. At coarser feeds, there is no peak in air recovery. Figure 6 shows that varying the particle size distribution of the feed for a given superficial gas velocity (the columns of the heat map) has a stronger effect on the air recovery; feeds $B$ and $C$ result in higher air recoveries for all superficial gas velocities investigated.

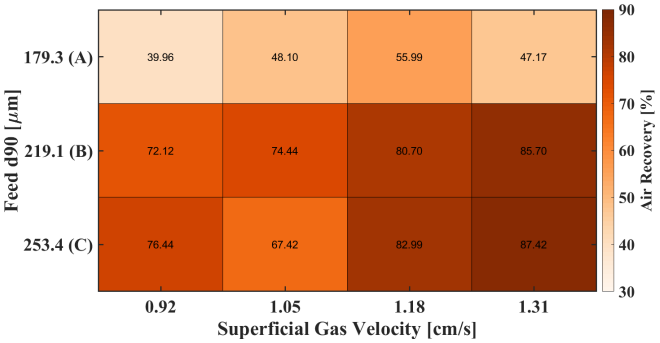



Figure 6: Heat map of air recovery for different feed $d_{90}$s and superficial gas velocities.

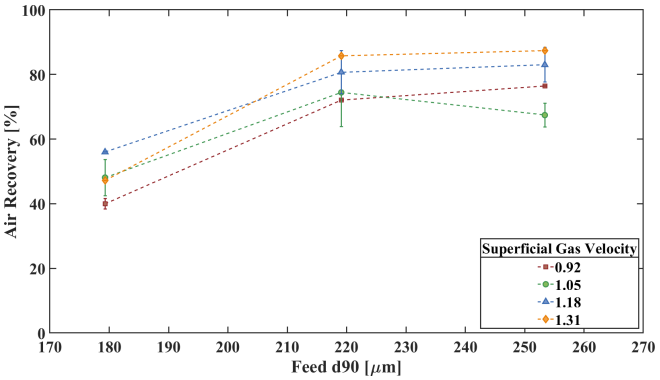



Figure 7: The variation in air recoveries with varying feed size at different superficial gas velocity. Error bars are one standard deviation.

For a better understanding of the relationship between feed size and air recovery, the data are presented in more detail in figure 7. The air recovery with varying feed size is plotted for each superficial gas velocity with error bars as one standard deviation. An ANOVA test was performed on these data (table 2), which shows that only changing the feed size had a statistically significant effect on the air recovery. This indicates that, regardless of the superficial gas velocity used, there is a clear improvement in froth stability at coarser feed sizes, with $d_{90}$ be-

Copyright © 2019.

Table 2: ANOVA table of air recovery with particle size distribution.

| Source | Sum of Squares | Degrees of Freedom | Mean of Squares | $F$-Stat | $p$-Value |
|---|---|---|---|---|---|
| Feed Size | 3329.7 | 2 | 1664.85 | 10.79 | 0.0103 |
| Superficial Gas Velocity | 436.05 | 3 | 145.35 | 0.94 | 0.4772 |
| Interaction | 222.77 | 6 | 37.13 | 0.24 | 0.9466 |
| Error | 926 | 6 | 154.33 | | |
| Total | 5495.59 | 17 | | | |

tween 220 µm and 260 µm. These data also correlate well with the relationships shown in the experiments performed by Norori-Mccormac et al. (2017) at the lower two superficial gas velocities they investigated, and the relationship shown by Mackay et al. (2018).

The experiments in this study were conducted using the same batch of ore as was used by Mackay et al. (2018), allowing a direct comparison between the two measures of froth stability, i.e. dynamic froth stability and air recovery, to be made. Figure 8 shows the two data sets plotted together, with dynamic froth stability on the left hand axis and air recovery on the right hand axis. Both data sets show high froth stabilities at approximately the same feed size, $d_{90}$ of ∼220 µm. The air recovery data, however, does not have a clear maximum value. It is likely that a maximum occurs at a feed particle size distribution between $B$ and $C$ corresponding directly with the peak in dynamic froth stability.

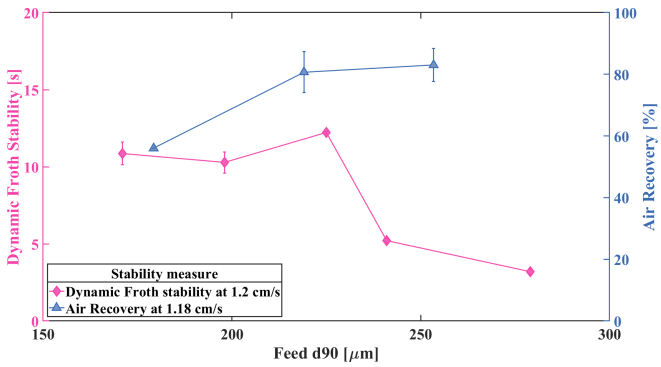



Figure 8: Comparison of dynamic froth stability (diamonds and left hand axis) and air recovery (triangles and right hand axis) for the same batch of copper tailings ore. Error bars are one standard deviation.

### *3.3. Flotation performance*

Whilst the feeds $B$ and $C$ were shown to result in the highest froth stability, it is important to understand how this trend is reflected in the flotation performance. One of the benefits of running experiments in the continuously overflowing cell, is that the air recovery can be measured while, at the same time, samples of the overflowing froth can be taken to determine flotation performance. The copper content of the feed and concentrate samples was analysed to determine grade and recovery. This was only done for experiments with superficial gas velocities of $0.92\,\mathrm{cm\,s^{-1}}$ and $1.18\,\mathrm{cm\,s^{-1}}$.

Figure 9 shows the copper grade of the concentrate from experiments with a superficial gas velocity of $0.92\,\mathrm{cm\,s^{-1}}$ and $1.18\,\mathrm{cm\,s^{-1}}$. It is observed that the grade decreases as superficial gas velocity increases. The analysis of variance results in table 3 show that this change is significant. This behaviour is expected, as higher superficial gas velocities will result in higher entrainment factors and therefore a reduced grade (Neethling and Cilliers, 2009). The analysis also shows that there is no statistically significant difference in the concentrate grade with different feed sizes.

Copyright © 2019.

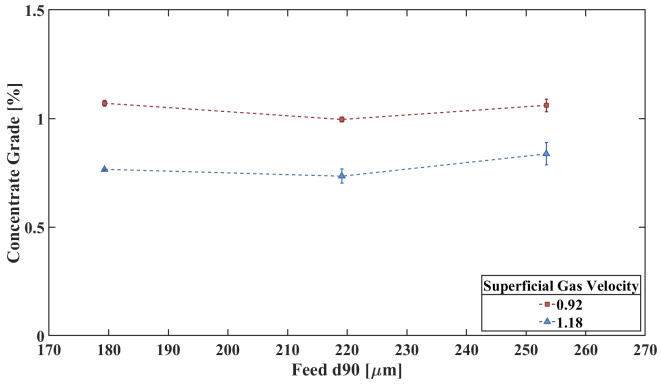



Figure 9: Concentrate grade for samples taken at $0.92\,\mathrm{cm\,s^{-1}}$ and $1.18\,\mathrm{cm\,s^{-1}}$. Error bars are 1 standard deviation.

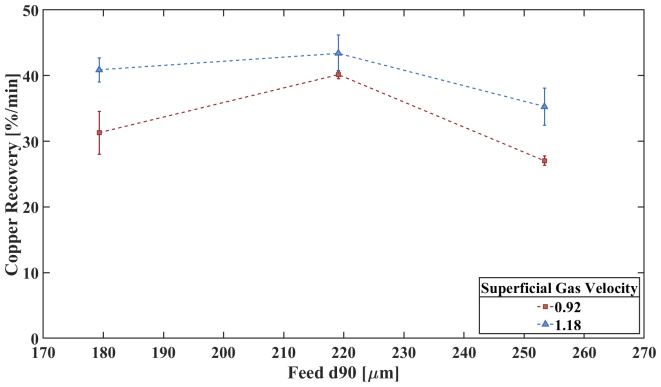



Figure 10: Copper recovery to the concentrate for samples taken at $0.92\,\mathrm{cm\,s^{-1}}$ and $1.18\,\mathrm{cm\,s^{-1}}$. Error bars are 1 standard deviation.

Figure 10 shows that the copper recovery is higher for the higher superficial gas velocity, which is often associated with an increase in mass pull. Feed $B$, which showed an improvement in air recovery, also has the best copper recovery at both superficial gas velocities. The analysis of variance in table 4 shows that both the feed size and the superficial gas velocity had a significant effect on the copper recovery. This is in line with the experimental results presented in Mackay et al. (2018), which showed that the feed with a similar particle size distribution to $B$, and which yielded a local peak in dynamic froth stability, corresponded to an improvement in copper recovery. Feed $C$, with a similar air recovery value to feed $B$, shows a decrease in flotation performance, despite the fact that they also have similar mineralogical composition. This indicates that the particle size distribution of feed $B$ is optimal for an improvement in flotation performance.

### *3.4. Implications for reprocessing mine tailings via froth flotation*

The samples of copper tailings used in this study were obtained from a plant currently reprocessing historic and fresh tailings material from a mine in Chile. The plant uses a primary hydrocyclone to split the material before processing. The underflow from the hydrocyclone, with a $d_{90}$ of 279 µm, is then processed via froth flotation.

The findings from section 3.3 indicate that the size distribution of the material currently being sent to flotation in this plant is not optimal. Instead, altering the cutsize of the hydrocyclone to produce a feed particle size distribution with a $d_{90}$ of approximately 220 µm would result in improved copper recovery from the tailings material. Altering the particle size distribution of the feed to the flotation circuit would also reduce the amount of material sent to final tailings, therefore reducing the environmental impacts from mine waste.

Previous work by other authors (Ip et al., 1999; Norori-Mccormac et al., 2017) has shown that the relationship between particle size and froth stability is not a simple one. The work in this paper compounds that fact, clearly showing that there can be an optimal particle size distribution for froth stability that correlates to an improvement in flotation performance. Evidence suggests that this behaviour is

Copyright © 2019.

Table 3: ANOVA table of concentrate grade with particle size distribution and superficial gas velocity.

| Source | Sum of Squares | Degrees of Freedom | Mean of Squares | $F$-Stat | $p$-Value |
|---|---|---|---|---|---|
| Feed Size | 0.01911 | 2 | 0.00955 | 2.29 | 0.1438 |
| Superficial Gas Velocity | 0.27563 | 1 | 0.27563 | 66.05 | 0 |
| Interaction | 0.00455 | 2 | 0.00227 | 0.55 | 0.5934 |
| Error | 0.05007 | 12 | 0.00417 | | |
| Total | 0.39589 | 17 | | | |

Table 4: ANOVA table of copper recovery with particle size distribution and superficial gas velocity.

| Source | Sum of Squares | Degrees of Freedom | Mean of Squares | $F$-Stat | $p$-Value |
|---|---|---|---|---|---|
| Feed Size | 301.12 | 2 | 150.56 | 5.43 | 0.021 |
| Superficial Gas Velocity | 197.59 | 1 | 197.59 | 7.12 | 0.0205 |
| Interaction | 29.456 | 2 | 14.728 | 0.53 | 0.6013 |
| Error | 332.904 | 12 | 27.742 | | |
| Total | 881.861 | 17 | | | |

exhibited by a variety of particle systems. It would therefore be wise for a tailings reprocessing plant to conduct simple froth stability tests to determine the optimal particle size distribution to improve recovery.

## 4 Conclusions

This study has investigated the effects of particle size, at a range of superficial gas velocities, on the froth stability and flotation performance of a copper tailings ore. These experiments were performed using a continuously overflowing bench scale flotation cell which is more representative of industrial systems than cells used for traditional batch tests. This cell had previously only been used to investigate effects with a single species, idealised system. In this study the cell was used to investigate a complex copper tailings ore, and was shown to be able to operate at steady state for an extended period of time.

The experiments in this study have enabled us to further investigate the operating conditions that yielded a local peak in dynamic froth stability previously shown in Mackay et al. (2018). For the first time, there has been a direct comparison between two different measures of froth stability: dynamic froth stability and air recovery. The results have shown that, for the same tailings ore, the feed particle size distribution that resulted in a local maximum in dynamic froth stability also yielded a maximum in air recovery. This helps to compound the fact that it is not simply a fine particle size distribution that improves froth stability, but that an intermediate distribution can result in the optimal froth stability. This effect was observed at multiple superficial gas velocities.

Flotation performance was also investigated. We show that the particle size distribution which yielded the optimal froth stability, both in terms of air recovery and dynamic froth stability, resulted in the highest copper recoveries. In the case of the processing plant from where the samples in this study were obtained, altering the particle size distribution of the material sent to flotation, to the optimal shown in this work, would not only translate into improved flotation performance but would also reduce the amount of material sent to final tailings.

The findings in this work have strong implications for the reprocessing of mineral resources from tailings, suggesting that froth stability tests to find the optimal particle size distribution should be carried out before reprocessing tailings by froth flotation.

Copyright © 2019.

This will allow for enhanced mineral recoveries to be achieved, thus contributing to a more efficient use of resources and the reduction of environmental impacts associated to mineral tailings. Future work will be carried out using the continuously overflowing bench scale cell to investigate a greater number of particle size distributions and a wider range of tailings material. This would further improve our understanding of how the relationship between particle size distribution and froth stability change with variations in mineralogy.

## Acknowledgements

I. Mackay's PhD was supported by the Engineering and Physical Sciences Research Council (award number 1661853) and the Society for Chemical Industry.

## References

Adiansyah, J. S., Rosano, M., Vink, S., Keir, G., 2015. A framework for a sustainable approach to mine tailings management: disposal strategies. Journal of Cleaner Production 108, 1050–1062.

Aktas, Z., Cilliers, J., Banford, A., 2008. Dynamic froth stability: Particle size, airflow rate and conditioning time effects. International Journal of Mineral Processing 87 (1-2), 65–71.

Alcalde, J., Kelm, U., Vergara, D., 2018. Historical assessment of metal recovery potential from old mine tailings: A study case for porphyry copper tailings, Chile. Minerals Engineering 127, 334–338.

Babel, B., Penz, M., Schach, E., Boehme, S., Rudolph, M., 2018. Reprocessing of a Southern Chilean Zn Tailing by FlotationA Case Study. Minerals 8 (7), 295.

Chen, T., Lei, C., Yan, B., Xiao, X., 2014. Metal recovery from the copper sulfide tailing with leaching and fractional precipitation technology. Hydrometallurgy 147-148, 178–182.

Edraki, M., Baumgartl, T., Manlapig, E., Bradshaw, D., Franks, D. M., Moran, C. J., 2014. Designing mine tailings for better environmental, social and economic outcomes: a review of alternative approaches. Journal of cleaner production 84, 411–420.

Falagán, C., Grail, B. M., Johnson, D. B., 2017. New approaches for extracting and recovering metals from mine tailings. Minerals Engineering 106, 71–78.

Feng, D., Aldrich, C., 1999. Effect of particle size on flotation performance of complex sulphide ores. Minerals Engineering 12 (7), 721–731.

Fuerstenau, M. C., Jameson, G. J., Yoon, R.-H., 2007. Froth flotation: a century of innovation. SME.

Gordon, R. B., 2002. Production residues in copper technological cycles. Resources, Conservation and Recycling 36 (2), 87–106.

Hadler, K., Cilliers, J., 2009. The relationship between the peak in air recovery and flotation bank performance. Minerals Engineering 22, 451–455.

Hadler, K., Smith, C., Cilliers, J., 2010. Recovery vs. mass pull: The link to air recovery. Minerals Engineering 23 (11), 994–1002.

Ip, S., Wang, Y., Toguri, J., 1999. Aluminum foam stabilization by solid particles. Canadian Metallurgical Quarterly 38 (1), 81–92.

Johansson, G., Pugh, R., 1992. The influence of particle size and hydrophobicity on the stability of mineralized froths. International Journal of Mineral Processing 34 (1-2), 1–21.

Leistner, T., Embrechts, M., Leißner, T., Chelgani, S. C., Osbahr, I., Möckel, R., Peuker, U. A., Rudolph, M., 2016. A study of the reprocessing of fine and ultrafine cassiterite from gravity tailing residues by using various flotation techniques. Minerals Engineering 96-97, 94–98.

Leistner, T., Peuker, U. A., Rudolph, M., 2017. How gangue particle size can affect the recovery of ultrafine and fine particles during froth flotation. Minerals Engineering 109, 1–9.

Copyright © 2019.

Lutandula, M. S., Maloba, B., 2013. Recovery of cobalt and copper through reprocessing of tailings from flotation of oxidised ores. Journal of Environmental Chemical Engineering 1 (4), 1085–1090.

Mackay, I., Mendez, E., Molina, I., Videla, A., Cilliers, J., Brito-Parada, P., 2018. Dynamic froth stability of copper flotation tailings. Minerals Engineering 124, 103–107.

McFadzean, B., Achaye, I., Wiese, J., Chidzanira, T., Harris, M., 2016. The effect of particle size on froth stabilities of different ores. XXVII International Mineral Processing Congress, 1–11.

Mesa, D., Brito-Parada, P. R., 2019. Scale-up in froth flotation: A state-of-the-art review. Separation and Purification Technology 210, 950–962.

Miettinen, T., Ralston, J., Fornasiero, D., 2010. The limits of fine particle flotation. Minerals Engineering 23 (5), 420–437.

Molina, I., Martins, P., Videla, A., 2016. On the interaction effect between xanthate colletor, frothers and solids: Alaboratory characterization of copper sulfide flotation. Procemin2016, 12th International Mineral Processing Conference, Santiago, Chile.

Moys, M., 1984. Residence time distributions and mass transport in the froth phase of the flotation process. International Journal of Mineral Processing 13 (2), 117–142.

Neethling, S., Brito-Parada, P., 2018. Predicting flotation behaviour–the interaction between froth stability and performance. Minerals Engineering 120, 60–65.

Neethling, S., Cilliers, J., 2009. The entrainment factor in froth flotation: Model for particle size and other operating parameter effects. International Journal of Mineral Processing 93 (2), 141–148.

Norori-Mccormac, A., Brito-Parada, P. R., Hadler, K., Cole, K., Cilliers, J. J., 2017. The effect of particle size distribution on froth stability in flotation. Separation and Purification Technology 184, 240–247.

Rahman, R. M., Ata, S., Jameson, G. J., 2012. The effect of flotation variables on the recovery of different particle size fractions in the froth and the pulp. International Journal of Mineral Processing 106-109, 70–77.

Ran, J.-c., Qiu, X.-y., Hu, Z., Liu, Q.-j., Song, B.-x., Yao, Y.-q., 2019. Effects of particle size on flotation performance in the separation of copper, gold and lead. Powder Technology 344, 654–664.

Valderrama, L., Rubio, J., 2007. Unconventional column flotation of low-grade gold fine particles from tailings. International Journal of Mineral Processing 86, 75–84.

Vieira, A. M., Peres, A. E., 2007. The effect of amine type, pH, and size range in the flotation of quartz. Minerals Engineering 20 (10), 1008–1013.

Wills, B. A., Finch, J., 2015. Wills' mineral processing technology: an introduction to the practical aspects of ore treatment and mineral recovery. Butterworth-Heinemann.

Yang, X., Huang, X., Qiu, T., 2015. Recovery of zinc from cyanide tailings by flotation. Minerals Engineering 84, 100–105.

Yin, Z., Sun, W., Hu, Y., Zhang, C., Guan, Q., Wu, K., 2018. Evaluation of the possibility of copper recovery from tailings by flotation through bench-scale, commissioning, and industrial tests. Journal of cleaner production 171, 1039–1048.

Copyright © 2019.

# Appendix B

# Analysis of variance results from the experiments with the two-species system in chapter 5.

The following sections contain ANOVA tables for the different variables calculated from the two-species experiments in chapter 5. Highlighted values indicate those that are statistically significant with a threshold p-Value of 0.05.

## B.1 Flotation Performance

**Table B.1:** Silica Recovery

| Source | Sum Of Squares | Degrees of Freedom | Mean of Squares | F-Stat | p-Value |
|---|---|---|---|---|---|
| Superficial Gas Velocity | 0.54 | 3 | 0.27 | 60.6 | $6.49 \times 10^{-8}$ |
| Design Modification | 1.02 | 2 | 0.51 | 115 | $7.83 \times 10^{-10}$ |
| Interaction | 0.13 | 4 | 0.03 | 7.44 | 0.002 |
| Error | 0.07 | 15 | 0.004 | | |
| Total | 1.83 | 23 | | | |

**Table B.2:** Silica Grade

| Source | Sum Of Squares | Degrees of Freedom | Mean of Squares | F-Stat | p-Value |
|---|---|---|---|---|---|
| Superficial Gas Velocity | 99.9 | 2 | 49.9 | 62.4 | $5.37 \times 10^{-8}$ |
| Interaction | 18.3 | 4 | 4.57 | 5.70 | 0.005 |
| Error | 12.0 | 15 | 0.80 | | |
| Total | 206 | 23 | | | |

### B.1.1 Entrainment

**Table B.3:** Water Flowrate

| Source | Sum Of Squares | Degrees of Freedom | Mean of Squares | F-Stat | p-Value |
|---|---|---|---|---|---|
| Superficial Gas Velocity | 809 | 2 | 404 | 158 | $8.25 \times 10^{-11}$ |
| Design Modification | 2560 | 2 | 1280 | 501 | $1.85 \times 10^{-14}$ |
| Interaction | 18.6 | 4 | 4.66 | 1.82 | 0.177 |
| Error | 38.3 | 15 | 2.55 | | |
| Total | 3760 | 23 | | | |

**Table B.4:** Magnetite Flowrate

| Source | Sum Of Squares | Degrees of Freedom | Mean of Squares | F-Stat | p-Value |
|---|---|---|---|---|---|
| Superficial Gas Velocity | 18.9 | 2 | 9.45 | 228 | $5.94 \times 10^{-12}$ |
| Design Modification | 18.2 | 2 | 9.11 | 220 | $7.75 \times 10^{-12}$ |
| Interaction | 0.74 | 4 | 0.19 | 4.47 | 0.014 |
| Error | 0.62 | 15 | 0.041 | | |
| Total | 41.5 | 23 | | | |

**Table B.5:** Entrainment Factor

| Source | Sum Of Squares | Degrees of Freedom | Mean of Squares | F-Stat | p-Value |
|---|---|---|---|---|---|
| Superficial Gas Velocity | 0.05 | 2 | 0.02 | 49.8 | $2.38 \times 10^{-7}$ |
| Design Modification | 0.49 | 2 | 0.25 | 512 | $1.56 \times 10^{-14}$ |
| Interaction | 0.01 | 4 | 0.002 | 4.09 | 0.019 |
| Error | 0.01 | 15 | $4.82 \times 10^{-4}$ | | |
| Total | 0.61 | 23 | | | |

## B.2 Particle Size

**Table B.6:** Flowrate of $< 10\,\mu\mathrm{m}$ particles

| Source | Sum Of Squares | Degrees of Freedom | Mean of Squares | F-Stat | p-Value |
|---|---|---|---|---|---|
| Superficial Gas Velocity | 2.48 | 2 | 1.24 | 842 | $3.93 \times 10^{-16}$ |
| Design Modification | 2.78 | 2 | 1.39 | 9340 | $1.74 \times 10^{-16}$ |
| Interaction | 0.12 | 4 | 0.029 | 19.7 | $7.91 \times 10^{-6}$ |
| Error | 0.02 | 15 | 0.002 | | |
| Total | 5.82 | 23 | | | |

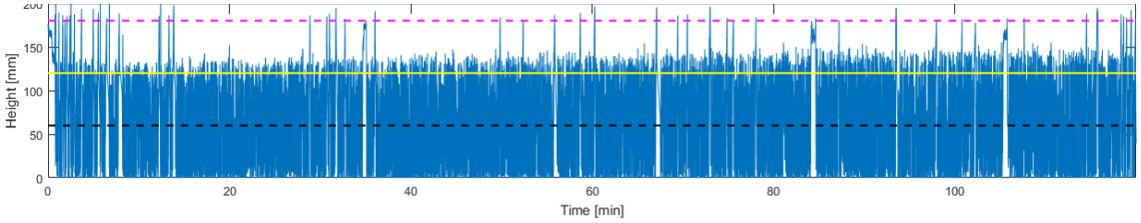
**Table B.7:** Flowrate of $> 80\,\mu\mathrm{m}$ particles

| Source | Sum Of Squares | Degrees of Freedom | Mean of Squares | F-Stat | p-Value |
|---|---|---|---|---|---|
| Superficial Gas Velocity | 0.03 | 2 | 0.01 | 12.8 | $2.82 \times 10^{-4}$ |
| Design Modification | 0.29 | 2 | 0.02 | 15.5 | $2.26 \times 10^{-4}$ |
| Interaction | 0.01 | 4 | 0.003 | 2.72 | 0.069 |
| Error | 0.01 | 15 | $9.69 \times 10^{-4}$ | | |
| Total | 0.08 | 23 | | | |

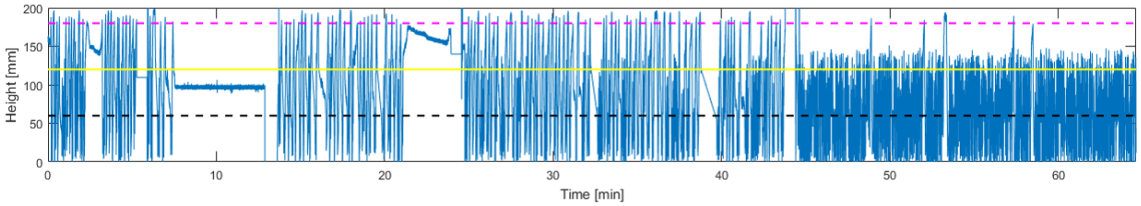
# Appendix C

# PEPT tracer locations

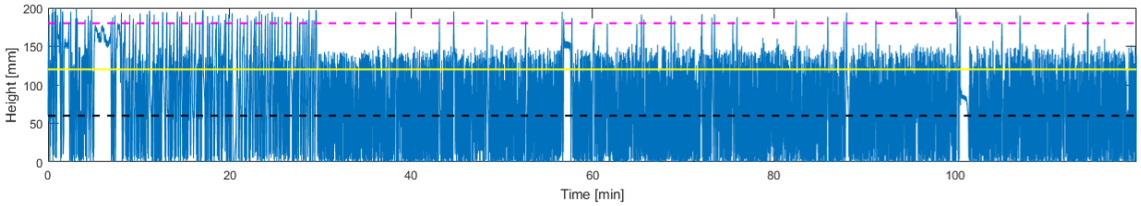
This appendix contains plots of the change of tracer height throughout the cell over time for all tracers used in chapters 6 & 7. The black dashed lines represent the height of the plane of the impeller, the dashed pink lines represent the height of the lip of the cell. The yellow solid lines represent the location of the mesh within the cell.



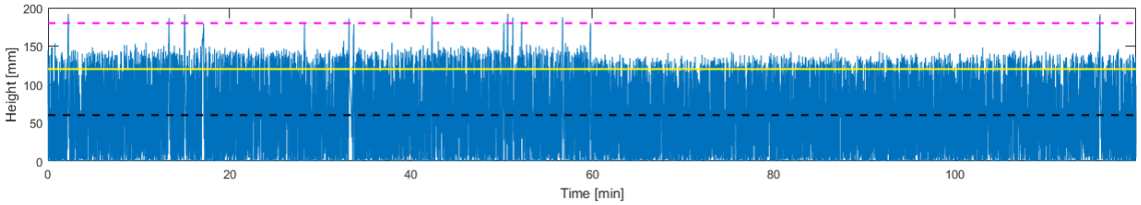

(a) $500\,\mu$m, hydrophilic tracer




(b) $400\,\mu$m, hydrophobic tracer

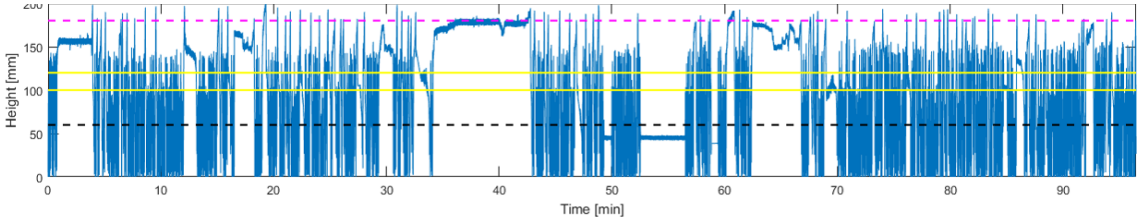



(c) $500\,\mu$m, hydrophobic tracer

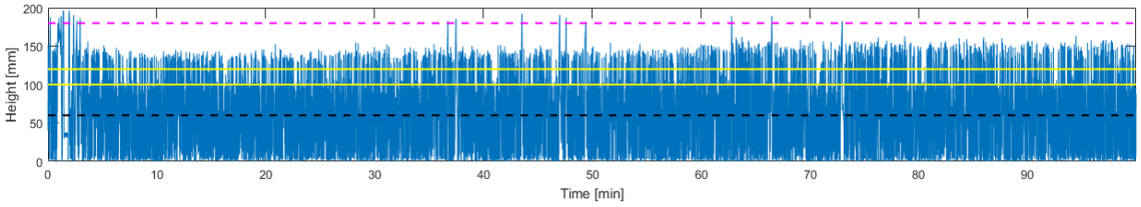



(d) $600\,\mu$m, hydrophobic tracer

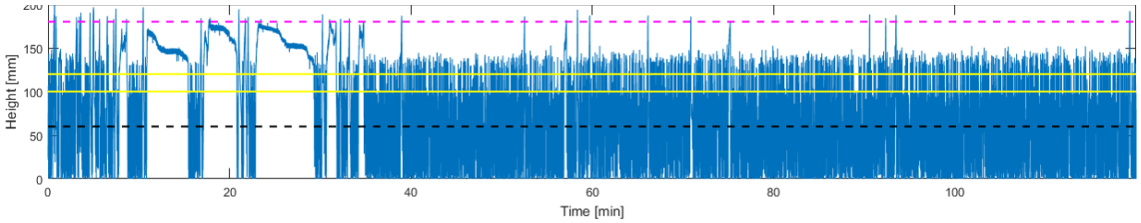
**Figure C.1:** Tracer height over time for tracers in the unmodified cell.



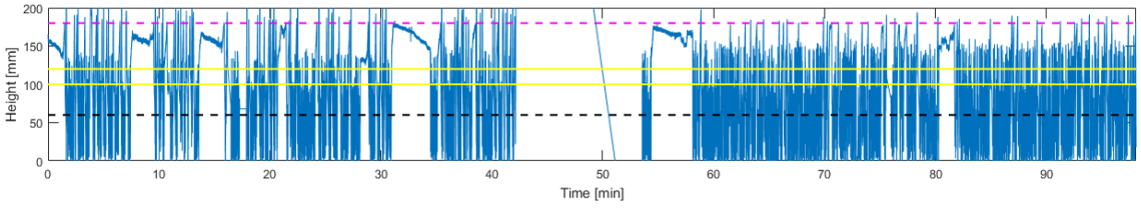

(a) $500\,\mu$m, hydrophilic tracer




(b) $400\,\mu$m, hydrophobic tracer

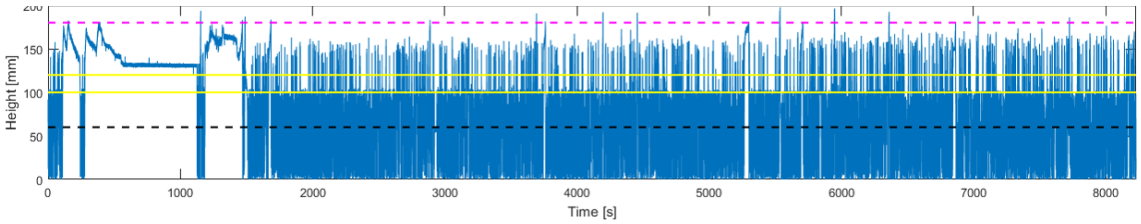



(c) $500\,\mu$m, hydrophobic tracer

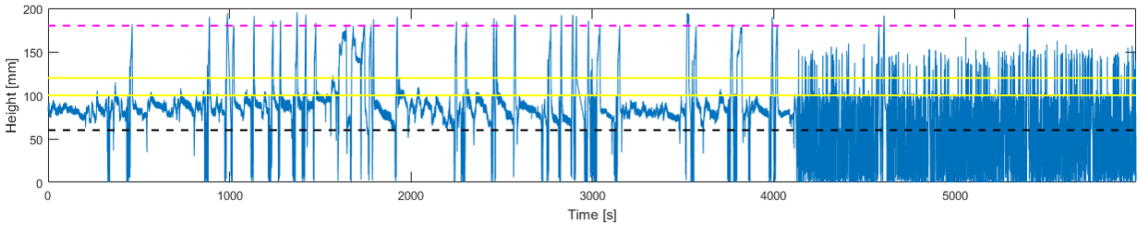



(d) $600\,\mu$m, hydrophobic tracer

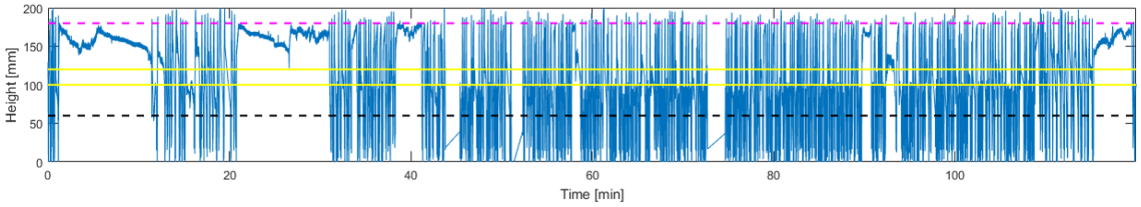
**Figure C.2:** Tracer height over time for tracers with the basic mesh inserted into the cell.



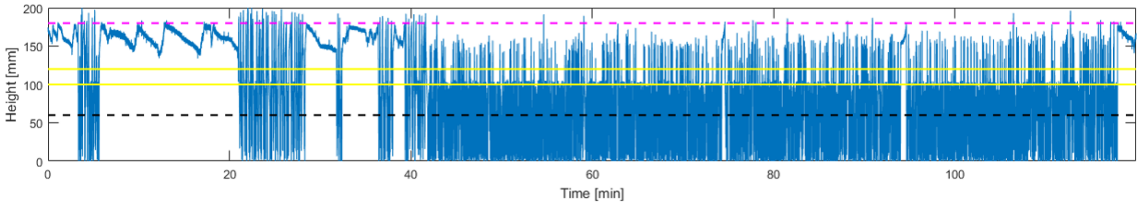

(a) $500\,\mu\mathrm{m}$, hydrophilic tracer




(b) $400\,\mu\mathrm{m}$, hydrophobic tracer




(c) $500\,\mu\mathrm{m}$, hydrophobic tracer




(d) $600\,\mu\mathrm{m}$, hydrophobic tracer

**Figure C.3:** Tracer height over time for tracers with the blocked mesh inserted into the cell.

# Appendix D

# Figure Replication Permissions

**ELSEVIER LICENSE**
**TERMS AND CONDITIONS**

Apr 27, 2019

This Agreement between Miss. Isobel Mackay ("You") and Elsevier ("Elsevier") consists of your license details and the terms and conditions provided by Elsevier and Copyright Clearance Center.

| | |
|---|---|
| License Number | 4577120400621 |
| License date | Apr 27, 2019 |
| Licensed Content Publisher | Elsevier |
| Licensed Content Publication | Minerals Engineering |
| Licensed Content Title | Simple relationships for predicting the recovery of liquid from flowing foams and froths |
| Licensed Content Author | S.J. Neethling,H.T. Lee,J.J. Cilliers |
| Licensed Content Date | Nov 1, 2003 |
| Licensed Content Volume | 16 |
| Licensed Content Issue | 11 |
| Licensed Content Pages | 8 |
| Start Page | 1123 |
| End Page | 1130 |
| Type of Use | reuse in a thesis/dissertation |
| Intended publisher of new work | other |
| Portion | figures/tables/illustrations |
| Number of figures/tables/illustrations | 1 |
| Format | both print and electronic |
| Are you the author of this Elsevier article? | No |
| Will you be translating? | No |
| Original figure numbers | Figure 1 |
| Title of your thesis/dissertation | Investigating flotation at the bench scale - the effect of design modifications on flotation performance and the link to particle size |
| Expected completion date | May 2019 |
| Estimated size (number of pages) | 150 |
| Requestor Location | Miss. Isobel Mackay<br>57 Castle Road<br><br>Salisbury, Wiltshire SP1 3RH<br>United Kingdom<br>Attn: Miss. Isobel Mackay |
| Publisher Tax ID | GB 494 6272 12 |
| Total | 0.00 USD |
| Terms and Conditions | |

## INTRODUCTION

**ELSEVIER LICENSE**
**TERMS AND CONDITIONS**

Aug 22, 2019

This Agreement between Miss. Isobel Mackay ("You") and Elsevier ("Elsevier") consists of your license details and the terms and conditions provided by Elsevier and Copyright Clearance Center.

| | |
|---|---|
| License Number | 4654261262576 |
| License date | Aug 22, 2019 |
| Licensed Content Publisher | Elsevier |
| Licensed Content Publication | Separation and Purification Technology |
| Licensed Content Title | The effect of particle size distribution on froth stability in flotation |
| Licensed Content Author | A. Norori-McCormac,P.R. Brito-Parada,K. Hadler,K. Cole,J.J. Cilliers |
| Licensed Content Date | Aug 31, 2017 |
| Licensed Content Volume | 184 |
| Licensed Content Issue | n/a |
| Licensed Content Pages | 8 |
| Start Page | 240 |
| End Page | 247 |
| Type of Use | reuse in a thesis/dissertation |
| Portion | figures/tables/illustrations |
| Number of figures/tables/illustrations | 2 |
| Format | both print and electronic |
| Are you the author of this Elsevier article? | No |
| Will you be translating? | No |
| Original figure numbers | Figures 6 and 7 |
| Title of your thesis/dissertation | Investigating flotation at the bench scale - the effect of design modifications on flotation performance and the link to particle size |
| Expected completion date | May 2019 |
| Estimated size (number of pages) | 150 |
| Requestor Location | Miss. Isobel Mackay<br>57 Castle Road<br><br>Salisbury, Wiltshire SP1 3RH<br>United Kingdom<br>Attn: Miss. Isobel Mackay |
| Publisher Tax ID | GB 494 6272 12 |
| Total | 0.00 USD |
| Terms and Conditions | |

## INTRODUCTION

1. The publisher for this copyrighted material is Elsevier. By clicking "accept" in connection with completing this licensing transaction, you agree that the following terms and conditions apply to this transaction (along with the Billing and Payment terms and conditions

**ELSEVIER LICENSE**
**TERMS AND CONDITIONS**

Apr 27, 2019

This Agreement between Miss. Isobel Mackay ("You") and Elsevier ("Elsevier") consists of your license details and the terms and conditions provided by Elsevier and Copyright Clearance Center.

| | |
|---|---|
| License Number | 4577120158418 |
| License date | Apr 27, 2019 |
| Licensed Content Publisher | Elsevier |
| Licensed Content Publication | Minerals Engineering |
| Licensed Content Title | Improving coarse particle flotation using the HydroFloat™ (raising the trunk of the elephant curve) |
| Licensed Content Author | J.N. Kohmuench,M.J. Mankosa,H. Thanasekaran,A. Hobert |
| Licensed Content Date | Jun 1, 2018 |
| Licensed Content Volume | 121 |
| Licensed Content Issue | n/a |
| Licensed Content Pages | 9 |
| Start Page | 137 |
| End Page | 145 |
| Type of Use | reuse in a thesis/dissertation |
| Portion | figures/tables/illustrations |
| Number of figures/tables/illustrations | 1 |
| Format | both print and electronic |
| Are you the author of this Elsevier article? | No |
| Will you be translating? | No |
| Original figure numbers | Figure 1 |
| Title of your thesis/dissertation | Investigating flotation at the bench scale - the effect of design modifications on flotation performance and the link to particle size |
| Expected completion date | May 2019 |
| Estimated size (number of pages) | 150 |
| Requestor Location | Miss. Isobel Mackay<br>57 Castle Road<br><br>Salisbury, Wiltshire SP1 3RH<br>United Kingdom<br>Attn: Miss. Isobel Mackay |
| Publisher Tax ID | GB 494 6272 12 |
| Total | 0.00 GBP |
| Terms and Conditions | |

## INTRODUCTION

1. The publisher for this copyrighted material is Elsevier. By clicking "accept" in connection with completing this licensing transaction, you agree that the following terms and conditions apply to this transaction (along with the Billing and Payment terms and conditions

established by Copyright Clearance Center, Inc. ("CCC"), at the time that you opened your Rightslink account and that are available at any time at http://myaccount.copyright.com).

**GENERAL TERMS**

2. Elsevier hereby grants you permission to reproduce the aforementioned material subject to the terms and conditions indicated.

3. Acknowledgement: If any part of the material to be used (for example, figures) has appeared in our publication with credit or acknowledgement to another source, permission must also be sought from that source. If such permission is not obtained then that material may not be included in your publication/copies. Suitable acknowledgement to the source must be made, either as a footnote or in a reference list at the end of your publication, as follows:

"Reprinted from Publication title, Vol /edition number, Author(s), Title of article / title of chapter, Pages No., Copyright (Year), with permission from Elsevier [OR APPLICABLE SOCIETY COPYRIGHT OWNER]." Also Lancet special credit - "Reprinted from The Lancet, Vol. number, Author(s), Title of article, Pages No., Copyright (Year), with permission from Elsevier."

4. Reproduction of this material is confined to the purpose and/or media for which permission is hereby given.

5. Altering/Modifying Material: Not Permitted. However figures and illustrations may be altered/adapted minimally to serve your work. Any other abbreviations, additions, deletions and/or any other alterations shall be made only with prior written authorization of Elsevier Ltd. (Please contact Elsevier at permissions@elsevier.com). No modifications can be made to any Lancet figures/tables and they must be reproduced in full.

6. If the permission fee for the requested use of our material is waived in this instance, please be advised that your future requests for Elsevier materials may attract a fee.

7. Reservation of Rights: Publisher reserves all rights not specifically granted in the combination of (i) the license details provided by you and accepted in the course of this licensing transaction, (ii) these terms and conditions and (iii) CCC's Billing and Payment terms and conditions.

8. License Contingent Upon Payment: While you may exercise the rights licensed immediately upon issuance of the license at the end of the licensing process for the transaction, provided that you have disclosed complete and accurate details of your proposed use, no license is finally effective unless and until full payment is received from you (either by publisher or by CCC) as provided in CCC's Billing and Payment terms and conditions. If full payment is not received on a timely basis, then any license preliminarily granted shall be deemed automatically revoked and shall be void as if never granted. Further, in the event that you breach any of these terms and conditions or any of CCC's Billing and Payment terms and conditions, the license is automatically revoked and shall be void as if never granted. Use of materials as described in a revoked license, as well as any use of the materials beyond the scope of an unrevoked license, may constitute copyright infringement and publisher reserves the right to take any and all action to protect its copyright in the materials.

9. Warranties: Publisher makes no representations or warranties with respect to the licensed material.

10. Indemnity: You hereby indemnify and agree to hold harmless publisher and CCC, and their respective officers, directors, employees and agents, from and against any and all claims arising out of your use of the licensed material other than as specifically authorized pursuant to this license.

11. No Transfer of License: This license is personal to you and may not be sublicensed, assigned, or transferred by you to any other person without publisher's written permission.

12. No Amendment Except in Writing: This license may not be amended except in a writing signed by both parties (or, in the case of publisher, by CCC on publisher's behalf).

13. Objection to Contrary Terms: Publisher hereby objects to any terms contained in any purchase order, acknowledgment, check endorsement or other writing prepared by you, which terms are inconsistent with these terms and conditions or CCC's Billing and Payment terms and conditions. These terms and conditions, together with CCC's Billing and Payment terms and conditions (which are incorporated herein), comprise the entire agreement between you and publisher (and CCC) concerning this licensing transaction. In the event of

any conflict between your obligations established by these terms and conditions and those established by CCC's Billing and Payment terms and conditions, these terms and conditions shall control.

14. Revocation: Elsevier or Copyright Clearance Center may deny the permissions described in this License at their sole discretion, for any reason or no reason, with a full refund payable to you. Notice of such denial will be made using the contact information provided by you. Failure to receive such notice will not alter or invalidate the denial. In no event will Elsevier or Copyright Clearance Center be responsible or liable for any costs, expenses or damage incurred by you as a result of a denial of your permission request, other than a refund of the amount(s) paid by you to Elsevier and/or Copyright Clearance Center for denied permissions.

**LIMITED LICENSE**

The following terms and conditions apply only to specific license types:

15. **Translation**: This permission is granted for non-exclusive world **English** rights only unless your license was granted for translation rights. If you licensed translation rights you may only translate this content into the languages you requested. A professional translator must perform all translations and reproduce the content word for word preserving the integrity of the article.

16. **Posting licensed content on any Website**: The following terms and conditions apply as follows: Licensing material from an Elsevier journal: All content posted to the web site must maintain the copyright information line on the bottom of each image; A hyper-text must be included to the Homepage of the journal from which you are licensing at http://www.sciencedirect.com/science/journal/xxxxx or the Elsevier homepage for books at http://www.elsevier.com; Central Storage: This license does not include permission for a scanned version of the material to be stored in a central repository such as that provided by Heron/XanEdu.

Licensing material from an Elsevier book: A hyper-text link must be included to the Elsevier homepage at http://www.elsevier.com . All content posted to the web site must maintain the copyright information line on the bottom of each image.

**Posting licensed content on Electronic reserve**: In addition to the above the following clauses are applicable: The web site must be password-protected and made available only to bona fide students registered on a relevant course. This permission is granted for 1 year only. You may obtain a new license for future website posting.

17. **For journal authors:** the following clauses are applicable in addition to the above:

**Preprints:**

A preprint is an author's own write-up of research results and analysis, it has not been peer-reviewed, nor has it had any other value added to it by a publisher (such as formatting, copyright, technical enhancement etc.).

Authors can share their preprints anywhere at any time. Preprints should not be added to or enhanced in any way in order to appear more like, or to substitute for, the final versions of articles however authors can update their preprints on arXiv or RePEc with their Accepted Author Manuscript (see below).

If accepted for publication, we encourage authors to link from the preprint to their formal publication via its DOI. Millions of researchers have access to the formal publications on ScienceDirect, and so links will help users to find, access, cite and use the best available version. Please note that Cell Press, The Lancet and some society-owned have different preprint policies. Information on these policies is available on the journal homepage.

**Accepted Author Manuscripts:** An accepted author manuscript is the manuscript of an article that has been accepted for publication and which typically includes author-incorporated changes suggested during submission, peer review and editor-author communications.

Authors can share their accepted author manuscript:

- immediately
    - via their non-commercial person homepage or blog
    - by updating a preprint in arXiv or RePEc with the accepted manuscript

- via their research institute or institutional repository for internal institutional uses or as part of an invitation-only research collaboration work-group
- directly by providing copies to their students or to research collaborators for their personal use
- for private scholarly sharing as part of an invitation-only work group on commercial sites with which Elsevier has an agreement

- After the embargo period
  - via non-commercial hosting platforms such as their institutional repository
  - via commercial sites with which Elsevier has an agreement

In all cases accepted manuscripts should:

- link to the formal publication via its DOI
- bear a CC-BY-NC-ND license - this is easy to do
- if aggregated with other manuscripts, for example in a repository or other site, be shared in alignment with our hosting policy not be added to or enhanced in any way to appear more like, or to substitute for, the published journal article.

**Published journal article (JPA):** A published journal article (PJA) is the definitive final record of published research that appears or will appear in the journal and embodies all value-adding publishing activities including peer review co-ordination, copy-editing, formatting, (if relevant) pagination and online enrichment.
Policies for sharing publishing journal articles differ for subscription and gold open access articles:
**Subscription Articles:** If you are an author, please share a link to your article rather than the full-text. Millions of researchers have access to the formal publications on ScienceDirect, and so links will help your users to find, access, cite, and use the best available version.
Theses and dissertations which contain embedded PJAs as part of the formal submission can be posted publicly by the awarding institution with DOI links back to the formal publications on ScienceDirect.
If you are affiliated with a library that subscribes to ScienceDirect you have additional private sharing rights for others' research accessed under that agreement. This includes use for classroom teaching and internal training at the institution (including use in course packs and courseware programs), and inclusion of the article for grant funding purposes.
**Gold Open Access Articles:** May be shared according to the author-selected end-user license and should contain a CrossMark logo, the end user license, and a DOI link to the formal publication on ScienceDirect.
Please refer to Elsevier's posting policy for further information.
18. **For book authors** the following clauses are applicable in addition to the above:
Authors are permitted to place a brief summary of their work online only. You are not allowed to download and post the published electronic version of your chapter, nor may you scan the printed edition to create an electronic version. **Posting to a repository:** Authors are permitted to post a summary of their chapter only in their institution's repository.
19. **Thesis/Dissertation**: If your license is for use in a thesis/dissertation your thesis may be submitted to your institution in either print or electronic form. Should your thesis be published commercially, please reapply for permission. These requirements include permission for the Library and Archives of Canada to supply single copies, on demand, of the complete thesis and include permission for Proquest/UMI to supply single copies, on demand, of the complete thesis. Should your thesis be published commercially, please reapply for permission. Theses and dissertations which contain embedded PJAs as part of the formal submission can be posted publicly by the awarding institution with DOI links back to the formal publications on ScienceDirect.

**Elsevier Open Access Terms and Conditions**
You can publish open access with Elsevier in hundreds of open access journals or in nearly 2000 established subscription journals that support open access publishing. Permitted third party re-use of these open access articles is defined by the author's choice of Creative Commons user license. See our open access license policy for more information.

**Terms & Conditions applicable to all Open Access articles published with Elsevier:**
Any reuse of the article must not represent the author as endorsing the adaptation of the article nor should the article be modified in such a way as to damage the author's honour or reputation. If any changes have been made, such changes must be clearly indicated.
The author(s) must be appropriately credited and we ask that you include the end user license and a DOI link to the formal publication on ScienceDirect.
If any part of the material to be used (for example, figures) has appeared in our publication with credit or acknowledgement to another source it is the responsibility of the user to ensure their reuse complies with the terms and conditions determined by the rights holder.
**Additional Terms & Conditions applicable to each Creative Commons user license:**
**CC BY:** The CC-BY license allows users to copy, to create extracts, abstracts and new works from the Article, to alter and revise the Article and to make commercial use of the Article (including reuse and/or resale of the Article by commercial entities), provided the user gives appropriate credit (with a link to the formal publication through the relevant DOI), provides a link to the license, indicates if changes were made and the licensor is not represented as endorsing the use made of the work. The full details of the license are available at http://creativecommons.org/licenses/by/4.0.
**CC BY NC SA:** The CC BY-NC-SA license allows users to copy, to create extracts, abstracts and new works from the Article, to alter and revise the Article, provided this is not done for commercial purposes, and that the user gives appropriate credit (with a link to the formal publication through the relevant DOI), provides a link to the license, indicates if changes were made and the licensor is not represented as endorsing the use made of the work. Further, any new works must be made available on the same conditions. The full details of the license are available at http://creativecommons.org/licenses/by-nc-sa/4.0.
**CC BY NC ND:** The CC BY-NC-ND license allows users to copy and distribute the Article, provided this is not done for commercial purposes and further does not permit distribution of the Article if it is changed or edited in any way, and provided the user gives appropriate credit (with a link to the formal publication through the relevant DOI), provides a link to the license, and that the licensor is not represented as endorsing the use made of the work. The full details of the license are available at http://creativecommons.org/licenses/by-nc-nd/4.0.
Any commercial reuse of Open Access articles published with a CC BY NC SA or CC BY NC ND license requires permission from Elsevier and will be subject to a fee.
Commercial reuse includes:

- Associating advertising with the full text of the Article
- Charging fees for document delivery or access
- Article aggregation
- Systematic distribution via e-mail lists or share buttons

Posting or linking by commercial companies for use by customers of those companies.

20. **Other Conditions**:

v1.9

**Questions? customercare@copyright.com or +1-855-239-3415 (toll free in the US) or +1-978-646-2777.**